Abstract

Title of dissertation:	HIGH STRENGTH SEMI-ACTIVE ENERGY ABSORBERS USING SHEAR- AND MIXED-MODE OPERATION AT HIGH SHEAR RATES
	Andrew Craig Becnel Doctor of Philosophy, 2014
Dissertation directed by:	Professor Norman M. Wereley Department of Aerospace Engineering

This body of research expands the design space of semi-active energy absorbers for shock isolation and crash safety by investigating and characterizing magnetorheological fluids (MRFs) at high shear rates (> 25,000 s^{-1}) under shear and mixed-mode operation. Magnetorheological energy absorbers (MREAs) work well as adaptive isolators due to their ability to quickly and controllably adjust to changes in system mass or impact speed while providing fail-safe operation. However, typical linear stroking MREAs using pressure-driven flows have been shown to exhibit reduced controllability as impact speed (shear rate) increases. The objective of this work is to develop MREAs that improve controllability at high shear rates by using pure shear and mixed shear-squeeze modes of operation, and to present the fundamental theory and models of MR fluids under these conditions.

A proof of concept instrument verified that the MR effect persists in shear mode devices at shear rates corresponding to low speed impacts. This instrument, a concentric cylinder Searle

cell magnetorheometer, was then used to characterize three commercially available MRFs across a wide range of shear rates, applied magnetic fields, and temperatures. Characterization results are presented both as flow curves according to established practice, and as an alternate nondimensionalized analysis based on Mason number. The Mason number plots show that, with appropriate correction coefficients for operating temperature, the varied flow curve data can be collapsed to a single master curve. This work represents the first shear mode characterization of MRFs at shear rates over 10 times greater than available with commercial rheometers, as well as the first validation of Mason number analysis to high shear rate flows in MRFs.

Using the results from the magnetorheometer, a full scale rotary vane MREA was developed as part of the Lightweight Magnetorheological Energy Absorber System (LMEAS) for an SH-60 Seahawk helicopter crew seat. Characterization tests were carried out on the LMEAS using a 40 vol% MRF used in the previous magnetorheometer tests. These were analyzed using both flow curves and apparent viscosity vs. Mason number diagrams. The nondimensionalized Mason number analysis resulted in data for all conditions of temperature, fluid composition, and shear rate, to collapse onto a single characteristic or master curve. Significantly, the temperature corrected Mason number results from both the bench top magnetorheometer and full scale rotary vane MREA collapse to the same master curve. This enhances the ability of designers of MRFs and MREAs to safely and effectively apply characterization data collected in low shear rate, controlled temperature environments to operational environments that may be completely different.

Finally, the Searle cell magnetorheometer was modified with an enforced eccentricity to work in both squeeze and shear modes simultaneously to achieve so called squeeze strengthening of

the working MRF, thereby increasing the apparent yield stress and the specific energy absorption. By squeezing the active MR fluid, particles undergo compression-assisted aggregation into stronger, more robust columns which resist shear better than single chains. A hybrid model describing the squeeze strengthening behavior is developed, and recommendations are made for using squeeze strengthening to improve practical MREA devices.

HIGH STRENGTH SEMI-ACTIVE ENERGY ABSORBERS USING SHEAR- AND MIXED-MODE OPERATION AT HIGH SHEAR RATES

by

Andrew C. Becnel

Dissertation submitted to the Faculty of the Graduate School of the
University of Maryland, College Park in partial fulfillment
of the requirements for the degree of
Doctor of Philosophy
2014

Advisory Committee:
Professor Norman M. Wereley, Chair/Advisor
Professor David Akin
Professor Inderjit Chopra
Professor Sung Lee
Professor Alison Flatau
Professor Amr Baz

Preface

The Illustrated Guide to a Ph.D.

Imagine a circle that contains all of human knowledge:

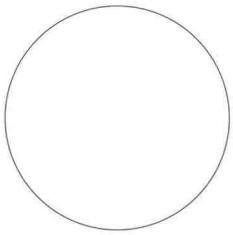

By the time you finish elementary school, you know a little:

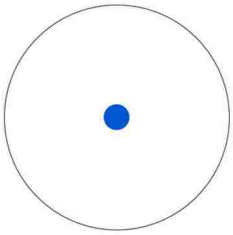

By the time you finish high school, you know a bit more:

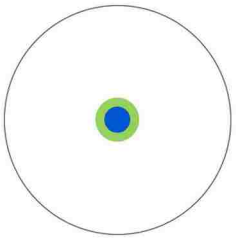

With a bachelor's degree, you gain a specialty:

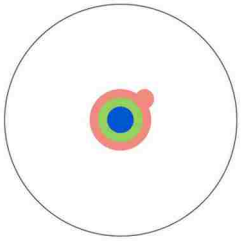

A master's degree deepens that specialty:

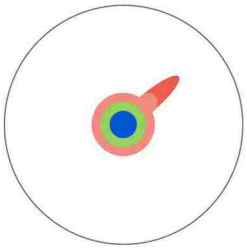

Reading research papers takes you to the edge of human knowledge:

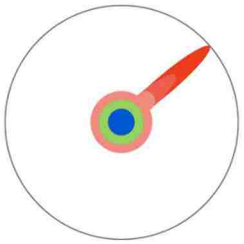

Once you're at the boundary, you focus:

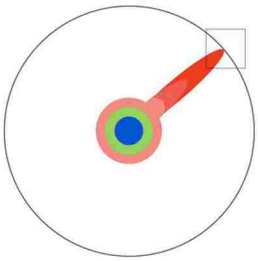

You push at the boundary for a few years:

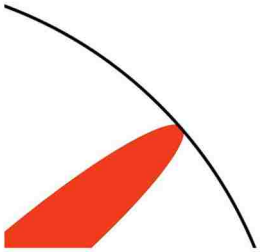

Until one day, the boundary gives way:

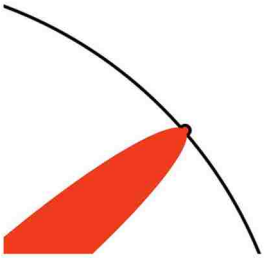

And, that dent you've made is called a Ph.D.:

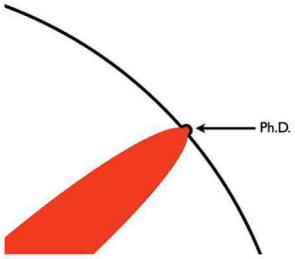

Of course, the world looks different to you now:

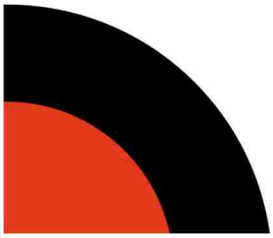

So, don't forget the bigger picture:

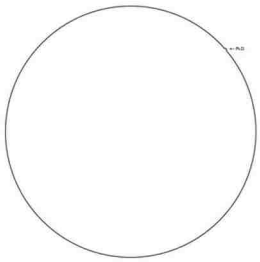

Keep pushing.

Dedication

This work is dedicated to my parents, Steve and Donna, for believing in and supporting me to pursue my dreams; to my sister, Steph, who always encouraged me to do so; and to my wife, Julie, who inspires me every day to never stop pushing.

Acknowledgements

Foremost in credit to my success and accomplishments while pursuing my M.S. and Ph.D., I have to give thanks to Dr. Norman Wereley for all of the support and guidance he has given me during my time at Maryland. From our first contact to discuss my coming to Maryland, to my decision to continue on through the Ph.D. program, and finally finishing the dissertation and defense, his even-handed and circumspect mentorship is the main reason I arrived where I am today. I can honestly say that had I had another adviser, I might not have made it through getting my Master's and I certainly would not have chosen to continue with my doctorate. He's very good at what he does while hardly making a point about doing anything at all, and is a role model for the kind of engineer and mentor that I'd like to become.

I'd also like to thank my dissertation committee members for their support and valuable contributions to this research. Dr. Inder Chopra, Dr. Sung Lee, Dr. Dave Akin, and Dr. Amr Baz have each enriched my time at Maryland with their unique perspectives and interesting stories. Dr. Alison Flatau offered me great support, critically in the form of numerous letters of recommendation.

Dr. Peter Hu helped me immensely, especially in my first few years, and though he already knows everything about MR fluids, he's still excited to learn more and improve his craft. Dr. Greg Hiemenz is an excellent engineer and an adept program manager, and I learned much from both his technical and non-technical guidance. Dr. Young Choi, Dr. Grum Ngatu, and Dr. Anirban Chaudhuri each provided valuable resources throughout my work.

The front office staff, Otto, Becky, Erika, Tom, Lavita, Deborah, Elton, and Mike deserve all of the credit for guiding me and my fellow students through paperwork and ensuring that we receive continuous financial support and meet important deadlines.

I'll have to start leaving out the formal "Dr." title from here on, but suffice to say just about everyone mentioned is either a current or soon-to-be Ph.D.

The No Talent Grass Clowns, our resident Aero department intramural soccer team, always served as a welcome reminder just how much fun grad school can be. In particular, Greg, Aaron, Joe, Voegele, and Hyslop, the Aussie rules football organizer at annual Man Weekends.

Ben Woods, Nick Wilson, Robbie Vocke, Hari Singh, Ami Powell, Ryan Robinson, Erika Hocking, Steve Sherman, and Tom Pillsbury have each, at many times, contributed to this work by helping me find a tool, understand a MATLAB function, complete a homework on time, or slog through a particularly difficult derivation or nondimensionalization. The atmosphere of our lab group, created and encouraged by Dr. Wereley, is another major component in me choosing to continue and making it to the end. Our group represents an interesting paradox, in that without them I would have both never begun my doctorate and finished it much faster.

My parents, sister, parents-in-law, and sister-in-law showed patience, support, encouragement, and willingness to travel cross-country for visits. My grandparents, aunts, uncles, cousins, and friends back home let me know that I was still on their minds. And of course my wife, Julie, who supported me in every way imaginable, always set a good example and never accepted anything but my best; I love you.

Table of Contents

List of Tables

List of Figures

Nomenclature

DR	Dynamic range or dynamic ratio
$\dot{\gamma}$	Shear rate, 1/s or s^{-1}
$\tau_{r\theta}$	Shear stress along the radial direction due to angular rotation, Pa
M	Moment measured by torque sensor, N m
Ω	Rotation speed, RPM
L_c	Active length of magnetorheometer bob, m
ω_i	Angular velocity, rad/s
r_c	Radius at cup inner wall, m
r_b	Radius at bob outer wall, m
τ_c	Shear stress at cup inner wall, Pa
τ_b	Shear stress at bob outer wall, Pa
v_θ	Angular component of fluid velocity, m/s
h	Active gap height, m
R	Bob radius, inner radius of active gap, m
R_c	Flux path inner radius, m
R_b	Bob minor radius, m
R_m	Coil outer radius, m
R_o	Flux path outer radius, m
L_m	Flux path length, m
L_p	Bob path length, m
N	Number of coil turns
Re	Reynolds number
ρ	Fluid density, kg/m^3
η_d	Fluid dynamic viscosity, Pa s
Ta	Taylor number
Φ_B	Magnetic flux, Wb
B	Magnetic flux density, T
I	Current, A
H	Magnetic field strength, A/m
M	Magnetization, A/m
B_{MR}	Magnetic flux density in active MR fluid, T
B_{s1}	Magnetic flux density in steel flux path 1
B_{s2}	Magnetic flux density in steel flux path 2
B_{s3}	Magnetic flux density in steel flux path 3
A_g	Cross sectional area of active gap, m^2
A_b	Cross sectional area of bob, m^2
A_o	Cross sectional area of outer flux path, m^2
H_g	Magnetic field strength in active gap, A/m

H_{s1}	Magnetic field strength in steel flux path 1, A/m
H_{s2}	Magnetic field strength in steel flux path 2, A/m
H_{s3}	Magnetic field strength in steel flux path 3, A/m
P_i	Magnetic potential at point i, A
K_p	Potential coil calibration constant
T_R	Temperature at thermocouple measurement point, °C
T_r	Temperature at arbitrary radius, °C
k	Thermal conductivity, W/m K
η	Apparent viscosity, Pa s
τ	Shear stress, Pa
τ_y	Yield stress, Pa
K	Consistency, Pa^n
n	Flow index
η_{ex}	Experimentally measured apparent viscosity, Pa
η_{HB}	Predicted apparent viscosity from Herschel-Bulkley model, Pa
η_0	Reference apparent viscosity, Pa s
β	Thermal scaling factor
T	Temperature, °C
T_o	Reference temperature, °C
η_o	Reference viscosity, Pa s
Mn	Mason number, as developed in Klingenberg, 2007
F^H	Hydrodynamic force, N
F_0	Polarization force, N
η_c	Carrier fluid viscosity, Pa s
a	Particle radius, m
m	Magnetic moment, A m^2
σ	Particle diameter, m
M_p	Particle magnetization, A/m
ϕ	Solids loading fraction
$\langle M \rangle$	Bulk magnetization, A/m
μ_0	Permeability of free space, = $4\pi \times 10^{-7}$ V s / A m
μ_c	Carrier fluid permeability V s / A m
Mn^*	Adjusted Mason number, = 32·Mn, Sherman & Wereley, 2013
M_0	Magnetization at T = 0K, A/m
T_B	Bloch temperature, K
T_C	Curie temperature, K
η_∞	High shear rate, field-off apparent viscosity, Pa s
η_N	Normalized apparent viscosity
F_{active}	Active or yield component of MR force, N

$F_{passive}$	Passive or viscous component of MR force, N
F_y	Yield force, N
F_L	Maximum desired stroking load, N
F_v	Viscous component of total force, N
F_k	Spring stiffness component of total force, N
F_T	Total transmitted force, N
c	Viscous damping coefficient, Pa s^2 /m
R_s	Shaft radius, m
v_{max}	Maximum sink rate, m/s
L_v	Rotary vane length, m
P	Gear ratio between rotary shaft and seat system
R_a	Coil armature outer radius, m
R_d	Damper body inner radius, m
$R_{v,i}$	Rotary vane inner radius, m
$R_{v,o}$	Rotary vane outer radius, m
h_i	Inner active gap height, m
h_o	Outer active gap height, m
K_{cr}	Critical Mason number fit parameter
τ^*	Interparticle reference stress, Pa
H_{crit}	Critical magnetic field strength, kA/m
τ_c	Conventional yield stress, Pa
τ_{SS}	Squeeze strengthened component of yield stress, Pa
τ_y^0	Non-strengthened yield stress, Pa
P_e	Compressive stress, Pa
τ_{ij}	Stress in the j^{th} axis from a strain along the i^{th} direction, Pa
σ_n	Normal stress on plane with normal direction *n*, Pa
τ_n	Shear stress on plane with normal direction *n*, Pa
Φ	Internal friction or "von Mises" stress angle, rad
τ_f	Interfacial film stress, Pa
τ_0	Particle shear stress, Pa
C	Ratio of film stress and particle stress
σ_s	Interparticle sliding stress, Pa
a_{ss}	Ratio of the squares of particle sliding stress and shear strength
F_τ	Shear component of force, N
F_σ	Normal component of force, N
F_{total}	Total force, N
ε_s	Squeeze strain, m/m
ϵ	Eccentricity
G	Fluid shear modulus, Pa

Acronyms & Abbreviations

ER	Electorheological
MR	Magnetorheological
EA	Energy Absorber
MRF	Magnetorheological Fluid
MREA	Magnetorheological Energy Absorber
Vol%	Percent-By-Volume
SS	Squeeze Strengthening
CAA	Compression Assisted Aggregation
FEA	Finite Element Analysis
AISI	American Iron and Steel Institute
AWG	American Wire Gauge
BP	Bingham plastic
HB	Herschel-Bulkley
SGA	Simple Genetic Algorithm
LMEAS	Lightweight Magnetorheological Energy Absorber System
FLEA	Fixed Load Energy Absorber
VLEA	Variable Load Energy Absorber
AATD	US Army's Aviation Applied Technology Directorate
SDOF	Single Degree of Freedom
BCT	Body Centered Tetragonal

Chapter 1

1. INTRODUCTION TO MAGNETORHEOLOGICAL FLUIDS AND ENERGY ABSORBERS

1.1. Motivation

The need to protect crew from deleterious vibration during normal vehicle operation and serious injury during a shock or crash event has resulted in a large body of research into effective energy absorption methods and devices. The overarching motivation of this work is to comprehensively report the theory, development and performance of a class of novel energy absorbers that advances the current state of the art. Improvements in operating range (both increased velocity and wider temperature variations), specific energy dissipation, and an improved unified analysis method will be discussed after a brief introduction to the field of energy absorbing devices.

1.2. Damping Techniques

Tuned mass dampers are additional stiffness or mass elements that shift the natural response of the entire system and have been shown to be effective at reducing vibration amplitude near resonance, but because they contain no energy dissipating component and are not effective at absorbing impact energy, they only address one half of the problem. Energy dissipating devices are classified as either passive, active, or semi-active depending on the nature of their force/velocity

characteristics. Passive devices such as viscous fluid, dry friction, or plastic deformation energy absorbers can be simple, compact, and are inherently stable because they are unable to introduce additional energy into the system. Despite these attractive qualities, they have a fixed force vs. velocity behavior and are therefore unable to adapt to perturbations away from a single system design point. Active systems, such as hydraulic or pneumatic energy absorbers, piezo-electrics, or electric motors can offer fully customizable force vs. velocity profiles and high force output. However, because they can inject energy into the system, they require robust control algorithms to ensure stability, along with the more complex and sometimes bulky supporting infrastructure needed to operate. Additionally, in the event of a power or control circuit failure they have no fail-safe energy absorption capabilities.

Semi-active systems combine the benefits of both passive and active damping systems to provide fail-safe protection and adjustable energy absorbing characteristics across a wide range of both vibration and shock inputs. For example, a passive system may be tuned to protect a 50th percentile male occupant during a typical shock event, but will fail to adequately protect occupants of varying weight with proportionately varying injury thresholds. Moreover, such a system would not adequately protect the 50^{th} percentile male occupant from other shock loads or from harmful whole-body vibration. Therefore, exchanging a passive seat suspension with an adaptive seat suspension system, which is capable of tuning damping for varying operating conditions (disturbance level and type) and occupant weight, would be a straightforward way to increase vibration isolation and improve injury protection for vehicle crew.

Examples of such semi-active devices include mechanically adjustable bypass orifices and electrorheological (ER) and magnetorheological (MR) energy absorbers (EAs). Able to vary their force-velocity profile, these devices can therefore be used to adaptively absorb the desired amount

of energy either from high frequency vibrations or high energy shock impacts. Because they use viscous forces to only dissipate energy from the system, they are both inherently stable and provide fail-safe operation. Among these semi-active options, only MR fluid devices offer the force levels and response times needed to address occupant protection challenges.

1.3. Magnetorheological Fluids

The discovery and development of the first MR fluids and devices in the late 1940s can be credited to Jacob Rabinow at the US National Bureau of Standards (Rabinow, 1948; Rabinow, 1951). A magnetorheological fluid (MRF) consists of magnetizable particles suspended in a nonmagnetizable carrier fluid. Commercially available MRFs use carbonyl iron spheres on the order of 1-10 microns in diameter as the magnetizable particles, either a silicon- or hydrocarbon-based oil as the carrier fluid, and various additives to improve stability and settling rate.

In the absence of an applied magnetic field, the particles are randomly dispersed and will move with the fluid as it flows. When exposed to a magnetic field, the particles form chains parallel to the magnetic field lines and the MRF "solidifies." These two conditions of MRF, called "passive" and "active" respectively, can be seen in Figure 1.1. The particle chains resist fluid motion until a certain yield stress is reached, beyond which fluid motion will occur, called post-yield flow (Jolly et al., 1999).

In practical MRF devices, the magnetic field is produced by a controllable electromagnet. In this way the applied magnetic field, and thus the yield stress, can be continuously and instantaneously adjusted (response time < 15 milliseconds), so that an appropriate amount of energy can be dissipated within the MREA. A typical set of yield stress and magnetization curves for two commercially available MRFs, 32 vol% and 40 vol% hydrocarbon-based fluids, are shown in

Figure 1.2 (LORD Corporation, 2012). A well-developed MRF used in production devices will have a yield stress from 30 to 100 kPa at magnetic saturation.

1.4. MR Devices and Applications

When combined with an appropriate feedback control system, magnetorheological energy absorbers (MREAs) adjust their energy absorption characteristics - especially stroking load – to variations in the system or its inputs, such as occupant weight or impact velocity. Even though MREAs have a low *off-state* (absence of magnetic field) velocity dependent (viscous) stroking load and produce a much higher stroking load in the *on-state* (maximum applied field), they do exhibit reduced performance at higher speeds, as defined by their dynamic range. Dynamic range, i.e. the ratio of the on-state force to the off-state stroking load shown in the following equation, is a common metric used to quantify the controllability of an MREA.

$$DR = F_{field\ on} / F_{field\ off} \tag{1.1}$$

Because they are viscous (velocity-dependent) components, devices must generate motion of MR fluid between two poles of a controllable electromagnet. There are three different modes of operation which MR devices can use to generate fluid stress and damping force, and these modes can be combined in mixed-mode operation.

1.4.1. Flow mode

In flow mode operation, also called valve mode or Poiseuille flow, a pressure gradient forces the MR fluid to flow between two stationary parallel plates, shown in Figure 1.3a. The magnetic field intensity within the valve regulates strength of the MR chains, which are aligned with the magnetic flux lines and perpendicular to the valve walls, thus controlling the force required to induce fluid flow.

Examples of operational flow mode MREAs include landing gear for aircraft (Batterbee et al., 2007; Choi and Wereley, 2004), primary suspensions for automobiles (Carlson et al., 1996), seismic damping elements for civil structures (Jolly et al., 1999), and lag dampers for helicopter main rotors (Hu and Wereley, 2005). Flow mode operation allows for hydraulic amplification, which is particularly useful for high force applications such as crash and impact shock absorption. The design and investigation of several semi-active crashworthy seat solutions has been reported for ground vehicles exposed to mine blasts (Choi and Wereley, 2005), combined vibration and shock protection for helicopter crews (Hiemenz et al., 2007), automobile crash safety systems (Mao, 2011), and high speed amphibious vehicles (Becnel et al., 2010). These crashworthy systems are all based on linear stroke energy absorbers, and have been shown to be effective in mitigating the potential for crew injuries in simulated crashes. In these linear stroking MR crashworthiness systems, an electromagnet piston forces fluid between two chambers of a cylinder through an annular MR valve, shown in Figure 1.4.

The aforementioned high speed limitations on controllability of linear stroke MREA-based systems are attributed to the inherent flow profile and viscous losses within the flow channel. Forcing the fluid through a complex annulus adds to this nonlinear viscous behavior, since minor losses, such as entrance/exit flows and sudden contractions/expansions, give rise to viscous pressure drops. Because these losses are given by the product of a Reynolds number-dependent discharge coefficient and the flow velocity squared, it has been shown that force output in flow mode devices is proportional to the square of fluid velocity, or $F \propto v^2$ (Choi et al., 2005). Thus, during high velocity crash scenarios the passive force component of flow mode devices quickly dominates the yield force component, leading to a reduction in dynamic range (down to $DR \leq 2$ at high $\dot{\gamma}$) (Mao et al., 2007).

This has motivated the development of MREA designs that overcome the high speed limitations of linear stroke MREAs.

1.4.2. Shear mode

In shear mode operation, also called Couette flow, one side of the active gap translates parallel to the other, directly shearing the MR fluid as shown in Figure 1.3b. A perpendicular magnetic field is applied across the plates, and the stress required to yield the MR particle chains via direct shearing can be modulated by applied field strength. Because there is no pressure driven flow through complex annuli, shear mode devices can be mechanically simpler than linear stroke devices, and with appropriate transmissions are well suited to both rotational and linear applications. Most importantly, shear mode operation allows for high dynamic range due to low field-off stresses. The force generated in shear mode operation is linearly proportional to the input velocity, or $F \propto v$. A shear mode device will therefore relatively minimize the detrimental passive force increases and maintain good controllability ($DR \geq 3$) at high velocities (Choi et al., 2005). A comparison between the force-velocity behavior of MR fluids in flow and shear mode operation is presented in Figure 1.5.

Shear mode devices typically have either direct shear, rotating plate, or rotary drum geometries (Wereley et al., 2008). Examples of shear mode devices include rotary clutches and brakes (Dong-won et al., 2009) (Guo and Liao, 2012), rotary dampers for occupant crash protection in helicopters (Hiemenz and Wereley, 2010), and fluid rheometry testing machines. Both devices presented in this research use the rotary drum configuration, in which one magnetic pole is rotated within a stationary, concentric pole to shear the MR fluid within the fluid chamber.

Squeeze mode

Squeeze mode operation utilizes a change in the active gap size parallel to the magnetic flux lines as in Figure 1.3c. This applies a stress along the axis of the MR chains within the fluid, causing the individual particles within the chains to reorganize and aggregate into columns. Due to the small gap and change in gap height, pure squeeze mode is traditionally limited to low stroke applications. These types of squeeze mode devices include variable stiffness isolators, engine mounts (Zhang et al., 2011), and rotating shafts (Wang et al., 2005).

Mixed mode

MR dampers can also be designed to use a combination of the three primary operation modes. A floating piston design shown in Figure 1.6 combines both flow and shear modes (Wilson, 2012), and Brigley et al. designed a mixed mode damper that employs all three primary modes (Brigley et al., 2007). More recently the particle aggregation effect that results from squeeze mode has been investigated as a mechanism to increase the MR fluid yield stress in either flow or shear mode devices, so called *squeeze strengthening*. Because the MR fluids tend to form single-particle chains initially, the yield stress arises from breaking the magnetic attraction between two adjacent particles. However, by squeezing these chains along their axes, the single chains undergo the process of compression-assisted aggregation, forming more robust columns that resist breakage more than single chains (Tang et al., 2000). Both linear shear (Tao, 2001) and rotating plate (Zhang et al., 2009) experiments have measured the squeeze strengthening effect in laboratory experiments.

1.5. Analysis and Validation Methods

No previous scientific studies investigated the shear mode behavior of MR fluids at high shear rates ($> 10{,}000\ s^{-1}$) that were expected to occur in the shear mode MREAs used in this research,

and it was at first unclear if the MR effect would persist at these high shear rates so that fluid controllability would be maintained. The lack of commercial instruments with which to investigate high shear behavior necessitated the fabrication of a custom fluid magnetorheometer. This magnetorheometer was used to validate the use of MR fluids in the high-speed operating environments experienced by crashworthy systems (Hu and Wereley, 2011). Encouraged by the results from this study, a full-scale rotary MR damper was constructed and its performance investigated on a transmission testing rig capable of handling the large torques generated by the device. For both devices, detailed magnetostatic simulations were carried out using commercial finite element analysis (FEA) software. The magnetorheometer was also outfitted with a custom sensing coil to measure the flux density within the magnetic circuit to verify the FEA predictions.

While shear mode or rotary drum-type (MREAS) are an attractive option for use in occupant or payload protection systems that operate at shear rates well over 25,000 s^{-1}, their design is still performed using material properties measured using low-shear rate (<1,000 s^{-1}) characterization techniques. This research details two methods for characterizing MR fluids at high shear rates, and presents characterization results for three commercially available MR fluids. In addition to the accepted method of generating families of flow curves for fluid samples at each operating condition, it is also proposed to utilize the perspective of apparent viscosity (the ratio of shear stress over shear rate) vs. a nondimensional Mason number group to describe the behavior of the fluid at these shear rates. Good agreement between the measured data and predictions of MR fluid behavior are achieved using this framework. By expanding the knowledge of MR fluid behavior to these high shear strain rates, the design of MREAs is enabled for occupant protection systems for crash and mine blast events.

1.6. Dissertation Outline

The motivation of the present research is to develop a method of characterizing and improving MR fluids exposed to high rate shear flow within a rotating geometry. These characterization measurements are analyzed using established flow curve plots, as well as a unifying nondimensional framework. Finally, the shear stress of these standard fluids is shown to be increased by a combined mode squeeze strengthening operation, applicable to the design of practical rotary MREAs.

Chapter 1 introduces MR fluids, the various modes of operation in which they're utilized, and the state of the art for vibration and shock isolation systems incorporating MREAs.

Chapter 2 details the development of a high shear rate magnetorheometer, a laboratory scale instrument designed to expand the range of testing speeds at which MR fluids can be characterized. The complete design of the magnetorheometer is discussed, including fluid flow analysis, magnetic circuit simulation and validation, and thermal control. Characterization tests are performed for three commercially available MR fluids from LORD Corporation, and results are presented and analyzed using an established model that accounts for the rate-dependent viscosity of MR fluids.

Chapter 3 presents an emerging analysis framework based on the normalized apparent viscosity and a nondimensional Mason number group. This analysis provides a means of collapsing a large set of characterization data, spanning shear rate, applied magnetic field, temperature, and iron particle concentration, onto a single master curve that completely describes the behavior of MR fluid devices using the same mode of operation.

Chapter 4 reviews a full scale rotary vane MREA developed for use in a crashworthy helicopter crew seat system, including design and testing. The nondimensional analysis from Chapter 3 is applied to this system, and it is shown that the data collapse holds across different scale shear mode devices. Temperature effects are accounted for, indicating that a limited set of characterization data can be used to predict the performance of a device in vastly different operating conditions.

Chapter 5 introduces a novel method to increase the strength of conventional MR fluids in rotating EAs without modifying their formulation, using a process called squeeze strengthening or compression assisted aggregation. The magnetorheometer from Chapter 2 is modified for use as a mixed mode squeeze-and-shear MREA. The strength of two commercially available MR fluids is shown to be increased using this device, and a qualitative model is developed based on previous phenomenological and tribological explanations.

Chapter 6 summarizes the original contributions of this dissertation and identifies fruitful areas for future work on high shear rate and mixed mode magnetorheology and MREAs.

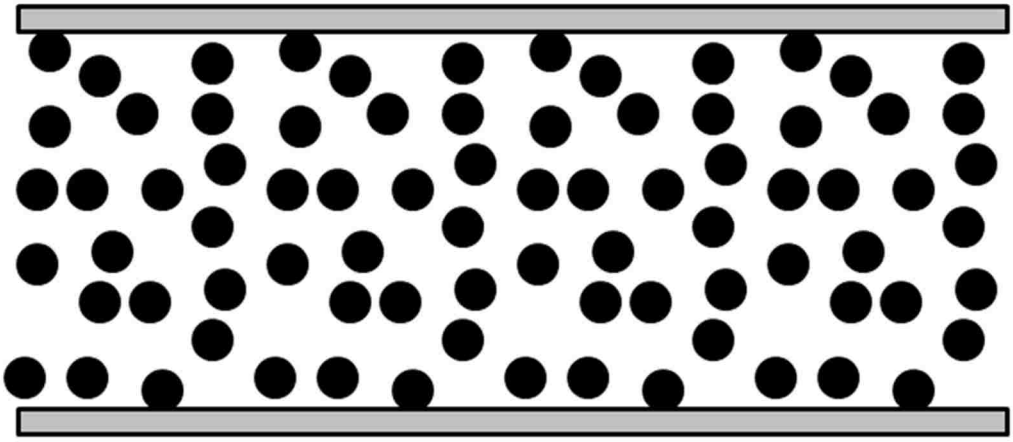

a)

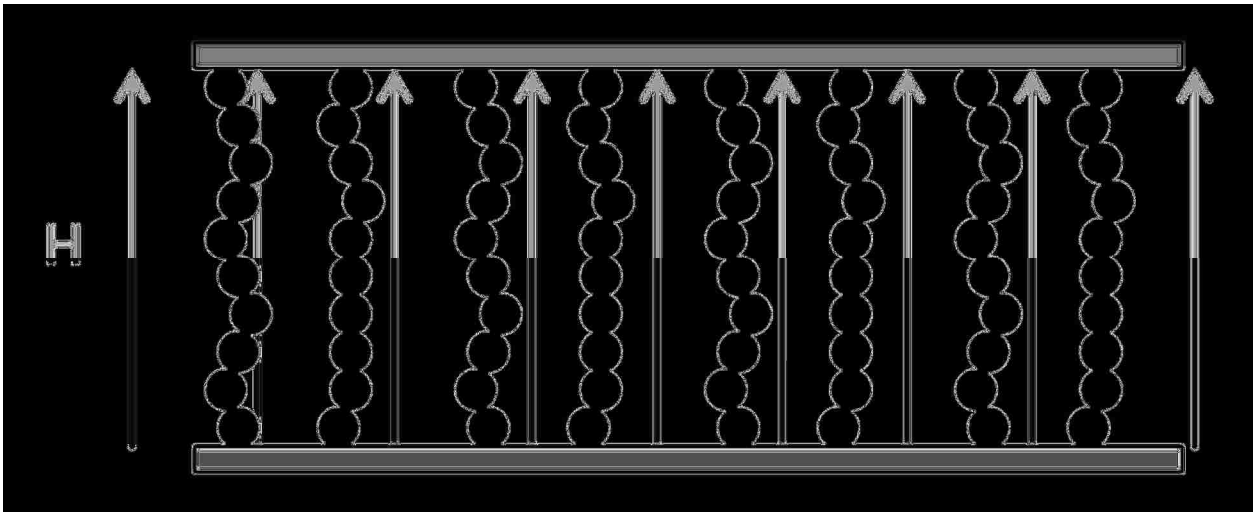

b)

Figure 1.1 - MR fluid a) under no applied magnetic field and b) exposed to a magnetic field. Note that chains form parallel to magnetic field lines.

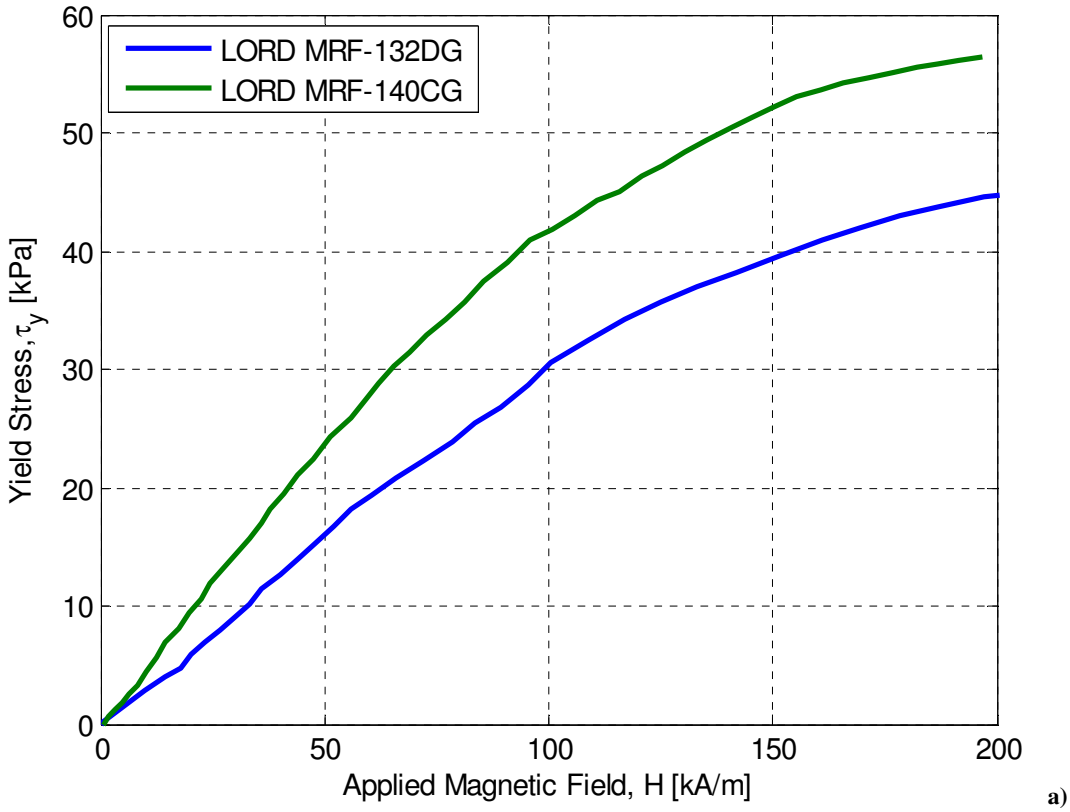

a)

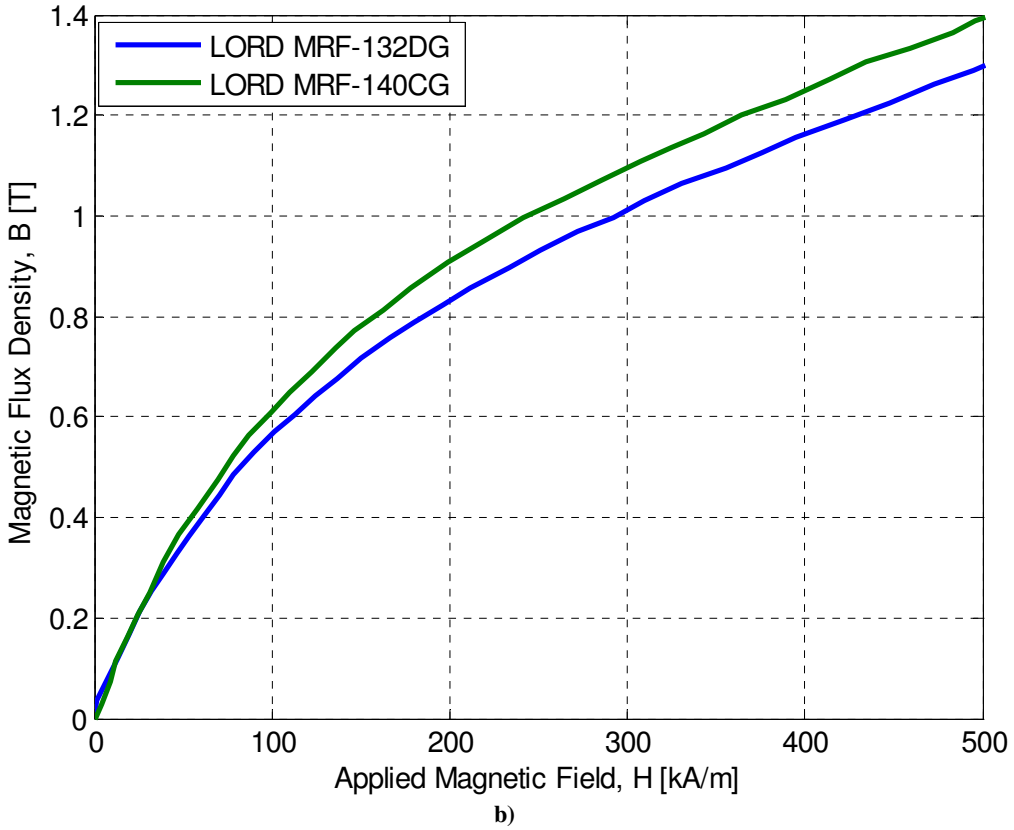

b)

Figure 1.2 - a) Yield stress and b) magnetization curves for two commercially available MRFs

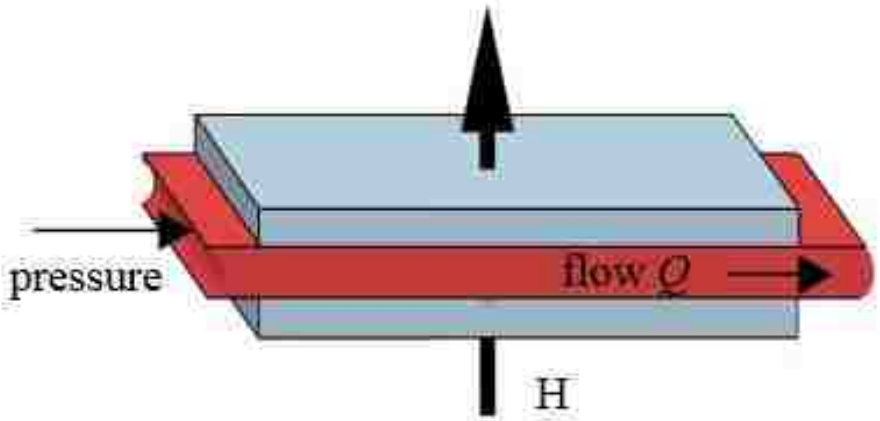

a)

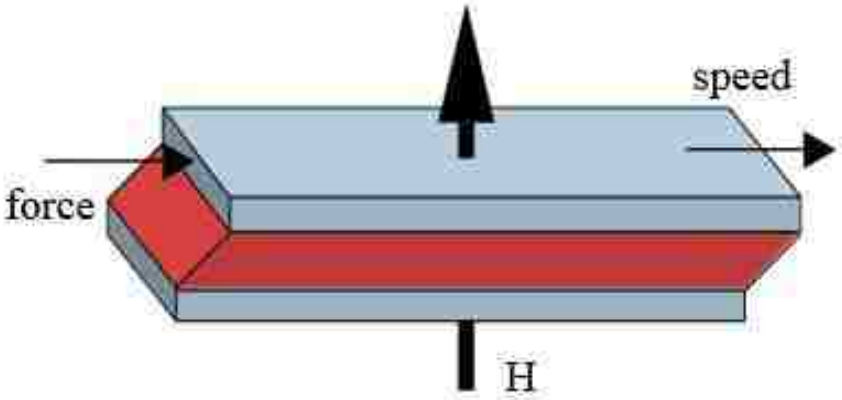

b)

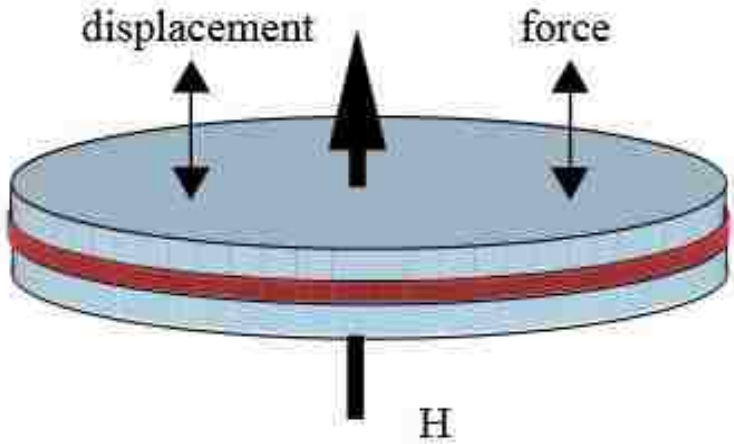

c)

Figure 1.3 - a) Flow mode, b) shear mode, and c) squeeze mode operation of MR energy absorption devices

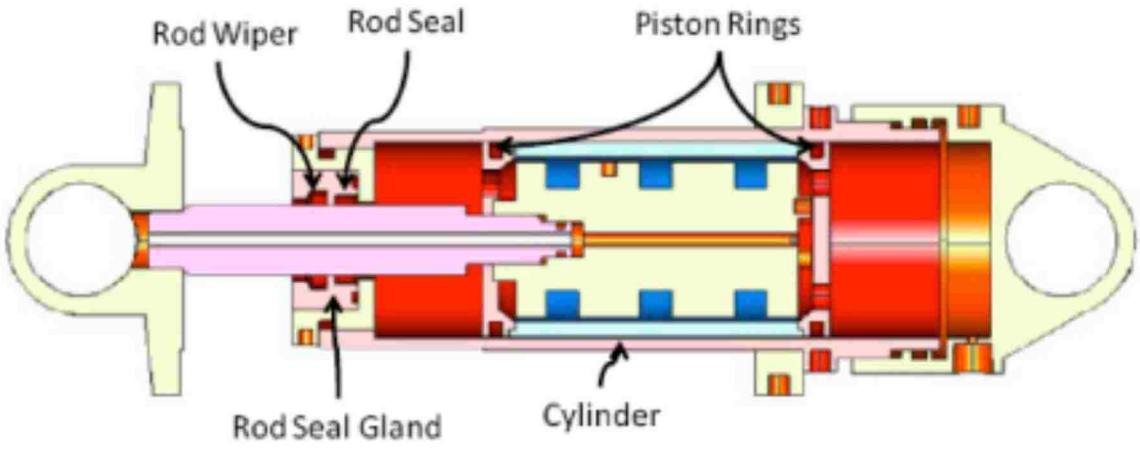

Figure 1.4 - Linear stroke flow mode MREA

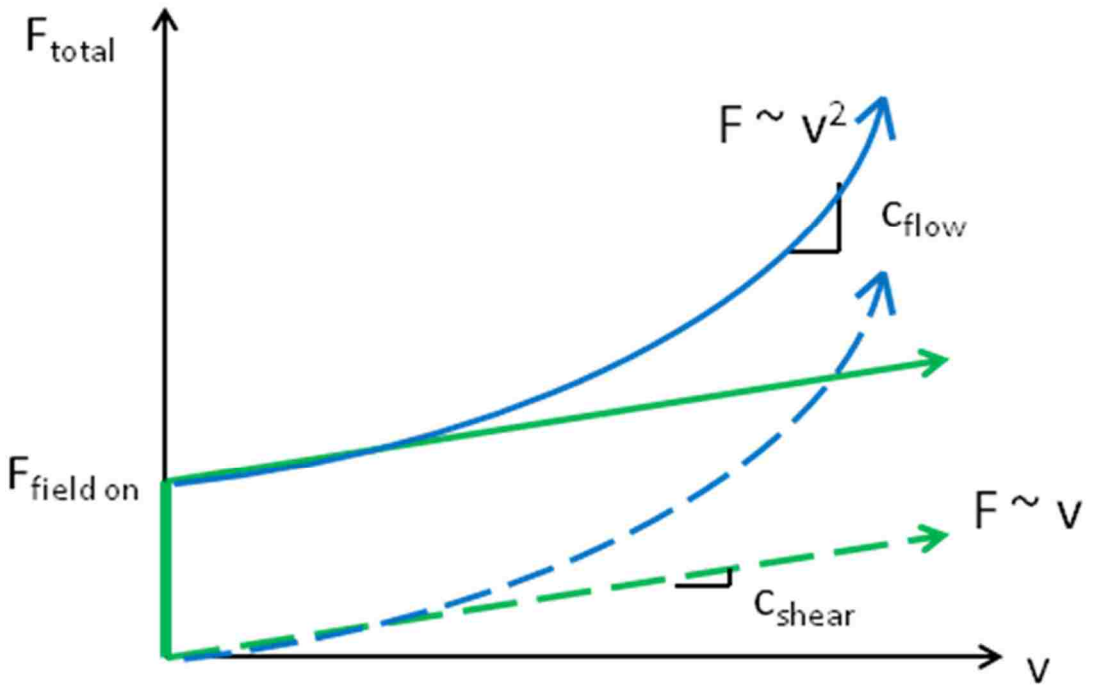

Figure 1.5 - Representative force versus velocity curves for a typical flow mode and shear mode MREA. Note that at higher velocities, the controllable field-on force is a diminishing component of the total force.

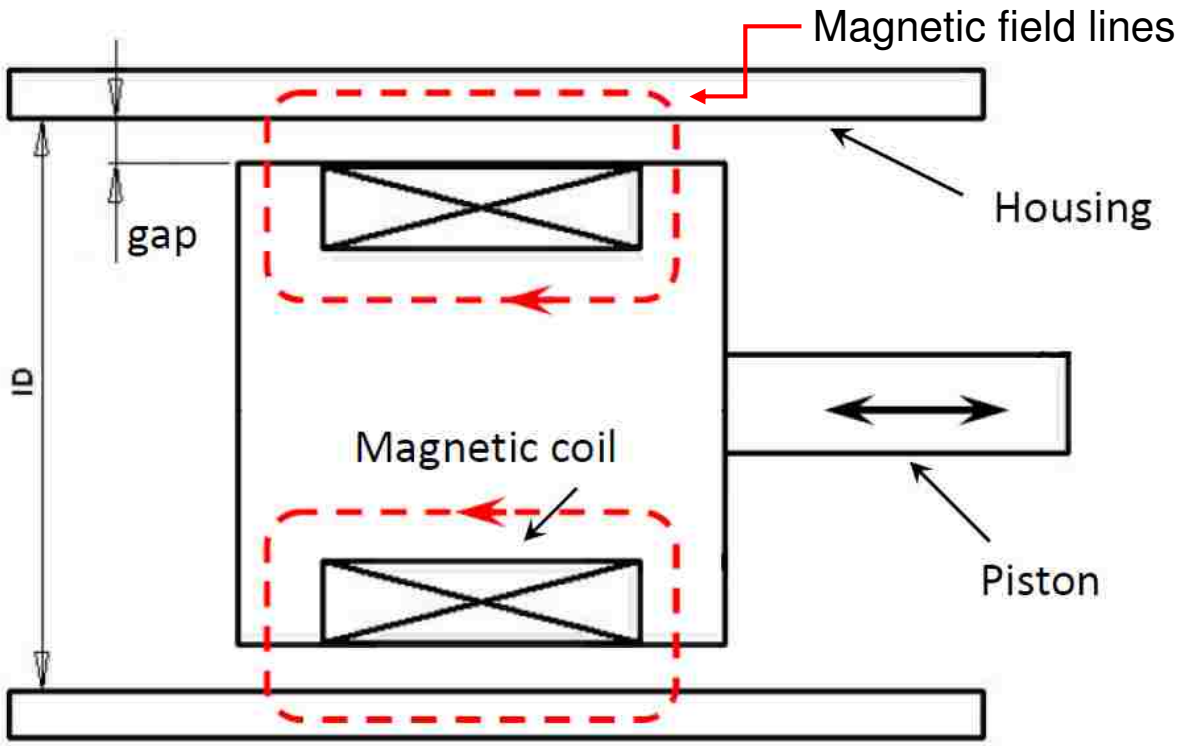

Figure 1.6 - Floating piston MREA utilizing both flow and shear modes of operation

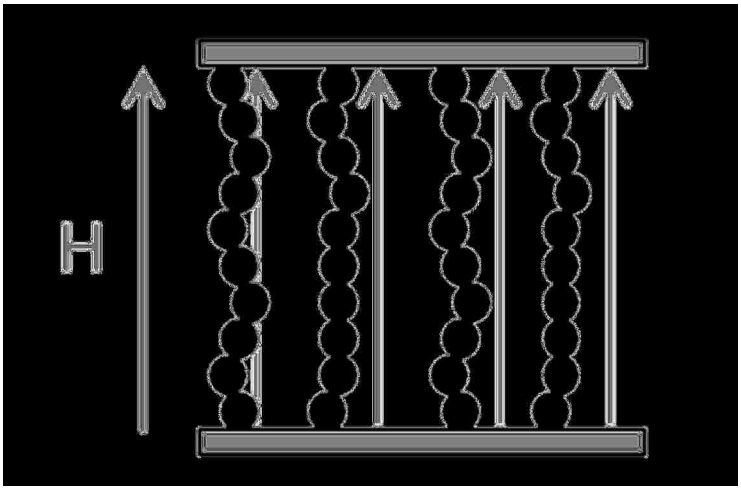

a)

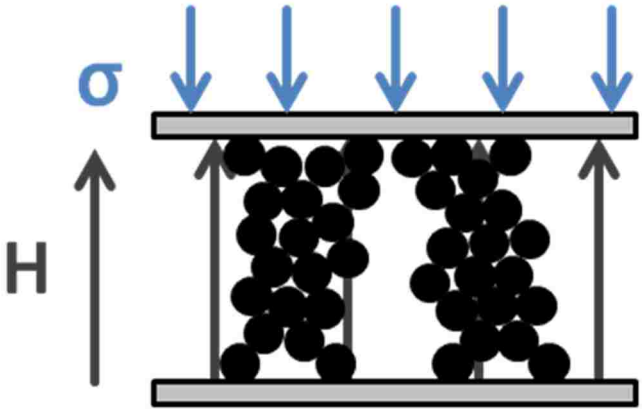

b)

Figure 1.7 - Squeeze strengthening of MR fluids: a) The single chains are formed under zero normal applied stress are then b) compressed and aggregate into more robust columns

Chapter 2

2. DESIGN AND TESTING OF A SEARLE CELL MAGNETORHEOMETER AT SHEAR RATES UP TO 25,000 s^{-1}

2.1. Abstract

The design and construction of the first Searle cell magnetorheometer capable of characterizing fluid samples at shear rates up to 25,000 s^{-1} is presented. Using sub-millimeter active gaps allows high shear rates to be achieved with a standard electric servomotor, and the concentric cylinder geometry ensures proper flow conditions and simplifies analysis. An electromagnet and a hybrid electromagnet/permanent magnet configuration are developed, and the magnetic characteristics of both system configurations are simulated and directly measured. A temperature control system is detailed which allows for fluid characterizations to be performed at a wide range of temperatures, while ensuring that the change in temperature is less than 0.5°C during a test. The characterizations of three commercially available MR fluids are presented, including test series comparing the performance effects of particle solids loading, temperature, shear strain rate and gap size.

2.2. Introduction

Rheometry is a measuring technology used to quantitatively determine the rheological, or manner of flow, characteristics of a fluid substance (Atkinson, 2008). Various measuring systems have been used to explore the viscous behavior of fluids using oscillatory and rotational tests, as well as to study the viscoelastic characteristics through creep and relaxation tests. In total, the goal of each of these tests is to produce the flow curve, a fundamental measurement of the dependence of the fluid's shear stress on the shear strain rate.

Magnetorheometers in particular are instruments incorporating a controllable magnetic field source and are used to study the yield stress and pre- and post-yield behavior of MR fluids. Because the post-yield behavior becomes a dominant factor in the dynamic range of practical MR devices at high speeds, instruments capable of emulating high shear rate conditions are desirable. A number of different instruments, some commercially available, have been developed to meet the needs of researchers studying MR fluids, but none so far provide all of the requirements necessary to expand the design space of high shear rate, high performance MR devices.

2.2.1 Standard rheometers

There are a number of rheometer designs, each appropriate to certain testing conditions and materials. Slit-flow, capillary (Ferguson and Kemblowski, 1991), and draining vessel (Roach and Henein, 2005) rheometers use a pressure differential to force fluid through an orifice. These are versatile and have well-developed theories and techniques, but are in some cases difficult to construct, exhibit non-homogeneous flow profiles, and generally operate at quasi-steady state. Oscillating rheometers relate the motion decay behavior of an oscillating member to a stationary member to determine the properties of an interstitial sample. These devices are usually relatively simple and have well understood analyses, but are suitable only for extremely low shear rate

experiments (Brooks et al., 2005). There are even containerless viscometers that utilize electromagnetic or aerodynamic levitation to characterize samples without contaminating them, but these are obviously extremely complex and generally operate at very high temperatures (Rhim et al., 1999).

Of the many methods available, the most commonly used method for magnetorheometry studies is applying shear stress directly to the fluid sample through a rotating surface. Parallel plate and cone-and-plate rheometers, of which there are numerous commercially available examples, consist of a horizontal, stationary "stage" upon which a fluid sample is placed. A circular, flat plate or cone is lowered onto the sample and rotated with a known angular velocity and torque, which results in a flow curve measurement. With low viscosity fluids and at high rates of rotation, this method has the disadvantage of fluid escaping the sample stage. In fact, commercial parallel plate magnetorheometers are generally operated at shear rates <1,000 s^{-1} (Hu and Wereley, 2011).

The other rotational geometry, which is the concentric cylinder geometry used in this research, overcomes the problems of sample containment and radially-varying shear rate, and has the added advantage of allowing for a simplifying infinite plate assumption. At high rates of shear, the fluid does not escape the sample container, and as shown in Figure 2.1, the shear strain rate is constant across the fluid sample (Ritwik, 2012).

2.2.2 Current state of the art

The fabrication and use of concentric cylinder rheometers for high shear rate studies has only a few notable examples of these promising devices being fabricated, and none for use with MR fluids. Barber achieved shear rates of < 500,000 s^{-1} using large diameter rotating elements and gaps as small as 6.35×10^{-7} m, and investigated the effects of high shear rate in low viscosity oil blends (Barber et al., 1955). Subsequent improvements with temperature control were carried out

on the same instrument by the same laboratory two decades later, making it possible to characterize the changes in fluid behavior related to heating (Manrique and Porter, 1975). A similar device was constructed the following decade in another laboratory and, taking advantage of the advances in precision machining, reported experimental results at shear rates up to 3×10^6 s^{-1} (van Os et al., 1982). More recent studies using commercial parallel plate rheometers are reported to reach shear rates up to 80,000 s^{-1}, achieved by using gap sizes down to 30 μm, which is approaching the precision of the positioning motor in the instrument (Pipe and Majmudar, 2008). However, because the parallel plate geometry produces a radially-varying shear rate, the reported data must be systematically corrected for error.

With one exception, MR fluids have so far only been investigated at shear rates above 1,000 s^{-1} using slit-flow geometries. A piston-driven capillary rheometer incorporating a magnetic valve to investigate dwell time effects on MR fluid performance was reported to generate apparent shear rates up to 250,000 s^{-1} (Goncalves et al., 2006). A slit die setup submitted to a magnetic field was used to generate apparent strain rates in MR fluid samples up to 40,000 s^{-1} (Laun et al., 1996). A similar 40,000 s^{-1} slit die setup was improved by incorporating pressure sensors on either side of the magnetic valve within the die to provide more accurate estimations of shear rate, though the data still required correction (Wang and Gordaninejad, 2006). Currently the only rotational geometry reported for studying MR fluids at high shear rates is a commercial parallel plate rheometer with a modified sample chamber that creates twin gaps between the chamber walls and the rotating plate. Using a 0.3 mm gap, the researchers report a peak apparent shear rate of 10,000 s^{-1} at the rim of the rotating plate, though flow curve data is only presented for shear rates up to 3,000 s^{-1} (Laun et al., 2010).

2.2.3 Searle cell magnetorheometer

The goal of this research is to create a magnetorheometer, capable of shear rates well over 1,000 s^{-1}, that replicates the mode of operation of practical rotary MR energy absorbers. The concentric cylinder geometry has the advantage of producing a simple flow profile which is straightforward to analyze at these high shear rates, yet has not been available in an instrument for use with MR fluids to date. In subsequent sections the design of the MR fluid sample cell will be discussed in detail, along with the development of the instrument's control and acquisition systems and analysis of experimental data.

2.3. Searle-cell Design Principles

A common and simple method to measure the viscous behavior of a fluid is to use two concentric co-rotating cylinders, or Couette geometry, to impart a known angular velocity on the fluid while measuring the torque produced. The relationship between these two measurements, known as flow curves, are the hallmark of rheometric studies and provide practical characterizations of fluid behavior. For reasons discussed in the following sections, an inner rotating cylinder (bob), combined with a fixed outer cylinder (cup), known collectively as a Searle cell, was chosen as the most appropriate design for the magnetorheometer (Estelle et al., 2008).

When designing a Searle cell rheometer, torque-shear stress and rotation speed-shear strain rate relationships provide the baseline specifications for the cell geometry, schematically shown in Figure 2.2. These relationships are given in (Choi et al., 2005) and shown below.

$$\tau_{r\theta} = \frac{M}{2\pi L(R+h)^2} \tag{2.1}$$

$$\omega_i = \int_{r_b}^{r_c} \frac{\dot{\gamma}}{r} dr = -\frac{1}{2}\int_{\tau_c}^{\tau_b} \frac{\dot{\gamma}}{\tau_{r\theta}} d\tau_{r\theta} \tag{2.2}$$

An expression for the shear rate can is obtained using cylindrical coordinates $\langle \hat{r}, \hat{\theta}, \hat{z} \rangle$, and noting that the 3D velocity vector field can be simplified to just a scalar, v_θ, by assuming that the inner bob is sufficiently long in the axial direction relative to the gap size, such that $v_z = 0$, and ensuring that the bob rotates at a constant angular velocity, such that $v_r = 0$.

For narrow gaps, it can be assumed that the fluid is fully sheared in the $\hat{\theta}$-direction with the gradient in the $\hat{r}$-direction (the velocity profile is linear in $\hat{r}$) as shown below (Morrison, 2001).

$$v_\theta = C_1 r + C_2 \tag{2.3}$$

The constants C_1 and C_2 can be found using the boundary conditions for the Searle cell design, namely that of stationary cup, $v_\theta = 0$ at $r = R + h$, and a rotating bob, $v_\theta = R\omega_i$ at $r = R$. This yields

$$v_\theta = \frac{R(r-1)}{h}\omega_i \tag{2.4}$$

The rate-of-deformation tensor is sparse and can therefore be calculated as merely the derivative of Eq. ((2.4) with respect to r, which greatly simplifies the issue of shear rate estimation and results in the narrow-gap shear rate expression (Estelle et al., 2008) given below.

$$\dot{\gamma} = \frac{dv_\theta}{dr} = \frac{R}{h}\omega_i \tag{2.5}$$

Given a desired shear strain rate, as well as considerations for the magnetic circuit (discussed later), the final geometry of the MR cell can be identified. For the high shear rate magnetorheometer developed for this research, the specific geometric parameters are listed in Table 2.1. Clearly, decreasing the gap size h has the effect of increasing the maximum achievable shear rate for a given angular velocity, and this relationship is exploited in the design of this high shear rate

magnetorheometer. Figure 2.4 demonstrates the shear rate amplification provided by narrower gaps.

Consideration must be given to the stability and uniformity of flows under high shear rates, particularly during characterization studies using concentric cylinder rheometers. Two different nondimensional parameters are typically employed to verify that the assumptions presented in the above analysis are valid. The Reynolds number indicates if the fluid is in the laminar or turbulent regime, and the Taylor number is used to determine the presence of so-called Taylor-Couette vortices, secondary eddy currents which affect the viscosity measurement.

Table 2.1 – Searle cell magnetorheometer dimensions

MR Cell Parameter	Measurement [mm]		
Active gap length, L_c		12.0	
Bob minor radius, R_b		6.0	
Bob radius, R	8.0	8.75	8.9
Active gap height, h	1.0	0.25	0.1
Coil outer radius, R_m		26.0	
Flux outer radius, R_o		35.0	
Flux path length , L_m		30.0	
Bob path length, L_p		18.0	
No. of coil turns, N		468	

2.3.1 Reynolds Number considerations

In concentric cylinder devices, accurate measurement of viscosity can only be obtained in uniform laminar flows, a condition which exists while the nondimensional ratio of inertial to viscous forces,

or Reynolds number, remains below 13,000 (Lathrop et al., 1992). An expression for the Reynolds number of a shear flow in a concentric cylinder rheometer is given below.

$$Re = \frac{\rho \omega_i R_o (R_o - R_i)}{\eta_s} \tag{2.6}$$

Note that decreasing the gap size, $h = R_o - R_i$, effectively reduces the Reynolds number; for this reason, narrow gaps are beneficial to realizing uniform laminar flow at high shear rates. Typical maximum Reynolds numbers for each bob used in the Searle cell magnetorheometer are presented in Table 2.2.

2.3.2 Taylor Number considerations

Even in laminar flows, secondary eddy currents may form under certain conditions. These currents, or Taylor vortices, have the effect of increasing the apparent viscosity obtained from experimental measurements, as in the artificial shear thickening behavior observed in (Colyer and Clegg, 1998). A practical expression to calculate flow stability and predict the onset of Taylor vortices is given below (Macosko, 1994).

$$Ta = \frac{\rho^2 \omega_i^2 (R_o - R_i)^3 R_i}{\eta(\dot{\gamma})^2} \tag{2.7}$$

As presented by Atkinson, as long as the Taylor number does not exceed 3,400, the flow can be assumed to be free of these detrimental secondary eddy currents (Atkinson, 2008).

2.4 Magnetic Circuit Design and Analysis

A recursive analytical method to estimate the magnetic flux density and field strength within the active gap region of MR devices is employed to determine the size and geometry of the magnetic flux path and electromagnetic coil (LORD Materials Division, 1999). First, the desired yield stress is selected in the MR fluid, which determines the operating point,(H_f, B_f), on the fluid

Table 2.2 – Searle cell magnetorheometer parameters and operating conditions

MR Cell Parameter	Value		
Bob Radius [mm]	**8.0**	**8.75**	**8.9**
Configuration is Defined by Nominal Gap [mm]	**1.0**	**0.25**	**0.1**
Maximum Shear Rate [s^{-1}]	**2,500**	**10,000**	**25,000**
Reynolds Number	**8,873**	**2,218**	**873**
Taylor Number	**1,090**	**8.6**	**1.2**

magnetization curve. The corresponding operating point in steel, (H_s, B_s) is found using Maxwell's 2nd equation, or Gauss's Law for Magnetic Fields, which requires that magnetic flux is conserved, as shown in the equation below.

$$\Phi_B = \nabla \cdot B = \iint_s B \, dS = 0 \tag{2.8}$$

Finally, the required number of Ampere-turns for the electromagnetic coil can be found from Kirchhoff's Law for Magnetic Circuits, shown below. A summary of this process is presented in Figure 2.4.

$$NI = \oint H \, ds \tag{2.9}$$

Here, B is the magnetic flux density, N is the number of turns, and I is the applied current. In Figure 2.5 an axisymmetric quarter section of the circuit geometry is shown, and denotes the relevant dimensions for use in the analysis. Eq. (2.8) states that the flux, Φ, is constant throughout the flux path; as area A decreases, flux density B increases. This equation is rewritten below using dimensions from the schematic,

$$B_{MR}A_g = B_{s1}A_b = B_{s2}A_0 = B_{s3}A_g \tag{2.10}$$

where $A_g = \pi R L_c$ is the area of the fluid gap, $A_b = \pi R_b^2$ is the cross-sectional area of the rotating bob, and $A_o = \pi(R_o - R_m)^2$ is the area of the outer flux path. Because the coil number and applied current are known, the field strength within the fluid gap, H_g, can be determined using information from the magnetization curves for the flux material, AISI 1010 steel, and the MR fluid sample, using the following equation (Hu and Wereley, 2011).

$$NI = 2H_g h + H_{s1}L_p + H_{s2}L_p + 2H_{s3}L_m \tag{2.11}$$

Here, L_p is the length of the flux arm forming the cup, L_m is the radial length of the flux path, and H_{s1}, H_{s2}, and H_{s3}, are the corresponding magnetic fields. For the given applied current, the field within the gap depends on the particle volume fraction of the fluid sample. As volume fraction increases, the gap field decreases.

This is a simplified analysis that does not account for factors such as the nonlinear properties of MR fluid and steel, or the possible losses at junctions, boundaries and area changes. Therefore, a more detailed finite element analysis is presented in the following section and used in the subsequent characterizations and analyses. A quarter-section view of the high shear rate magnetorheometer is shown in Figure 2.6.

2.4.1 Magnetostatic Finite Element Analysis

The magnetorheometer geometry is created as an axisymmetric model in the commercial FEA software *MAXWELL* in order to perform a more detailed magnetostatic analysis and verify the expected field strength (ANSYS, Inc., 2009). The mesh is shown in Figure 2.7, and consists of 12,726 triangular elements. Colors indicate important features of the model, specifically that green shades correspond to low permeability materials such as aluminum and Teflon, red

shades indicate areas that make up the magnetic flux path, gray represents the MR fluid, and blue is the EM coil. The background red material is air, which does not carry any magnetic flux. The results for direction and density of magnetic flux resulting from 1 Ampere of applied current are shown in

Figure 2.8, as the flux lines and solid color map, respectively. A magnitude plot of the corresponding magnetic flux intensity shows that the magnetic field is uniform across the top and bottom active gaps, shown in Figure 2.9. The simulation achieves a total error energy less than 0.05% for each applied current case, and provides improvement over the simplified analysis performed during the MR cell design by incorporating the nonlinear magnetization curves for the MR fluid and steel elements. In other words, the magnetic field strength within the gap is not linearly related to the current applied to the coil, and precise knowledge of the field is required to characterize flows well.

Even this analysis has limitations, so efforts to experimentally validate the magnetic field in the active gap were undertaken to definitively characterize the conditions within the MR cell. Unfortunately, even the smallest Hall sensors, used to measure magnetic fields, were too large to fit within the narrow active gap. Instead, two methods to determine the gap field were adapted from (Janicke, 1997) and compared. It was determined that a method using a custom sensing coil more accurately measured the magnetic field within the MR cell, however both methods are presented in the following subsection.

2.4.2 Potential coil method

A magnetic potentiometer is a small, tightly wound coil of fine wire wrapped around a nonconducting core that is used to measure magnetic potential, or flux differential, across gaps

within a magnetic circuit as shown in Figure 2.11. Potential difference can be related to the magnetic field within that gap according to the equation below (Walker LDJ Scientific, 2013).

$$P_A - P_B = \int_A^B H\,(s)ds \tag{2.12}$$

A given potential coil has an associated calibration constant, which gives a straightforward measurement of the gap field using the relationship below.

$$H_g = \frac{2\,\Phi\,K_p}{h} \tag{2.13}$$

A potential coil, model PM/S83, was used in combination with a programmable fluxmeter, model MF-10D, both from Walker LDJ Scientific. The PM/S83 coil has a reported K_p coefficient of 4.6 A/μWb, and is shown in Figure 2.11.

2.4.3 Sensing coil method

In this method, a custom sensing coil is wound from 31 AWG enameled copper wire around the bob, and the bob is set in place within the MR cell, shown in Figure 2.12. The sensing coil leads are connected to the fluxmeter, and as the applied current is varied the corresponding changes in the magnetic field induce a current within the sensing coil, which is registered and recorded by the fluxmeter. This measurement represents the total flux within the circuit, and with knowledge of the bob cross sectional area can thus be related to the flux and magnetic field strength through the active gap using Eq. (2.10) and the magnetization curve of the MR fluid sample, respectively.

Ultimately, the sensing coil method proved advantageous compared with the potentiometer for a number of reasons. The very small gap, combined with the presence of magnetized MR fluid and the need to remove the top cap and retaining bearing during measurements made the potentiometer less reliable and repeatable. Though the sensing coil could only be used while the bob remained

static, these measurements correspond well with the FEA simulation at applied currents above 0.1A, and remained consistent and predictive throughout the use of different gap sizes and fluid samples.

At currents of 0.1 A down to no applied current, the MR cell exhibited magnetic remanence not predicted by the simulations. Measurement of this phenomenon proved to be important during nondimensional analysis of the test results, described in Chapter 4. Measurement results for LORD MRF-132DG using both methods, including the remnant magnetization are shown in Figure 2.13. Measurement and simulation results for LORD MRF-140CG are shown in Figure 2.14.

2.4.4 Electromagnet flux source

From the magnetic circuit analysis above, it was determined that a coil wound from 24 gauge enameled copper wire having 540 turns (18 turns per layer, 30 layers) is sufficient to produce 0.9 T of magnetic flux through the active gap region at 1 A of applied current, which is near the saturation magnetization of the MR fluids used. A Delrin plastic armature was fabricated to meet these specifications, along with the previously detailed geometry of the Searle cell which would allow for high shear rate tests to be performed.

2.4.5 Hybrid Electromagnet/permanent magnet flux source

Combinations of permanent and electromagnet flux sources have been reported for linear stroking MR devices, allowing for a non-zero yield force to exist without the need to apply a bias current. Two advantages of this system were noted. An applied current would generate a field which enhanced that of the permanent magnet, and which would otherwise have required a much larger current and led to large resistive heating of the device. Alternatively, by reversing the polarity of

the applied current, the magnetic field from the permanent magnet could be effectively cancelled out, permitting operation at zero yield stress (Boese and Ehrlich, 2010).

With this in mind, a hybrid electromagnet/permanent magnet combination was designed for use with the high shear rate concentric cylinder MR cell geometry, shown Figure 2.15. Two axially magnetized bonded neodymium magnets of appropriate geometry were enclosed in a two part Delrin spacer, and inserted within a custom coil similar to that described above. The coil was sized with a larger inner diameter to allow for placement of the permanent magnet rings, and contained 468 turns (18 turns per layer, 26 layers). Results from *MAXWELL* simulations are compared to flux density measurements taken with the custom sensing coil for MRF-132DG with a 0.25 mm gap in Figure 2.16.

2.5 Data Acquisition and Control Design

Control and data acquisition in the magnetorheometer are accomplished through the graphical programming software *LabVIEW* by National Instruments (National Instruments, 2012). To generate the desired input rotation speed, a 0.75 HP (560 W) electric servomotor, model SilverMax 34-HC1 by QuickSilver Controls, Inc., is connected through a QCI CLCF-01 motor controller which receives voltage commands from the desktop PC running *LabVIEW*. This servomotor is capable of a maximum of 3,000 RPM at 100 oz-in (0.706 N-m) of torque, ensuring that the commanded voltage results in a reliable motor speed (QuickSilver Controls, Inc., 2011). This performance was also verified using a laser tachometer to measure the speed of rotation at a given voltage, which confirmed the input accuracy.

The torque output is measured by a 100 ounce-inch (0.706 N-m) torque transducer, model RTS-100, and the voltage signal is passed through a TM-02 signal conditioner, both by Transducer

Techniques, which interfaces with the PC through a National Instruments BNC-2110 data acquisition box. Alternatively, a 500 oz-in transducer, model RTS-500, can be used for lower speed measurements of a higher viscosity fluid, simply by adjusting the $\frac{V}{N \cdot m}$ gain setting in the program's front panel. The *LabVIEW* program is shown in Figure 2.17.

The control and data acquisition program produces a staircase voltage signal, a waveform consisting of a series of discrete steps. This provides eight quasi-steady shear rate levels and allows for any transient effects to diminish following the speed changes. The user controls the maximum desired rotation speed, and the program divides this maximum into equally spaced steps, commands the servomotor, and outputs torque and temperature data. The direction of the staircase signal, either ascending or descending, can be controlled as well. A sample of collected raw data for a test series is shown in Figure 2.18.

2.6 Temperature Control

In addition to plots of motor RPM and torque output, the magnetorheometer Searle cell was fit with a custom cooling jacket made from 12 turns of 0.25 inch copper tubing and an internal K-type thermocouple. The cooling jacket is connected to a circulator pump with thermostat-controlled refrigerating and heating capability, Julabo model F25-MD, allowing precise control over the internal fluid sample temperature. The internal thermocouple is inserted through the top cap of the magnetorheometer and rests within the central fluid chamber, without passing through the active gap region to avoid interfering with the flow.

The cooling jacket is a nonintrusive feature which allowed for isothermal tests to be performed. Temperature control is challenging in high shear rate concentric cylinder rheometry (Barber et al., 1955; Manrique and Porter, 1975) because of viscous heating, and this is exacerbated in

magnetorheometric devices due to the resistive heating caused when current flows through the electromagnet (Hu et al., 2012). The torque measurement, M, is affected by the temperature gradient across the gap according to the equation below (Palma et al., 1967).

$$T_R - T_r = \frac{M^2}{8\pi^2 h_0^2 k R^2 \eta}\left[ln\left(\frac{r}{R}\right) - \frac{1}{2}\left(\frac{r^2 - R^2}{r^2}\right)\right] \quad \textbf{(2.14)}$$

Apparently, this temperature gradient is minimized in narrow gaps, such as those employed in this magnetorheometer. Using the cooling jacket to bring the entire MR cell to a steady temperature prior to starting an experiment, it is therefore possible to maintain a near constant temperature in the fluid sample while gathering rheometric data during the 21 second tests, as shown in Figure 2.21.

2.7 Testing and Characterization Results

Three popular commercially available MRFs were selected for this study. LORD Corporation's MRF-132DG (32 vol% of Fe), MRF-140CG (40 vol% of Fe), and MRF-145BG (45 vol% of Fe) were selected for testing because of their applicability to MREAs under development. They consist of solid spherical carbonyl iron particles 6-10 μm in diameter, suspended in hydrocarbon carrier oil. Each set of characterizations was performed using an increasing applied field and ascending staircase angular speed signal, while taking care to rest the sample for 5 minutes between consecutive test runs to maintain the desired temperature. In this way, remnant magnetization effects and particle settling were minimized by keeping the MRF sample in a well-mixed state.

A typical data set collected the commanded rotation input and the resulting measured torque output of the torque load cell at 1 kHz. Quasi-steady measurements were made, up to the maximum shear strain rate, by commanding a step input to the servomotor and selecting data from the region of each rate step corresponding to the middle 75% of points for that step, shown in Figure 2.18. This

method generated consistent and repeatable results across multiple samples of the same fluid, and was used to ensure that transient perturbations would have minimal effect on the rheometric tests. Averages are taken at each quasi-steady step, and the reduced data set of bob rotation speed and torque output is then converted to shear strain rate and shear stress information using Eq. (2.1) and Eq. (2.5) for analysis, shown as flow curves in Figure 2.22 (MRF-132DG), Figure 2.23 (MRF-140CG), and Figure 2.24 (MRF-145BG).

2.7.1 High Shear Rate Model

Because the focus of these experiments is identifying shear stresses developed at high shear rates, it is useful to frame the characterization in terms of the apparent viscosity, η, vs. the shear rate, $\dot{\gamma}$. Apparent viscosity is defined as the ratio of the shear stress, τ, to the shear rate, $\dot{\gamma}$. This approach is taken to better capture the shear thinning behavior of the MRFs, especially near the extreme of 10,000 s^{-1} investigated here. Apparent viscosity, η, therefore depends on both applied field as well as shear rate.

The Herschel-Bulkley (HB) model has proven to be a useful constitutive model when characterizing shear thinning MRFs (Choi et al., 2005). In the HB model shown below,

$$\eta = \frac{\tau}{\dot{\gamma}} = \frac{\tau_y}{\dot{\gamma}} + K\dot{\gamma}^{(n-1)} \tag{2.15}$$

the apparent viscosity is the sum of the "active" contribution from the yield stress of the MRF, and a "passive" viscosity power law of shear rate. Here, n is the *flow index*, which measures the degree to which the fluid is shear thinning ($n < 1$) or shear thickening ($n > 1$). Note that $n = 1$ implies a Bingham-plastic material, which yields just two terms, yield stress and dynamic viscosity. Also, K is the *consistency*, or the proportionality constant between viscous stress and shear rate raised to the power of the flow index (Choi et al., 2005).

2.7.2 Parameter Identification

To identify the HB model parameters, τ_y, K, and n, a curve fitting technique based on a simple genetic algorithm (SGA) was used. An SGA is a non gradient-based statistical method used to minimize some objective function, in this case the normalized mean squared error between experimental data and the HB model fit. The algorithm seeks to minimize the normalized mean squared error fitness function shown below.

$$Error\% = \sum \left[\frac{(\eta_{exp} - \eta_{HB})}{\eta_{exp}} \right]^2 \quad \textbf{(2.16)}$$

Here η_{exp} denotes experiment data, and η_{HB} denotes the HB model with the parameters, τ_y, K, and n as shown in Eq. (2.15).

Once the change in fitness between successive generations ceases to exceed a set tolerance, the algorithm is assumed to have found parameter values that produce a satisfactory fit to the data. Histograms of the SGA minimization results were analyzed, and the parameter values which both minimize the fitness function and fall within one standard deviation of the corresponding data set were selected (Chaudhuri et al., 2006).

2.7.3 Trends with solids loading

Parameter identification results for three MRFs with different solids loading, characterized at shear rates up to 10,000 s^{-1} are presented in Figure 2.25 (MRF-132DG), Figure 2.26 (MRF-140CG), and Figure 2.27 (MRF-145BG). Yield stress and consistency are monotonically increasing versus applied magnetic field, while the flow index is monotonically decreasing. To validate the experimental results, the yield stress vs. applied magnetic field is plotted in Figs. 25-27 a), along with the predicted yield stress obtained from the empirical relationship developed in Carlson's work (Carlson, 2005). This empirical formula is based on results from characterization tests

performed at shear rates below 1,000 s^{-1}, yet there is good agreement with the current data at 10X those shear rates, indicating that the MR effect persists at these high shear rates. Finally, HB models with the resulting parameters are overlaid on the flow curves in Figure 2.22 (MRF-132DG), Figure 2.23 (MRF-140CG), and Figure 2.24 (MRF-145BG).

2.7.4 Trends with temperature

The identified yield force and viscosity of MRF-132DG at 9°C, 20°C, 38°C and 55°C are shown as a function of the applied magnetic field in Figure 2.28 and Figure 2.29, respectively. A viscosity estimate is found using the average consistency, K, and flow index, n, for each test to provide a more intuitive understanding of temperature effects on MRFs at shear rates up to 10,000 s^{-1}. The temperature effect on the viscosity of the MR fluid is more significant than the effect on the yield stress of the fluid. As the temperature increases from 9°C to 55°C, the viscosity of MRF-132DG decreases monotonically from 0.3 to 0.1, or 66%. In comparison, the yield stress varies less than 10% within this temperature range. The identified yield force and viscosity of MRF-140CG at four temperatures are shown in Figure 2.30 and Figure 2.31, respectively. Similar to the previous result, the effect of the temperature on the flow behavior of MRF-140CG is more pronounced in the viscosity measurement, where it can be seen to decrease from 0.7 to 0.2, or 56% (Hu et al., 2012).

It should be noted that the yield stress shown here increases as the temperature increases, which contradicts experimental results of MR grease at low shear rates (Sahin et al., 2009). Since the MR cell expands in all directions when at elevated temperatures, the gap thickness could be smaller than at room temperature. While this size change may have a noticeable effect on the shear rate, and thus the viscous component of shear stress, the effective magnetic field in the gap could also be increased leading to a more pronounced yield stress at higher temperatures.

A typical hydrocarbon-based MR fluid has a viscosity that is related to its temperature through the relation given below (Hu et al., 2012; Knezevic and Savic, 2006).

$$\eta = \eta_0 e^{\beta\phi(T-T_0)} \tag{2.17}$$

From experimental data giving the fluid viscosity at various temperatures, the scaling constant β can be calculated. This provides insight into the sensitivity of viscosity with respect to temperature, and demonstrates the importance of careful control and monitoring during rheometric experiments. Table 2.3 provides the scaling factor for two fluids, as well as the expected change in sample viscosity for temperature-controlled and temperature-uncontrolled experiments conducted at 100°F.

Table 2.3 – Thermal scaling factor for viscosity-temperature relationship, and representative viscosity changes during tests with and without temperature control

Fluid	β	$\Delta\mu$, T controlled	$\Delta\mu$, T uncontrolled
MR132-DG, $\mu_0 = 0.092$	0.0664	0.002 (2%)	0.01 (10%)
MR140-CG, $\mu_0 = 0.21$	0.0653	0.005 (2%)	0.02 (11%)

Figure 2.32 shows the viscosity change with temperature for MRF-132DG and MRF-140CG along with the power law trend from Eq. (2.17). Clearly, temperature plays an important role on the off-state viscosity of the fluid, as the passive viscous force drops considerably at higher temperatures.

2.7.5 Trends with gap size and shear rate

Three precision machined bobs having radii of 8.0 mm (1.0 mm gap), 8.75 mm (0.25 mm gap), and 8.9 mm (0.1 mm gap) were used to shear MRF-132DG samples at room temperature, achieving

maximum shear rates of 2,500 s^{-1}, 10,000 s^{-1}, and 25,000 s^{-1}, respectively. Figure 2.33 shows a comparison between the Herschel-Bulkley parameters fit to each data set. There was no significant difference between the 2,500 s^{-1} and 10,000 s^{-1} shear rate data, verifying that the MR effect remains useful at shear rates above data available in prior literature. The 25,000 s^{-1} tests proved to be very difficult, especially at magnetic field strengths exceeding 100 kA/m. Although the bobs of concentric cylinder rheometers tend to be self-centering, the presence of a strong magnetic field in this magnetorheometer tends to pull the bob out of alignment, causing it to contact the outer cup wall. This friction force disturbs the torque reading, making tests with the narrowest gap very difficult to conduct and repeat. While this was problematic, efforts to maintain common centers were eventually successful using a supporting bearing within the fluid chamber.

2.8 Summary

In this chapter a detailed description of a concentric cylinder, or Searle cell, magnetorheometer is presented including an overview of the design methodology for the fluid chamber and electromagnetic circuit. Three bobs, each having a similar shape but different outer radii, are used to affect the active gap size and achieve shear rates up to 25,000 s^{-1} while maintaining uniform, laminar flow. An initial linear analysis of the electromagnetic circuit was augmented with a finite element analysis incorporating the nonlinear B-H properties of steel and MR fluid. Two measurements of the flux within the circuit confirmed the numerical simulation results.

A *LabVIEW* control and data acquisition graphical user interface was developed to input the desired rotation speed and record the output torque and monitor temperature. During fluid characterization tests, a heating/refrigerating circulator along with a custom-built copper cooling jacket maintained any desired temperature with an accuracy of $\pm 0.5°C$. The temperature within

the MR fluid sample was monitored with an immersed thermocouple which did not interfere with the flow within the active gap.

The shear-rate dependent Herschel-Bulkley model for non-Newtonian fluids with a yield stress was used to capture the shear-thinning behavior of the MRF samples. Three commercially available MRFs from LORD Corporation, each containing a different solids loading, were characterized across a range of gap sizes, shear rates, and temperatures.

2.9 Conclusions

Narrow gaps are a key feature that enables effective high shear rate studies. Given a fixed maximum rotation rate from a servomotor, using narrower gaps leads to a proportionally higher maximum shear rate. A smaller gap more easily maintains uniform, laminar flow. It tends to minimize the effects of fluid inertia within the flow, and helps delay the onset of turbulence (Reynolds number) and secondary eddy currents (Taylor number). Analysis of shear flow data is simplified when using the narrow gap assumption, as the fluid can be assumed to have a linear velocity profile and be completely sheared.

Though a linear analysis based on flux continuity is suitable for preliminary device design, a numeric simulation should be performed to account for the nonlinear electromagnetic behavior of the Searle cell's components. Particularly near zero magnetic field, remnant magnetization can confound characterization test results. It is therefore advisable to compare simulations with measurements of the field within the gap, though this is difficult with narrow gap geometries. It is shown that, using a sensing coil to record measurements, the flux through the bob correlates well with the active gap magnetic field.

The Herschel-Bulkley description works well to model this high shear rate data. As expected, yield stress increases with increased solids loading, from 32 vol%, 40 vol%, and 45 vol%. For all

three fluids, the consistency parameter ranges from K = 2-15, and increases monotonically with increasing magnetic field, while the flow index, n, decreases monotonically and ranges from 0.3 to 0.05. Along with the yield stress, the average consistency and flow index for two fluids, MRF-132DG and MRF-140CG, are used to calculate an average viscosity of each fluid across the range of applied fields at four different temperatures: 9°C, 20°F, 38°F and 55°F. Temperature is found to have a more pronounced effect on viscosity than on yield stress, making the measured low temperature viscous stress up to 66% higher than expected, while the difference between high and low temperature yield stress was less than 10%. Regardless, precise temperature control was found to be vitally important to the consistency of rheological measurements.

Narrow gap magnetorheology does have practical complications. Though the bob in a concentric cylinder rheometer tends to be self-centering, the bob in a magnetorheometer tends to be pulled out of alignment in strong magnetic fields. It was found that the 1 mm and 0.25 mm gaps produced reliable and repeatable measurements at shear rates up to 2,500 s^{-1} and 10,000 s^{-1}, respectively. However, the 0.1 mm gap proved challenging due to magnetic force induced eccentricity between the bob-cup centers. Because the gap size approaches that of the carbonyl iron particles there could be only about 10-15 particles in a chain stretching across the gap. These effects resulted in an increase in the yield stress beyond what is predicted by Carlson's equation relating τ_y to H, and serves as the basis of investigation for a subsequent chapter.

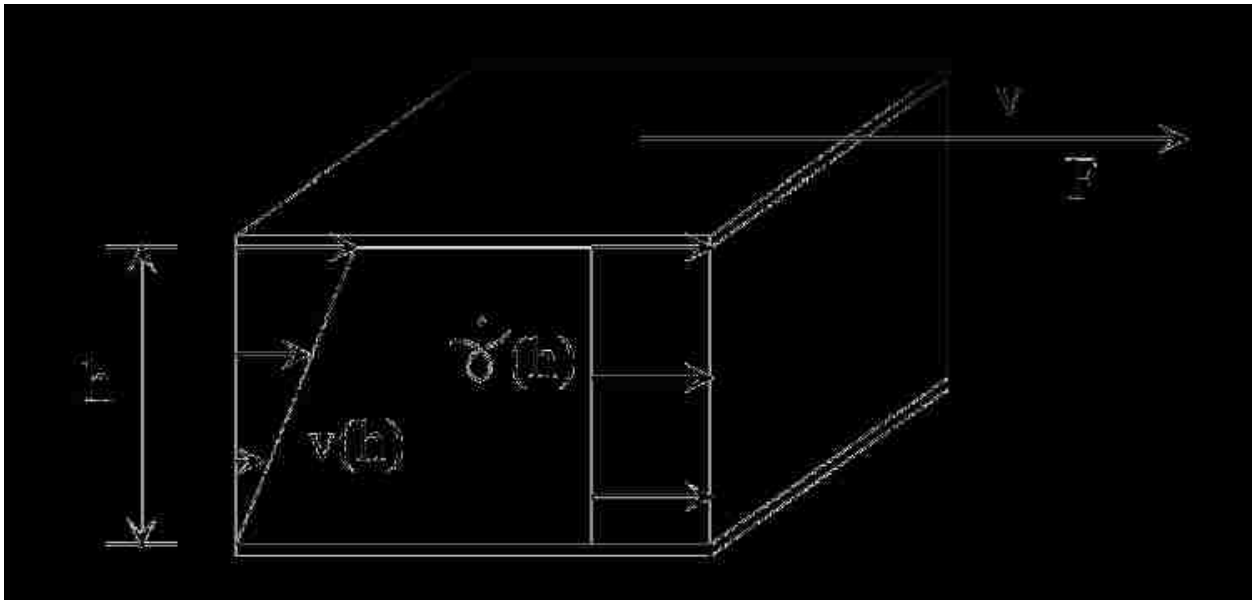

Figure 2.1 – Parallel plate schematic showing fundamental elements of fluid flow

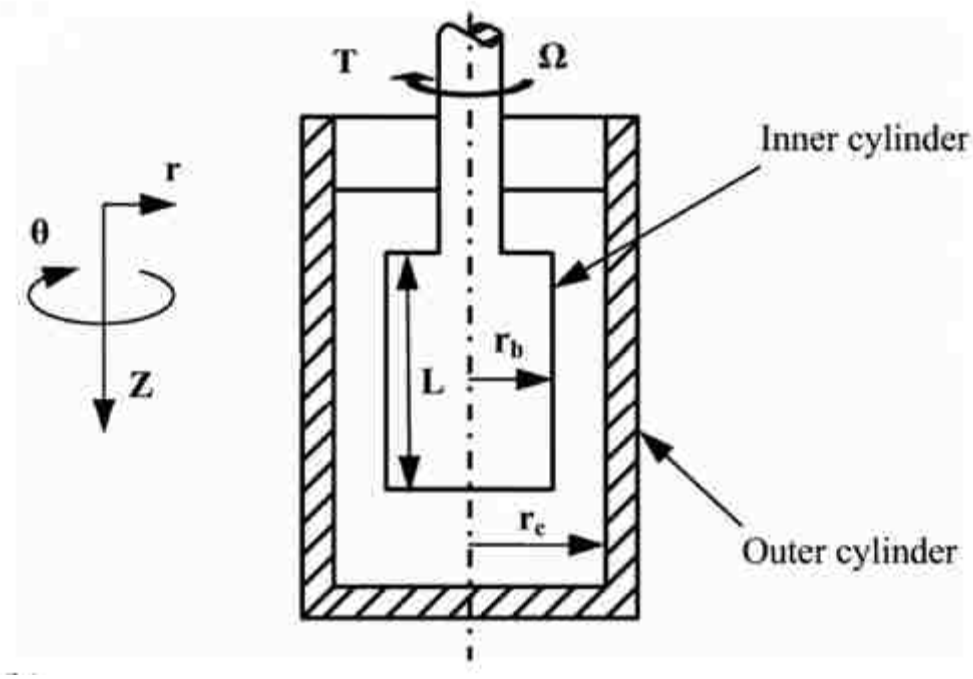

Figure 2.2 – Concentric cylinder, or Couette, geometry. With the inner cylinder rotating, this is known as a Searle cell.

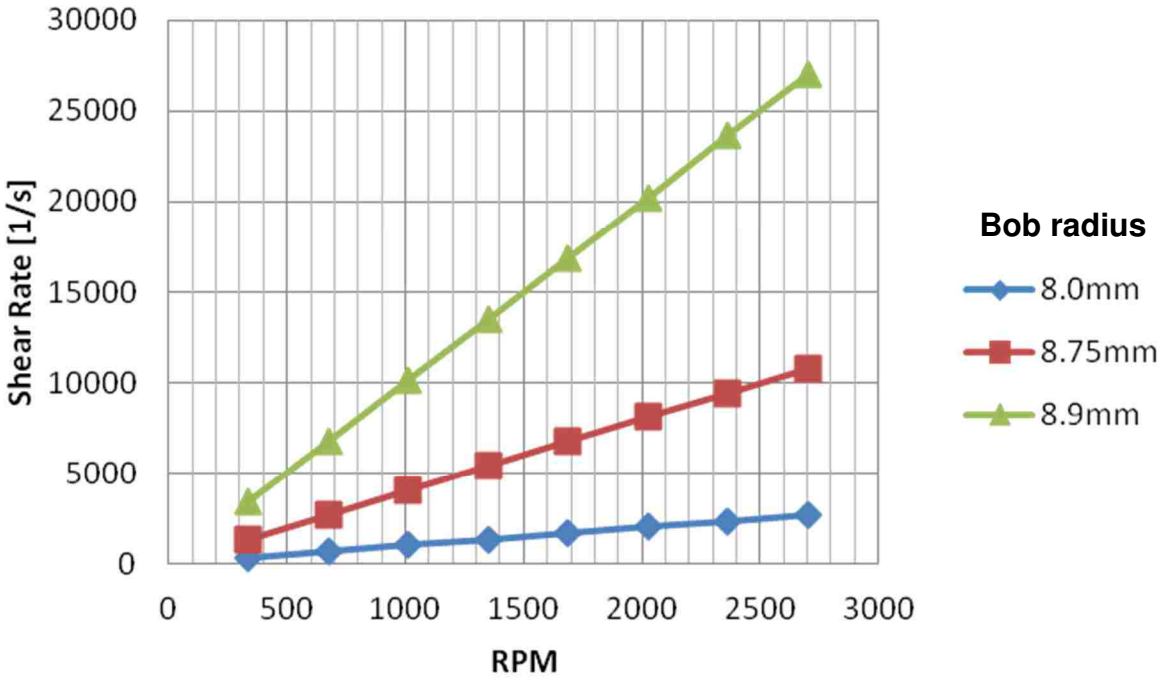

Figure 2.3 – Bob rotation speed versus shear rate for different bob radii. Smaller gaps amplify the maximum shear rate.

Select operating point (H_f, B_f) for desired yield stress, τ_y, in MR fluid using the magnetization curve.

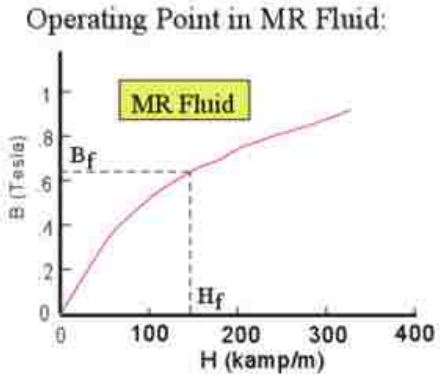

a)

The total magnetic flux is conserved throughout the flux path. Determine the corresponding operating point (H_s, B_s) in steel.

$$\Phi = B_f A_g = B_s A_s \rightarrow B_s = \frac{B_f A_g}{A_s}$$

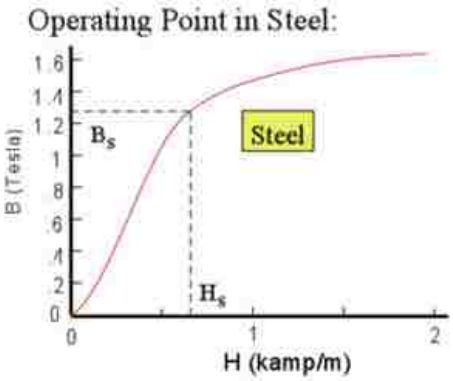

b)

Determine required electromagnet Ampere-Turns (NI) from Kirchhoff's Law for Magnetic Circuits

$$NI = \oint H \cdot ds = \sum_i H_i \cdot L_i$$

$$= H_f \cdot g + H_s \cdot L$$

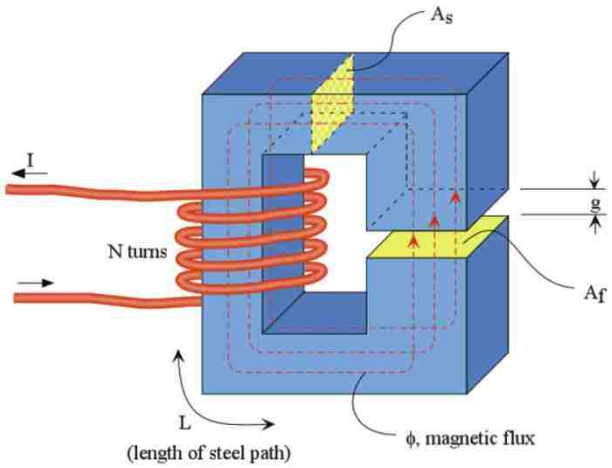

c)

Figure 2.4 - Design of the electromagnetic circuit for an MR device (LORD Materials Division, 1999)

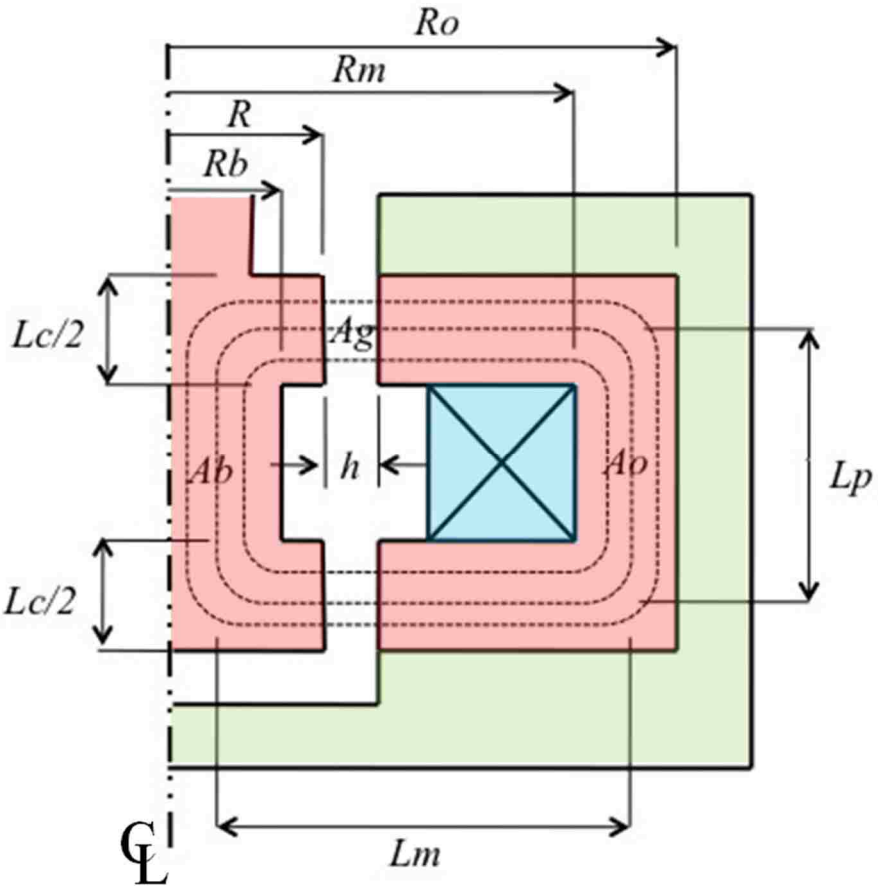

Figure 2.5 – Axisymmetric schematic for the Searle cell magnetic circuit. Red denotes the magnetic circuit, blue is the electromagnet, and green is the nonconducting housing.

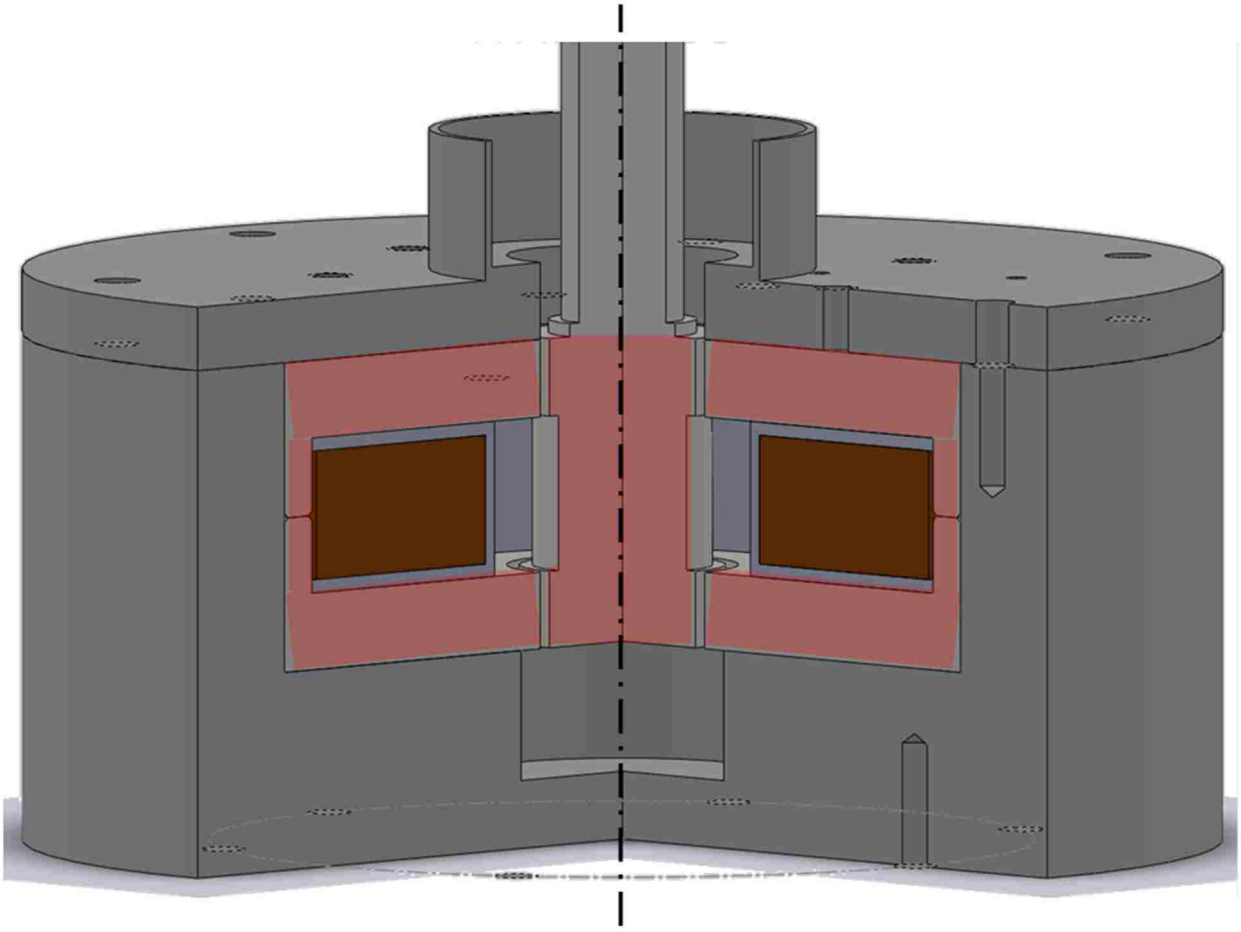

Figure 2.6 - Quarter-section of the magnetorheometer cell. Red corresponds to the magnetic flux path, brown is the electromagnet.

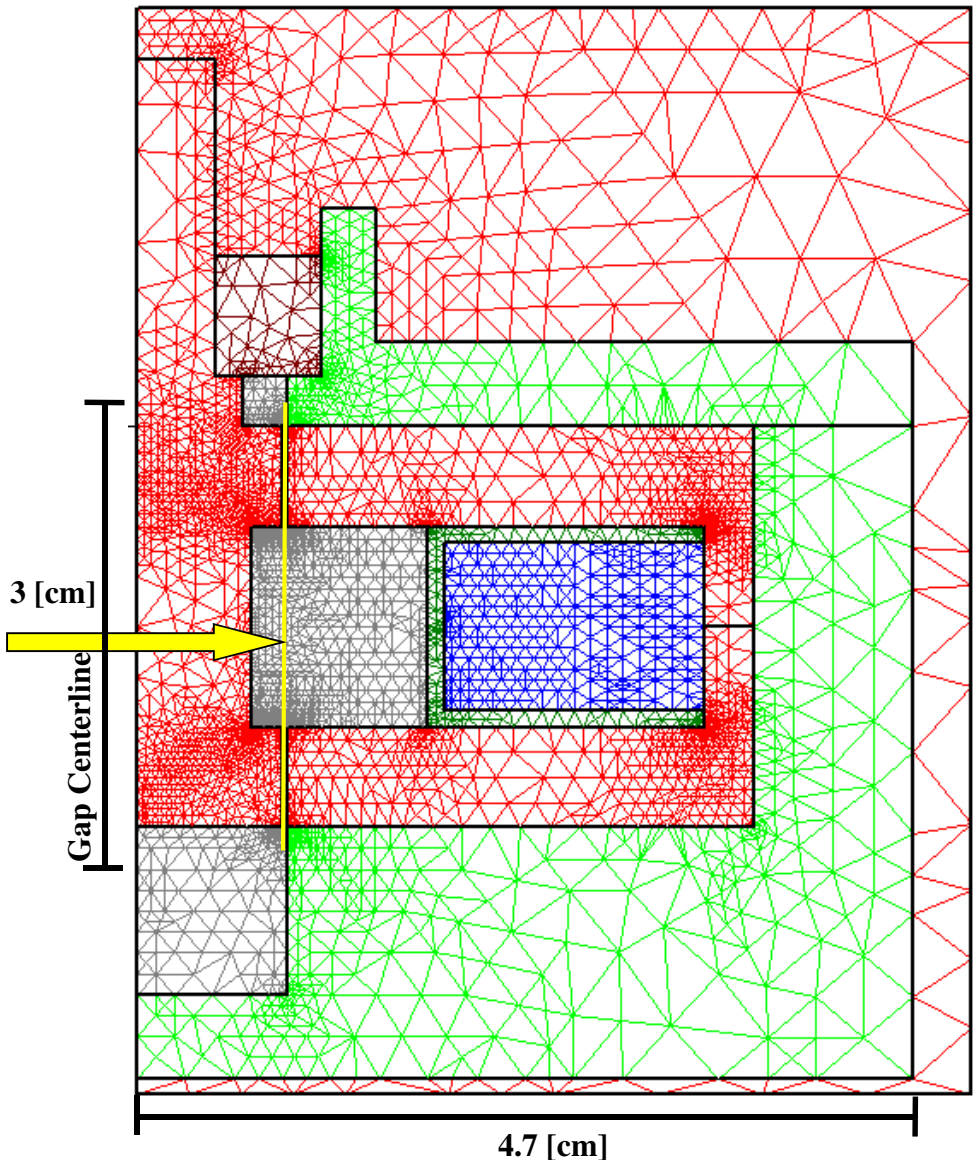

Figure 2.7 – Triangular mesh used in MAXWELL magnetostatic simulations. Green shades correspond to low permeability materials, red shades indicate areas that make up the magnetic flux path, gray represents the MR fluid, and blue is the EM coil. The background red material is air, and the yellow line indicates the active gap detailed in Figure 2.9.

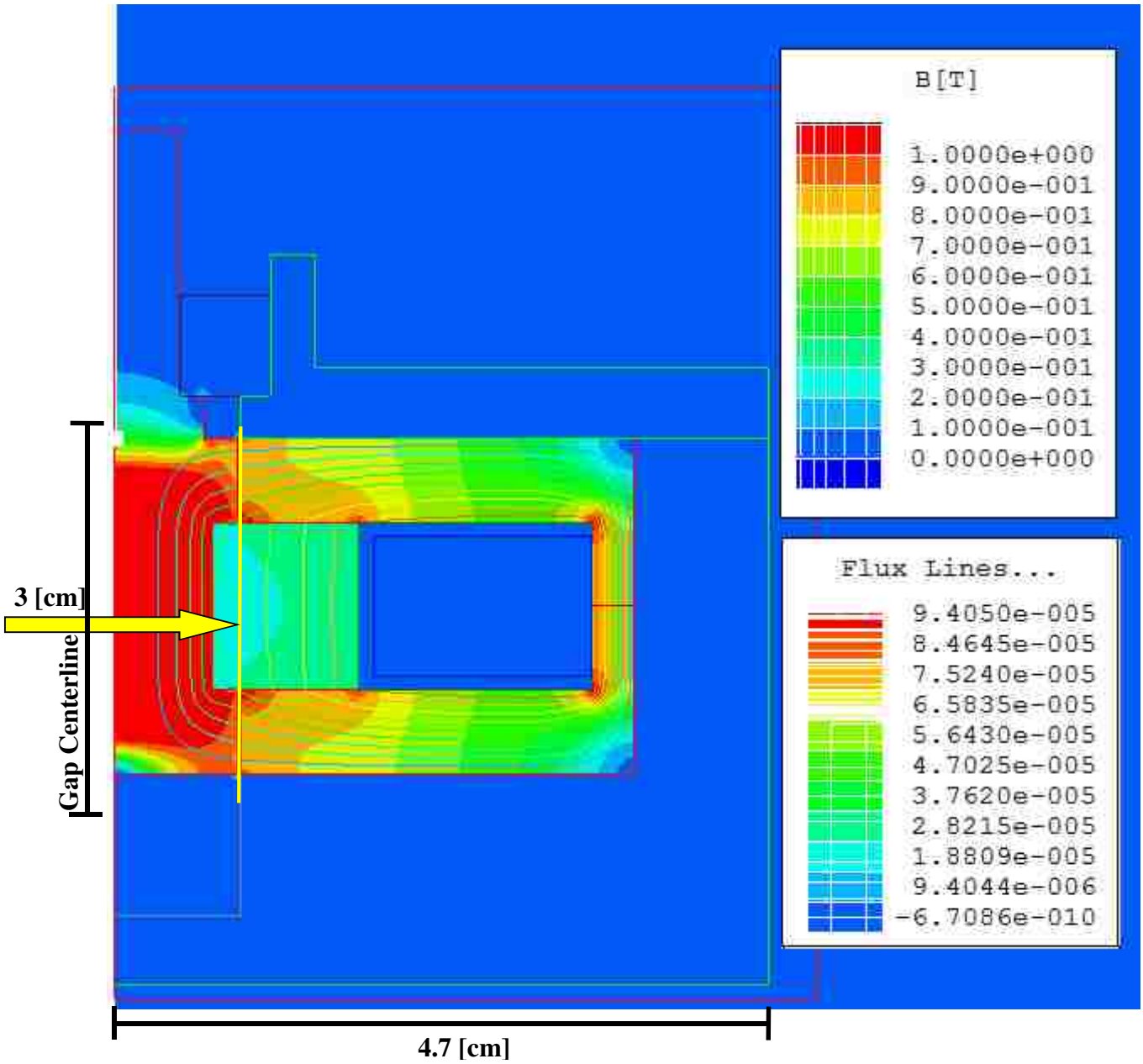

Figure 2.8 – Magnetostatic FEA results for 1 A applied current. The flux density magnitude, B [T], is indicated by solid colors, while the direction of magnetic flux is indicated by thin flux lines. The yellow line indicates the active gap detailed in Figure 2.9.

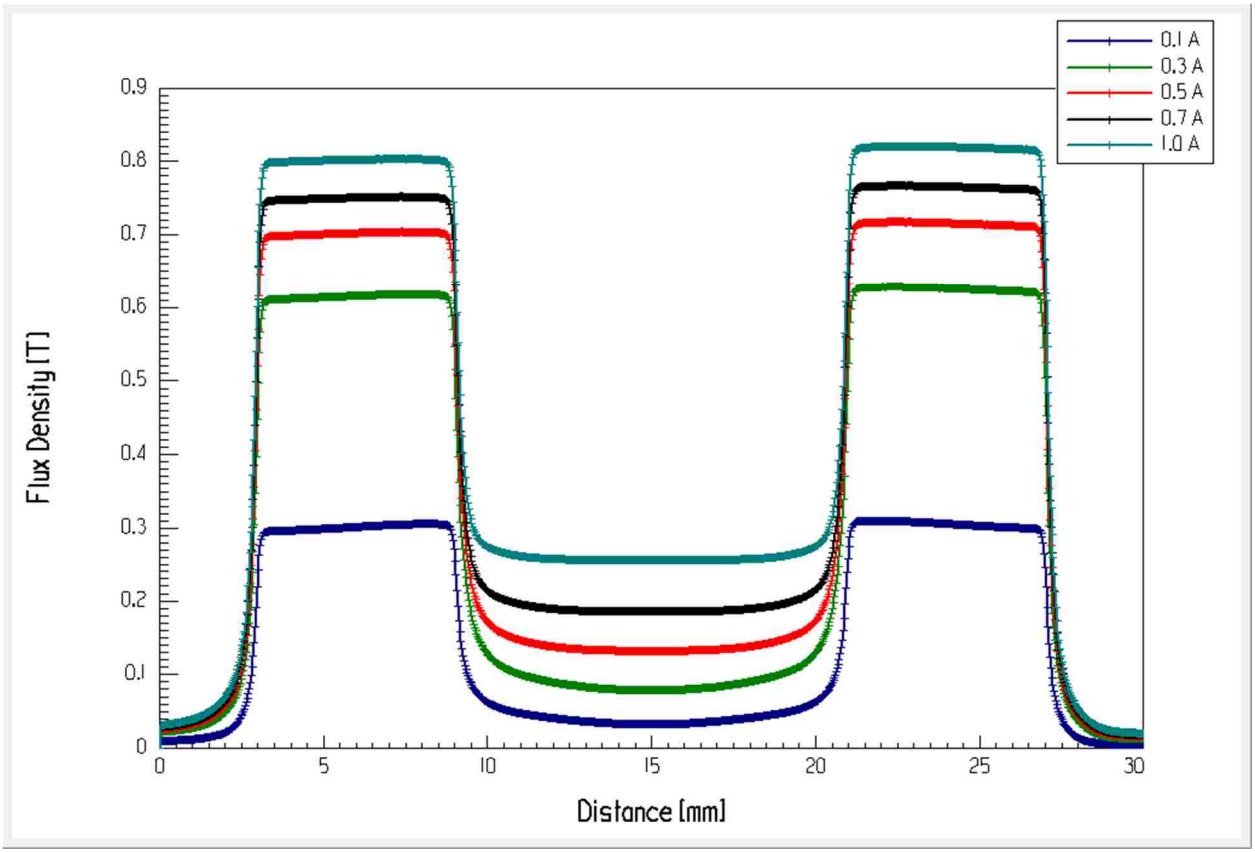

Figure 2.9 – Flux density magnitude in the center of the active gap for MRF-132DG at 1 A applied current and 0.25 mm gap. Note that the peaks correspond to flux direction perpendicular to shear flow, while the trough is flux in the axial direction.

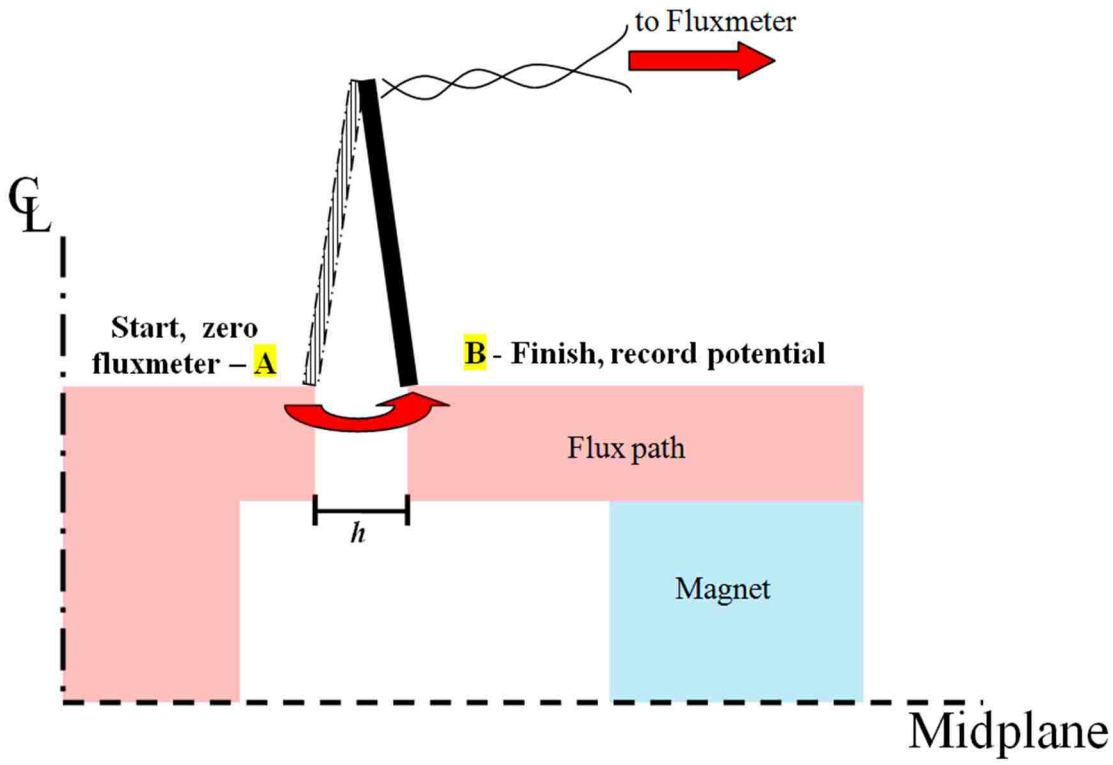

Figure 2.10 - Measurement of the field strength H in the gap of a magnetic circuit:
A) Measure the potential difference between points A and B close to the gap, $P_B - P_B$.
B) Divide the difference by the width h of the gap. $H = {}^{P_A - P_B}/_{h}$

Figure 2.11 – Potential coil probe, Walker LDJ Scientific model PM/S83 (Walker LDJ Scientific, 2013)

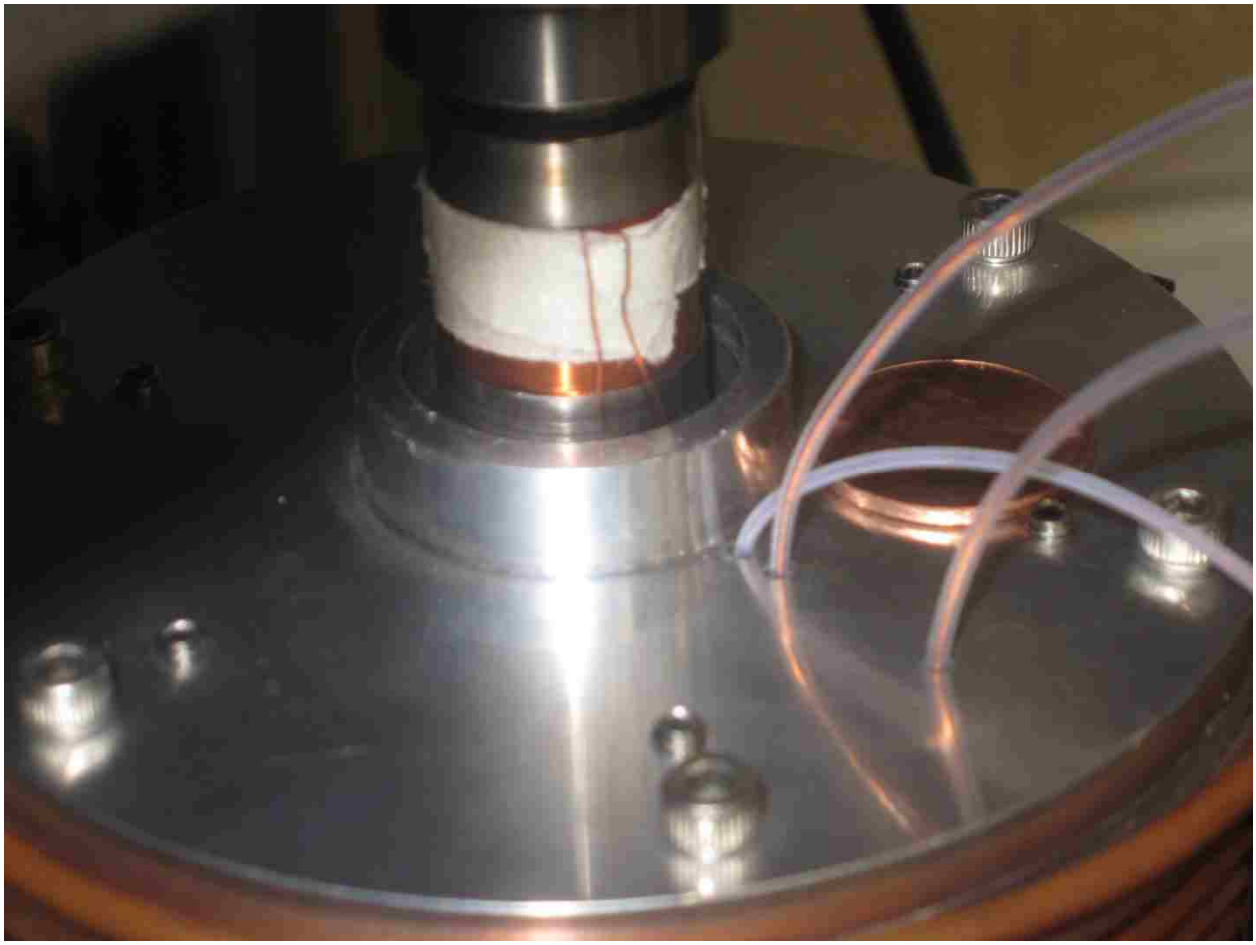

Figure 2.12 – Custom sensing coil on 0.25 mm bob. The two outermost entering wire connections power the electromagnet, while the innermost connects the sensing coil leads to the integrating fluxmeter. The sensing coil leads are fed out from the central fluid chamber to avoid interference from the high magnetic field within the active gaps.

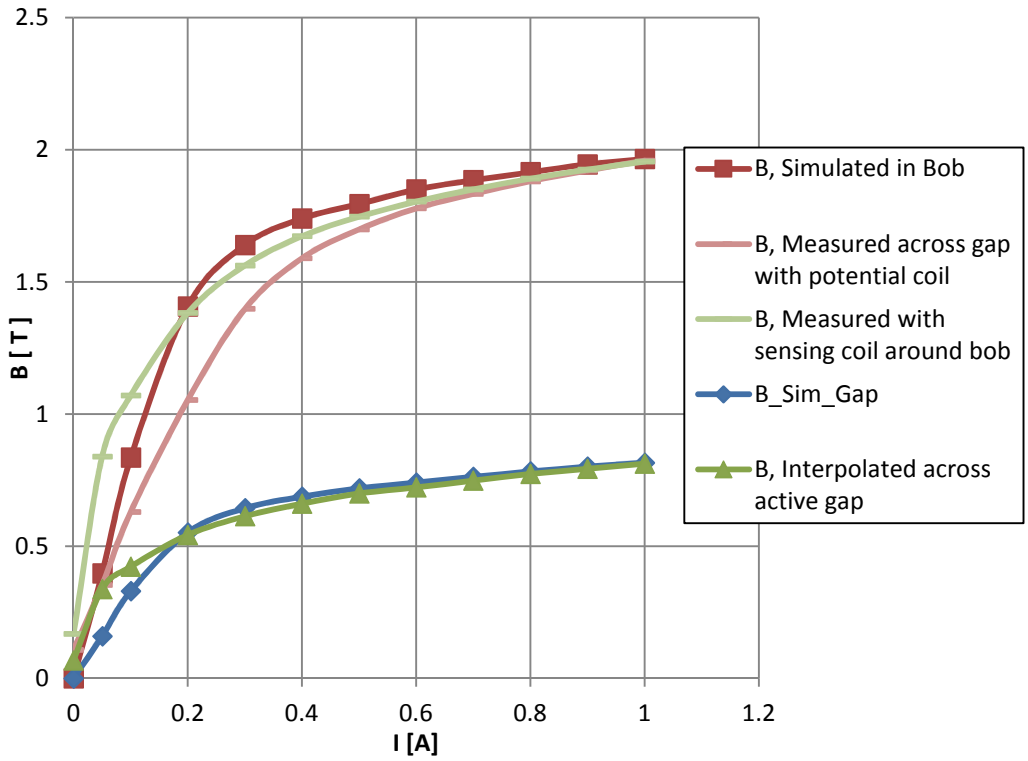

Figure 2.13 – Magnetic flux density vs. applied current from FEA simulation and potential and sensing coil measurements for MRF-132DG

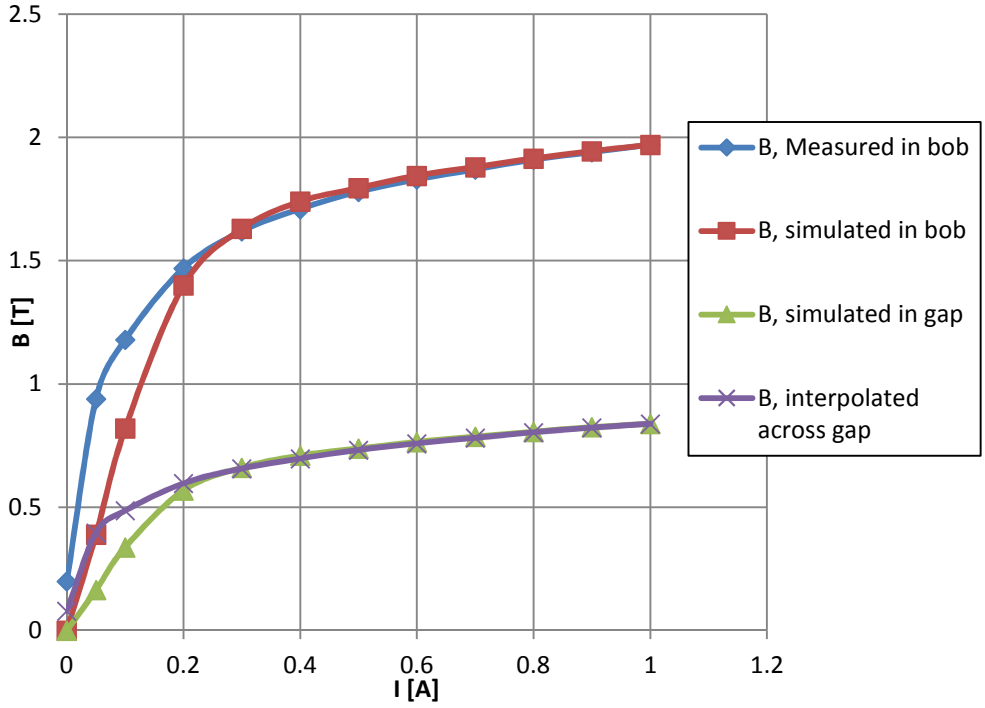

Figure 2.14 – Magnetic flux density vs. applied current from FEA simulation and sensing coil measurements for MRF-140CG

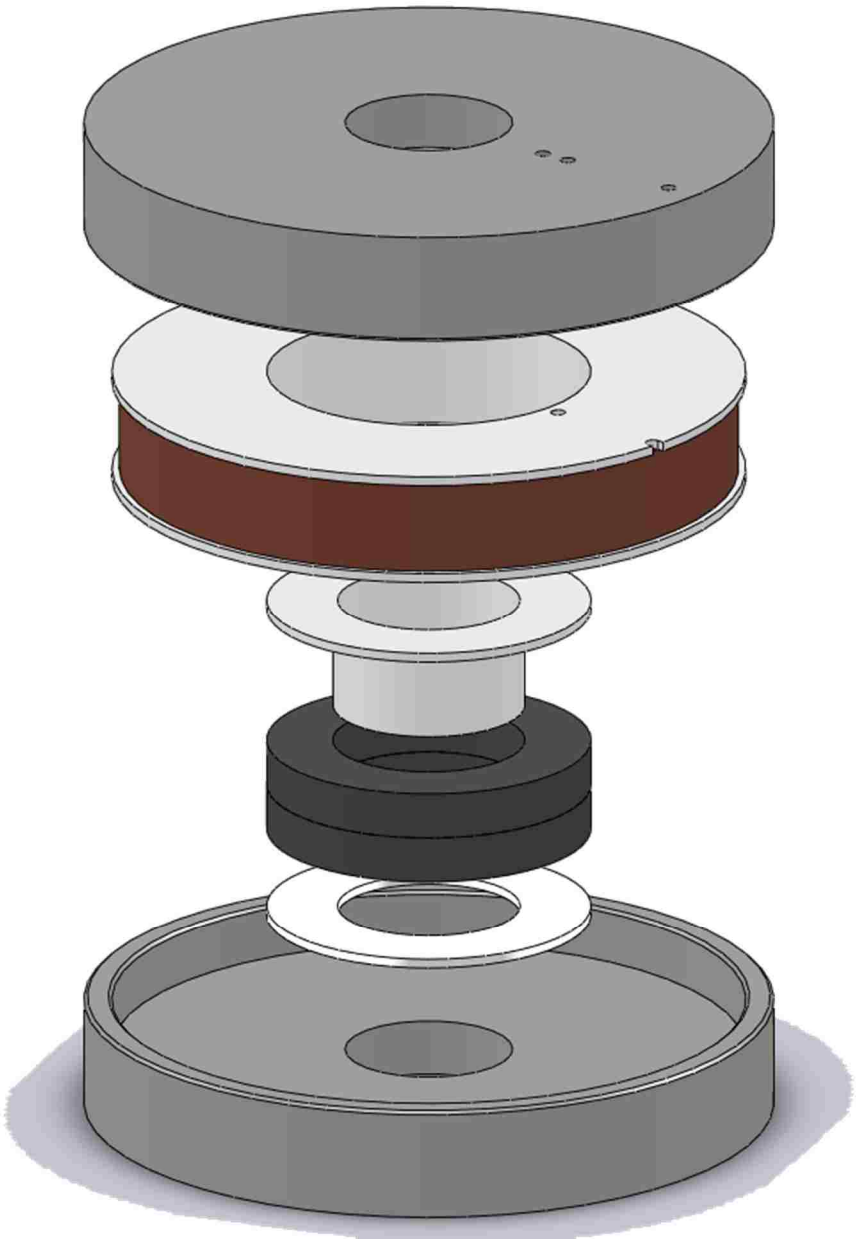

Figure 2.15 - Exploded view of the hybrid electromagnet/permanent magnet configuration of the magnetorheometer cell

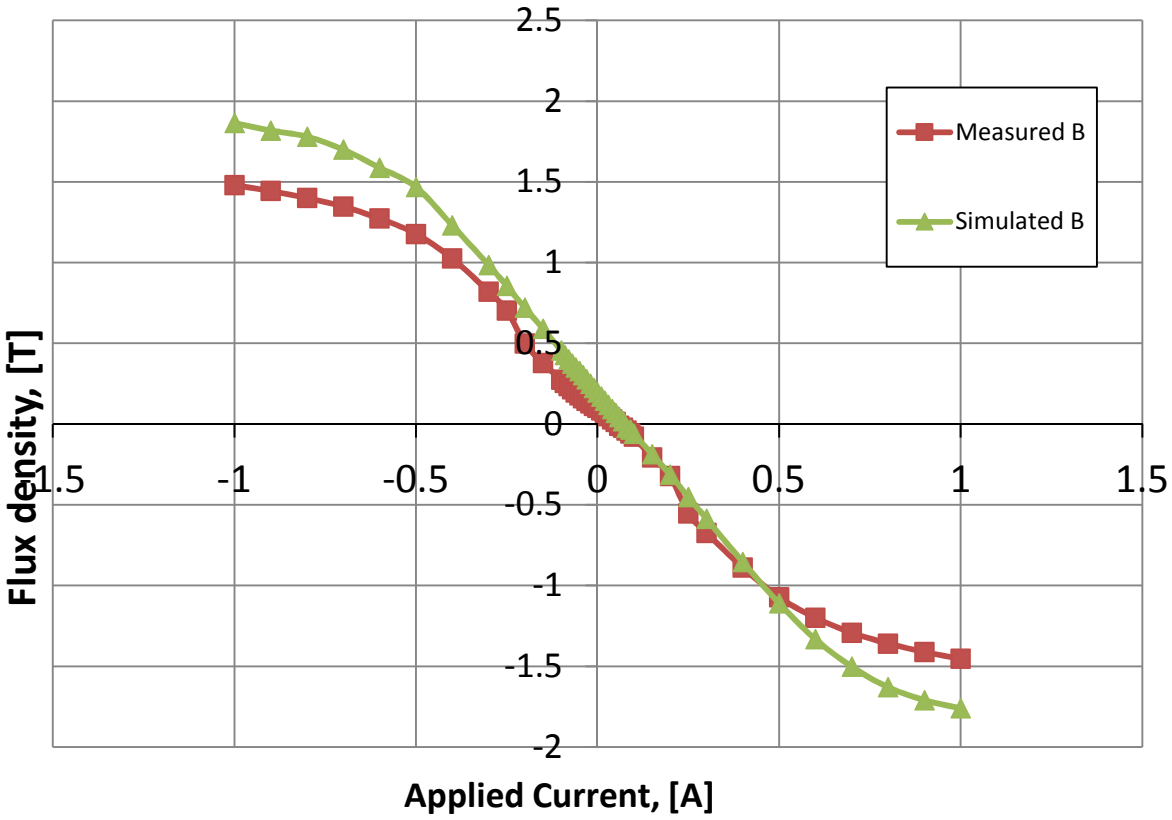

Figure 2.16 – Simulated and measured values for flux density within the bob vs. applied current for the hybrid electromagnet/permanent permanent magnet configuration of the Searle cell magnetorheometer

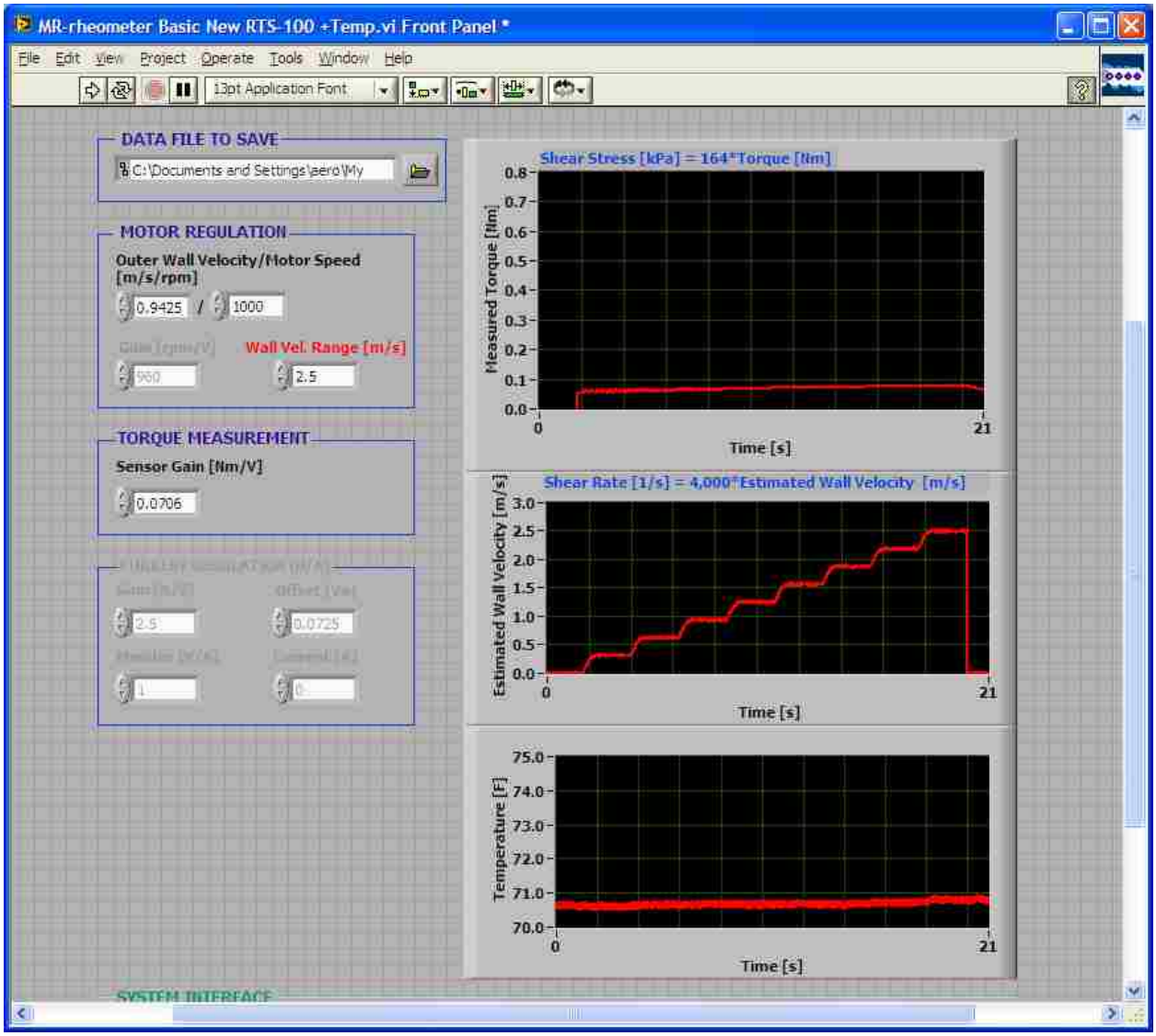

Figure 2.17 – *LabVIEW* control and data acquisition graphical user interface, displaying (top) measured torque, (middle) estimated wall velocity, (bottom) temperature, with sample data trace

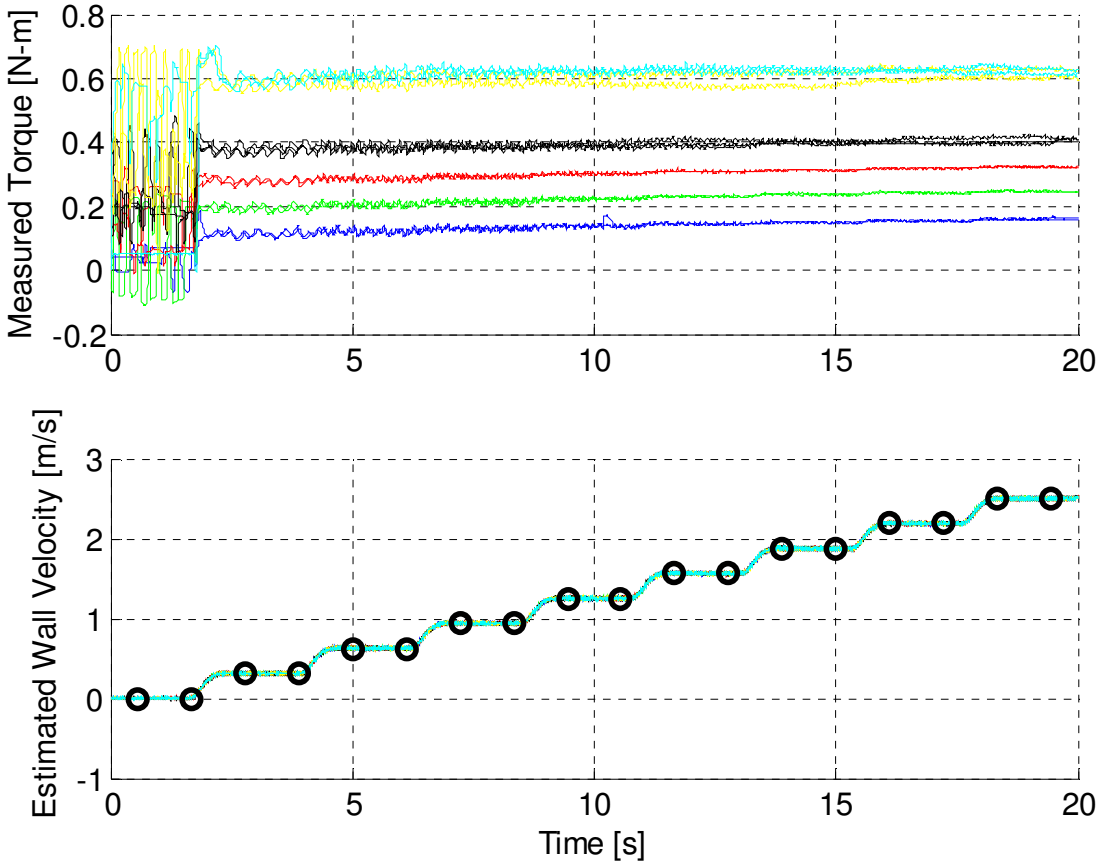

Figure 2.18 – Raw data for a range of applied fields. Black circles denote the sections of data compiled for analysis.

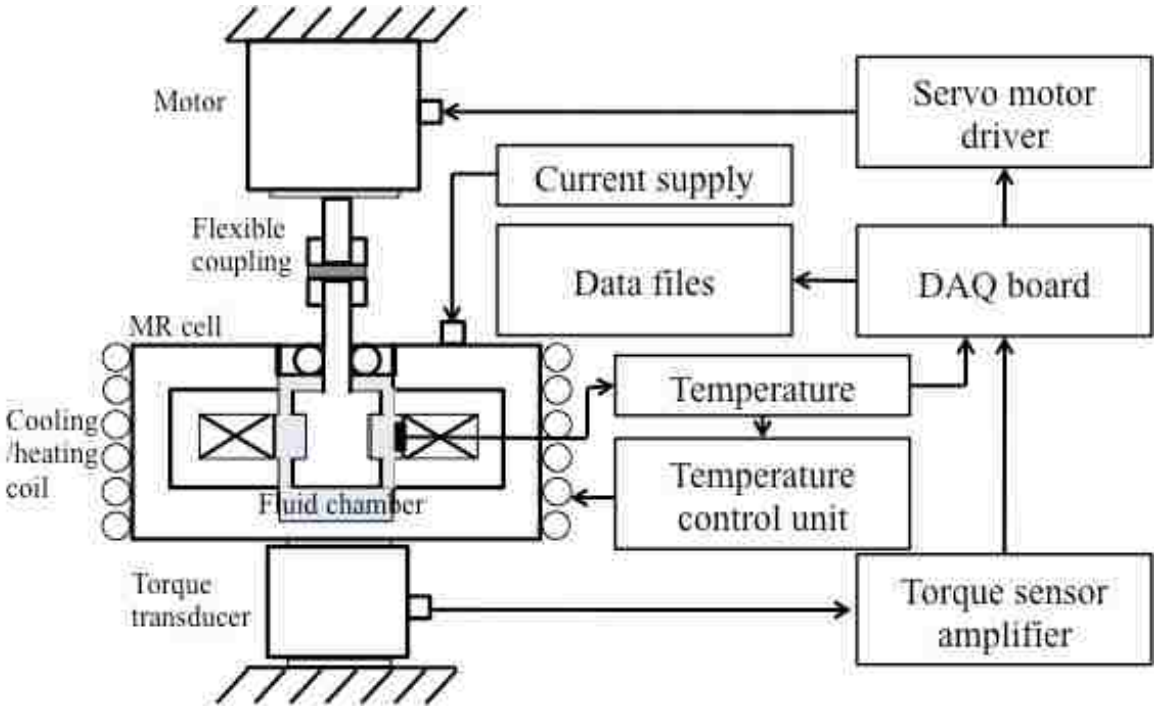

Figure 2.19 – High shear rate magnetorheometer schematic

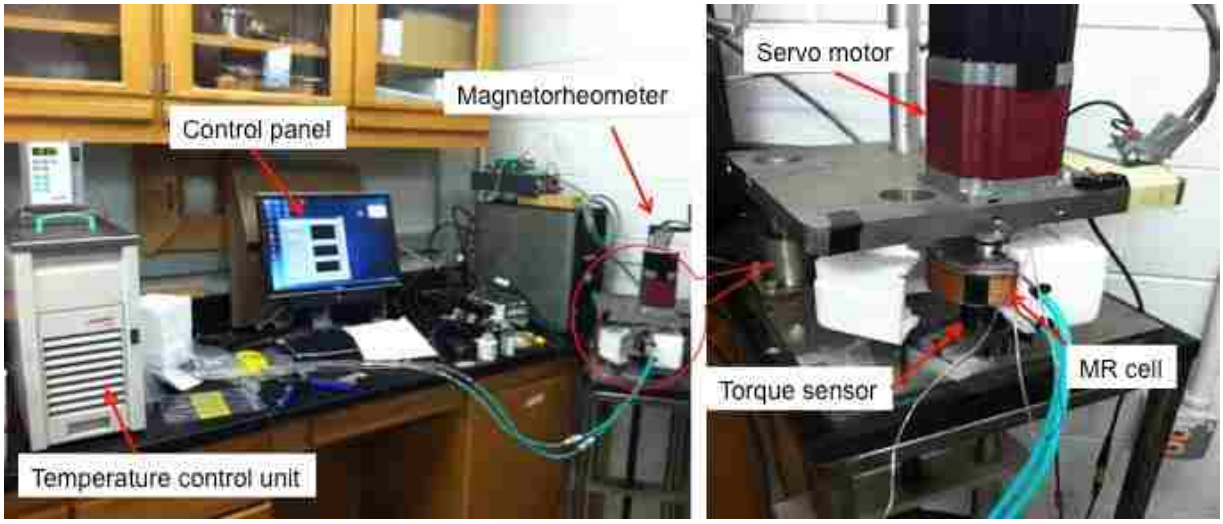

Figure 2.20 – Magnetorheometer system featuring computer control, data acquisition, and integrated temperature control

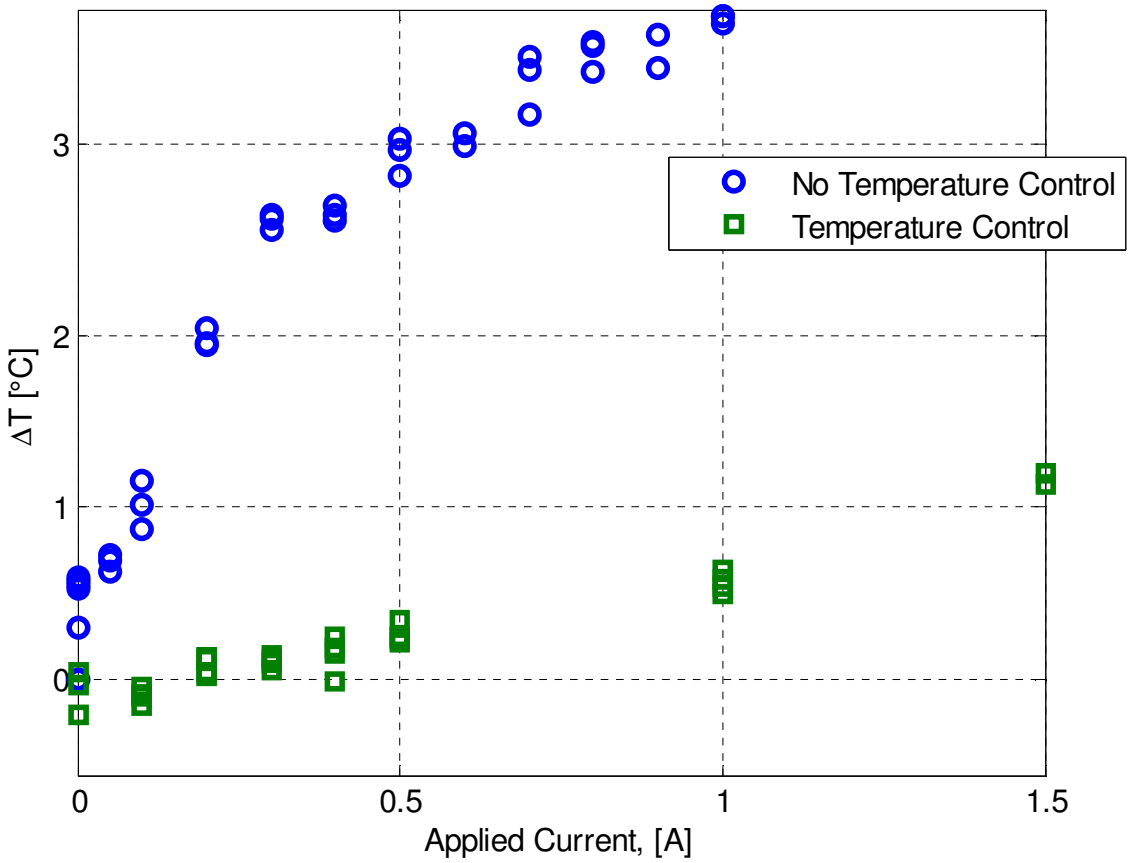

Figure 2.21 – Comparison of temperature change for baseline and temperature controlled configurations during 21 second test runs across a range of applied current using the 0.25 mm gap

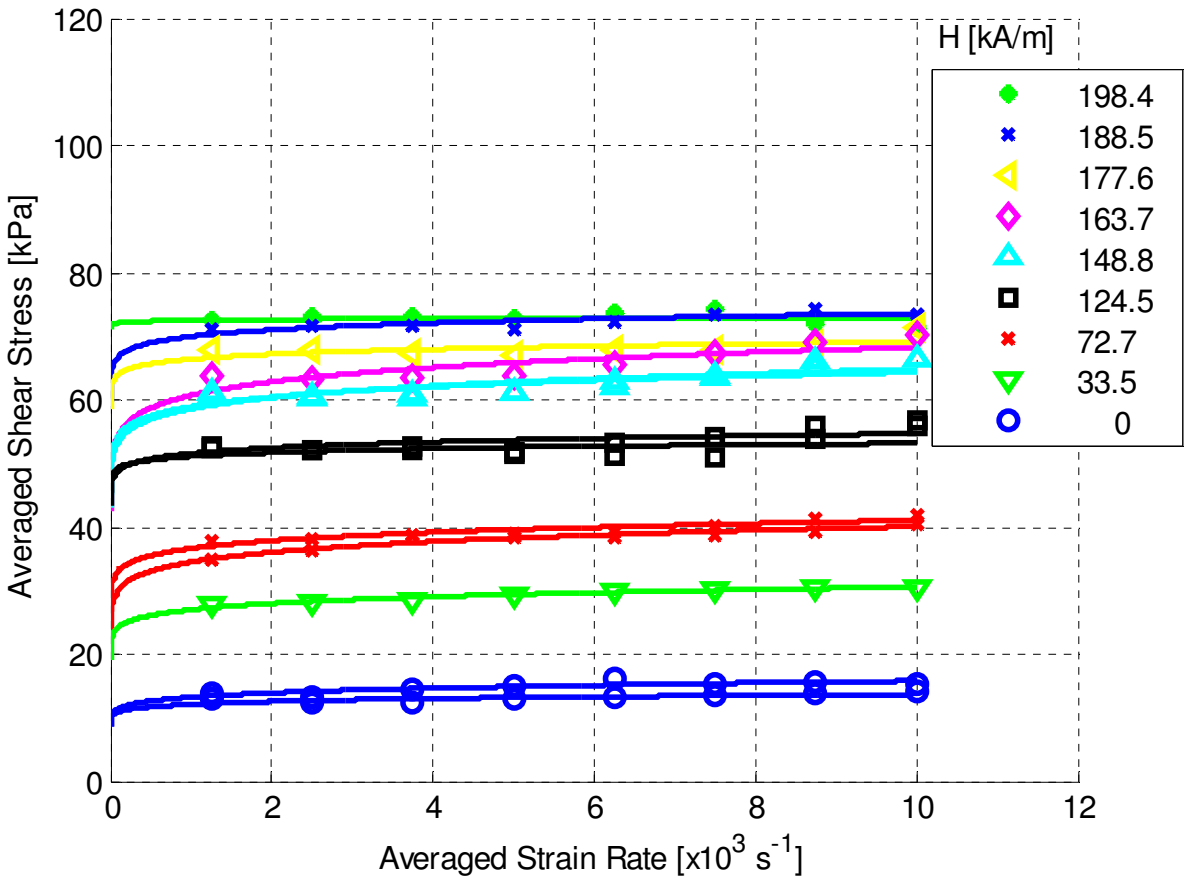

Figure 2.22 – Flow curves for LORD MRF-132DG with Herschel-Bulkley model fit at each magnetic field strength, 20°C

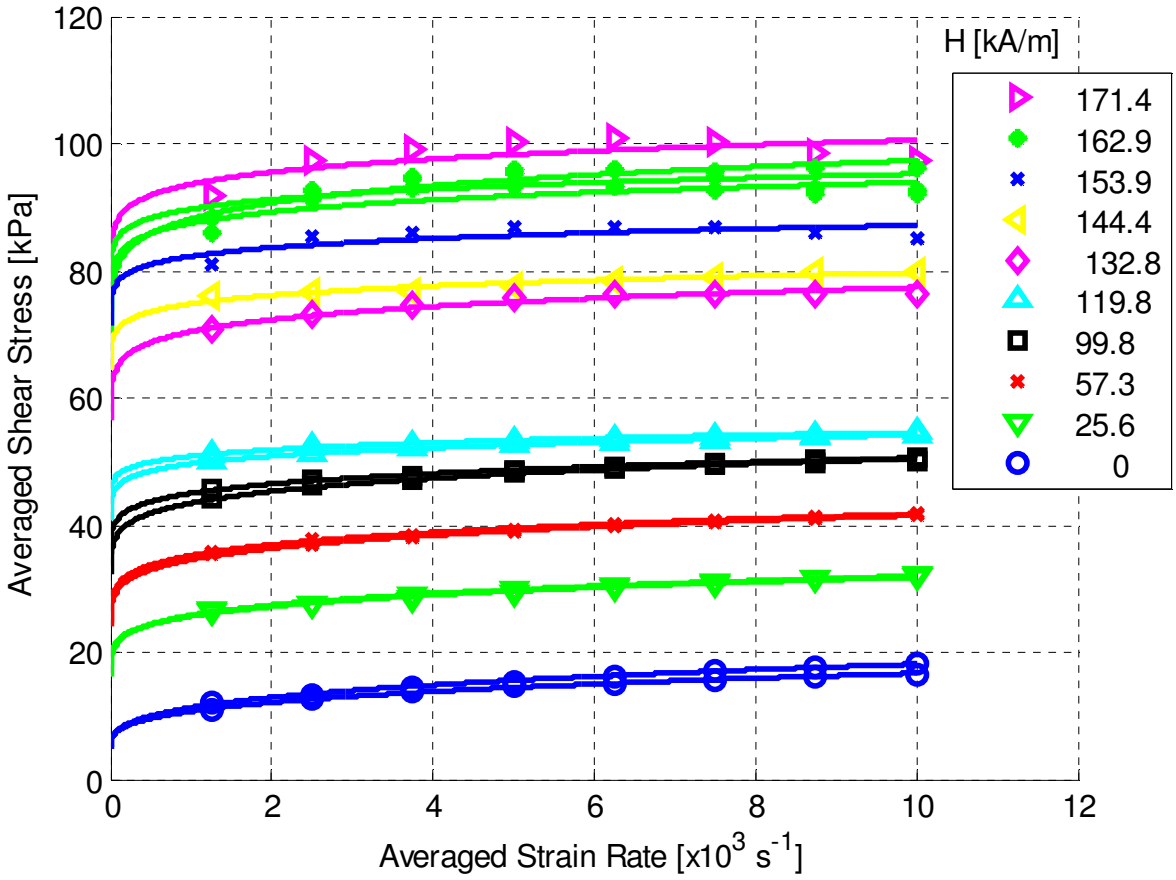

Figure 2.23 - Flow curves for LORD MRF-140CG with Herschel-Bulkley model fit at each magnetic field strength, 20°C

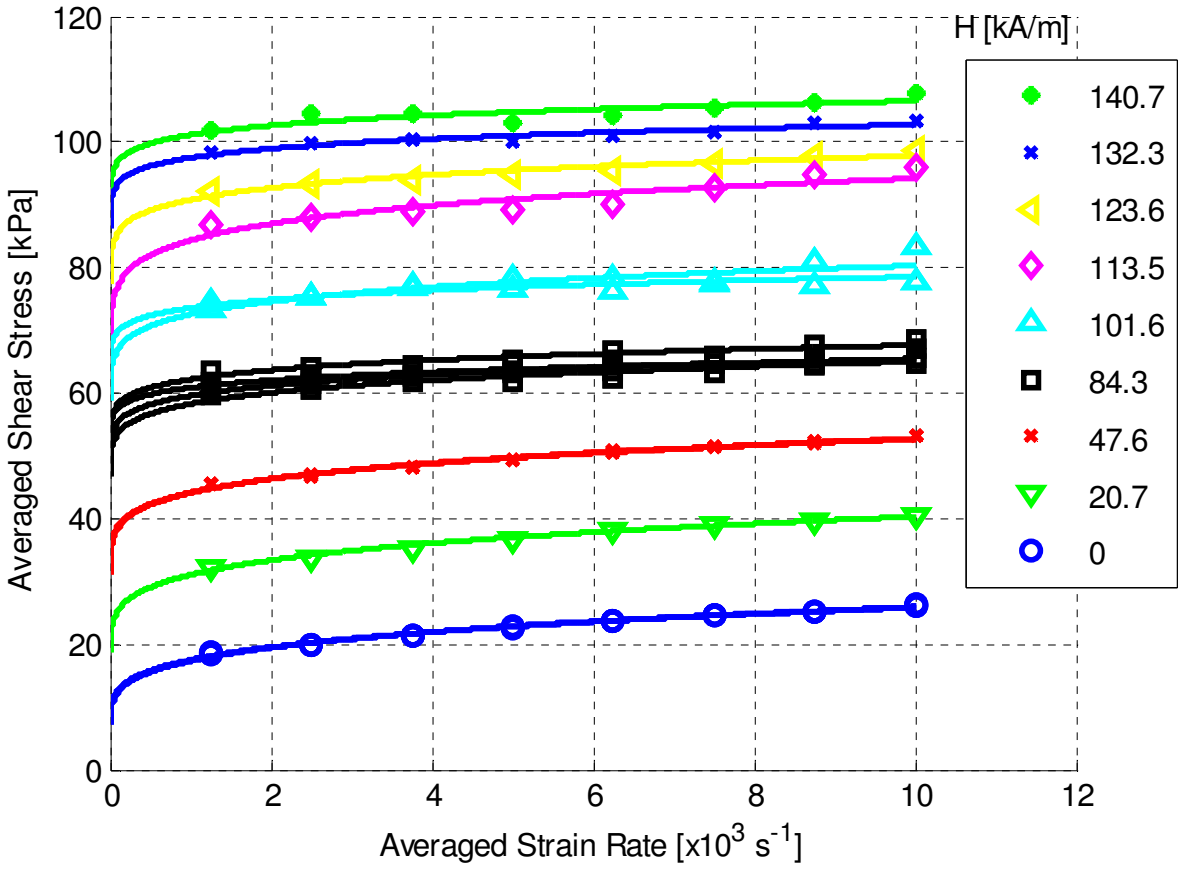

Figure 2.24 - Flow curves for LORD MRF-145BG with Herschel-Bulkley model fit at each magnetic field strength, 20°C

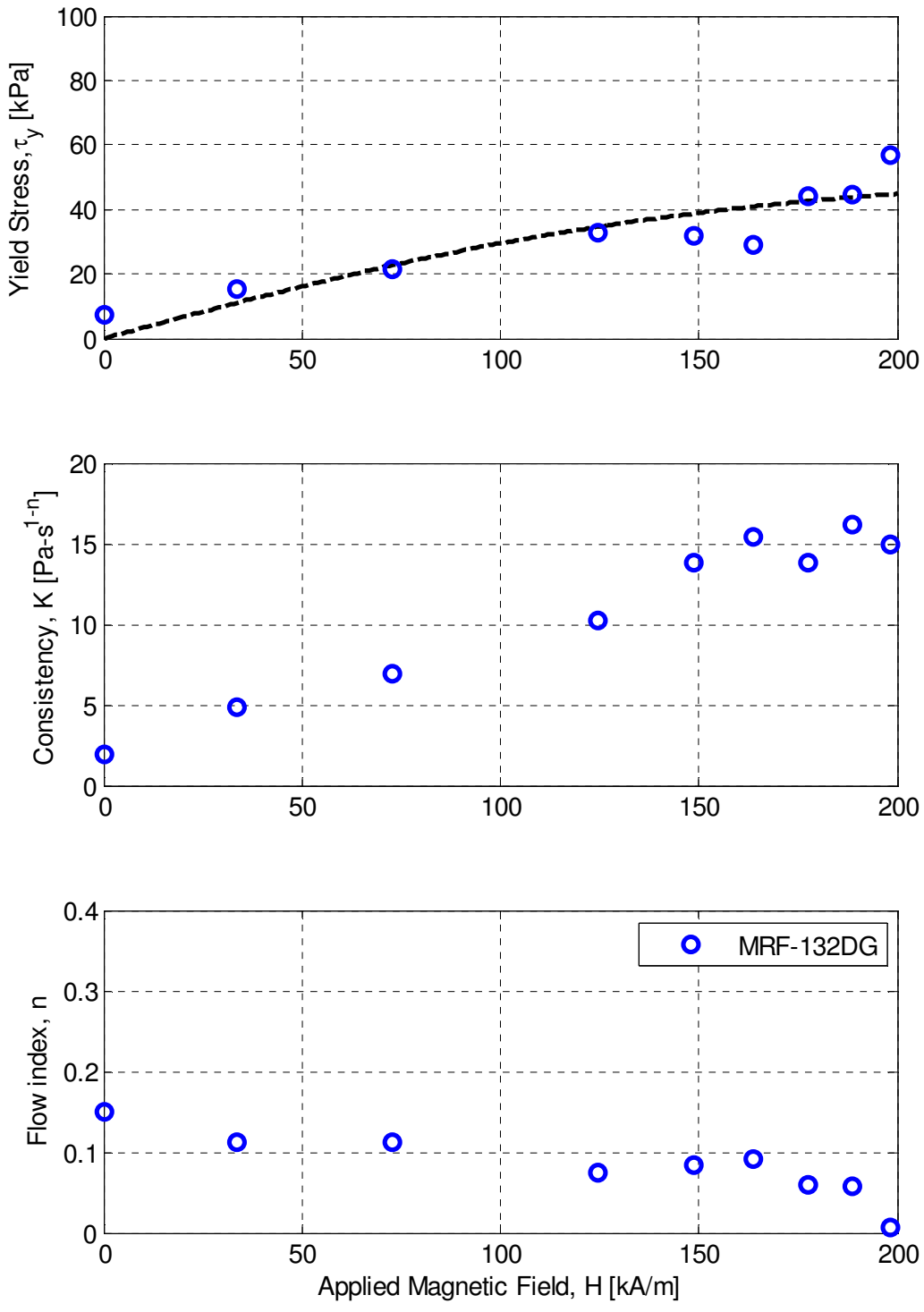

Figure 2.25 – Herschel-Bulkley parameters vs. applied magnetic field for MRF-132DG at $\dot{\gamma}_{max} = 10,000\ [s^{-1}]$, 20°C

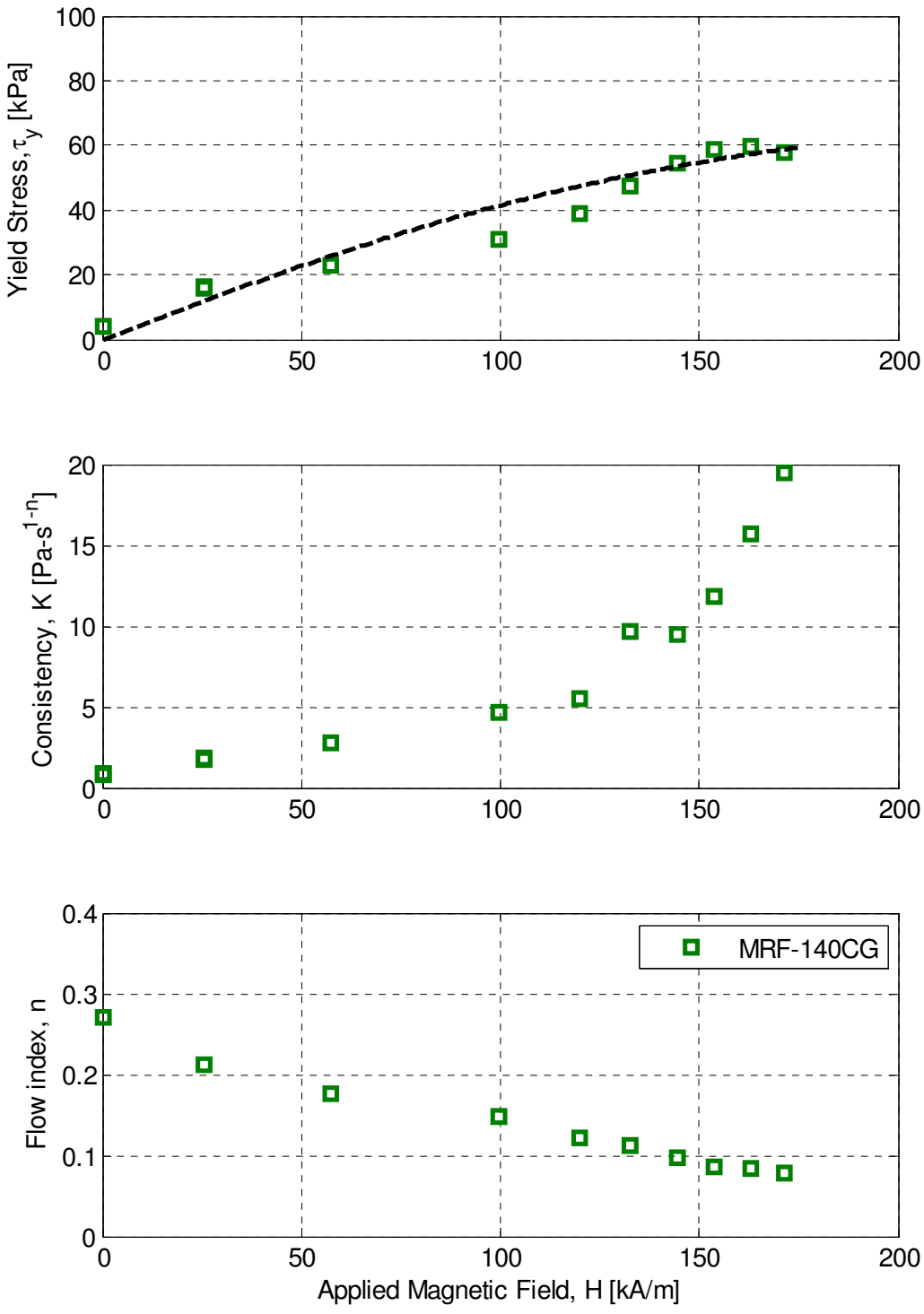

Figure 2.26 - Herschel-Bulkley parameters vs. applied magnetic field for MRF-140CG at $\dot{\gamma}_{max} = 10,000\ [s^{-1}]$, 20°C

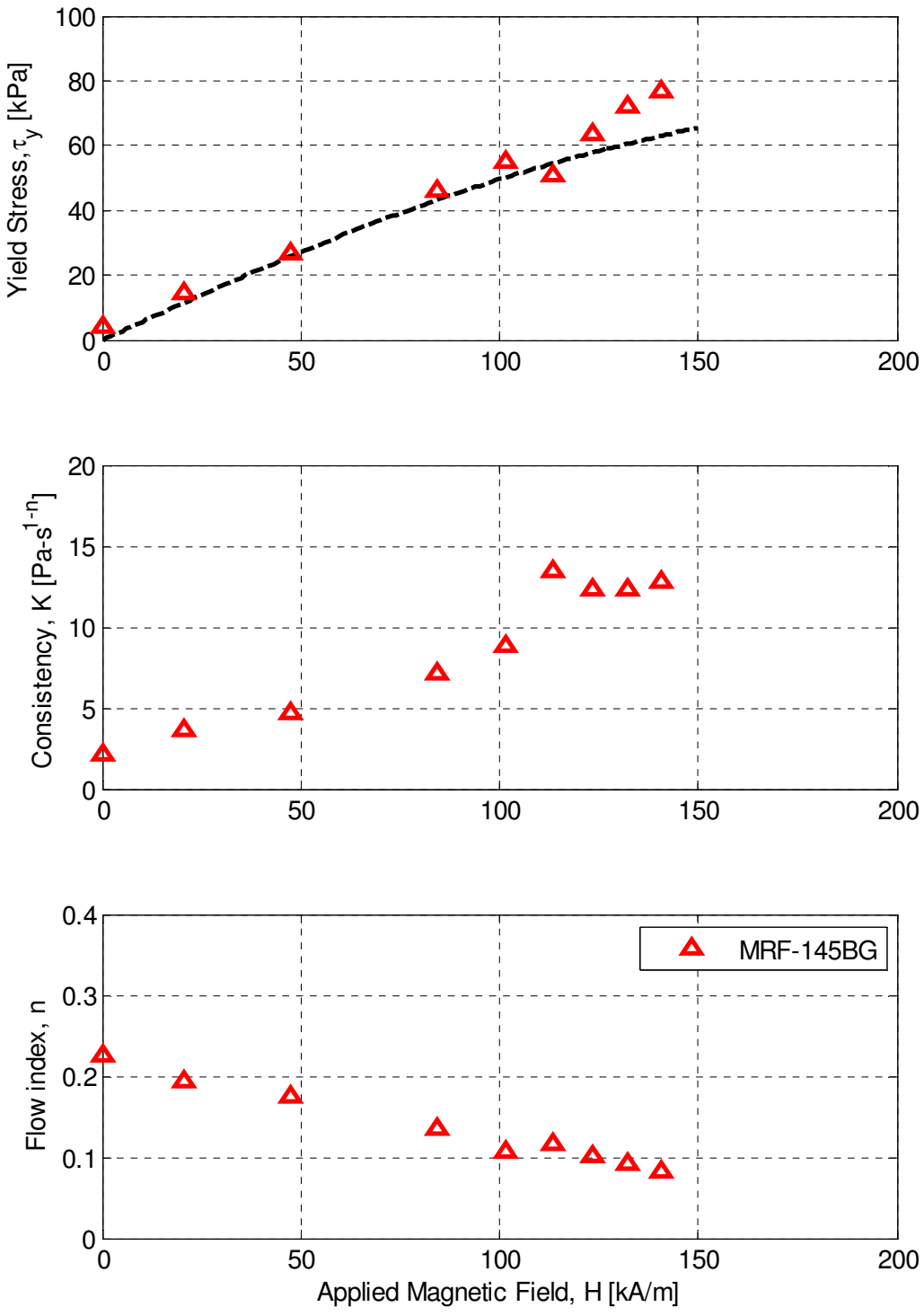

Figure 2.27 - Herschel-Bulkley parameters vs. applied magnetic field for MRF-145BG at $\dot{\gamma}_{max} = 10,000\ [s^{-1}]$, 20°C

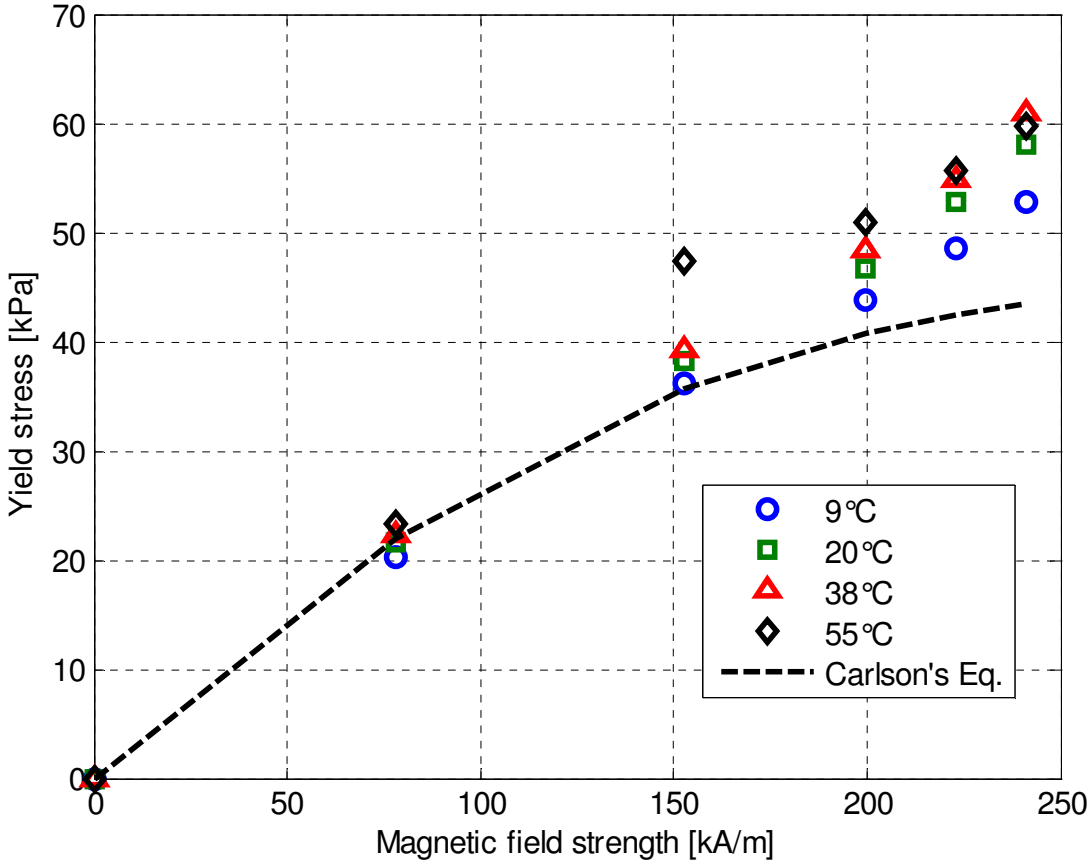

Figure 2.28 – Temperature effects on yield stress for MRF-132DG at $\dot{\gamma}_{max} = 10,000\ [s^{-1}]$

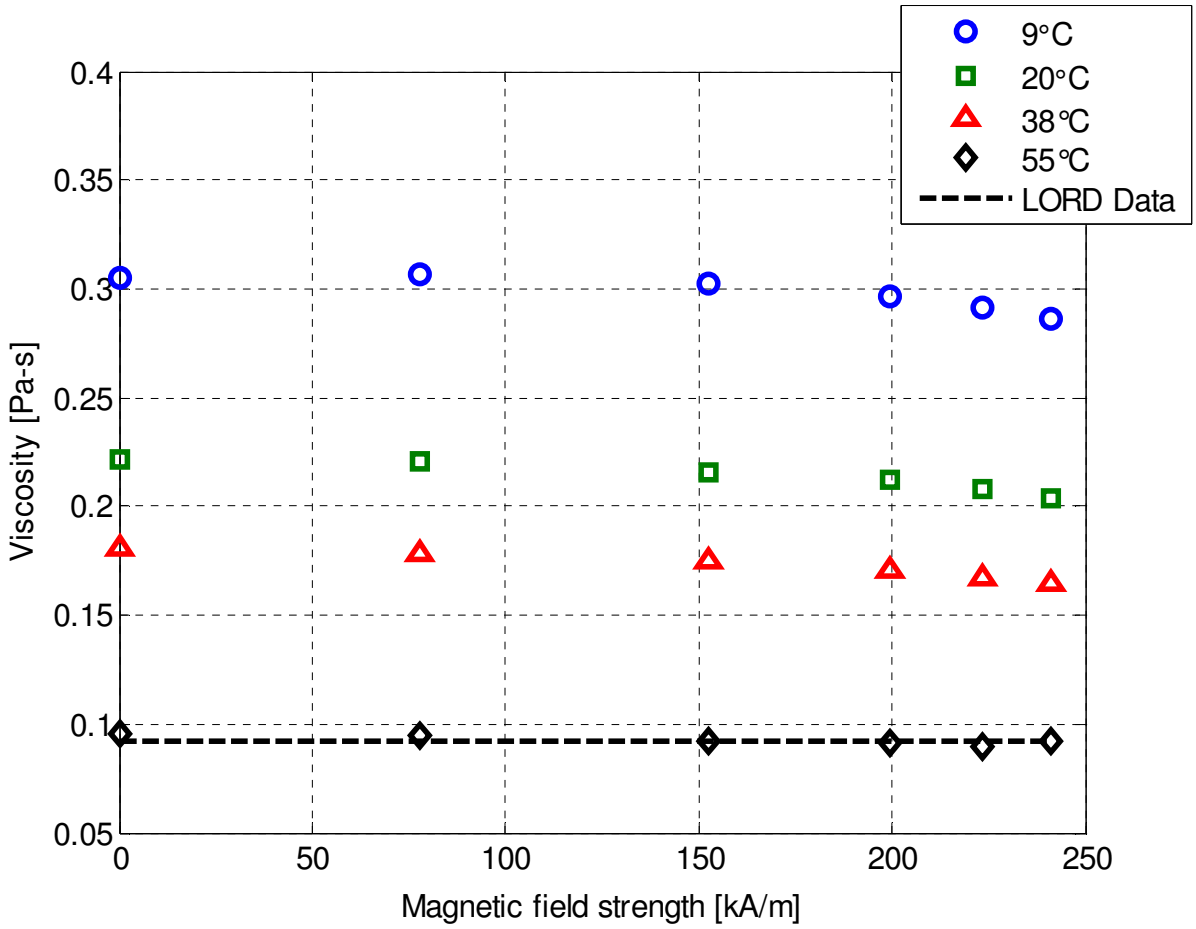

Figure 2.29 – Temperature effects on viscosity of MRF-132DG at $\dot{\gamma}_{max} = 10,000\ [s^{-1}]$

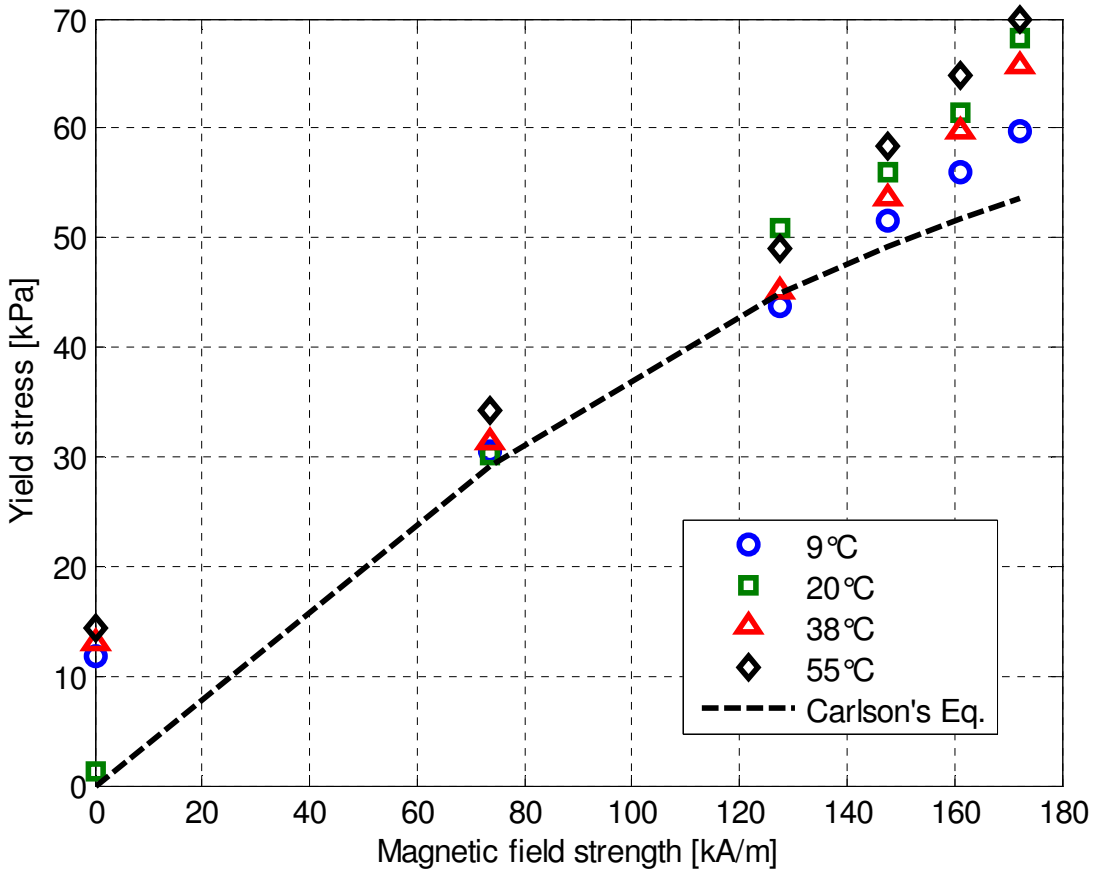

Figure 2.30 - Temperature effects on yield stress of MRF-140CG at $\dot{\gamma}_{max} = 10,000\ [s^{-1}]$

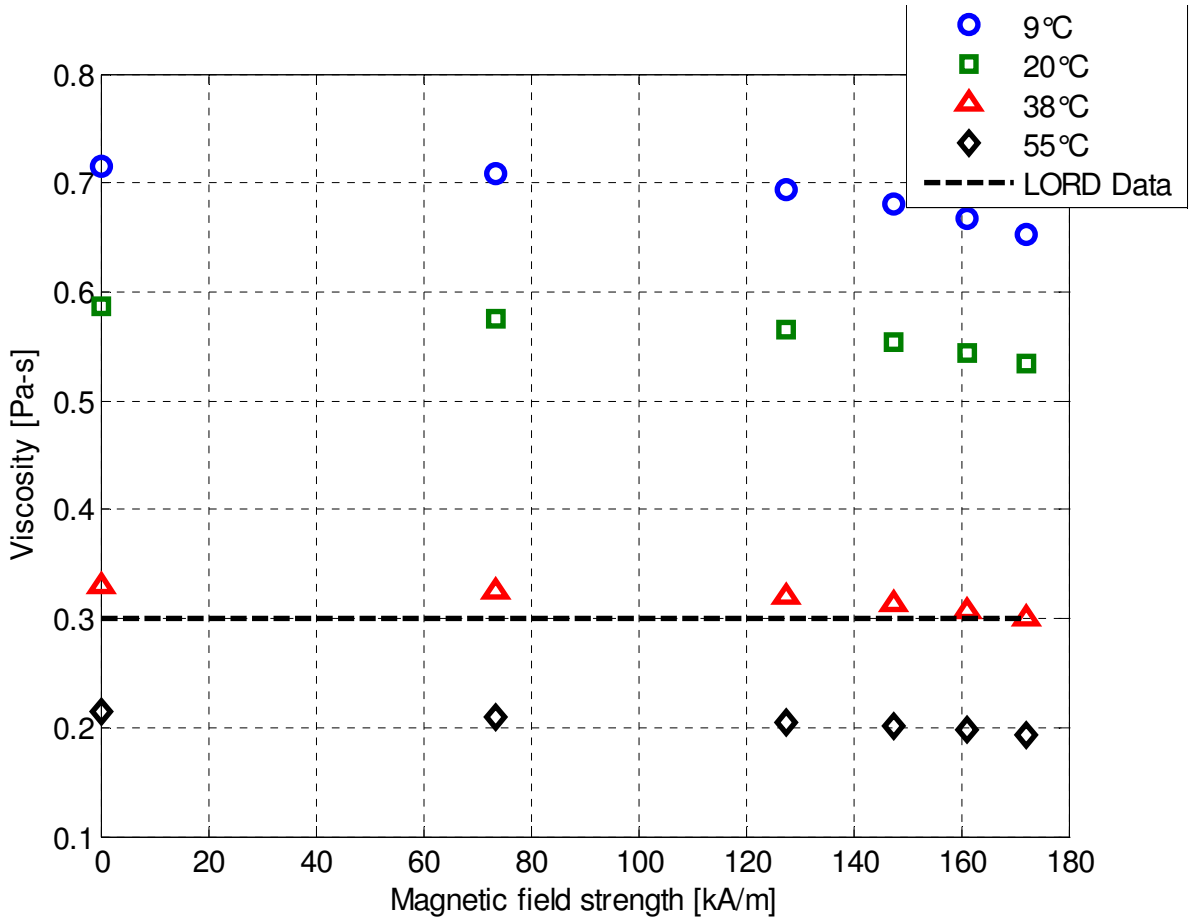

Figure 2.31 - Temperature effects on viscosity of MRF-140CG at $\dot{\gamma}_{max} = 10,000\ [s^{-1}]$

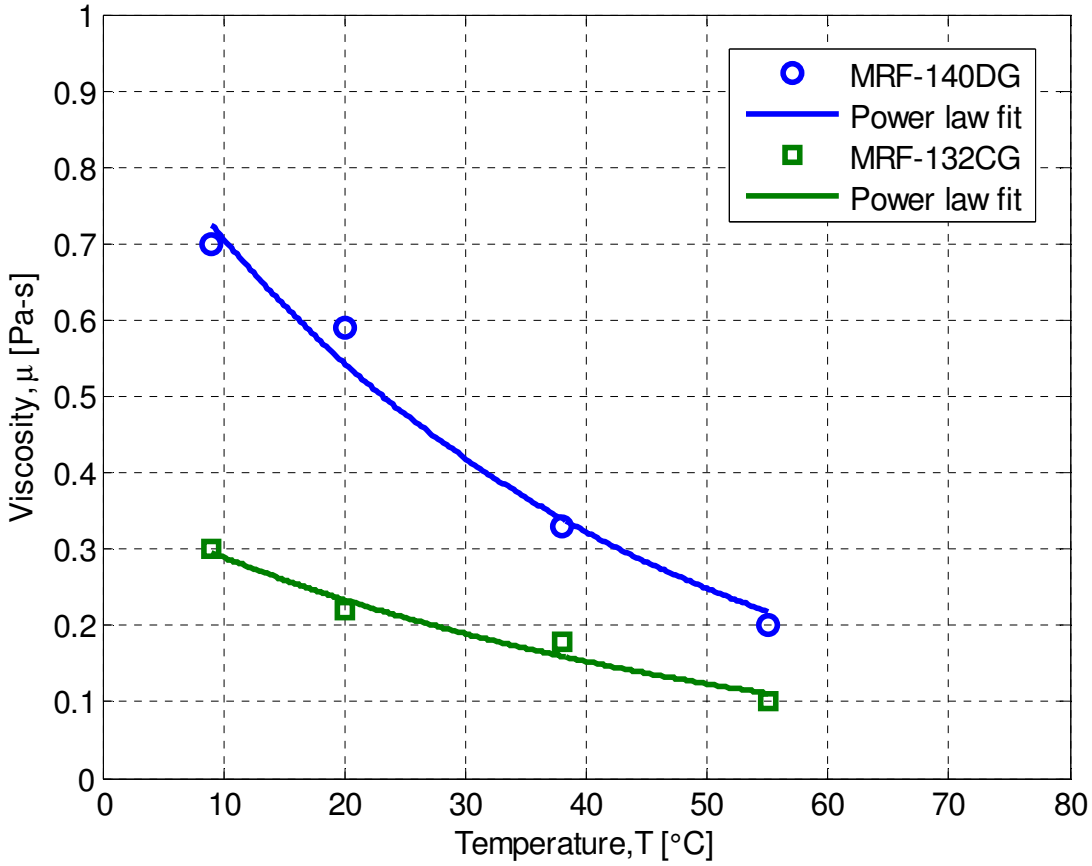

Figure 2.32 – Comparison of the temperature-dependent viscosities of MRF-132DG and MRF-140CG, along with Reynolds Law fits from Eq. (2.17)

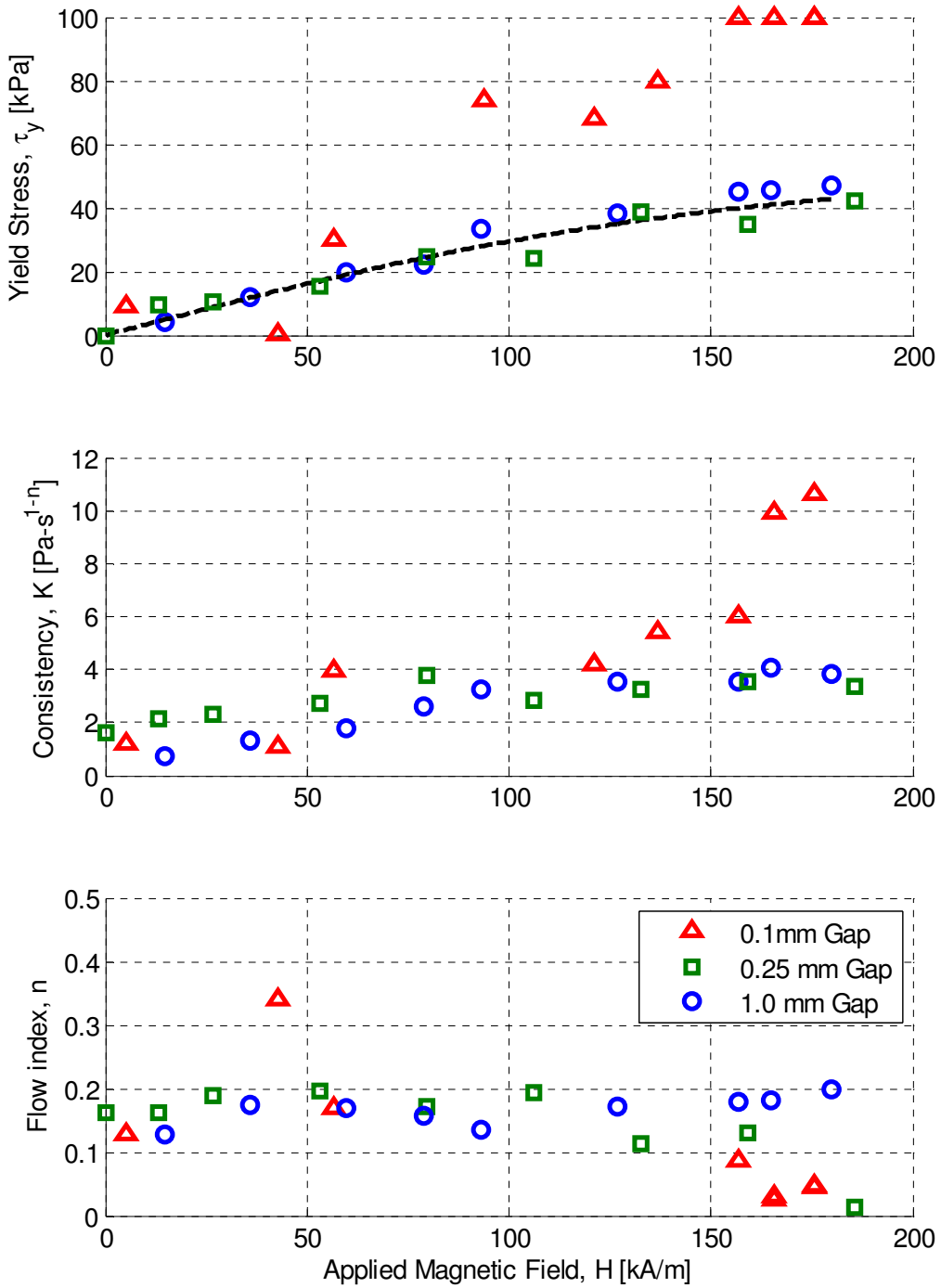

Figure 2.33 – Herschel-Bulkley parameters for different gap sizes, corresponding to $\dot{\gamma}_{max} = 2,500\ [s^{-1}]$, $\dot{\gamma}_{max} = 10,000\ [s^{-1}]$, and $\dot{\gamma}_{max} = 25,000\ [s^{-1}]$, 20°C

Chapter 3

3. MASON NUMBER ANALYSIS

3.1. Abstract

A nondimensional Mason number is developed and used to produce a single master curve applicable for three MR fluids with different solids loading, characterized at shear rates up to 10,000 s^{-1}, at different temperatures and applied magnetic fields. The Mason number is a ratio of the hydrodynamic and polarization forces on individual particles that combines the effects of shear rate and magnetization into a single nondimensional group. A temperature-dependent viscosity term is added to modify the Mason number and expand its applicability to the range of temperatures encountered in practical applications. Normalized viscosity data from MR fluid characterization tests can be plotted versus Mason number to produce a single master curve, which reduces the number and range of simulated conditions required for a comprehensive understanding of MR fluid performance. This analysis technique expands the design space of MR devices to high shear rates and allows for comprehensive predictions of overall performance across a wide range of operating conditions.

3.2. Introduction

Magnetorheological energy absorbers (MREAs) have been successfully implemented in occupant

protection systems to protect occupants against impact, shock and blastloads, especially to protect the lumbar region of the human spine (Mao et al., 2007; Hiemenz et al., 2008; Hiemenz et al., 2009). Shear rates in these MREAs typically range up to 25,000 s^{-1} or higher. However, data from low shear rate (up to 1,000 s^{-1}) characterization tests are typically extrapolated up to these high shear rates because of the dearth of high shear rate data.

Therefore, the objective of this study is to use a Searle-type magnetorheometer capable of testing at shear rates as high as 25,000 s^{-1}, and to assess the performance of three commercially available magnetorheological fluids (MRFs) over this range of shear rates: LORD Corporation MRF-132DG MRF-140CG, and MRF-145BG. While predictive models, such as the Herschel-Bulkley (HB) constitutive model, are typically employed to characterize measured rheological behavior, this approach must rely on a huge data set of characterization tests to be useful across the entire range of expected operating conditions.

Both MR yield stress and fluid viscosity have been shown to vary with temperature (Sahin et al., 2009; Knezevic and Savic, 2006). Furthermore, MRFs are highly shear thinning materials, and so they exhibit a significant reduction in viscosity as shear rate varies up to 25,000 s^{-1} in these characterizations. For these reasons, a wide variety of fluid characterization tests, which vary temperature, shear rate, and gap size, are currently required to adequately determine the performance of a given MR fluid utilized in certain device and environment. It is desireable therefore to reduce the overall amount of data required for determination of the MR fluid behavior, while maintaining the ability to accurately predict any off-nominal change in performance. Thus, a key objective of this study is to quantitatively assess the magnetorheological behavior of three commercially available MR fluids at high shear rates using only a limited set of test data, providing critical design information for MREAs operating over this shear rate range (0 – 25,000 s^{-1}). This

can be accomplished through the use of a nondimensional Mason number which incorporates temperature dependent parameters, discussed in the following sections.

3.2.1. Mason number for MR fluids

Classic work by Mason and colleagues showed that a nondimensionalized ratio of dominating physical forces described particle behavior in shear and electric fields, and influenced following researchers to use a similar ratio (Allan and Mason, 1962). This dimensionless group came to be known as the Mason number. A minimized expression for a Mason number is shown below as the ratio of hydrodynamic force to polarization force.

$$Mn \equiv \frac{F^H}{F_0} = \frac{hydrodynamic}{polarization} \tag{3.1}$$

Efforts to correlate experimental electrorheological (ER) fluids in shear flow by Marshall et al. used a Mason number approach to successfully develop a scaling relationship that accounts for volume fraction, field strength, shear rate, and temperature. In this case, the polarization force is a result of an externally applied electric field, and is proportional to the square of the electric field strength. This enabled the researchers to test detailed predictive models of the ER response without the need for a wide range of test variables previously required. In fact, a distinguishing characteristic of using this kind of analysis is that apparent viscosity data for numerous experiments with different test parameters will collapse to a single master curve when plotted versus Mason number (Marshall et al., 1989).

Building on this framework, Klingenberg et al. (2007) developed a Mason number for MR fluids based on the fluid shear rate and suspension magnetization. Recognizing the analogy that ER and MR fluids are electric field- and magnetic field-dependent, respectively, they first attempted a simple substitution of the magnetic field strength, H, in the polarizing force term. Their sample

data, which was collected from concentric cylinder magnetorheometer experiments, used hydrocarbon-based MR fluids similar in composition to the MR fluids used in the current research. Unlike the high shear rate ($\dot{\gamma} \leq 25{,}000$ s^{-1}) studies of the current research, however, the data used by Klingenberg et al. (2007) was sheared at a maximum rate of 900 s^{-1} (Ulicny et al., 2005).

The direct substitution of magnetostatic for electrostatic variables did yield the desired collapse of experimental data for cases of solids loading $\leq$ 0.30 vol%, as well as for large applied magnetic field strengths. However, in a 45 vol% fluid and at low magnetic field strengths, the collapse of data did not occur. They reasoned that because the magnetization, M, was actually a nonlinear function of magnetic field strength within each particle (Ginder and Davis, 1994), a more appropriate polarization force term was one that was a function of particle magnetization rather than the applied magnetic field. This expression for the magnetostatic force did indeed produce the desired data collapse across the entire range of applied magnetic fields and in MR fluids with high solids loading.

While the research by Klingenberg et al. (2007) applied the same expression as for the hydrodynamic force present within the fluid, shown given as

$$F^H = 6\pi\eta_c a^2 \dot{\gamma} \tag{3.2}$$

where η_c is the carrier fluid viscosity, a is the particle radius, and $\dot{\gamma}$ is the shear strain rate, they calculate the polarization force term as a modified point-dipole which accounts for nonlinearities in particle magnetization, M_p. Realizing that the magnetic moment is related to the average magnetization of a single spherical particle, m, by

$$m = \frac{\pi}{6}\sigma^3 M_p \tag{3.3}$$

and that the bulk suspension magnetization, $\langle M \rangle$ is related to the particle magnetization by the solids loading fraction, ϕ, given by the equation

$$M_p = \frac{1}{\phi}\langle M \rangle \tag{3.4}$$

Klingenberg et al. (2007) derive the magnetic polarization force to be the expression shown below.

$$F_0 = \frac{\pi}{48}\frac{\mu_0 \sigma^2 \langle M \rangle^2}{\phi^2} \tag{3.5}$$

where μ_0 is the permeability of free space, $4\pi \times 10^{-7}\left[\frac{V \cdot s}{A \cdot m}\right]$.

When experimental measurements of MR fluid apparent viscosity are plotted versus Klingenberg's version of the Mason number, the curves for various shear rates and magnetic field strengths collapse to a single function of Mason number, shown below.

$$Mn(\dot{\gamma}, M) \equiv \frac{F^H}{F_0} = \frac{9}{2}\frac{\eta_c \phi^2}{\mu_0 \mu_c}\frac{\dot{\gamma}}{\langle M \rangle^2} \tag{3.6}$$

Here, μ_c is the carrier fluid permeability. The two experimentally measured variables are the shear rate, $\dot{\gamma}$, and suspension magnetization, $\langle M \rangle$, and using this nondimensional group allows for disparate experimental data to be modeled as a single curve, greatly expanding the useable information about MR fluid behavior over a wide range of operating conditions.

It is worth mentioning that there are a number of other Mason numbers modified to account for surface friction and flow channel topography (Kavlicoglu et al., 2011), suspensions of magnetizable particles in nonconducting media versus nonconducting particles in ferromagnetic media (Volkova et al., 2000), and particle sizes in inverse ferrofluids (de Gans et al., 2000). A study currently under review points out that there is an inconsistency in the choice of the

characteristic particle dimension in Klingenberg's Mason number, specifically the use of particle radius, a, in the hydrodynamic force term of equation (3.2) and particle diameter, σ, in the magnetostatic force term of equation (3.6). The adjusted Mason number, Mn^*, would therefore be $Mn^* = 32 \cdot Mn$ (Sherman and Wereley, 2013). For this research Klingenberg's definition of Mason number is used for consistency with prior work.

3.2.2. Temperature dependence of model parameters

Among the parameters in the Mason number given in Eq. (3.6), both the carrier fluid viscosity, η_c, and suspension magnetization, $\langle M \rangle$, have been shown to be dependent on temperature (Knezevic and Savic, 2006; Sahin et al., 2009). Therefore, a complete expression for the Mason number should reduce the complex coupling of shear rate, gap size, solids loading and temperature by accounting for these dependencies. In order to evaluate the relative impact of temperature on both fluid viscosity and magnetization, studies were carried out to quantify the change in fluid behavior over a range of temperatures typically seen in crashworthy MREA operating environments. The operating range stated in the fluid manufacturer's technical data report, together with the capabilities of the laboratory testing equipment were also considered. Table 3.1 lists the manufacturer supplied operating range (LORD Corporation, 2012), the range of the temperature-controlled circulator used in the characterization tests, and the typical temperature range encountered in military standard crashworthy applications (MIL-STD-810F, 2003).

3.2.2.1. *Viscosity*

Using characterization tests performed on LORD MRF-132DG and MRF-140CG at shear rates up to 10,000 s^{-1}, measurements of the average fluid viscosity can be obtained from the Herschel-Bulkley model parameters for consistency, K, and flow index, n. Four data sets for each of the two fluids, at temperatures of 9°C, 20°C, 38°C, and 55°C, are analyzed and the average viscosity is

plotted versus temperature in Figure 3.1. Clearly, temperature has a significant effect on the MR fluid viscosity, and thus the hydrodynamic (i.e. viscous) force term used in the Mason number. For LORD MRF-132DG, the viscosity ranges from 0.3 Pascal-seconds at 9°C to 0.1 Pa-s at 55°C. In the higher volume percent fluid, MRF-140CG, the viscosity ranges from 0.7 Pa-s at 9°C to 0.2 Pa-s at 55°C.

Table 3.1 – Temperature range of MR fluids in relevant applications

Operating Requirement	Minimum Temperature [°F/°C]	Maximum Temperature [°F/°C]
LORD MRF Technical Data	-40 / -40	266 / 130
Julabo Circulating Pump	48 / 9	185 / 85
MIL-STD Energy Absorbers	-40 / -40	140 / 60

Comparing these values to the manufacturer's reported viscosities, measured at 40°C reveals that the viscosity for MRF-132DG can be 289% greater than the reported nominal value, while MRF-140CG can be 233% greater. As the viscous force term in the Mason number in Eq. (3.6) is directly proportional to the carrier fluid viscosity, it is clear that temperature effects must be taken into account when using this analysis framework.

Table 3.2 – Change in viscosity from nominal at temperature extremes of the current research

LORD MR Fluid	Reported Viscosity [Pa-s]	Viscosity at 9°C [Pa-s]	Viscosity at 55°C [Pa-s]	Difference [(+/-)%]
MRF-132DG	0.092 ± 0.015	0.3	0.1	289% / 6.5%
MRF-140CG	0.28 ± 0.07	0.7	0.2	233% / 4.7%

The mathematical study by Knezevic and Savic (2006) provides applicable viscosity-temperature relationships which can be evaluated for fit over the temperature range presented in Figure 3.1. A simple two parameter equation, known as the Reynolds equation, is shown below.

$$\mu_0 = be^{-aT_A} \tag{3.7}$$

The researchers point out that this relationship is accurate only for a limited temperature range, but fail to specify how limited. This is a similar model to that presented by Hu et al. (2012) as equation (2.17). Also presented by Knezevic and Savic (2006) is the three term Vogel viscosity-temperature equation, which is described as the most accurate over large temperature ranges and therefore useful for engineering calculations, as shown below (Stachowiak and Batchelor, 2005).

$$\mu_0 = ae^{b/(T_A - c)} \tag{3.8}$$

Using the viscosity measurements at each of four temperatures in experiments with both MRF-132DG and MRF-140CG, Figure 3.1 shows the trend line fits associated with equations (3.7) and (3.8). Apparently, both models are almost equivalent over the temperature range tested, 9°C - 55°C, and both have $R^2 \cong .98$ indicating a good fit. Clearly, their predictions of low temperature viscosity differ significantly, but as the experimental data do not cover this range, the simpler of the two models, the Reynolds equation, is used henceforth. It is also necessary to point out that this analysis examines the bulk fluid viscosity, while the Mason number uses viscosity of the hydrocarbon carrier liquid; this measurement is performed in a later section, but it is assumed that this viscosity-temperature relationship is analogous.

3.2.2.2. *Suspension magnetization*

As noted in the previous chapter, a similar analysis of the yield force dependence on temperature was performed and found that for both MRF-132DG and MRF-140CG, the yield stress varied less than 10% over the entire temperature range. This indicates that the magnetostatic force given by equation (3.3), which is dependent on the square of suspension magnetization, would therefore be relatively unchanged and have a minimal effect on the Mason number.

As a further investigation into the temperature dependence of the suspension magnetization, it is informative to consider the ferromagnetic properties of the magnetizable particles, in this case carbonyl iron. The Bloch $T^{3/2}$ law states that at temperatures below approximately 20% of the Curie temperature (T_C = 770°C for Fe, so in this case for temperatures below ~150°C), the change of saturation magnetization of a material is related to the absolute temperature change by the expression given below.

$$M = M_0\left(1 - \left({}^{T}/_{T_B}\right)^{3/2}\right) \tag{3.9}$$

At low temperatures (near room temperature), the Bloch temperature, T_B, can be found from the Curie temperature by the following relation.

$$T_B \cong 4T_C \tag{3.10}$$

For the iron particles in MR fluid, we will then assume $T_B \cong 3080$°C, which provides an estimate of the impact that the temperature variations will have on the suspension magnetization over the full operating temperature range (Smit and Wijn, 1959). Table 3.3 lists the relevant parameters used in this calculation. Over the widest range of temperatures from Table 3.1, the MR fluid operating temperature range, the suspension magnetization only changes by 0.01%, which is

negligible when compared to the change in viscosity over the same range. Because the suspension magnetization term only varies on the order of 10^{-2} percent over the relevant temperature range, and furthermore due to the fact that Mason number is inversely proportional to $\langle M \rangle^2$, this variation become vanishingly insignificant.

From these results, it's clear that a temperature-dependent viscosity must be included in the Mason number in order to produce the data collapse as desired, while a temperature-independent magnetization estimate can reasonably be assumed.

Table 3.3 – Effect of temperature on suspension magnetization

Carbonyl Iron M_0 [A/m]	**Operating ΔT [°C] (Max. – Min.)**	**Bloch Temp. T_B [°C]**	**M [A/m]**	**$\Delta M = 1 - M/M_0$ [%]**
1.5×10^6	(130 – (- 40)) = 170	3080	1.499×10^6	10^{-2}

3.3. Parameter overview and identification

3.3.1. Carrier fluid viscosity measurements

As stated in prior sections, the Mason number requires the carrier fluid viscosity as an input parameter. Because the specific formulation of the hydrocarbon carrier fluid used by LORD Corporation is proprietary, efforts were undertaken to experimentally measure the carrier fluid viscosity using a standard commercial rheometer. To obtain a carrier fluid sample, a well-mixed MR fluid sample was allowed to separate over a period of 3 days into the constituent fluid and solid particles, as shown in Figure 3.4. This sample, taken from MRF-132DG, was then tested on

an Anton-Paar MCR-300 rotating parallel plate rheometer at 25°C to measure the carrier fluid viscosity.

The shear stress vs. strain rate results of three tests are shown in Figure 3.5, and the instantaneous viscosity measurements vs. strain rate are shown in Figure 3.6. Each data set was edited to remove the initial points during which the fluid sample is spreading over the shear surface, as is standard practice with parallel plate rheometers. The results of these three characterization tests are consistent, with an average viscosity calculated as 0.00987 [Pa-s], or about 10% of the MR fluid viscosity. This carrier fluid viscosity value is used throughout the subsequent Mason number analyses, as it is assumed that the family of MR fluids studied vary only by their solids loading fraction.

3.3.2. Magnetization measurements

As discussed in section 2.4.3, a custom sensing coil was used to directly measure the total magnetic flux within the bob versus applied current. By Gauss's law for magnetism, shown as equation (2.8), it is clear that the total magnetic flux is therefore constant throughout the circuit, and is given by the equation below.

$$\Phi_B = B \cdot S \tag{3.11}$$

Using this continuity, we can then relate the magnetic flux density in the active fluid gap region to applied current, as detailed previously in equation (2.10). Since the Mason number relies not on flux density or magnetic field strength but on the suspension magnetization, the magnetization vs. applied current relationship can be obtained using the definition of magnetic flux density in the equation below.

$$B = \mu_0(H + M) \tag{3.12}$$

Figure 3.7 shows the relationship between magnetization, magnetic field strength and magnetic flux density versus applied current given by equation (3.12). Two important characteristics can be seen in the magnetization curve. First, the rate at which magnetization increases at low field strengths is larger than it is for high magnetic field strengths; there is an elbow in the magnetization curve. This accounts for the failure of characterization data to collapse reported by Klingenberg et al. (2007) when attempting to use a magnetostatic equivalent of the Mason number developed by Marshall et al. (1989), and demonstrates why using suspension magnetization in the Mason number is more appropriate and ultimately successful in MR fluids. Second, from section 2.4.3, the presence of a non-zero remnant magnetization must also be accounted for during Mason number analyses. In order to ensure that disparate data will collapse to a master curve by using the Mason number, accurate accounts of both fluid viscosity and suspension magnetization are required.

3.4. Mason number analysis of MR fluids at high shear rates

Clearly, the performance of MR fluids is dependent on a number of independent variables, namely shear rate, magnetization, and a temperature-dependent viscosity. A classical presentation of the apparent viscosity versus applied current and shear rate is shown in Figure 3.13 for a single temperature, in this case 20°C. To achieve the ultimate goal of reducing the number of experiments required to accurately characterize MR fluids across a wide range of operating temperatures, it is clear that analysis via Mason number offers a reduction in complexity from four variables (shear rate, magnetization, viscosity, and temperature) to two (shear rate and magnetization).

3.4.1. Normalized apparent viscosity versus Mason number

The Mason number given by equation (3.6) reduces the abscissa of the experimental characterization plots to a nondimensional expression, but in order to achieve the data collapse to a master curve it is helpful to also nondimensionalize the ordinate. An accepted way to do this is to use apparent viscosity, the ratio of total shear stress by shear rate given in equation (2.15), and normalize this value by the high shear rate viscosity in the absence of applied field, as shown in the following equation (Klingenberg et al., 2007).

$$\eta_N = {}^{\eta_{app}}/_{\eta_\infty} \tag{3.13}$$

The same data set shown as the three dimensional surface for the 32 vol% MR fluid in Figure 3.8 is presented again as the normalized apparent viscosity versus Mason number in Figure 3.9, with applied magnetic field substituted for applied current. Clearly, using the ratio of shear rate to suspension magnetization provided by the Mason number allows for the data to collapse to a single line. Similarly, characterization data for two other MR fluids having different solids loading, 40 vol% and 45 vol%, are shown in Figure 3.10 and Figure 3.11, respectively. Again, the classic flow curves, when transformed via Mason number and apparent viscosity, collapse to lines. In these characterizations, the same current was applied to the electromagnet; due to the different magnetic permeability of the three fluids, the magnetic field strengths listed in the legend varies.

It becomes clear why using normalized apparent viscosity is appropriate in this Mason number analysis when the three figures are combined, as shown in Figure 3.12. Data from testing of the three fluids all lie along the same line, or master curve, despite possessing different passive and active stress characteristics. This requirement of normalized apparent viscosity is explainable because an MR fluid with a higher solids loading will be stronger due to a higher available yield stress, but the off state viscosity will also be larger. Therefore, a direct comparison across solids

loading can be achieved by such a normalization. By relating the bulk suspension magnetization to the polarizing force through volume fraction in equations (3.3) and (3.4), Klingenberg's Mason number implicitly accounts for the fact that the same applied magnetic field will result in different, solids loading-dependent polarizing force.

Small deviations from the single master curve are attributed to imprecise knowledge of the current-magnetization relationships during the series of tests which generated this data. Later experiments corrected for these errors, and resulted in a more distinct master curve.

3.4.2. Trends with gap size and shear rate

Mason number analyses for MR fluids should, in theory, allow for low shear rate characterization data collected on laboratory equipment to be safely extrapolated to the high shear rates encountered in crash and shock scenarios. Leveraging the capability of the high shear rate magnetorheometer, this section examines this predictive aspect by comparing low ($< 1{,}000\ s^{-1}$) and high ($> 10{,}000\ s^{-1}$) shear rate characterization tests using normalized apparent viscosity versus Mason number.

Three different active gap sizes were used to test LORD MRF-132DG samples at 20°C. Three different rotating bobs were used to provide a 1 mm, 0.25 mm, and 0.1 mm gap, which allowed for maximum shear rates of $1{,}000\ s^{-1}$, $10{,}000\ s^{-1}$, and $25{,}000\ s^{-1}$ to be generated. Sample temperature was maintained within ±0.5°C, as detailed in section 2.6. Figure 3.13 shows the result of this analysis set and indicates that using Mason number, developed from interparticle force models and previously validated at low shear rates, maintains applicability across the high shear rate range.

For the narrowest gap size, corresponding to a maximum shear rate of $25{,}000\ s^{-1}$, deviation from the expected master curve is observed. In this case, the gap size approaches the length scale of the

particles. The particle chains which contribute to the yield stress can only be 10-15 particles across. The Mason number only accounts for the interparticle viscous and magnetic forces, with no regard to friction; however, in this limiting case it is believed that frictional forces come into play and result in the discrepancies evident in Figure 3.13. The success and consistency demonstrated at shear rates up to 10,000 s^{-1} encouraged the research efforts, such that this magnetorheometer configuration was used throughout the rest of the characterization experiments.

3.4.3. Trends with temperature

In MR energy absorbing devices operating at high shear rates, temperature fluctuations are both inevitable and difficult to design for. Using the knowledge gained in sections 2.7.4 and 3.2.2.1, and presented in Figure 3.1, a temperature-dependent Mason number can be defined from equations (2.17) and (3.6) as

$$Mn(\dot{\gamma}, M, T) \equiv \frac{9}{2}\frac{\eta_c e^{-\beta\phi(T-T_0)}\phi^2}{\mu_0\mu_c}\frac{\dot{\gamma}}{\langle M\rangle^2} \tag{3.14}$$

where the carrier fluid viscosity, η_c, is measured at reference temperature, T_0. The β-coefficients for the 32 vol% and 40 vol% fluids are both approximately 0.066, given in Table 2.3. As shown in Figure 3.14, without this temperature-corrected Mason number, the characterization data fail to collapse to the expected master curve because of the substantial effect temperature has on the carrier fluid viscosity. One would expect low-temperature tests to exhibit a higher viscous force component than high-temperature tests, and therefore have a slightly higher apparent viscosity for a given shear rate and magnetization, or Mason number. The temperature correction term from equation (3.6) accounts for this higher viscosity and shifts the lower-temperature curves rightward, since the Mason number is directly proportional to the viscosity.

Figure 3.14 shows the results of using the temperature-corrected Mason number given by equation (3.14). The data collapse to a single master curve, representing that the final unaccounted for variable – temperature – can now be presented along with shear rate, solids loading, and suspension magnetization to completely characterize the MR fluid performance across a wide range of shear rates. The carefully detailed experiments that provided the various data sets used in this series of analysis have become unnecessary, as a single master curve of normalized apparent viscosity versus Mason number can now be used to extrapolate to a wide array of operating conditions.

3.5. Summary

In this chapter a nondimensional ratio of the viscous and magnetostatic forces on MR fluid particles, known as the Mason number, is presented as an effective analysis tool that enables disparate data sets to collapse to a single master curve. Three different MR fluids from LORD Corporation, MRF-132DG (32 vol%), MRF-140CG (40 vol%), and MRF-145BG (45 vol%) were characterized at shear rates up to 10,000 s^{-1} using a concentric cylinder magnetorheometer capable of varying the testing temperature and applied magnetic field.

Using a Mason number developed by Klingenberg et al. (2007), it was shown that the characterization data across the range of applied magnetic fields, presented as normalized apparent viscosity versus Mason number, collapsed to a single curve for each fluid. Furthermore, when these plots were superimposed, the master curve for each of the three fluids was shown to be the same.

A sensitivity analysis was conducted to determine the effect that a change in temperature would have on the data collapse, and it was determined that the viscous force was far more sensitive to temperature than the magnetostatic force. Both the Reynolds and Vogel temperature-viscosity

relations were examined over the operating temperature range, and it was found that the Reynolds description was sufficient to modify the Mason number appropriately. Plots of normalized apparent viscosity versus Klingenberg's version of Mason number and the modified temperature-dependent Mason number were presented and showed that data collected across the testing temperature range collapsed to the master curve when using the temperature-dependent Mason number.

3.6. Conclusions

The temperature-dependent Mason number developed in this research is a powerful analysis tool which allows for a wide array of testing parameters to be condensed and represented as a single nondimensional group, reducing the total number and range of characterization data required and simplifying the design process for MR fluid devices. Developed from analysis of the elementary forces on MR suspension particles, and originally validated in other research with low shear rate experimental data, the modified Mason number has been shown to be effective at shear rates up to 10,000 s^{-1}. This is an important development in the field of magnetorheometry because most commercially-available instruments are limited to shear rates below 1,000 s^{-1}, while MR energy absorbers used in crashworthy applications exceed that. Therefore, by using the apparent viscosity versus Mason number framework presented, researchers can safely extrapolate low shear rate characterization data if appropriate precautions are taken.

Most importantly, the inclusion of the Reynolds viscosity-temperature relationship expands the Mason number's applicability to predict MR fluid performance across a range operating temperatures. Obviously, at high shear rates and applied magnetic fields viscous and resistive heating effects will affect the carrier fluid viscosity, and thus the total apparent viscosity presented by an MR fluid. The contribution of temperature variation to changes in particle magnetization

was shown to be negligible over the experimental temperature range. Though the range of temperatures presented in this research does not span the published MR fluid operating temperature range, the Vogel viscosity-temperature relationship was presented as an alternate expression that may be of use in extreme temperature environments.

Several studies were undertaken to identify the relevant parameters used in the Mason number analysis. A consistent measurement of carrier fluid viscosity was obtained for LORD MRF-132DG by decanting and testing on a commercial rotating parallel plate rheometer, and this value was used during the calculation of the Mason number as well as the modification using the Reynolds relationship. The remnant magnetization characteristics of the high shear rate Searle cell magnetorheometer were included with the nonlinear magnetization properties of MR fluids to ensure a proper estimate of the suspension magnetization.

Not only did the individual fluid data sets collapse to a master curve, but by including the solids loading percent each of the three fluids' (32 vol%, 40 vol%, and 45 vol%), curves were shown to collapse to a single master curve when the apparent viscosity was normalized by the off-state high shear rate viscosity. Characterization test matrices which once required four variables to completely describe now only require a single nondimensional group, the Mason number. This powerful idea connects the microscale particle dynamics to bulk fluid properties which are readily measureable, and greatly simplifies the design process for MR fluid devices.

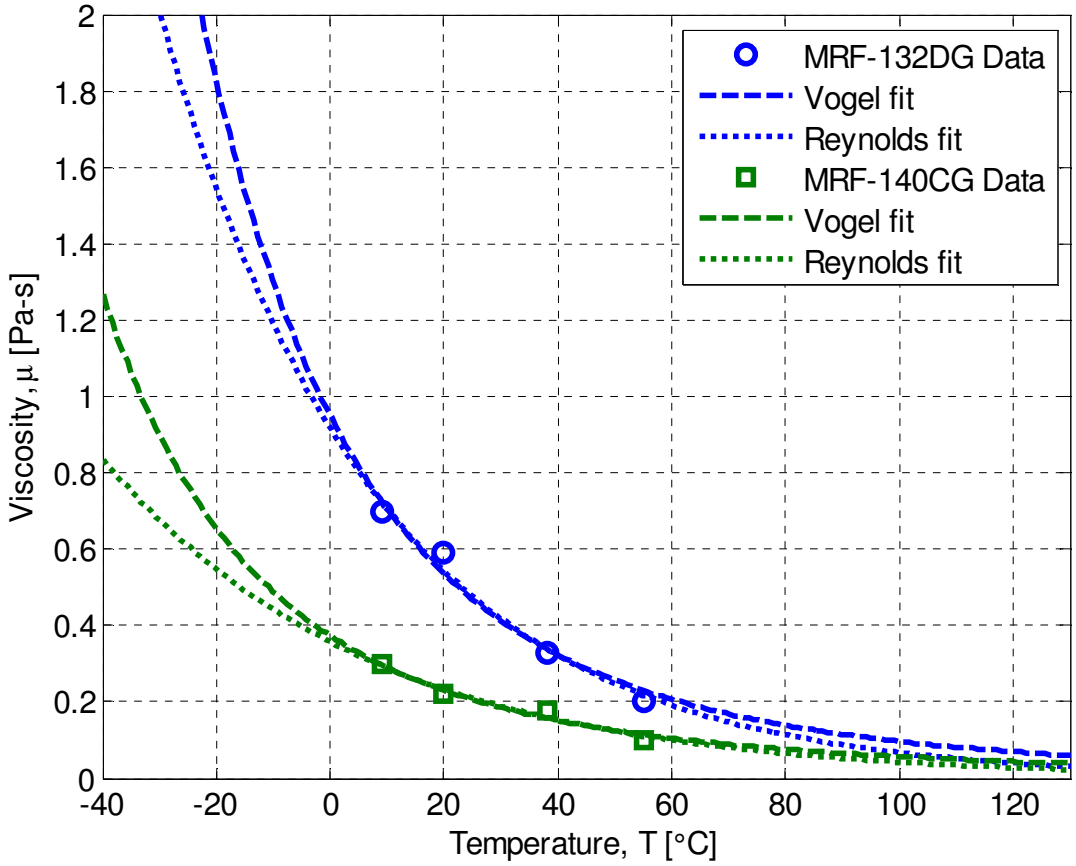

Figure 3.1 - Comparison of the temperature-dependent viscosities of MRF-132DG and MRF-140CG, along with Reynolds and Vogel law fits over the operating temperature range listed in the manufacturer data sheet

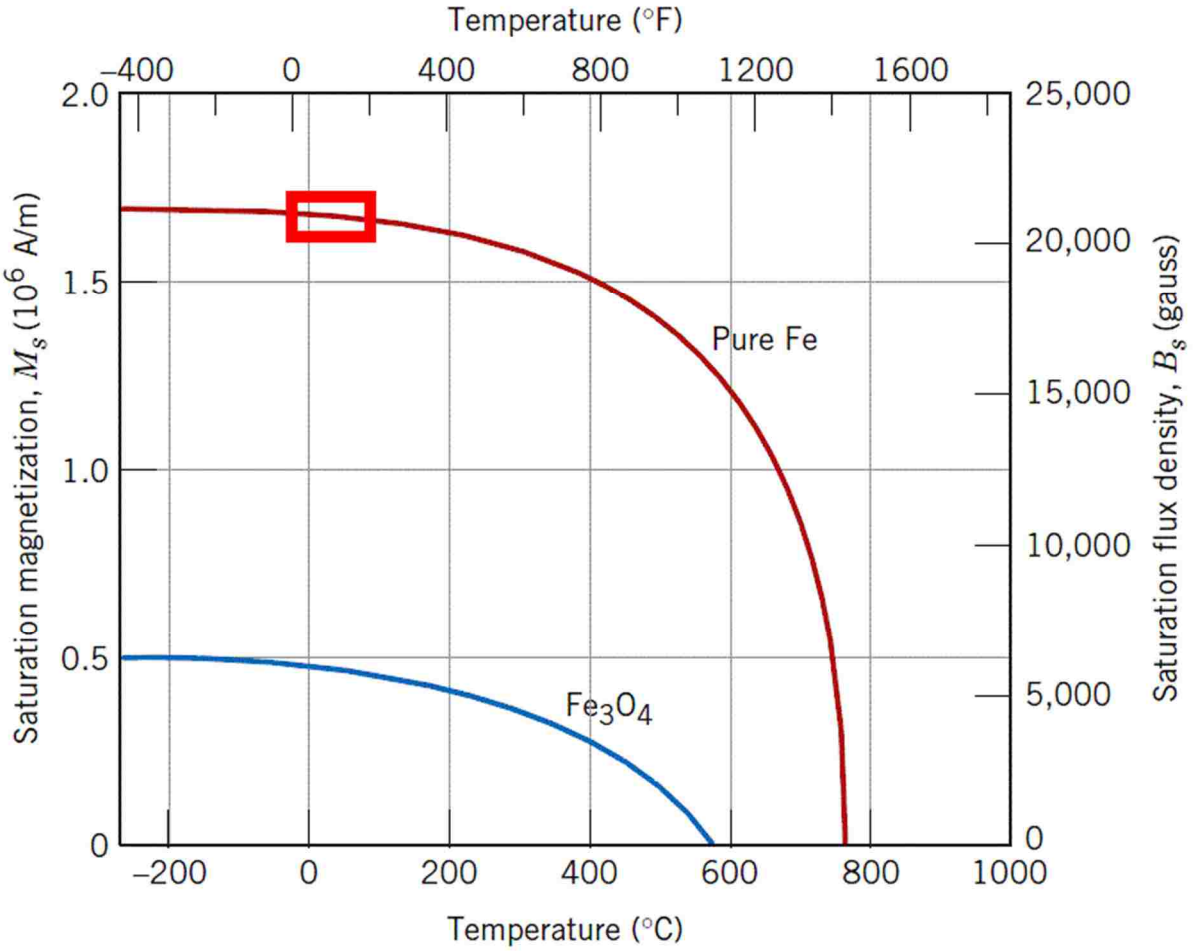

Figure 3.2 – Saturization magnetization versus temperature for iron particles used in the MR fluids presented. The red box indicates the range of temperatures at which tests were conducted, from 9°C to 85°C. Adapted from (Smit and Wijn, 1959).

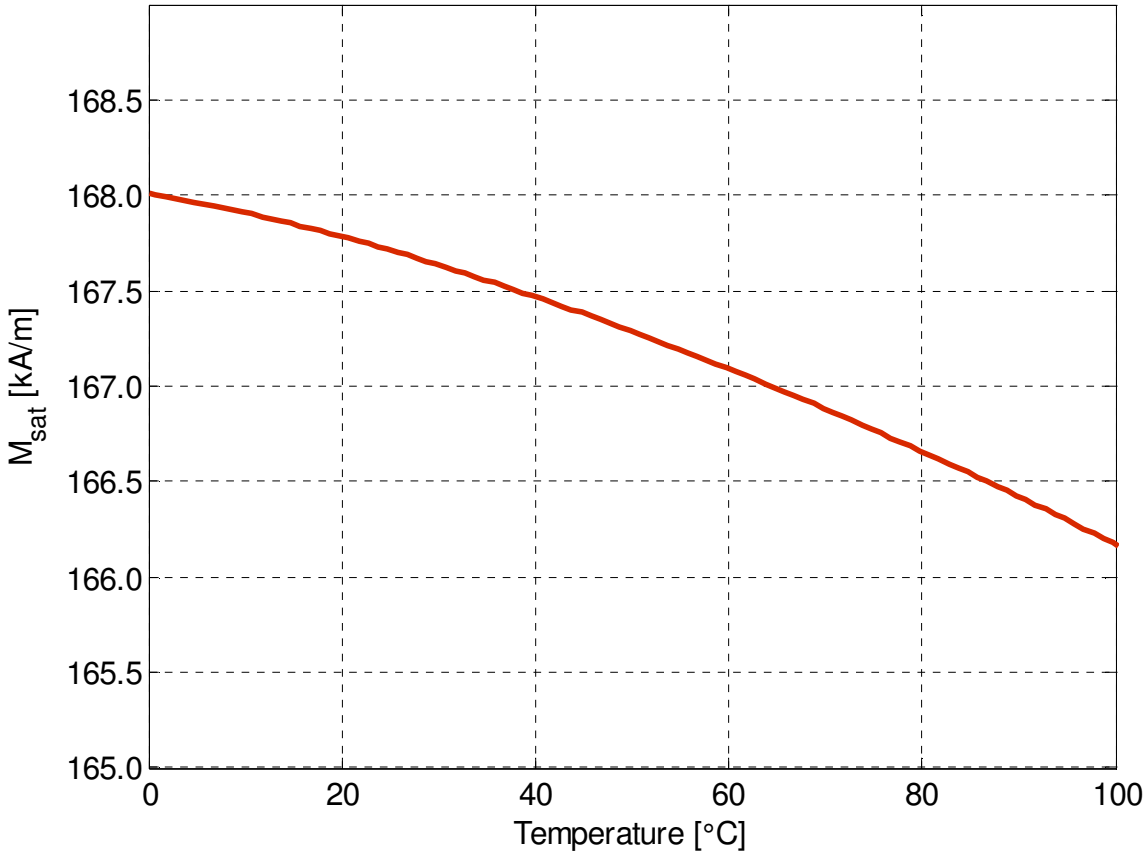

Figure 3.3 – Detail view of the temperature range used in experimental tests. Magnetic saturization (and with it particle magnetization) is shown to vary by only 1% per 100°C, indicating that particle magnetization is nearly independent of temperature in this range.

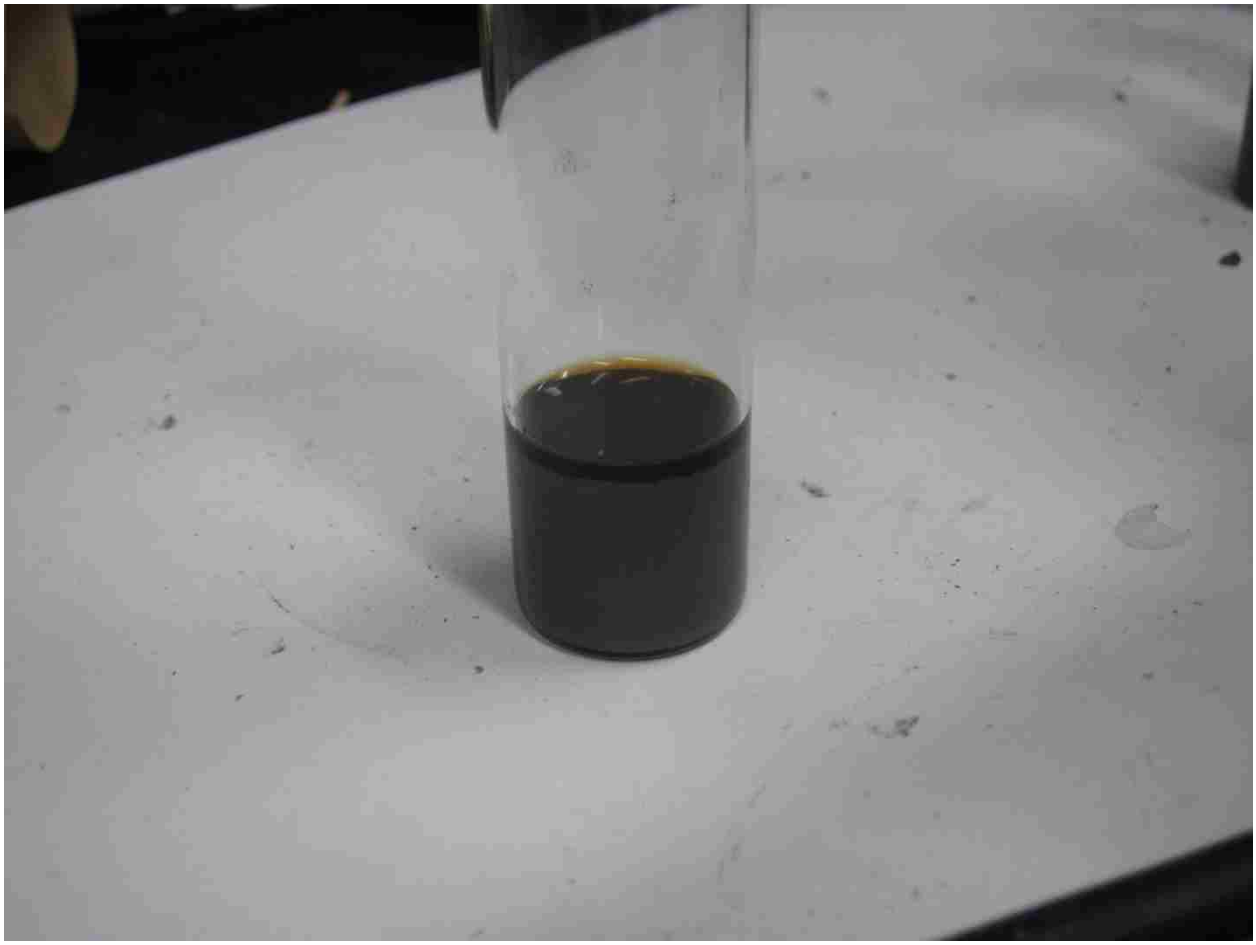

Figure 3.4 – MR fluid after settling into constituent parts. A thin layer of carrier fluid can be decanted from the surface.

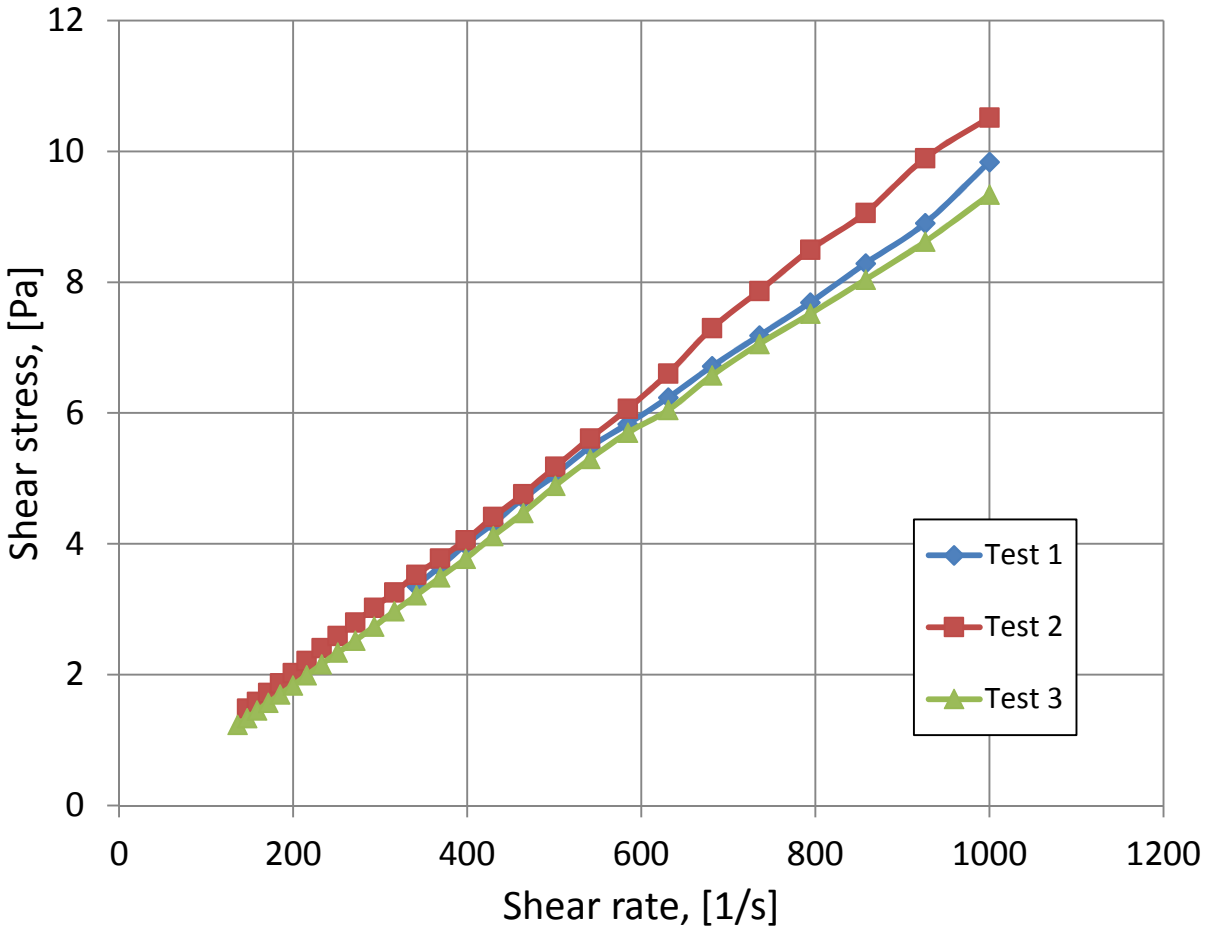

Figure 3.5 – Shear stress vs. shear rate rheometric data for three samples of the carrier fluid decanted from LORD MRF-132DG. The viscosity is calculated as the slope of these lines.

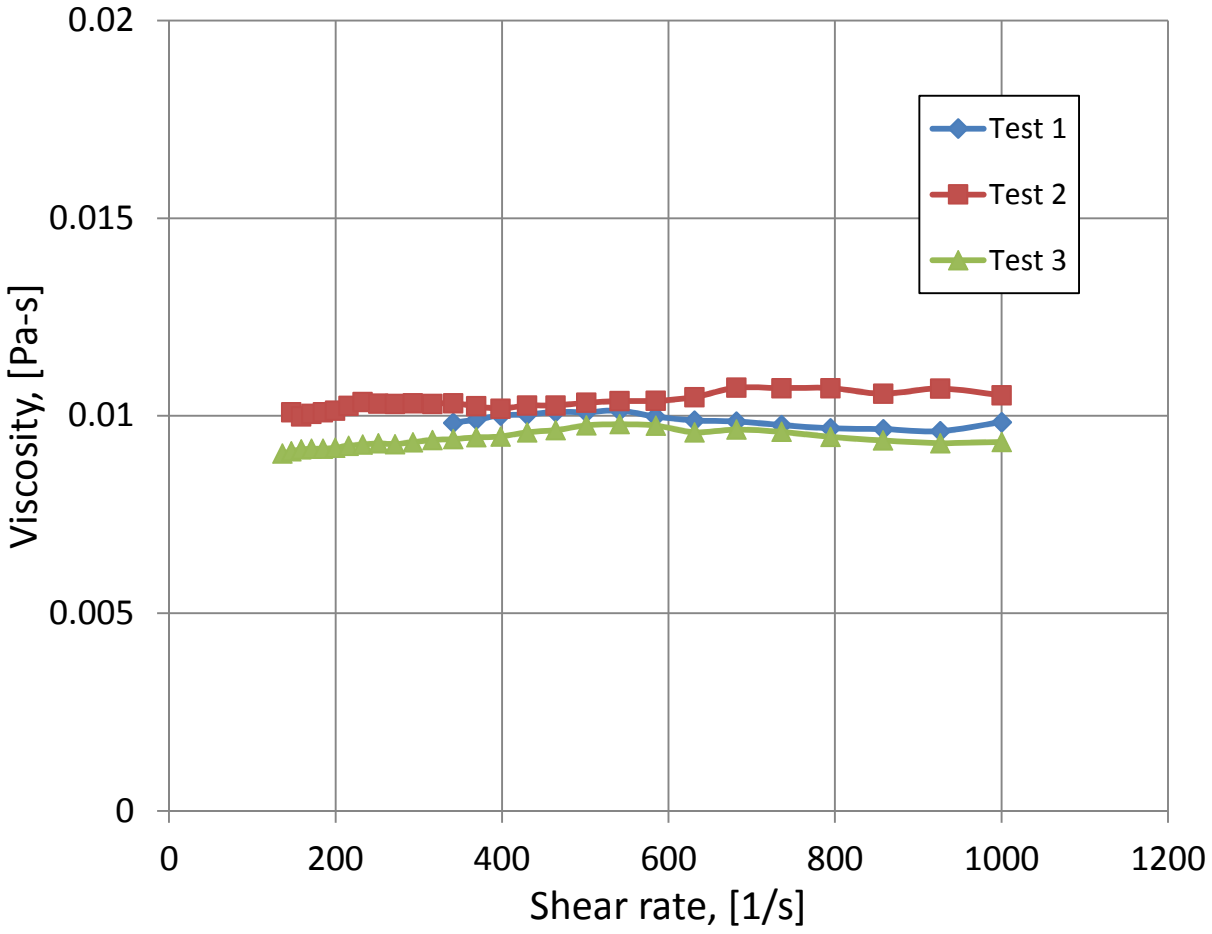

Figure 3.6 – Viscosity vs. shear rate for three samples of the carrier fluid decanted from LORD MRF-132DG. The average viscosity across all three samples was calculated as 0.00987 [Pa-s].

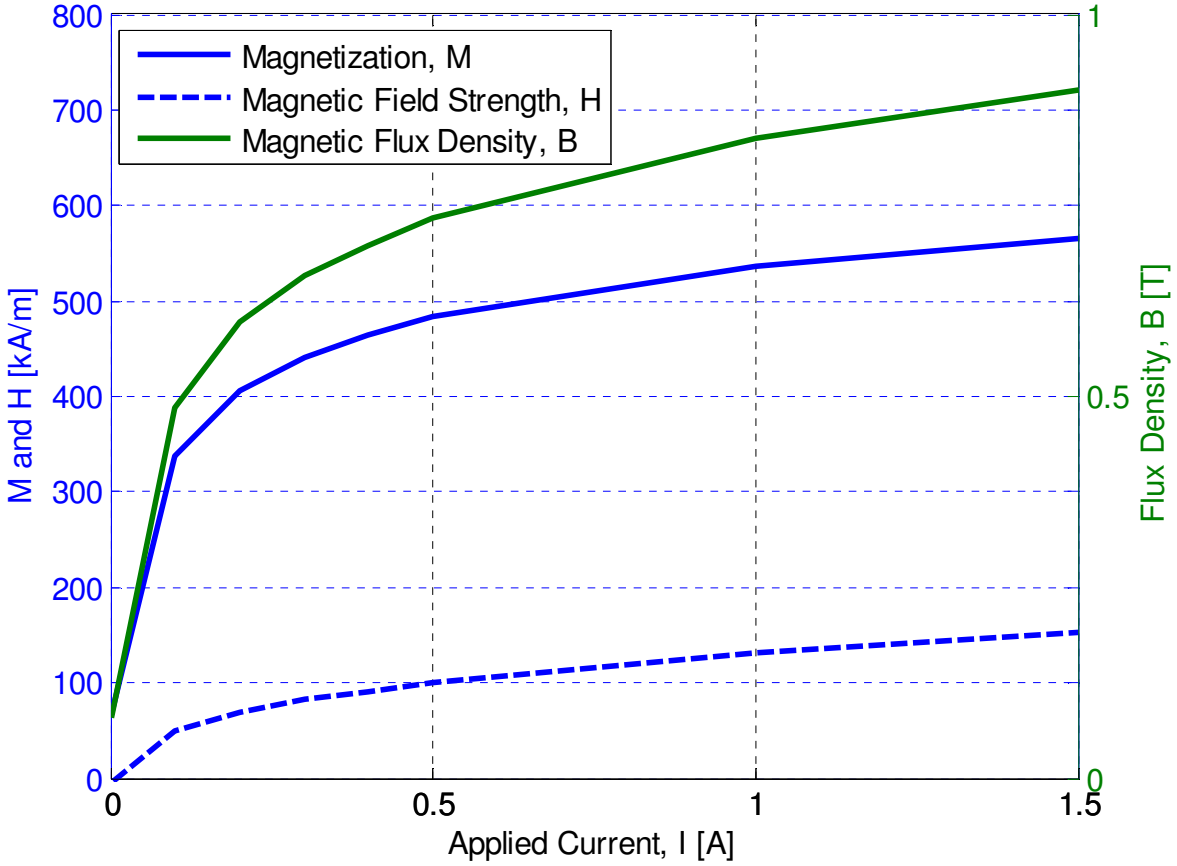

Figure 3.7 – Magnetization, magnetic field strength, and flux density vs. applied current for MRF-132DG at 20°C. Note the sharper rise in magnetization compared to field strength at low applied currents, as well as the non-zero remnant magnetization.

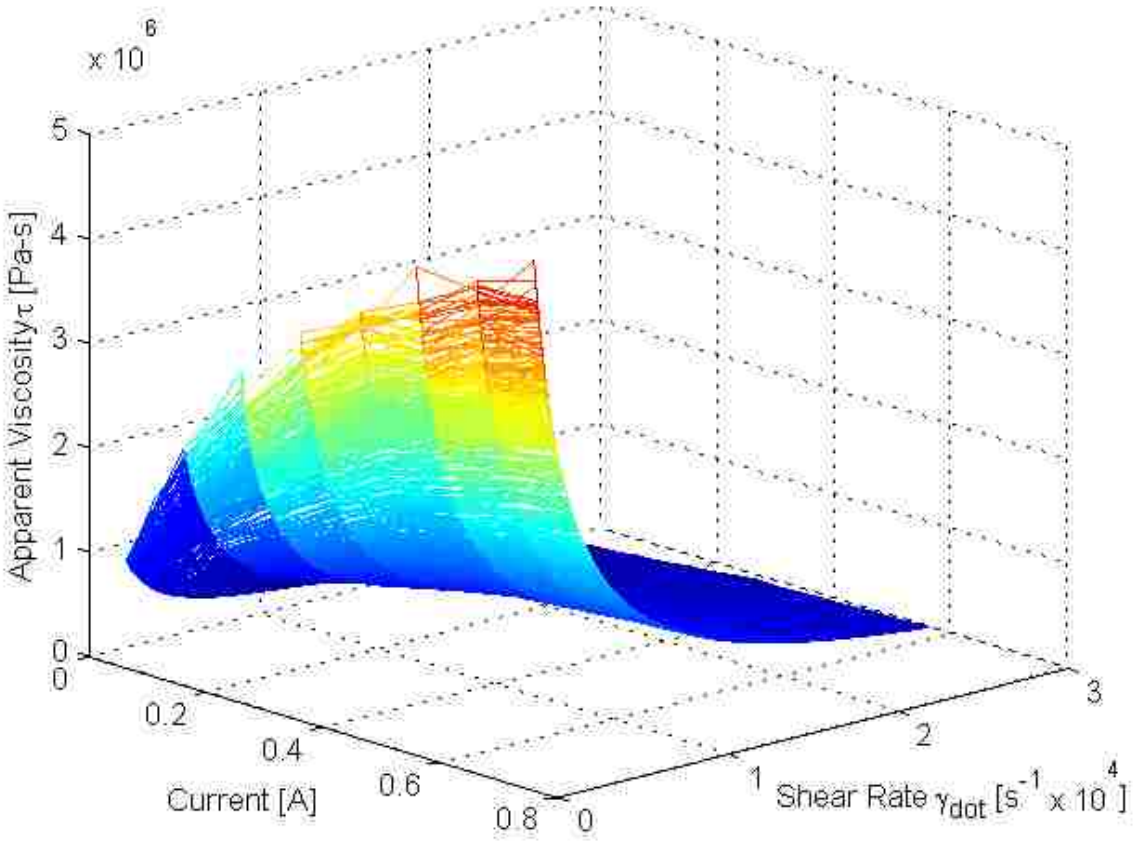

Figure 3.8 – Surface relating apparent viscosity to applied current and shear rate for MRF-132DG at 20°C. To present temperature dependence as well, a four-dimensional hypersurface is needed.

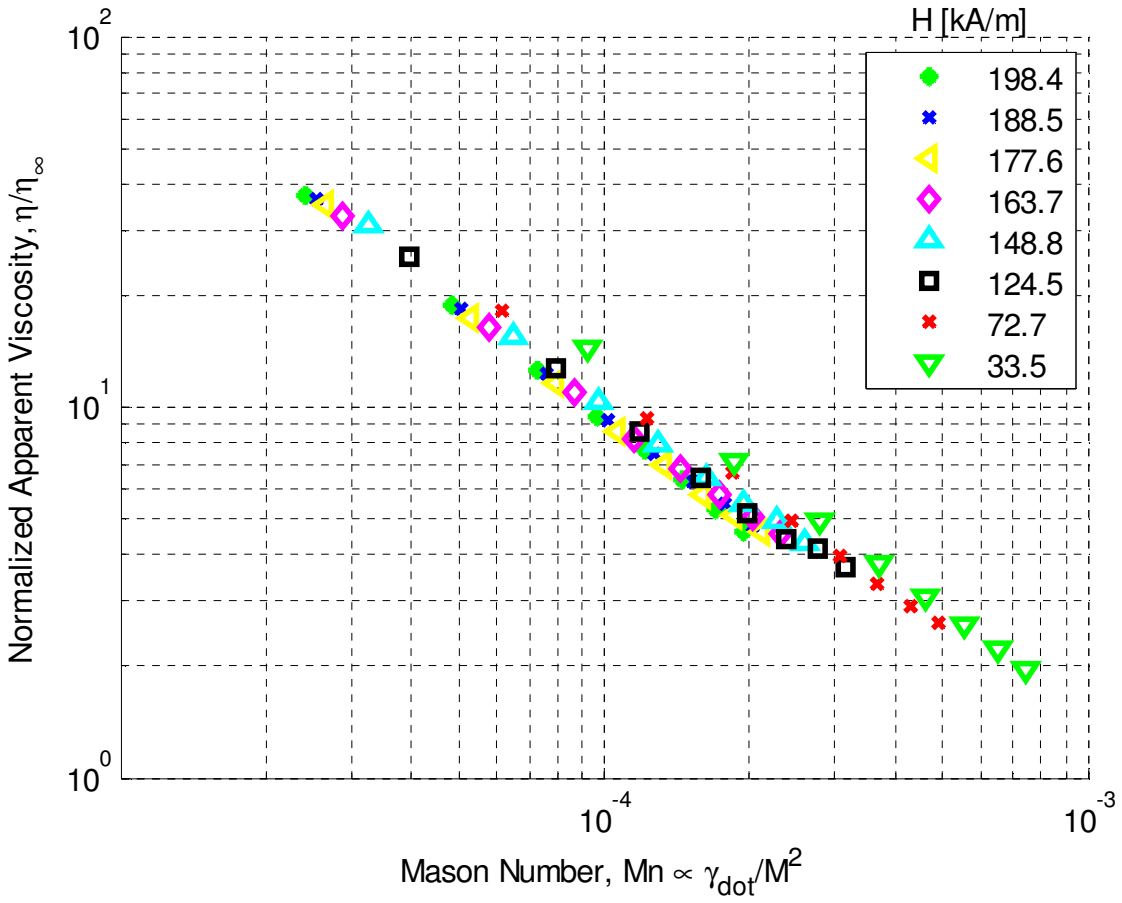

Figure 3.9 – Normalized apparent viscosity versus Mason number for MRF-132DG at shear rates up to 10,000 s^{-1}, using a gap size of 0.25 mm at 20°C.

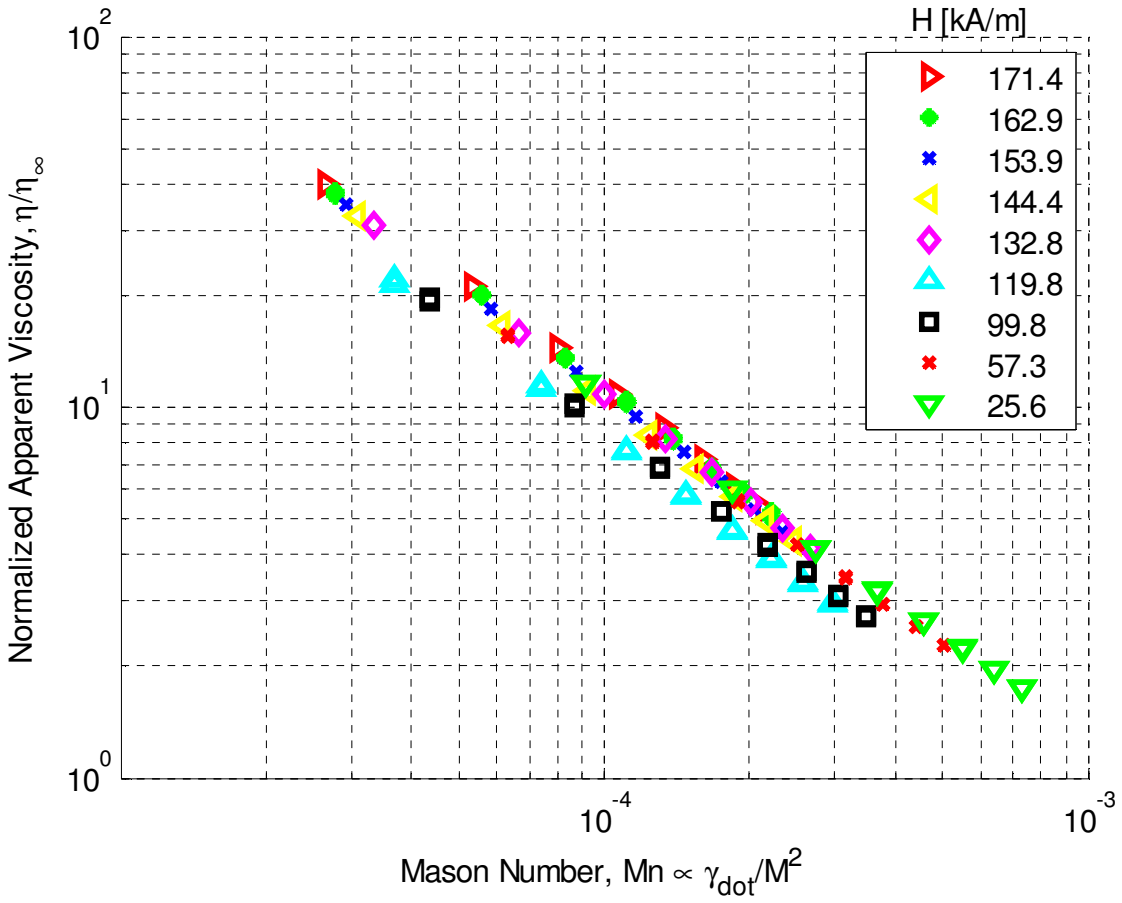

Figure 3.10 - Normalized apparent viscosity versus Mason number for MRF-140CG at shear rates up to 10,000 s^{-1}, using a gap size of 0.25 mm at 20°C.

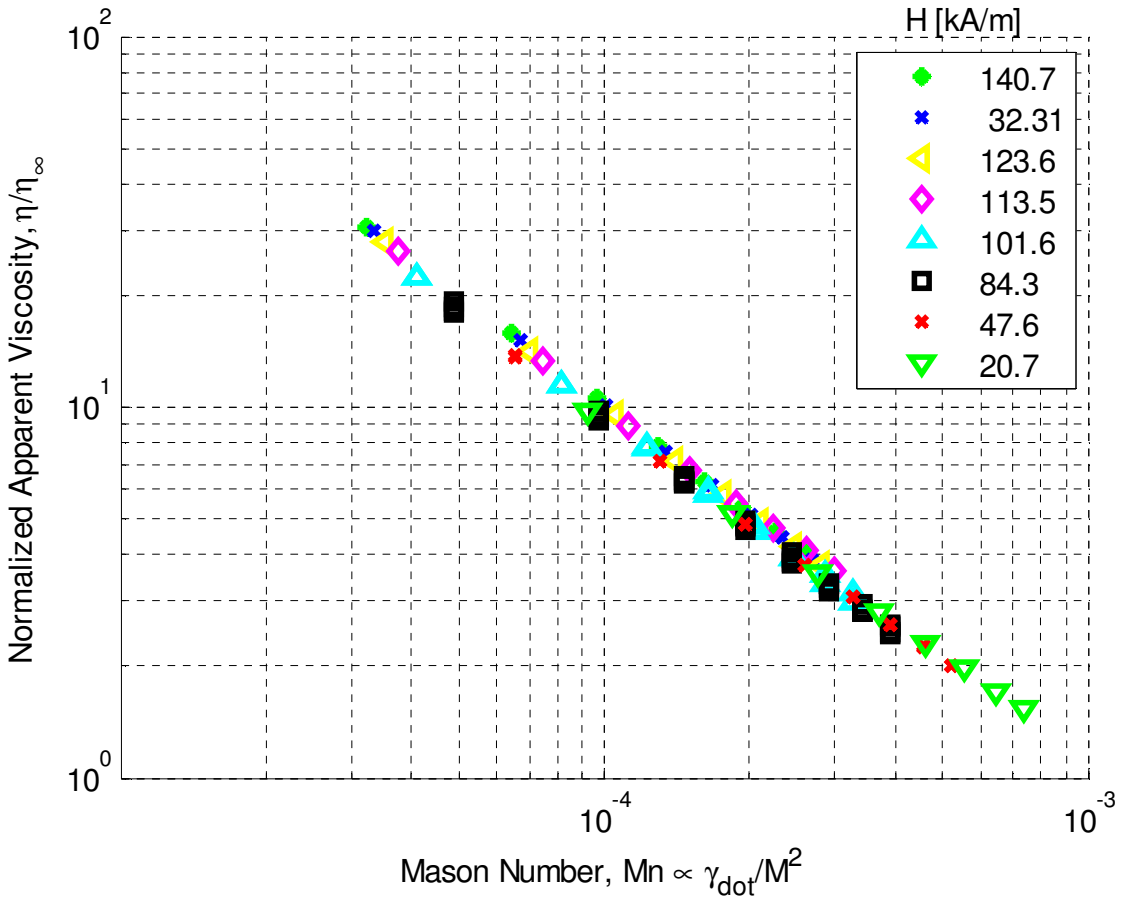

Figure 3.11 - Normalized apparent viscosity versus Mason number for MRF-145BG at shear rates up to 10,000 s^{-1}, using a gap size of 0.25 mm at 20°C.

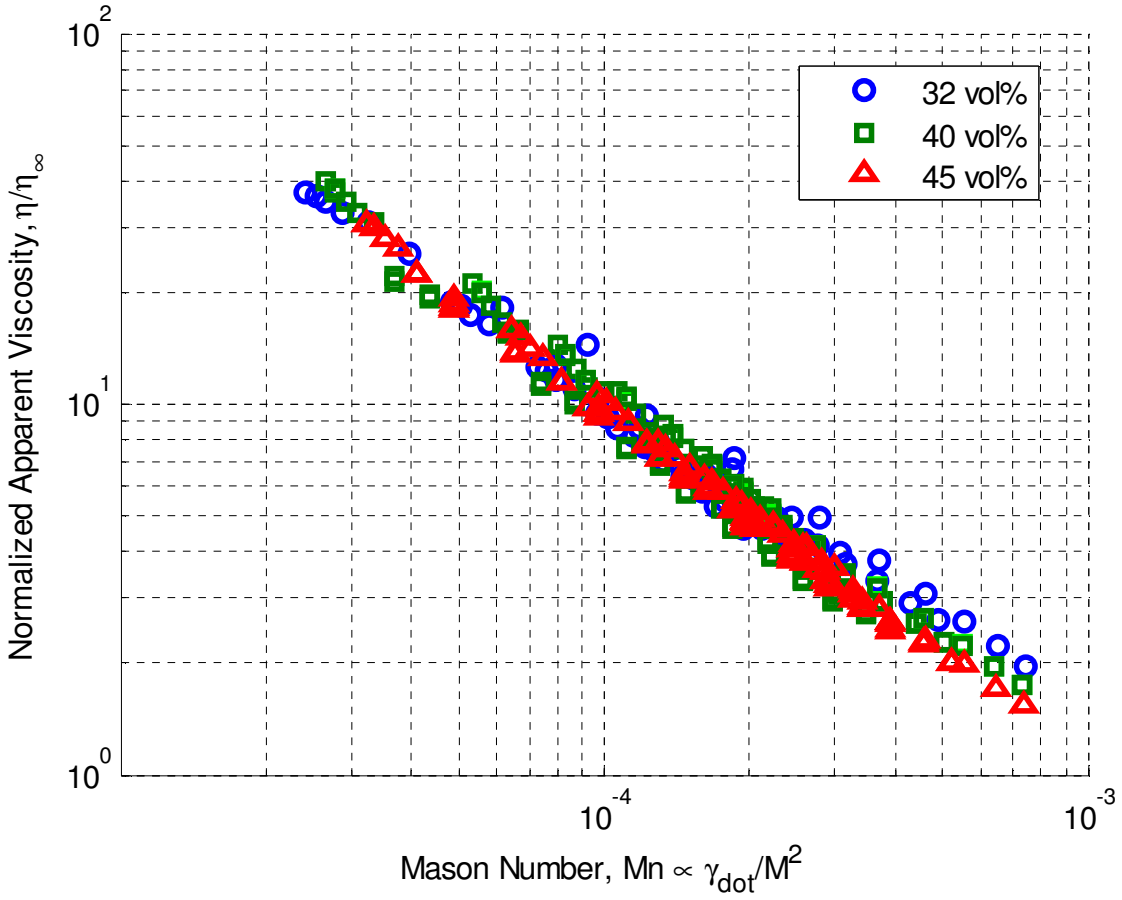

Figure 3.12 - Normalized apparent viscosity versus Mason number for three different solids loading fractions: 32 vol%, 40 vol%, and 45 vol%. Each data set was collected at shear rates up to 10,000 s^{-1}, using a gap size of 0.25 mm at 20°C.

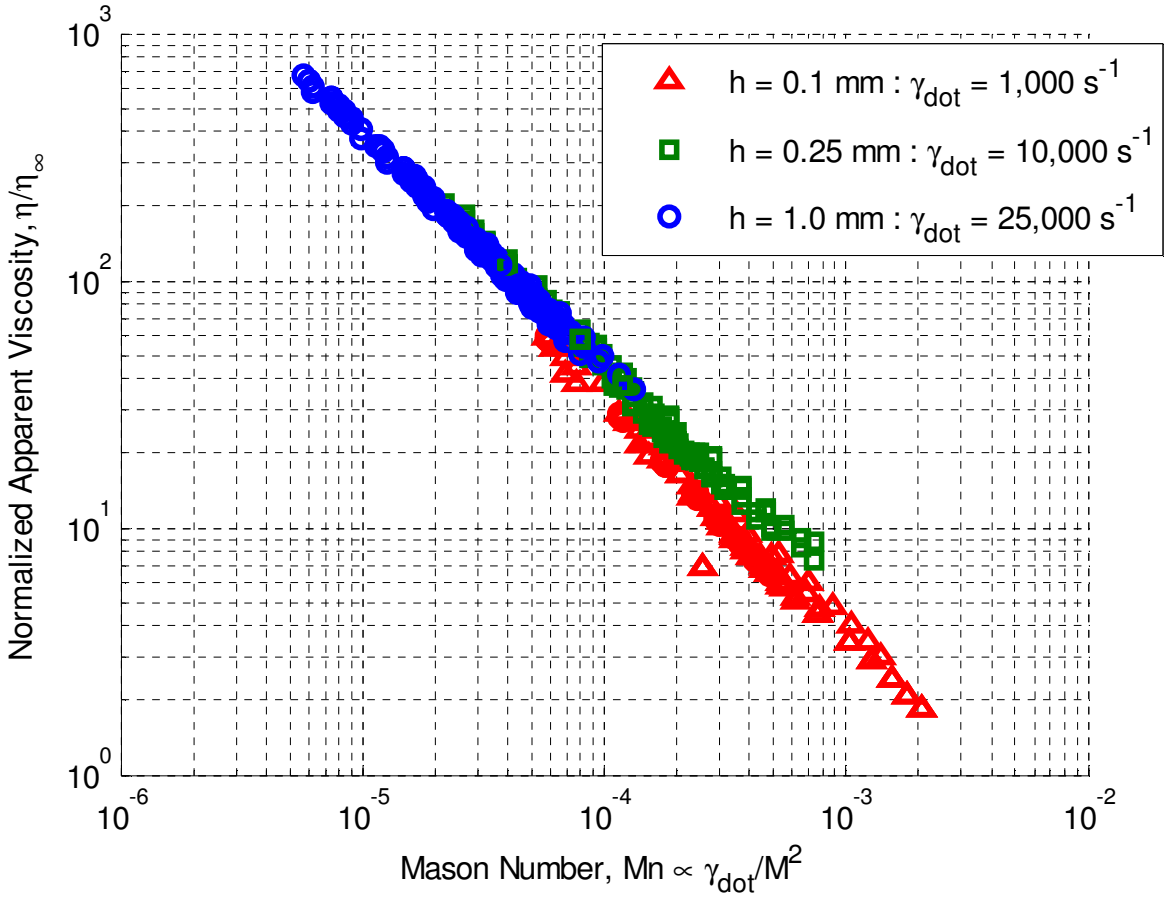

Figure 3.13 – Normalized apparent viscosity versus Mason number for LORD MRF-132DG at 20°C for three different gap sizes. Maximum shear rate $\dot{\gamma}$ = 25,000 s^{-1} is to the far right in red. Data for the two larger gap sizes collapse well, while the smallest gap size exhibits a curve with a slightly different slope.

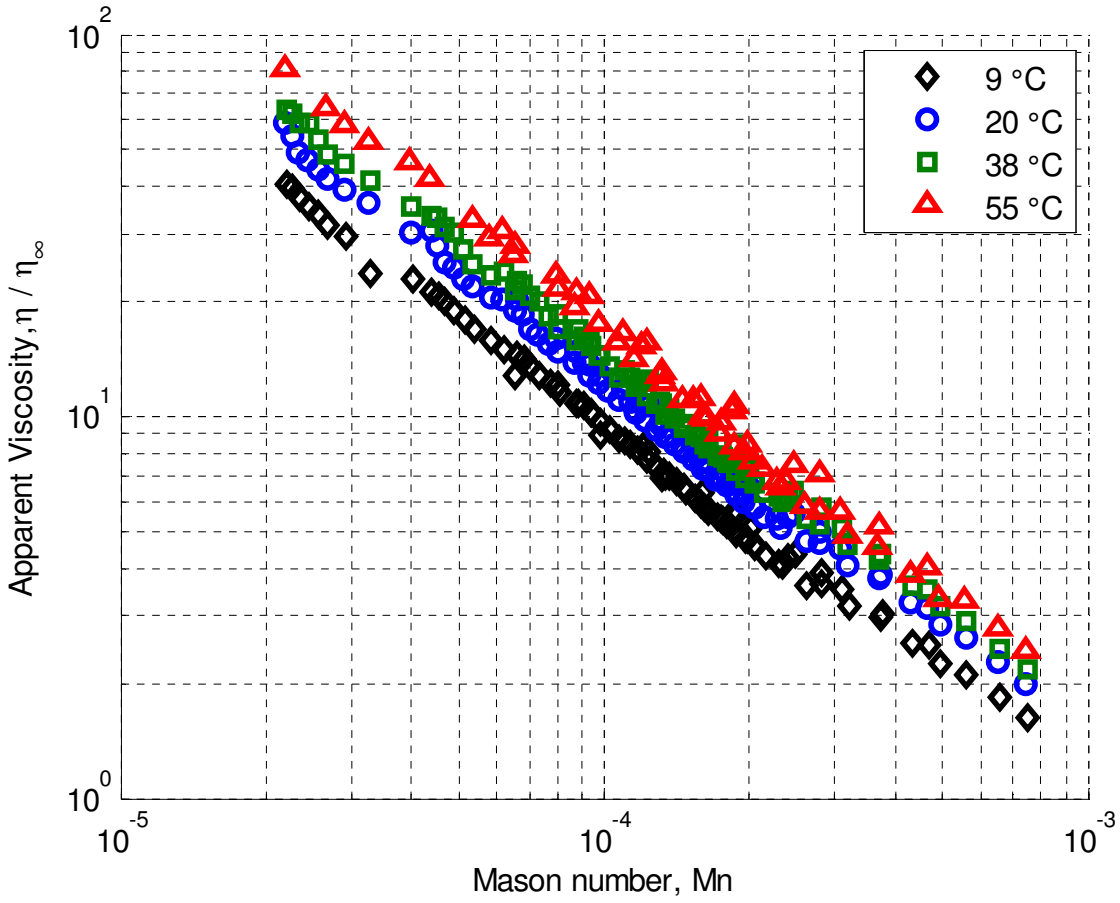

Figure 3.14 – Normalized apparent viscosity versus Mason number in MRF-132DG at 9°C, 20°C, 38°C, and 55°C. Each test series was performed with a maximum shear rate of 10,000 s^{-1}.

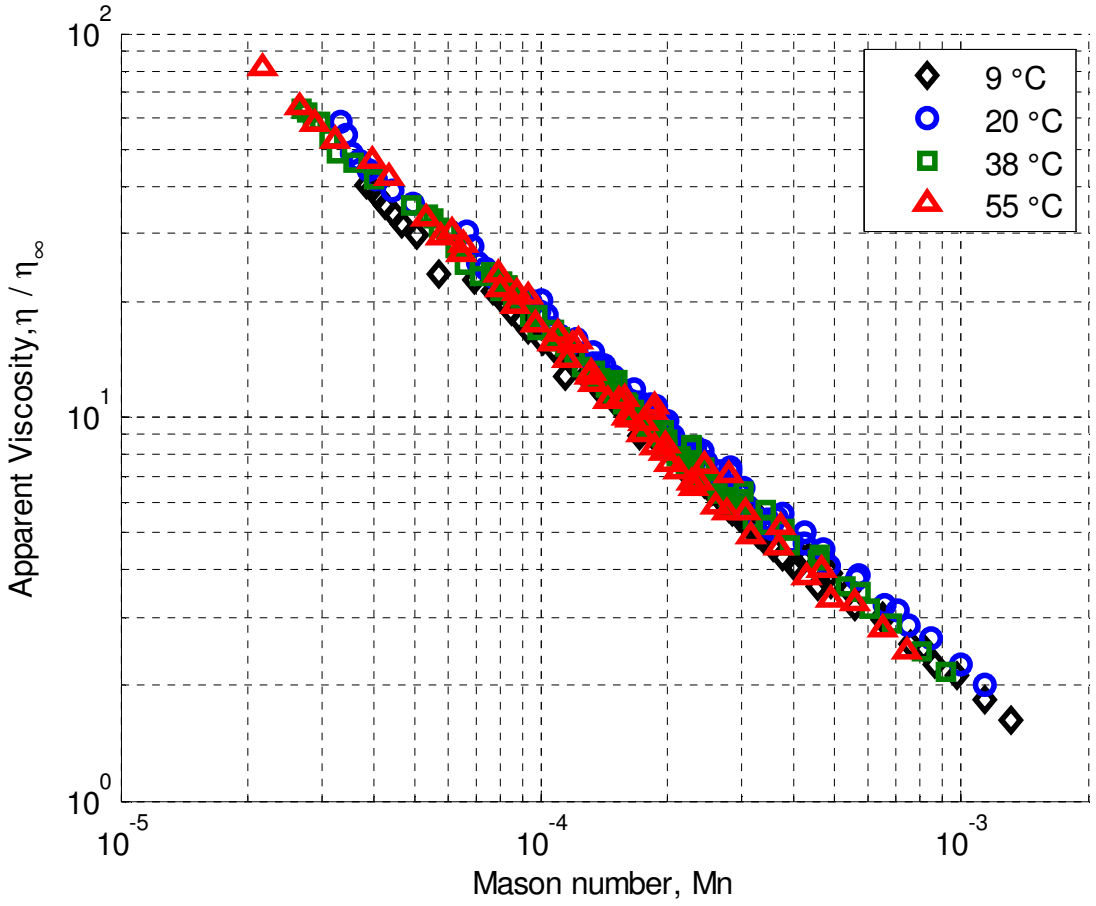

Figure 3.15 – Normalized apparent viscosity versus temperature-corrected Mason number for LORD MRF-132DG with a maximum shear rate of 10,000 s^{-1}.

Chapter 4

4. SCALING MR FLUID DEVICE PERFORMANCE USING MASON NUMBER

4.1. Abstract

A high shear rate rotary-vane magnetorheological energy absorber (MREA) along with a benchtop Searle cell magnetorheometer are used to investigate device scaling using Mason number for high rate shear-mode MR devices. The rotary-vane MREA was designed as a part of the lightweight magnetorheological energy attenuation system (LMEAS), previously developed to enhance crash safety and provide vibration isolation for rotorcraft seats. A pair of rotary-vane MREAs in the LMEAS system provide a large controllable yield force and a low viscous damping to accommodate both crash safety and vibration performance requirements. High shear rate, full system scale rotation tests were conducted to evaluate the rotary vane MREA performance, and these experimental results are discussed, analyzed, and compared with the results from a lab scale Searle cell magnetorheometer using apparent viscosity and Mason number. This nondimensional analysis shows that device performance across a wide range of temperatures and operating speeds

can be predicted from only knowledge of the MR fluid properties, successfully connecting laboratory experiments with practical operations.

4.2. Introduction

Occupant seats designed for crashworthiness utilize energy absorbers (EAs) in a seat suspension to attenuate the vertical crash impact loads that are transmitted from the base frame of the aircraft to the occupant of the seat (Richards and Podob, 1997). These EAs can be classified as fixed-load energy absorbers (FLEAs) or variable-load energy absorbers (VLEAs) (Richards and Podob, 1997; Desjardins et al., 1989; Desjardins, 2006). These devices cannot adapt their load-stroke profile as a function of occupant weight or as a function of real-time environmental measurements, such as operating temperatures or impact levels during a crash or hard landing. In addition, existing EAs are not designed to isolate occupants from rotorcraft vibration during normal operation. Extended exposure to whole-body-vibration often results in crew fatigue, discomfort, and long-term injuries (Harrer et al., 2005; Bongers and Dijkstra, 1990; Shanahan et al., 1986).

Adaptive energy absorption systems, such as the magnetorheological energy absorber (MREA) discussed in this research, have emerged as an innovative way to achieve what is effectively a continuously adjustable energy absorber (Choi and Wereley, 2005; Hiemenz and Hu, Aug. 25-28, 2008; Hiemenz et al., 2007). MREAs can adapt their stroking load as a function of occupant weight in combination with a semi-active feedback controller. By smoothly adjusting the load-stroke profile of the MREA as the seat strokes during a hard landing or crash event, MREAs have the capability of providing an optimal combination of completely utilizing the available stroking distance while minimizing lumbar loads, automatically compensating for occupant weight and load level or impact severity. Furthermore, MREAs offer the unique ability to use the same seat suspension system for both shock isolation to protect the occupant during hard landings and crash

impacts, as well as semi-active vibration isolation during normal flight operations. Thus, the LMEAS offers protection from impact loads and also reduces the risk of health issues resulting from prolonged whole body vibration (McManus et al., 2002; Wu and Griffin, 1997; Choi et al., 1999). Compared with conventional passive seat suspensions, a semi-active suspension employing MREAs has shown a significant shock load reduction across a range of impact conditions (Choi and Wereley, 2005). Additionally, McManus et al. (2002) demonstrated significant attenuation in the severity of end-stop impacts using MR seat suspensions, as well as reduced vibration levels (McManus et al., 2002).

Most MREAs developed to date are linear stroke MR dampers that use flow mode, also known as Poiseuille flow or pressure-driven flow of the MR fluid through an annular valve. In a typical linear stroke MREA, a coil bobbin (i.e., the electromagnet) is integrated into the piston head of the damper, and reciprocating motion of the piston head forces MR fluid to flow through an annular valve. Known as the "active gap", this flow passage can either be through the piston head itself via an attached concentric tubular flux return, or through the gap between the bobbin and the cylinder body. The stroking load can be adjusted by increasing or decreasing the applied current, generating a corresponding magnetic field. Large force generation can be realized in a linear stroke MREA because of hydraulic amplification, the ratio of piston to the smaller annular valve cross-sectional areas. Therefore the flow-mode MREA can provide a large damper force while using a relatively small hydraulic cylinder diameter (Wereley and Pang, 1998).

However, the linear stroke flow mode MREA configuration has shortcomings. One drawback is that the length of a linear stroke MREA is dictated by the required stroke; that is, the length of the MREA equals the sum of the lengths of the piston, twice the required stroke, and hydraulic end caps. Thus, the total length of a practical linear stroke flow-mode MREA can be more than twice

the required stroke length, leading to an untenable weight and size. The most important drawback, however, arises when these devices are used at velocities representative of crash impacts, which correspond to very high (> 25,000 s^{-1}) shear rates.

Using the performance measure known as the *dynamic range* reflects the "controllability" of an MREA, or the maximum active "field-on" force versus the minimum passive "field-off" force, expressed as the ratio shown below.

$$DR = \frac{F_{active}}{F_{passive}} \approx \frac{\tau_y}{\mu\dot{\gamma}} \tag{4.1}$$

It has been shown previously that the passive (viscous) damping force component of a flow-mode MREA tends to increase as the square of the piston velocity (Becnel et al., 2010). The peak stroking load is defined by the threshold lumbar load that can be accommodated by an occupant. Therefore, the maximum crash velocity at which a linear stroking MREA can be effective in protecting occupants is limited by this quadratic relationship between velocity (shear rate) and force (shear stress), since the passive force alone equals the peak lumbar load, and no control is feasible. Thus, there is a prime motivation to overcome both of these drawbacks if a feasible MREA for compact, lightweight applications is to be realized (Hu et al., 2012).

Contrary to this quadratic force-velocity relationship inherent to flow mode devices, direct shear mode operation results in a linear dependence of force to velocity. In shear mode, also known as Couette flow, one of the magnetic poles moves with respect to the other, shearing the MR fluid in the gap. Figure 4.1 presents the force-velocity relationships for both flow and shear mode operation, clearly showing that shear mode maintains a better dynamic range at high shear rates. Based on this understanding and the successful proof of concept using the Searle cell magnetorheometer, a

shear-mode rotary vane MREA was developed to extend the range of controllable operating speeds and improve performance throughout this range (Hiemenz and Wereley, 2010).

In this novel MREA design, a thin concentric vane is mounted between a stationary cylindrical damper body and the internal electromagnetic coil armature, shown as an isometric quarter section cutaway in Figure 4.2 and a schematic view in Figure 4.3. As the vane rotates, the MR fluid between the vane and inner and outer wall surfaces is sheared, developing a resistive torque. For LMEAS the rotary vane is connected to a rotary reel wheel shaft, such that rotary motion is converted to linear motion and resistive torque can be converted to a linear stroking force. Since the viscous force in shear-mode flow is a linear function of the rotation speed, the shear-mode MREA can provide high yield force and unlimited stroke, while maintaining a low off-state (absence of magnetic field) viscous force. Because of this improved dynamic range, the rotary vane shear-mode MREA is also cost effective as it uses a much smaller volume of MR fluid as compared to a flow mode EA designed for the same stroking load. Analyses performed under a US Army Aviation Applied Technology Directorate (AATD) sponsored effort, performed by Techno-Sciences, Inc., the University of Maryland and BAE Systems have shown that rotary vane MREAs can realize an 80% reduction in weight when compared to their linear stroke counterparts.

Challenges arise when manufacturer data for yield stress and off-state viscosity are applied to an MREA design which may operate under different environmental conditions than those at which the reported data was collected. Particularly at higher shear rates, like those encountered in crash simulations, the Mason number provides a useful and convenient nondimensionalization across the range of applied fields and temperatures, and relies only on a limited number of variables; carrier fluid viscosity, η_c, particle volume fraction, ϕ, and knowledge of the strain rate and magnetization within the fluid as well as the operating temperature range. This analysis method

can scale device performance from fluid characterization tests performed in a controlled laboratory environment, reducing the size of the required test matrix while still providing accurate predictions.

This chapter will discuss the initial design and characterization of the rotary MREA based on an established device analysis method, and discrepancies between the predicted and measured performance will be addressed by proposing an alternate, nondimensionalized analysis using apparent viscosity and Mason number as developed in previous chapters. Additionally, the benefits of this design tool are presented with respect to the use of laboratory scale tests with the Searle cell magnetorheometer, and it is shown that the performance of both devices are well correlated when using this nondimensional framework. By incorporating the temperature corrected Mason number as a design and analysis benchmark, the specific design of any shear mode MR device can be improved across a wide range of operating conditions from knowledge of MR fluid properties that were gathered experimentally over a much narrower range.

4.3. Rotary MREA design for LMEAS

The rotary vane MREA was initially developed using a well-established analysis method based on an assumed Bingham plastic fluid model, which requires knowledge of two major performance parameters, i.e. maximum controllable yield force and off-state viscous force. In order to establish values for these MREA design criteria, a single-degree-of-freedom (SDOF) MR seat suspension model was simulated as a performance prediction tool. Since LMEAS is an adaptive energy absorbing system, it should perform well as both a vibration attenuator and a shock absorber. A schematic for this LMEAS model is shown in Figure 4.4. The equation of motion for this SDOF system can be expressed as shown below.

$$m\ddot{z} + c\dot{z} + kz = -m\ddot{y} - F_y sgn(\dot{z}) \tag{4.2}$$

where m is the effective occupied seat mass, k is the spring stiffness used in the suspension, c is the linear viscous damping, $z = x - y$ is the relative motion between the seat and floor, y is the absolute motion of the cockpit floor, and F_y is the controllable yield force.

For any well-designed vibration isolation system, the seat suspension system resonance should be much less than the dominant vibration frequency. In the case of LMEAS, the dominant frequency is that of the SH-60 Blackhawk rotor; 4P, or 4 per rev, approximately 17 Hz. This suggests that the upper and lower bounds on the desired system resonance should be 2 Hz to 6 Hz, respectively. Based on this, the system spring stiffness and the viscous damping (one of the two rotary MREA properties) were chosen. The selected system parameters were verified using computational simulation of the SDOF MR suspension system discussed above, and it is worth noting that these simulations predicted over 75% attenuation of vertical 4/rev vibration.

The maximum yield force required of the MREA was then obtained by assuming that MREA would stroke at 14.5 times the effective occupied seat weight, in order to attenuate the peak floor deceleration pulse set forth in standard crash design guidelines (Desjardins et al., 1989). In order to determine this required force, the SDOF MR suspension simulation discussed above was used to emulate a high speed seat qualification test, i.e. 12.6 m/s (42 ft/s) vertical sink rate, 51 g peak acceleration, 0.051 sec duration triangular pulse (Desjardins et al., 1989). The spring in this simulation was set to break away when the total force reaches three times the weight of the heaviest occupant. The controllable yield force of the MREA, F_y, is calculated as shown.

$$F_y = F_L - F_v - F_k \;\; such\ that \;\; F_T \leq F_L \tag{4.3}$$

where F_v and F_k are the contributions from viscous and spring stiffness effects, respectively, and F_L is the maximum desired stroking load for the given occupant weight. Using the above equation,

the feedback controller modulates the MREA yield force such that the total transmitted force, F_T, does not exceed the limit load, F_L. The maximum MREA yield force requirement was determined based on this analysis, and the selected viscous damping, c, was verified.

The design of the rotary vane MREA's "active gap", i.e. the height of the gap within which the MR fluid will be sheared, directly determines the magnitude of both the active yield force and passive viscous force. An iterative procedure uses these desired performance metrics along with a finite element model of the magnetic circuit to define the geometry of the rotary vane MREA. Using the maximum sink rate and transmitted force in standard crash design guidelines from Desjardins et al. (1989), the active gap height which fulfills both of these requirements can be determined using the following general equations.

$$\dot{\gamma}\frac{h}{R}\frac{2\pi}{60}P\omega_i R_s = v_{max} \tag{4.4}$$

$$\sum_{N_v} \tau_{r\theta} 2\pi L_v (R+h)^2 P R_s = F_{max} \tag{4.5}$$

Here, R_s = 0.5 inch is the radius of the shaft used to convert radial to linear motion, and P is the gear ratio between the rotary shaft and the seat system. For the rotary vane MREA developed in this work, one vane was used for mechanical simplicity, but in general the output force can be increased by using more vanes; however, an effective magnetic circuit design becomes much more difficult. A schematic flowchart of this design procedure is provided in Figure 4.5.

4.3.1. Magnetic circuit design

By examining equations (4.4) and (4.5), it becomes clear that increasing the gap height favorably decreases the passive viscous force, but negatively impacts the magnetic flux density, i.e. the available maximum yield force, and vice versa. This tradeoff is at the heart of any practical MR

device design problem, and requires that the magnetic circuit should be cleverly designed to deliver a perpendicular, uniform field through the MR fluid within the active gap.

In this design, a heat treated steel coil armature is seated in the center of a cylindrical fluid chamber. The three electromagnetic coils are wound alternating clockwise-counterclockwise-clockwise in their channels to provide three self-contained, nearly identical magnetic fields. Between the armature and outer body cylinder wall is a thin, cup-shaped rotary vane. As the rotary vane rotates between the stationary coil and outer cylinder, the MR fluid in the double-faced gaps between the armature, vane, and the cylinder wall is sheared and flow induced.

Since the shear stress of the MR fluid is dependent of a magnetic field, the output torque of the rotary vane MREA can be controlled. Magnetic field analyses were conducted using ANSYS MAXWELL software and the design variables were iteratively modified based on the FEM results. The magnetic flux distribution obtained from the FEM analysis is shown in Figure 4.6, and the magnitude of the magnetic flux density along the gap thicknesses is shown in Figure 4.7. From the manufacturer reported properties of the MR fluid used, it was determined that the desired magnetic field strength is 0.9 Tesla. At 3.5 Ampere applied current, the average magnetic field strength in the inner and outer gaps matches this requirement, validating the electromagnetic design of the MREA.

4.4. Experiment

The MREA was characterized using a high torque output transmission test machine, and the measured output force as a function of the applied current was compared to analytical predictions using the values for yield force and fluid viscosity provided by the fluid manufacturer. Experimental data was analyzed to identify the two major performance parameters required for the

characterization of a rotary vane MREA, i.e. maximum controllable yield force and linear viscosity. In addition to this established Bingham plastic analysis method, the data is plotted as normalized apparent viscosity versus Mason number, with special consideration given to temperature effects not accounted for in the established analytical method.

4.4.1. Test setup

To evaluate the performance of the rotary vane MREA, a high speed transmission test rig (US Drives, Inc. Phoenix AC drive, connected to a Vector 75 HP drive motor) was used for torque measurements at speeds corresponding to low crash velocities. The complete test setup is shown in Figure 4.8. The MREA was mounted on a stationary frame, while the rotary shaft of the MREA was connected to a DC motor via two flexible couplings and a torque sensor. A non-contact laser tachometer measured rotational speed, and a thermocouple was fixed to the outer surface of the MREA cylinder to monitor MREA temperature variation during testing (not shown in Figure 4.8). The DC motor is provides a rotational speed of up to 1800 rpm, which translates into a velocity of approximately 2.5 m/s (8 ft/s) with a one-inch diameter shaft, $R_s = 1$ inch. A BKPrecision XLN10014 DC power supply was used to supply constant current to the MREA during testing.

4.4.2. Preliminary results

During the initial round of characterization tests, the nominal currents supplied were 0, 1.5 and 3.5 A. For each applied current, the rotational speed for testing was increased from 0 rpm to 1800 rpm within 3 seconds and held at 1800 rpm for 2 seconds. The recorded 0 A and 3.5 A testing results for the one MREA are shown in Figure 4.9. Using the commercially available LORD MRF140-CG magnetorheological fluid, two identical MREAs were tested on the rotation test rig, and the each MREAs measured force as a function of the velocity and current is shown in Figure 4.10, along with the predicted value (Hu et al., 2012).

Apparently, both rotary EAs behave similarly to each other and the predicted results, though the measured viscous force seems to decrease as the velocity increases. This phenomenon, discussed in more detail in previous chapters, becomes more pronounced as the applied current increases, likely due to both the shear thinning of the fluid and the temperature-dependence of fluid viscosity. It should be noted, however, that these temperature effects are not a concern for the LMEAS. In operational vibration mode, the energy absorption rate requirement will be much lower (low velocities and low MREA forces), while in crash mode, the energy absorption occurs over a very short duration (less than 0.1 second). Since it is observed that these temperature increases occur only when there is very high impact energy absorption by the MREAs under the kind of prolonged operation in these characterization tests, these temperature effects can be neglected when evaluating the maximum MREA force for impact energy attenuation. Temperature and shear thinning effects are important, however, when characterizing the flow environment within the rotary vane MREA, and are discussed in more detail in the following sections.

4.5. Results and Analysis

The relationship between torque output and total MR fluid shear stress within the rotary vane MREA can be obtained through a modified version of equation 2.1, where the Searle cup inner radius $(R + h)$ has been replaced with an expression reflecting the new shear surface radii. The equation below reflects the fact that, in the case of the multiple shear gaps of the rotary vane MREA (between the coil armature and the inner vane surface, referred to as the "inner gap", and between the outer vane surface and the cylinder damper body, referred to as the "outer gap"), the total fluid shear stress can be amplified by using more shear surfaces, or vanes.

$$\tau = \frac{M}{2\pi L_v\left({R_a}^2 + {R_o}^2\right)} \tag{4.6}$$

Here, L_v is the vane length, R_a is the coil armature outer radius and R_o is the inside radius of the cylinder damper body. For the inner gap, the shear stress expression contains only the R_a term; similarly, the outer gap shear stress expression contains only the R_o term. The fluid shear rate within each narrow gap as a function of rotation rate in RPM, Ω, is given as the set of equations below (Morrison, 2001).

$$\dot{\gamma}_i = \frac{R_{v,i}}{h_i}\frac{2\pi}{60}\Omega \tag{4.7}$$

$$\dot{\gamma}_o = \frac{R_{v,o}}{h_o}\frac{2\pi}{60}\Omega \tag{4.8}$$

These equations are used to generate the flow curves for the rotary vane MREA, a typical characterization plot for MR fluid devices. The flow curves, shown in Figure 4.11, can be used to identify the Bingham-plastic model parameters of yield stress and viscosity, and these values are examined to validate the experimental results. The yield force and viscous damping of the rotary vane MREA are identified as shown in Figure 4.12 and compared to the predicted results provided by the fluid manufacturer (LORD Corporation, 2012). The values match well across the range of applied currents. The slight reduction in viscosity as applied magnetic field increases is again the result of increased temperature from higher applied currents. It's clear that even as shear rates approach 25,000 s^{-1}, the MR effect persists and ensures controllability at low velocity crash speeds.

4.5.1. Nondimensional analysis

Unlike the experiments using the Searle cell magnetorheometer instrument, the rotation testing of the rotary vane MREA was not performed with a controlled temperature environment. Each test was begun from room temperature, but from Figure 4.9 it is clear that increased amounts of resistive and viscous heating occurred at higher applied currents. To minimize variations from this

temperature difference, the first six seconds of experimental measurements can be used from each dataset to yield a common, average temperature of approximately 55°C.

The Mason number can be calculated for both the inner and outer gap regions, but since the shear rate and shear stress are dependent on the chosen radius, the two Mason number values are nearly identical; in all proceeding analysis, the inner gap region is used. Using the Mason number nondimensional group framework discussed in the previous chapter, the flow curves for the rotary vane MREA can be reduced to a single master curve, shown in Figure 4.13. Here, the apparent viscosity is normalized by the field-off apparent viscosity at high shear rate (Klingenberg et al., 2007).

This nondimensionalized plot for the rotary vane MREA performance can now be directly compared with the results from the Searle cell magnetorheometer, even though these systems differ in maximum operating speed and system scale. Because the rotary vane MREA has an operating gap diameter nearly 10X that of the Searle cell magnetorheometer, it can generate 15.5 ft-lbs of torque at shear rates up to 25,000 s^{-1}, as compared to the Searle cell instrument's 0.5 ft-lbs of torque at rates up to 10,000 s^{-1}. Figure 4.14 provides a scale comparison between the devices.

Figure 4.15 shows the result of both nondimensionalized plots using Klingenberg's Mason number for the full-scale rotary vane damper and the Searle cell magnetorheometer, each performed using the 40 vol% MR fluid manufactured by LORD Corporation, MRF-140CG. Note that while both curves exhibit the characteristic collapse within themselves, the two lines are not superimposed due to the temperature differences present during each characterization test. This can be ameliorated by using the temperature-corrected Mason number (Eq. 3.13) to shift the curves by modifying the carrier fluid viscosity term appropriately. After doing this, Figure 4.16 demonstrates

that the two plots lie along the same master curve, indicating that the performance of these two different shear mode MR energy absorbers, operating at different shear rates, magnetic field strengths and temperatures can be described through the nondimensional Mason number as suggested in Chapter 3.

A curve can be fitted to this data using an equation of the following form (Marshall et al., 1989).

$$\eta_{app}/\eta_{\infty} = 1 + KMn^{-1} \tag{4.9}$$

Here K is a fit parameter that can be expressed in terms of two physically relevant nondimensional ratios, the normalized yield stress (yield stress over a reference interparticle stress), τ_y/τ^*, and the normalized plastic viscosity, η_{∞}/η_c. K is sometimes referred to in the literature as a "critical Mason number", and this can be extended to show that K varies linearly with the MR fluid volume fraction, ϕ. Our analysis uses a modified form of Klingenberg's Mason number, which contains a volume fraction term, and so this results in an expression of the well known result that yield stress varies linearly with volume fraction. In Figure 4.16 the form used for K is given below, where the nondimensional ratio parameters are η_{∞} = 0.59 Pa-s and τ_y/τ^* = 0.5.

$$K = 3\pi \frac{\tau_y/\tau^*}{\eta_{\infty}/\eta_c} \tag{4.10}$$

Therefore, if the fluid parameters used to determine K are known, either experimentally determined for novel MR formulations or provided by the manufacturer, the master curve can be calculated and a temperature correction factor can be used as a design benchmark for a family of scalable, shear mode devices.

4.6. Summary and Conclusions

In this chapter the design of a rotary vane, shear mode MREA for use in an SH-60 Blackhawk helicopter crashworthy crew seat system is discussed. Using an established, iterative method to tune the maximum yield force and passive viscous force components based on the Bingham plastic model parameters, a practical shear mode MREA that exhibited increased controllability at high speeds when compared to conventional, linear-stroking flow mode dampers. A high torque transmission testing rig was used to characterize two rotary vane MREAs, whose performance was shown to be consistent. The force-velocity data from these tests was used to produce flow curves comparing the fluid shear stress to the shear rate within the active gaps.

The modified nondimensional apparent viscosity and Mason number analysis presented in a previous chapter was applied to the MREA characterization data, and the characteristic coalescence across magnetic fields was observed. To scale experimental data between this device and the benchtop Searle cell magnetorheometer, the temperature-corrected Mason number was used to shift the curve, and good agreement was seen between these two different devices and operating environments. Additionally, a curve of the form reported by Marshall et al. (1989) is well fit to both experimental data, indicating that the analytical basis of the normalized apparent viscosity versus Mason number framework has practical use for both device design and experimental observation.

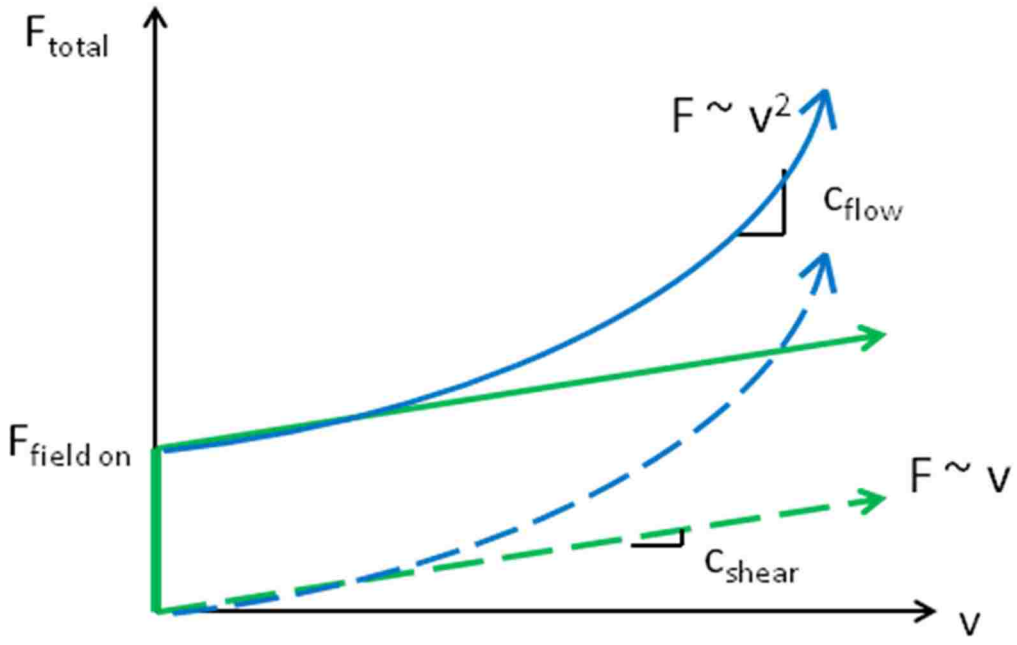

Figure 4.1 - Force (shear stress) versus velocity (shear rate) trends for flow mode and shear mode operation

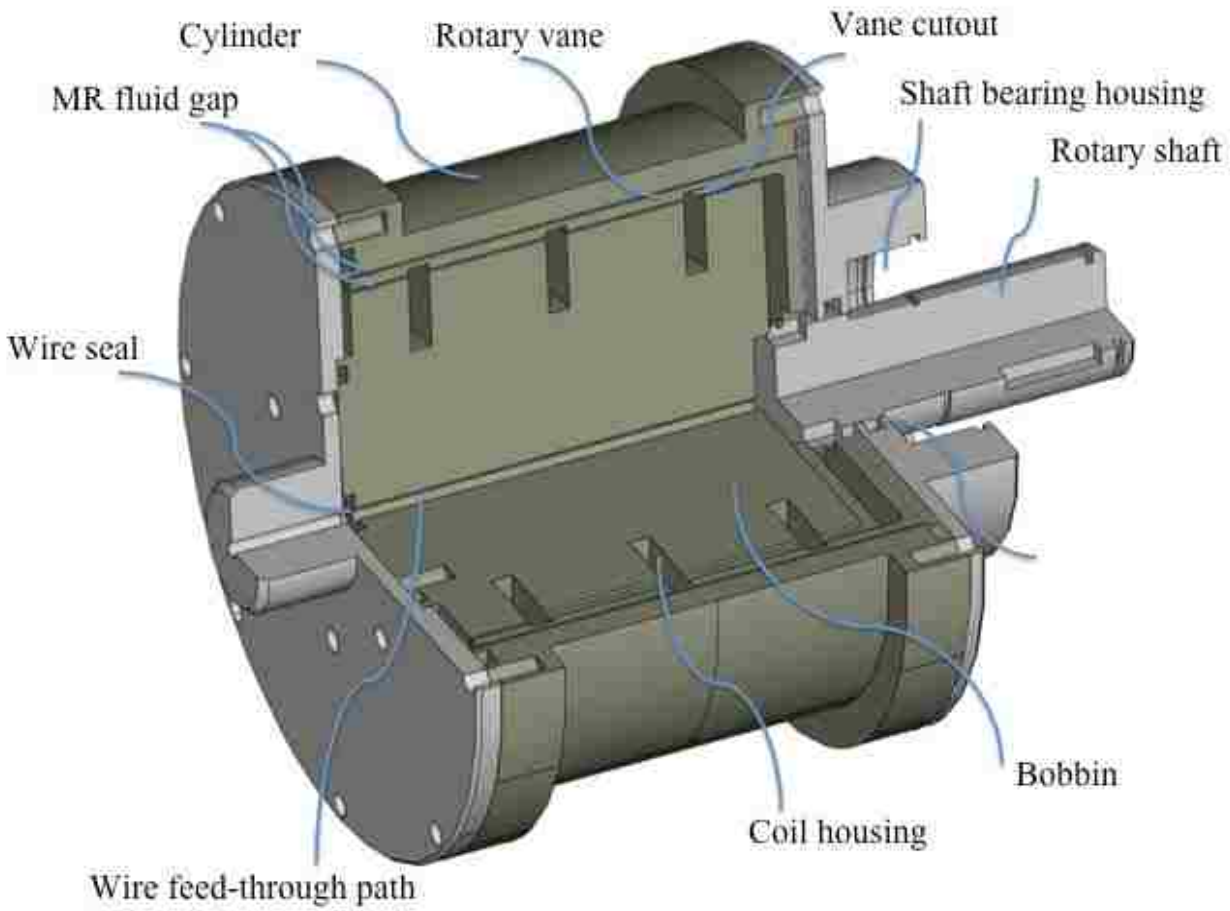

Figure 4.2 - Rotary vane magnetorheological energy absorber used in the LMEAS program

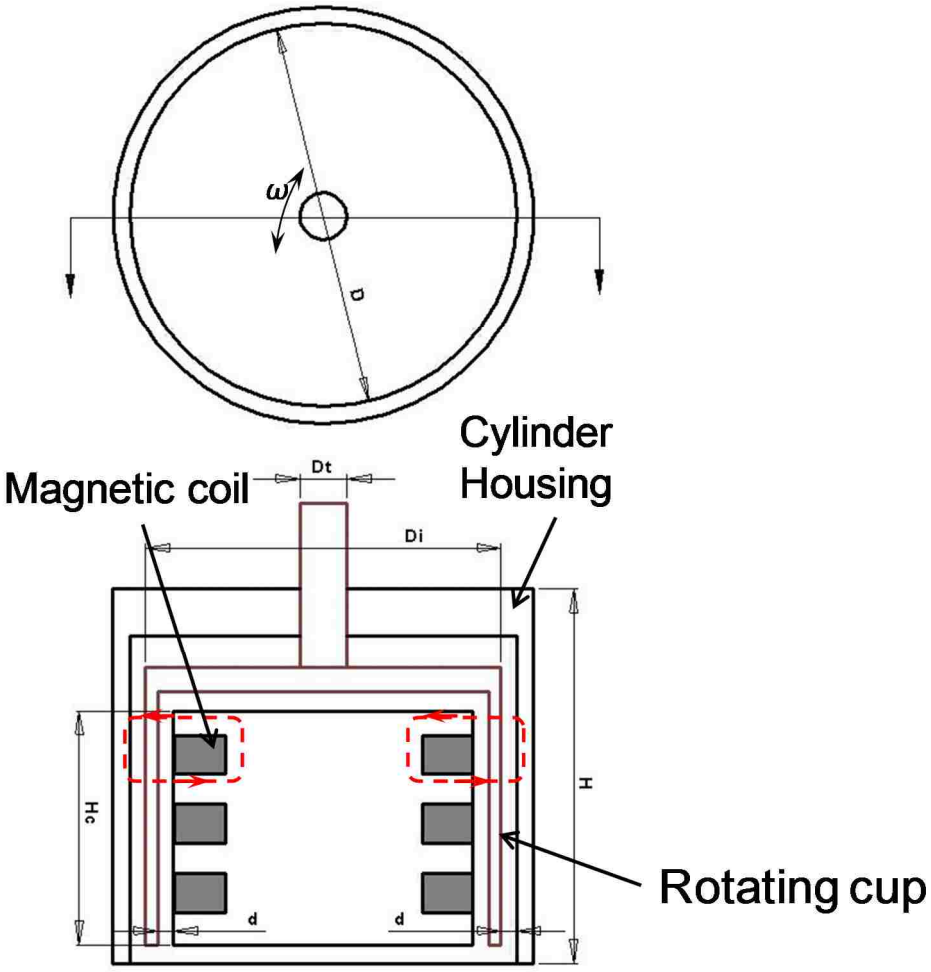

Figure 4.3 - Top and side schematic views of the rotary vane MREA

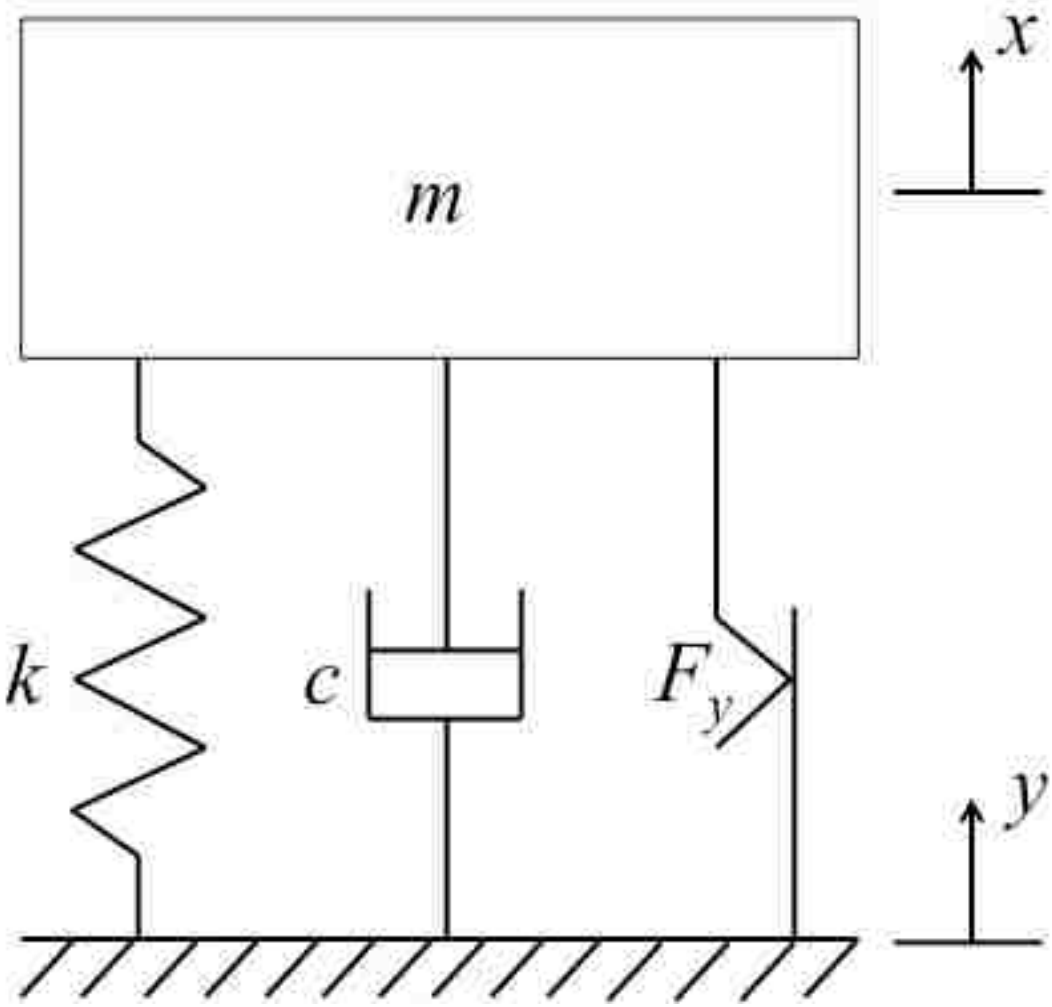

Figure 4.4 - SDOF model schematic for LMEAS

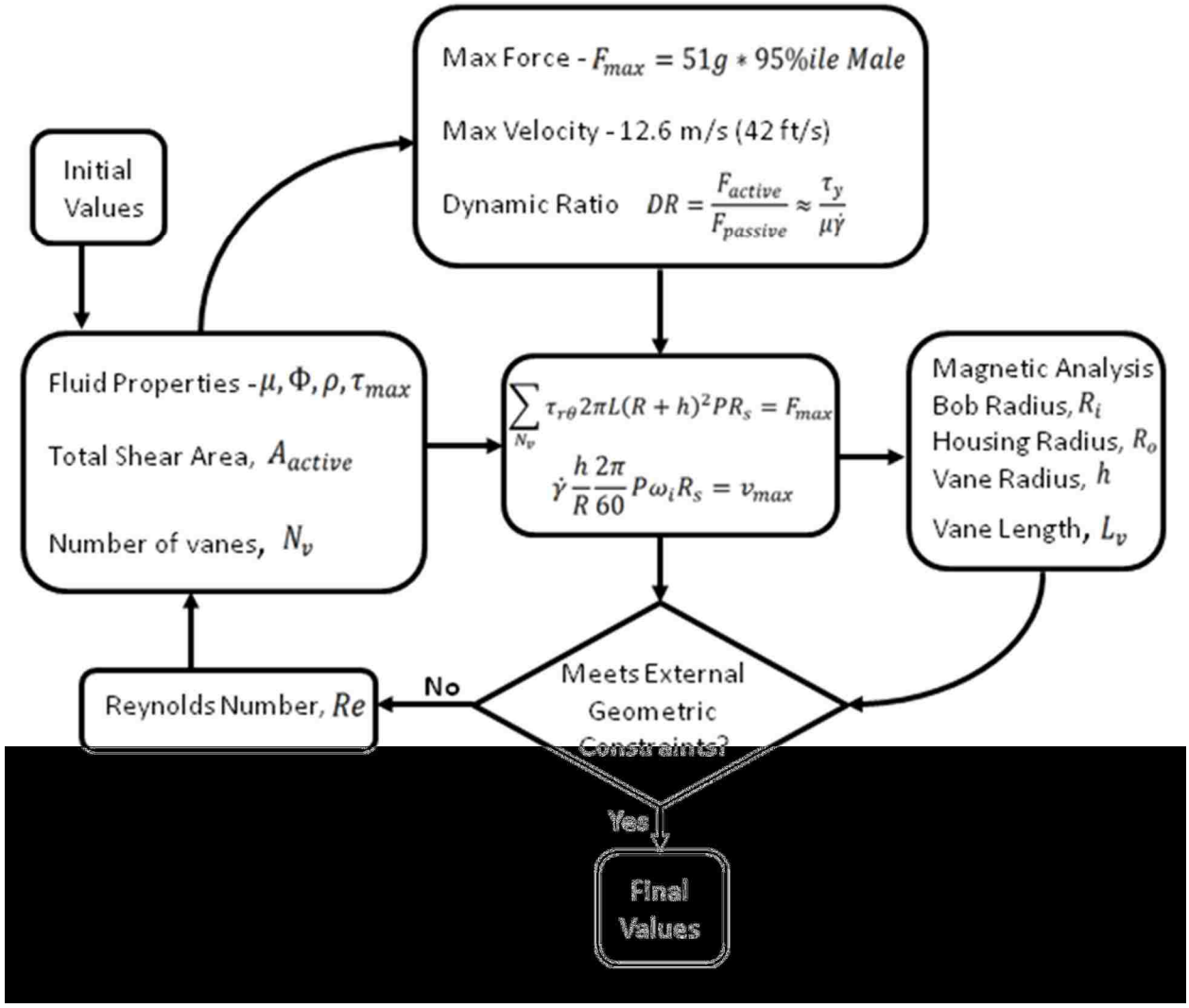

Figure 4.5 - Iterative design process for the rotary vane MREA

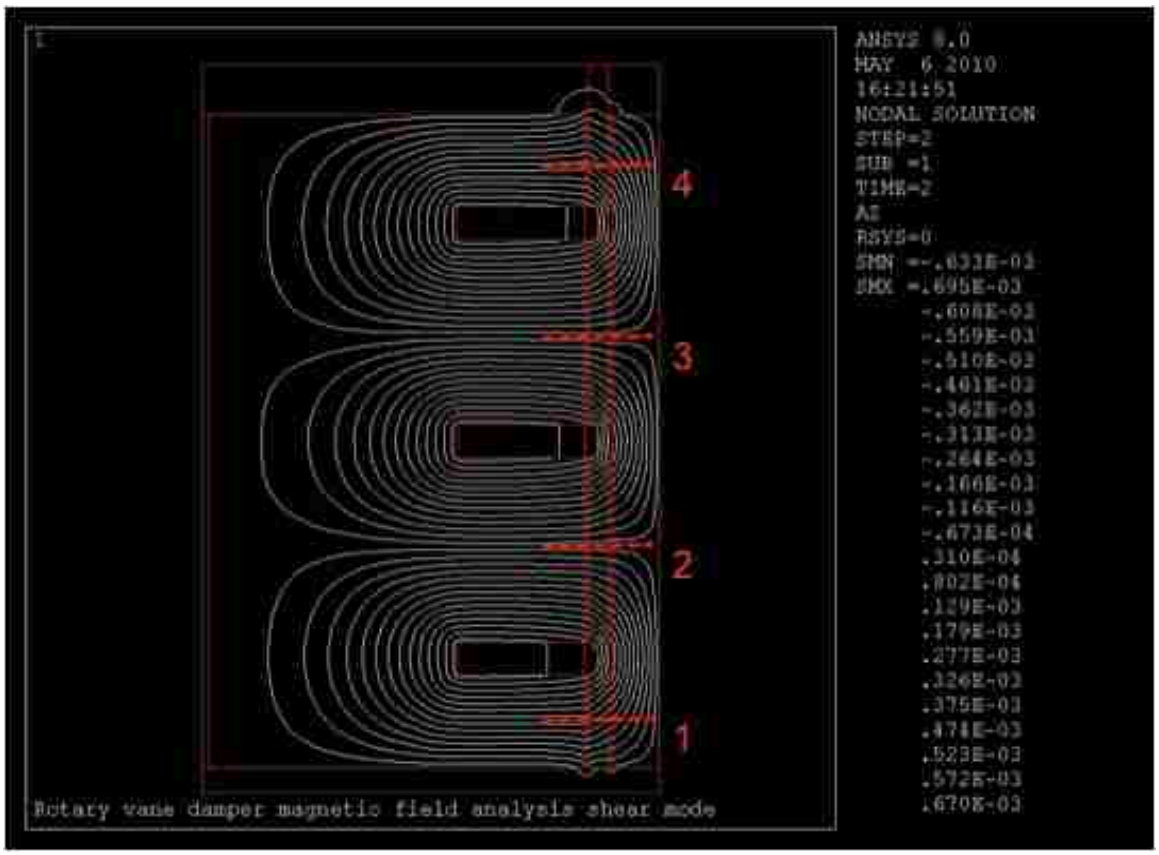

Figure 4.6 - Axisymmetric magnetostatic simulation of magnetic flux line distribution in the MREA. Each horizontal dashed line corresponds to the location of the desired uniform field.

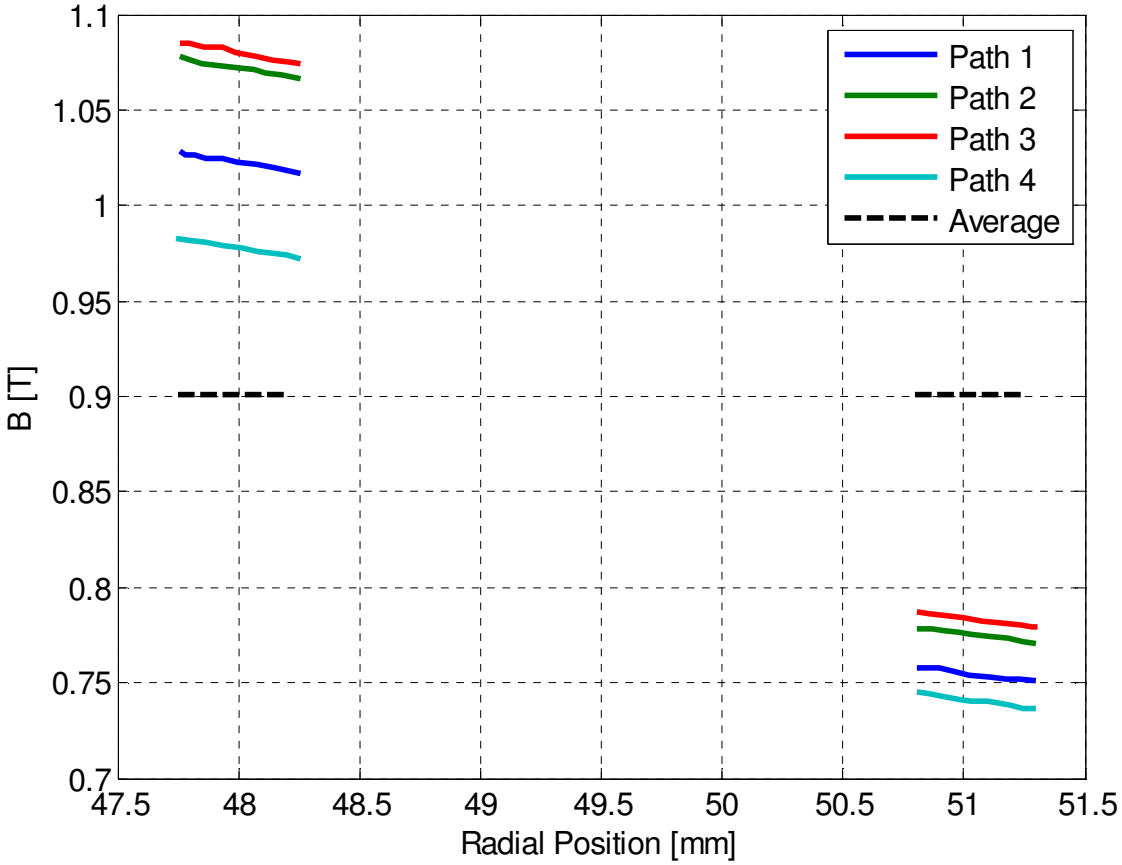

Figure 4.7 - Magnetic flux density within the inner and outer active gap regions, compared to the flux density required to achieve the specified maximum yield force output

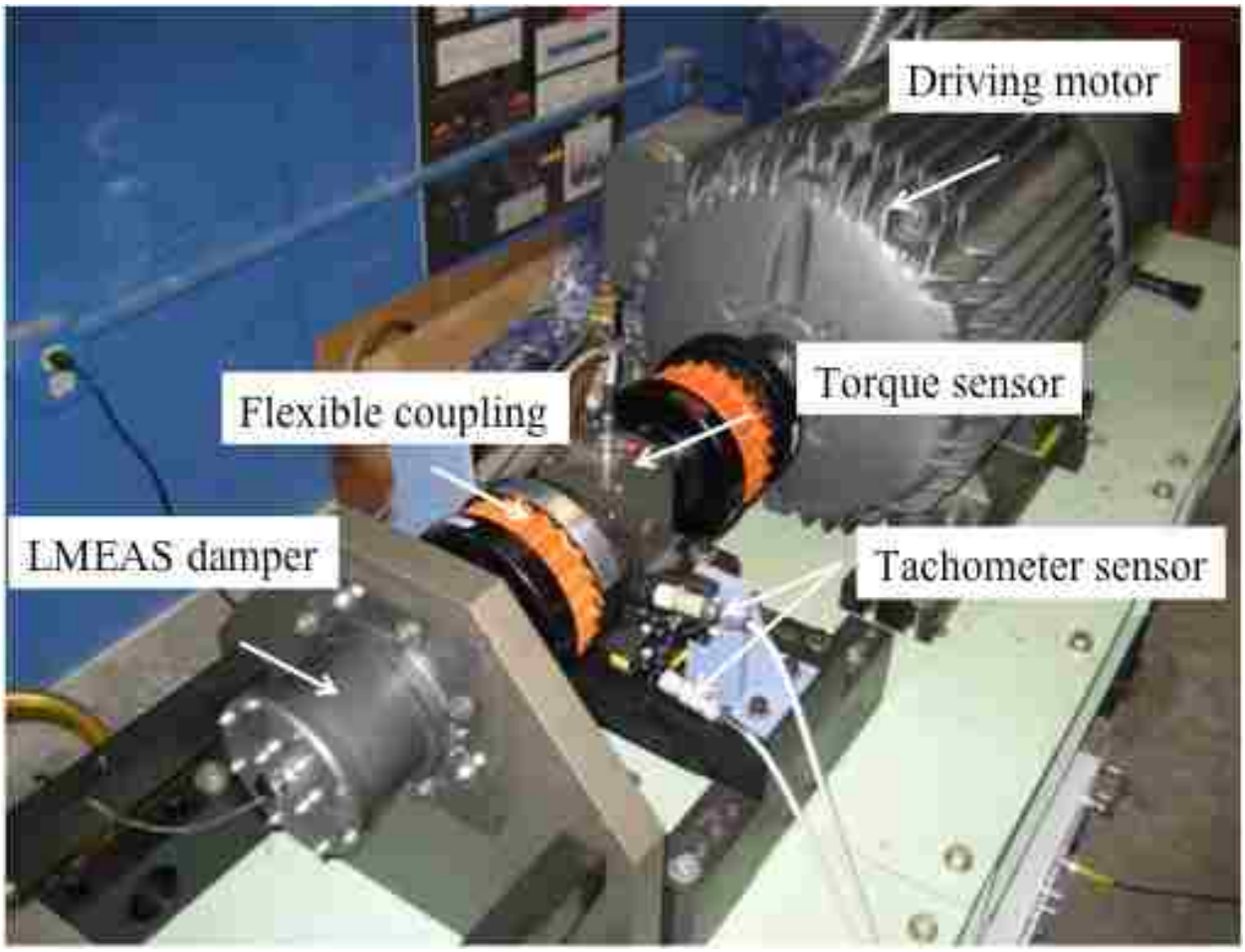

Figure 4.8 - High speed rotation testing rig used in rotary vane MREA experiments

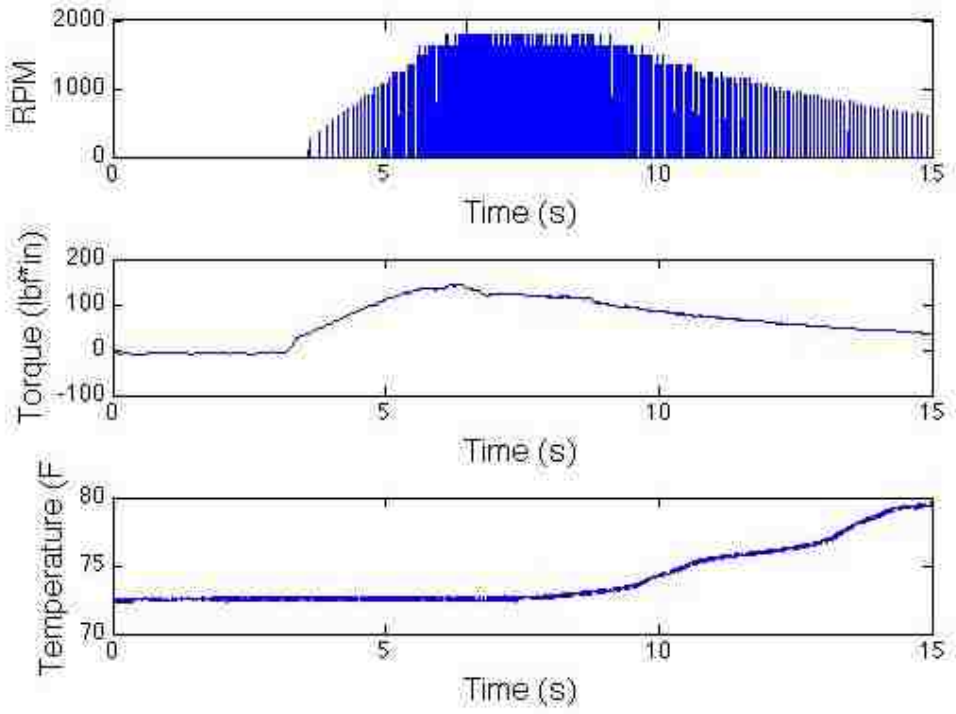

a) 0 A

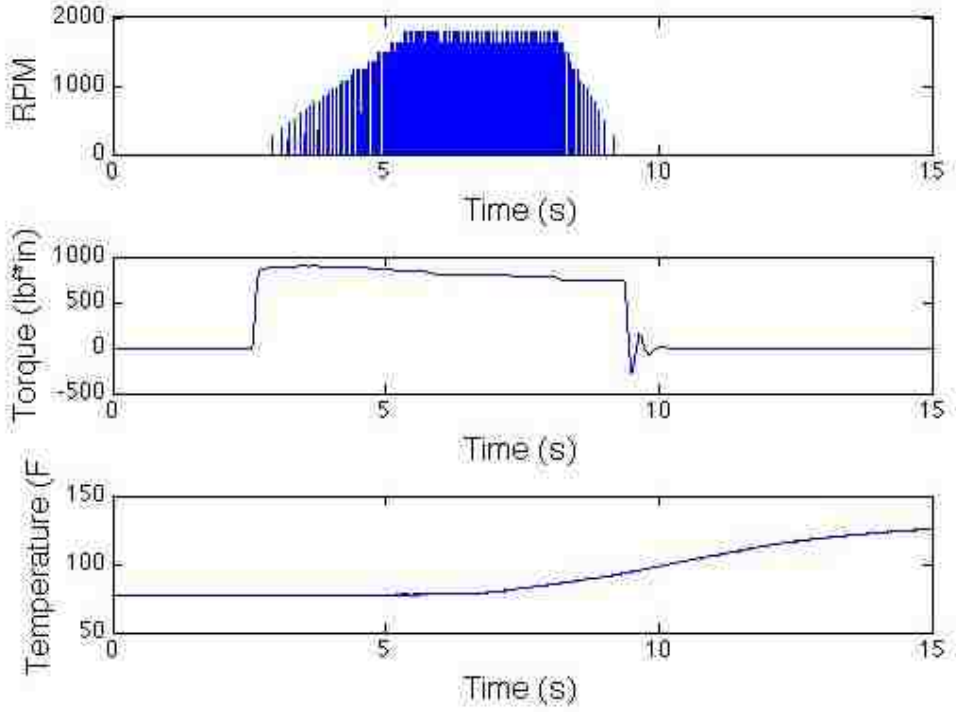

b) 3.5A

Figure 4.9 - Raw rotary vane MREAexperiment data from transmission testing rig for a) 0 A and b) 3.5 A applied current

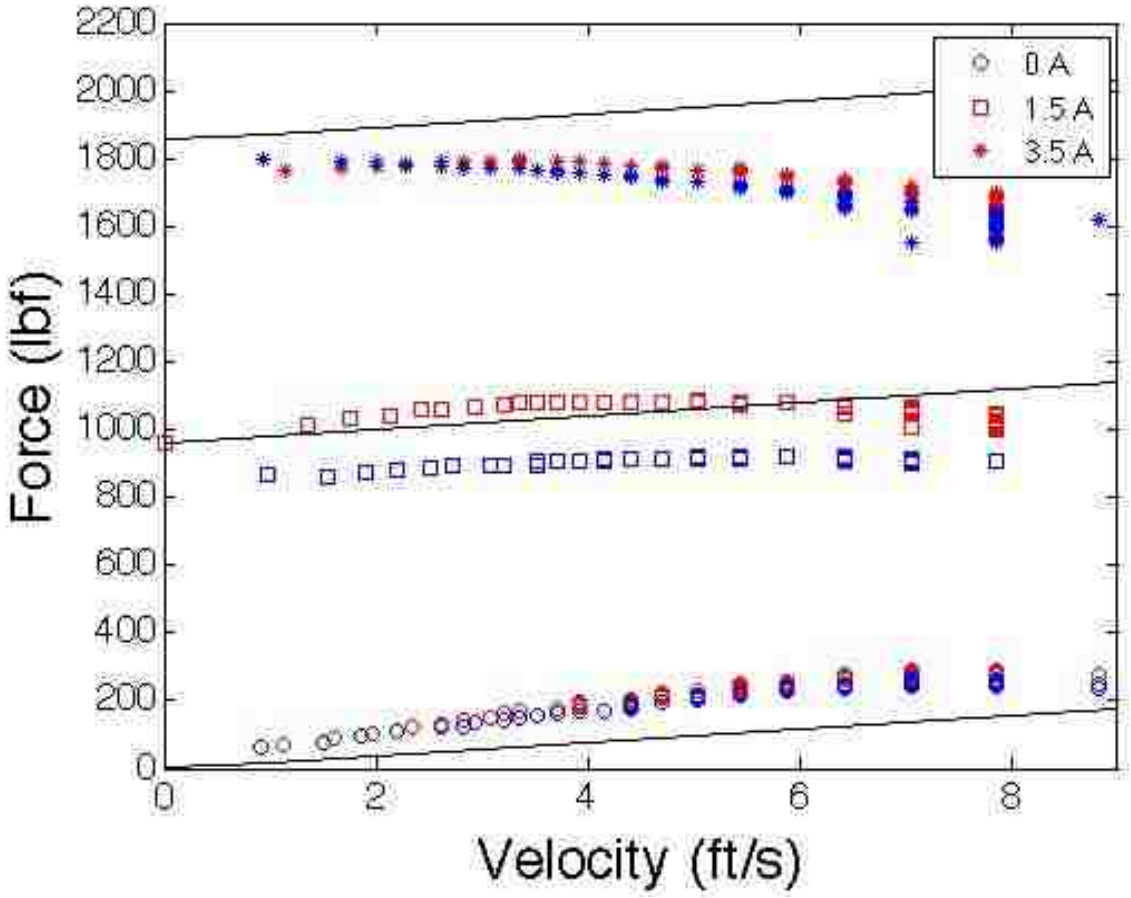

Figure 4.10 - MREA force as a function of velocity and applied current for both rotary vane MREAs (experiment vs. predicted performance)

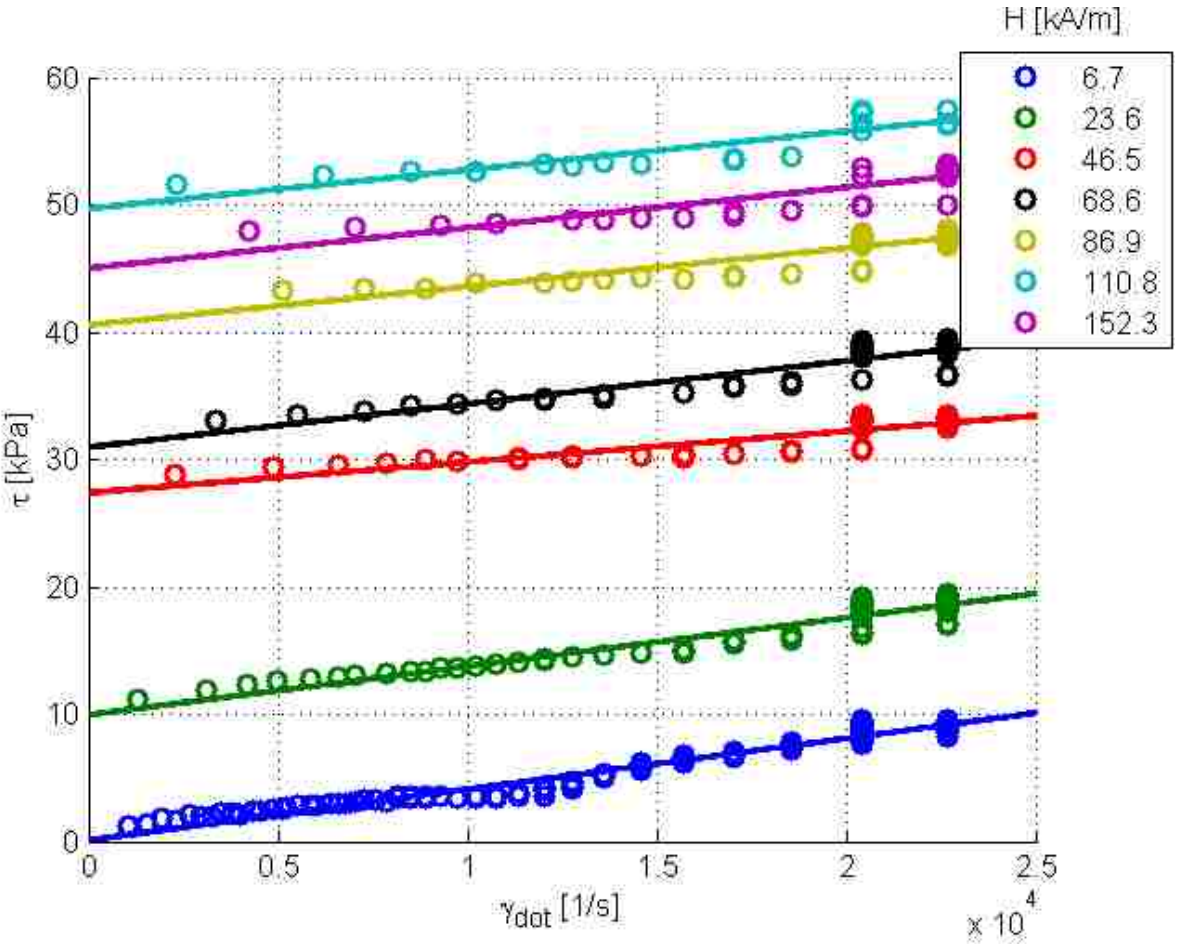

Figure 4.11 - Flow curves for the rotary vane MREA under different applied currents with Bingham plastic curve fits

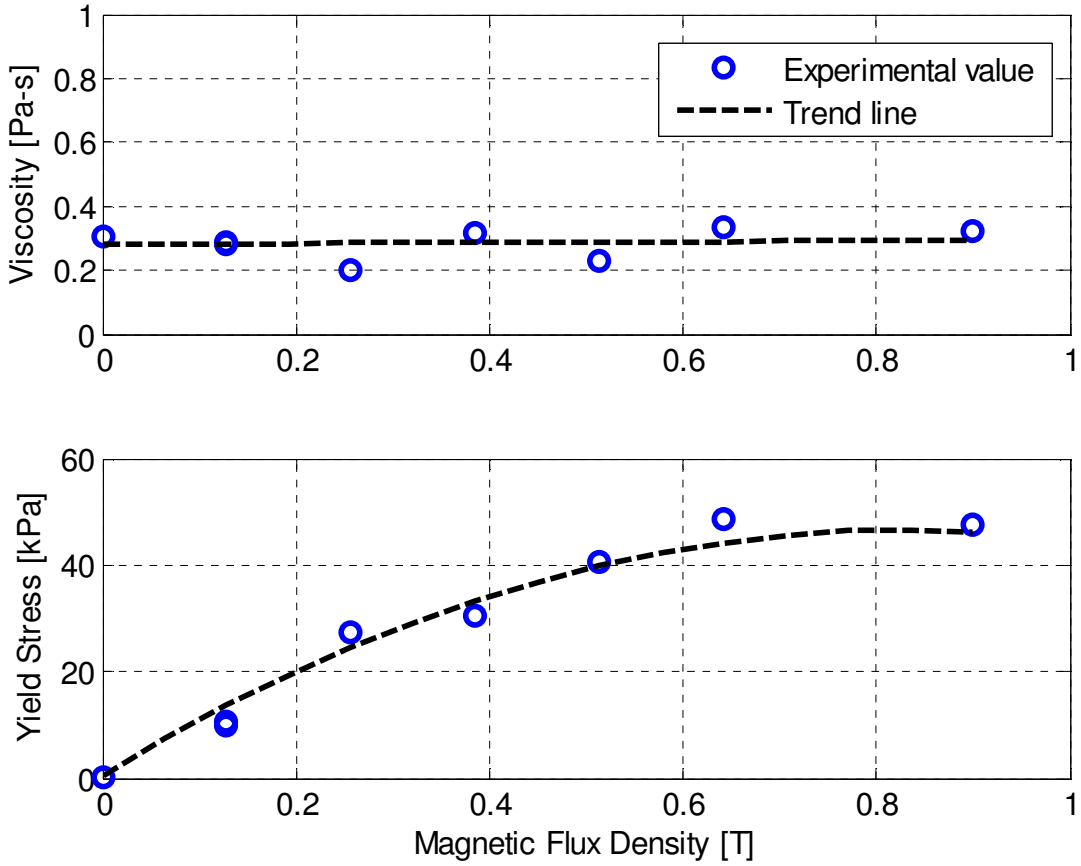

Figure 4.12 - Bingham-plastic stress components versus applied magnetic field in the rotary vane MREA with trends

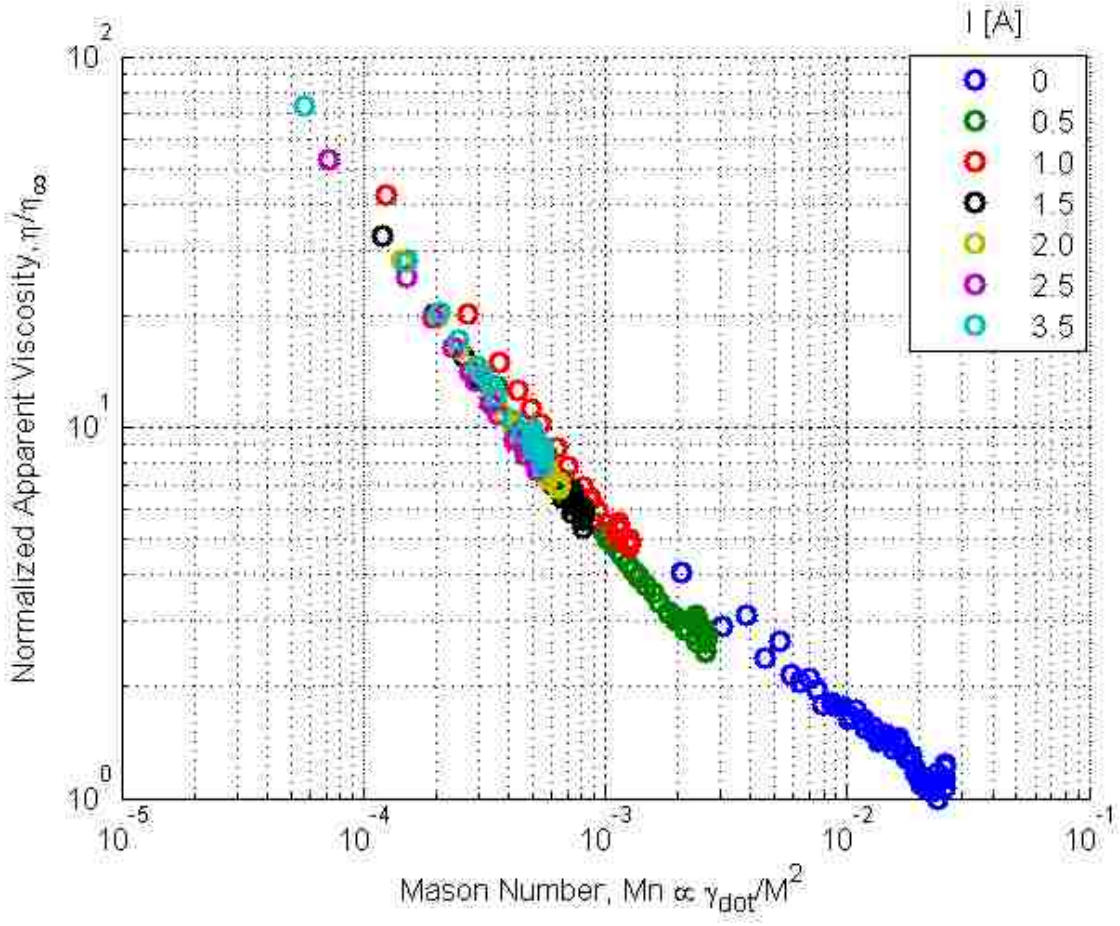

Figure 4.13 - Normalized apparent viscosity versus Mason number for the rotary vane MREA, shear rates up to $\dot{\gamma} = 25{,}000\ s^{-1}$

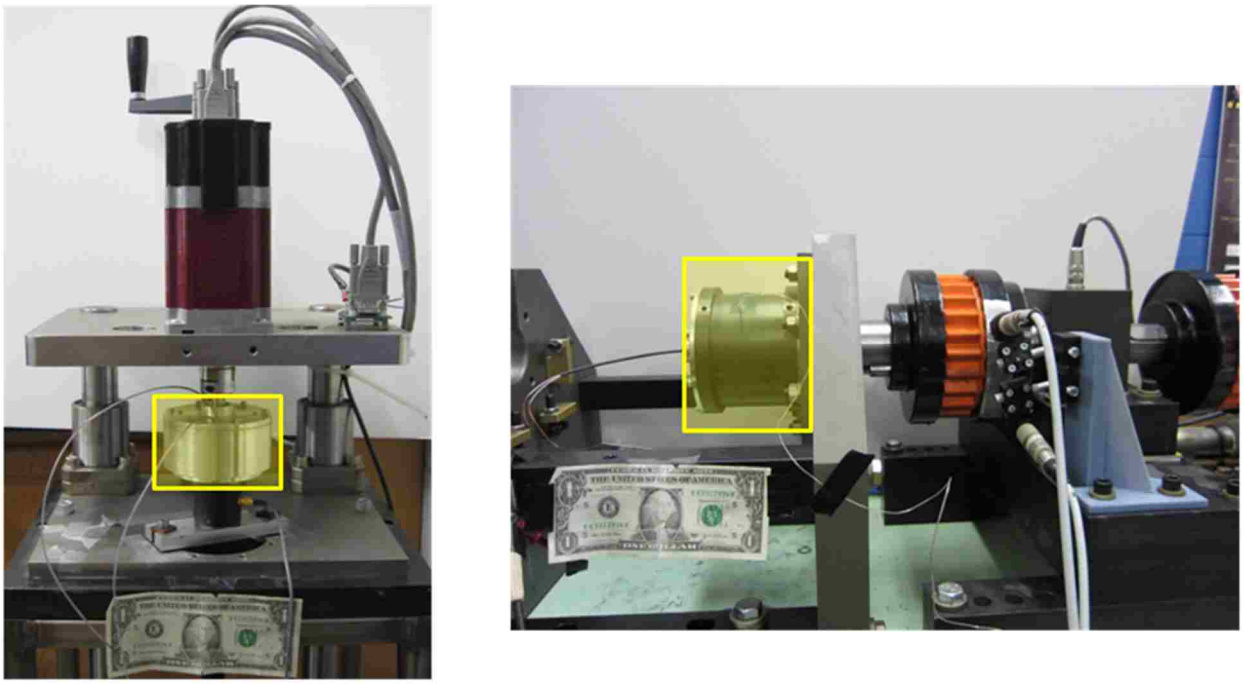

Figure 4.14 - a) Searle cell magnetorheometer and b) rotary vane MREA. The MREA has an operating gap diameter nearly 10X larger than the Searle cell, and generates 15.5 ft-lbs of torque at shear rates up to 25,000 s^{-1} compared to the magnetorheometer's 0.5 ft-lbs of torque at rates up to 10,000 s^{-1}.

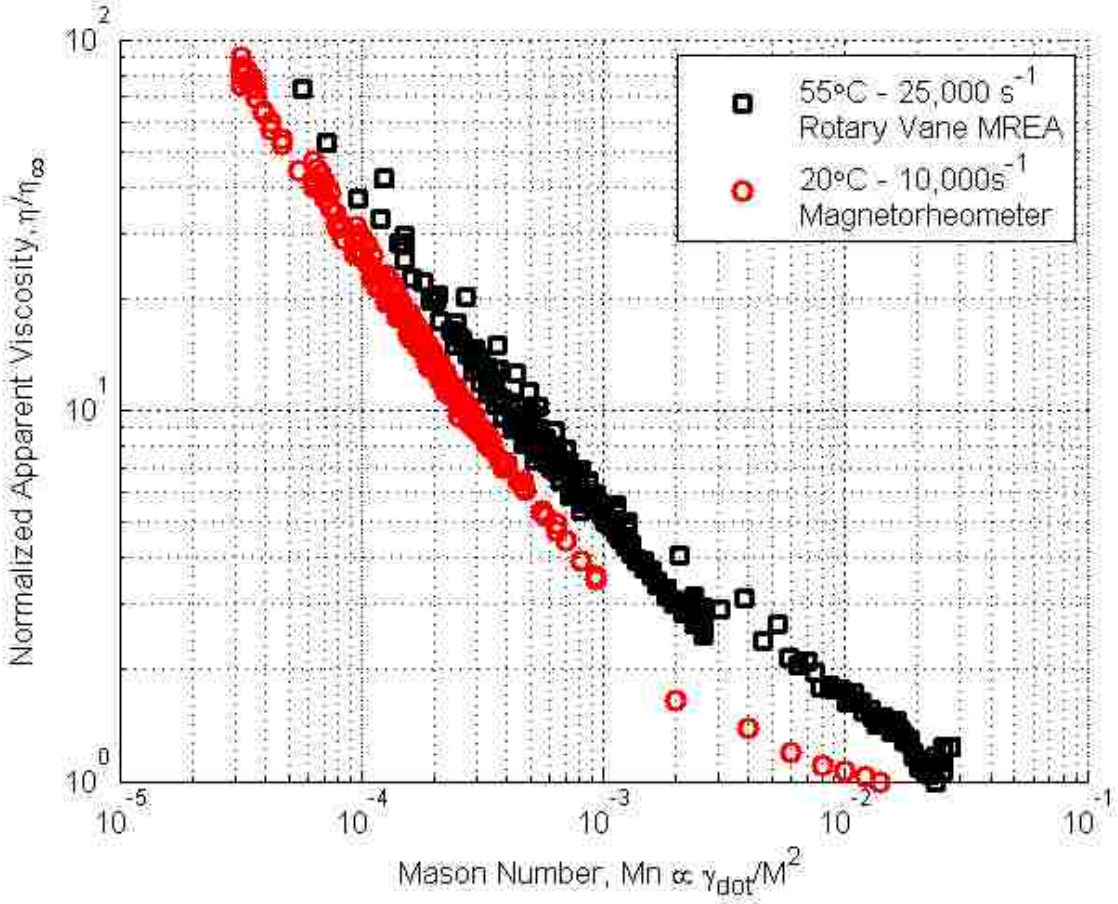

Figure 4.15 - Normalized apparent viscosity versus Mason number for the full scale rotary vane MREA and the instrument scale Searle cell magnetorheometer. Temperature effects are not accounted for, and the curves are not superimposed.

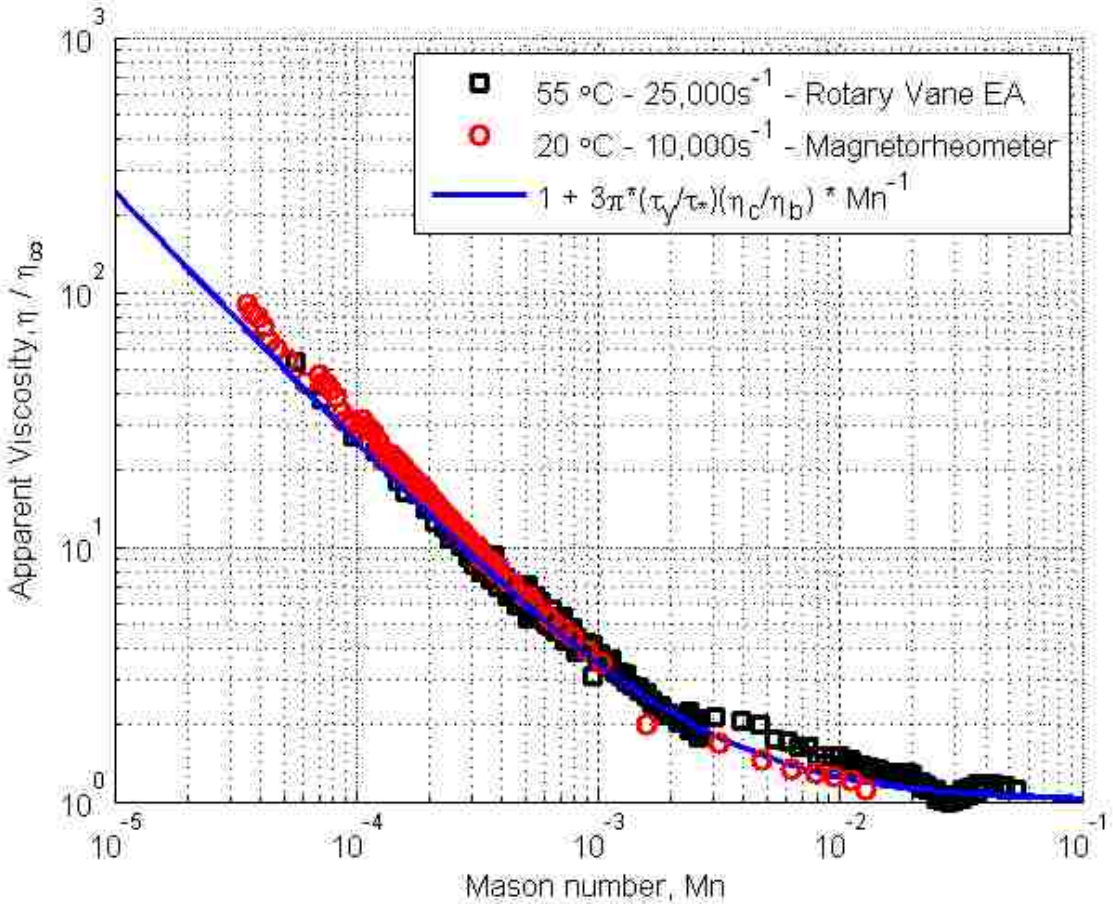

Figure 4.16 - Normalized apparent viscosity versus temperature corrected Mason number for the full scale rotary vane MREA and the instrument scale Searle cell magnetorheometer. Also shown is a curve fit of the form $1 + KMn^{-1}$.

Chapter 5

5. SQUEEZE STRENGTHENING OF MR FLUIDS

5.1. Abstract

This research details a novel method of increasing the shear yield stress of magnetorheological (MR) fluids by combining shear and squeeze modes of operation to manipulate particle chain structures, to achieve so-called compression-assisted aggregation. The contribution of both the nominal active gap size and particle concentration are experimentally measured using a custom-built Searle cell magnetorheometer, which is a model device emulating a rotary Magnetorheological Energy Absorber (MREA). Characterization data from large (1 mm) and small (250 μm) gap geometries are compared to investigate the effect of the gap on yield stress by compression enhancement. Two MR fluids having different particle concentrations (32 vol% and 40 vol%) are also characterized to demonstrate the effect of solids loading on compression-assisted chain aggregation. Details of the experimental setup and method are presented, and a chain microstructure model is used to explain experimental trends. The torque produced by practical rotary MREAs is directly related to the strength of the MR fluid used, as measured by the shear yield stress. This study demonstrates that it is feasible, utilizing the compression-enhanced shear yield stress, to either (1) design a rotary MREA of a given volume to achieve higher energy

absorption density (energy absorbed normalize by device volume), or (2) reduce the volume of a given rotary MREA to achieve the same energy absorption density.

5.2. Introduction

After over sixty years of research in the field, the development of stronger MR fluids for practical applications remains a primary goal since their invention in the 1940's (Rabinow, 1948). The limiting factor with respect to the maximum strength achievable with MR fluids has been the particle saturation magnetization. For example, under a magnetic field of nearly 400 kA/m ($B = 0.5\ T$), a 25 vol% MR fluid containing iron-cobalt particles was shown to produce a yield shear stress of 80 kPa (Ashour et al., 1996). This is about 33% larger as compared to carbonyl iron-based MR fluids, like those used in this study, which provide a yield stress of 60 kPa at the same volume fraction. Obviously, the particle material's magnetic properties can be improved, but provide only modest increases in yield strength. In fact, Ginder and Davis (1994) carried out finite element calculations on single MR fluid particle chains that showed a maximum predicted yield stress of 200 kPa was theoretically achievable, using a highly-loaded 50 vol% fraction at magnetic saturization of iron, 2.1 T. This magnetization is extremely difficult to produce in practice; however, at a more reasonable (but still prohibitive) 1 T, the achievable yield stress is 100 kPa (Ginder and Davis, 1994). This implies that improving the magnetic properties of magnetic particles alone is unlikely to increase the strength substantially and is inherently limited by the maximum force possible within the single chains.

5.2.1. Squeeze Strengthening

This study details a completely different approach to increase the strength of MR fluids by improving the chain microstructure through a process known as compression-assisted aggregation, or squeeze strengthening. Long, thin chains of particles in MR fluids have inferior strength when

compared to thicker, columnar structures in the ideal body centered tetragonal (BCT) arrangement (Gulley and Tao, 1993). This BCT structure can be developed in two ways; shearing for relatively long time scales (Martin et al., 1992; Tao and Jiang, 1994), or compressing the active fluid parallel to the direction of applied field, shown in Figure 5.1. Tang et al. (2000) reported achieving yield stresses up to 800 kPa, over 10 times the value in the absence of compression, by reordering the particle microstructure (Tang et al., 2000). This process is known as compression-assisted aggregation, in which a normal compressive force applied to the active MR fluid rearranges the single chains into BCT columns, shown in Figure 5.1 (Tao, 2001). While their method employed separate compression and shearing steps, combined shearing & squeezing was shown to be a valid mode to form these stronger structures quickly (See et al., 2006).

Additionally, Tao (2001) showed that single particle chains tend to break at their ends, near the magnetic pole surfaces. During compression-assisted aggregation, the single chains not only reorganize into stronger BCT columns, but the bases of these columns near each pole becomes more robust, as seen in Figure 5.2. These robust bases shift the likely breaking point away from the poles, ensuring that the strong BCT column structure is indeed the location that determines the yield stress (Tao, 2013).

Practically speaking, the required amount of compression is provided by normal (or "squeeze") strain, usually created by decreasing the active gap separation. For small initial gaps, such as in the Searle magnetorheometer used in this study, a small absolute change in gap separation produces comparably large strains along the MR particle chains. According to Mazlan et al. (2008), the particle chains in the commercially available fluid from LORD Corporation, MRF-132DG, initiate aggregation around a strain of 0.18, and are completely reorganized into stronger BCT structures above a strain of 0.3, shown in Figure 5.4. Compression speed and magnitude of

magnetic field were shown to have no effect on these results, with one exception. Below $\vec{H}_{crit} \approx$ 50 kA m^{-1}, the particle microstructure is not sufficiently strong to support the internal pressure, so aggregation does not occur (Mazlan et al., 2008).

In the current study, a Searle cell magnetorheometer, which is a model device emulating a rotary Magnetorheological Energy Absorber (MREA), is used to demonstrate the feasibility of utilizing compression-assisted yield stress enhancement to enhance the performance of rotary MREAs. Such a mixed mode rotary MREA that simultaneously exploits direct shear and squeeze modes would enable the development of rotary MREAs that are stronger, lighter, and more compact.

5.2.2. Model Review and Development

Three current models to fit the results of squeeze-strengthening in MR fluid samples will be reviewed, and a new hybrid model is developed by incorporating these and modifying the formulation for a Searle cell geometry. Each model relies on empirical fitting to varying degrees, highlighting the rich possibilities for future research on the underlying mechanisms related to the squeeze strengthening phenomenon.

Tang et al. (2000) provide an empirical expression which includes both the conventional and compression-enhanced components of the MR yield stress, shown below.

$$\tau_y = \tau_c + \tau_{SS} = \tau_y^0 + K_{(H)} P_e \tag{5.1}$$

Here, τ_c is the conventional yield stress, accepted values for which can be obtained from the fluid manufacturer or Carlson's empirical equations (Carlson, 2005). $K_{(H)}$ is a field-dependent, empirical constant which relates the squeeze-strengthened shear stress to the applied normal stress, P_E. This simple expression provides a convenient basis for determining the total increase in

strength within a fluid sample, provided that the normal compressive stress is known (Tang et al., 2000).

A supporting phenomenological model for the squeeze strengthening effect in MR fluids is based on Mohr-Coulomb theory, which shows how the yield shear stress will linearly increase with the normal stress. The model, put forth by Tao (2001), describing the squeeze strengthening phenomenon is detailed below, and a graphical representation of the resulting Mohr's circle is provided in Figure 5.5.

Assuming that the MR fluid is uniform throughout and denoting the three principal axes by $\vec{n}_i(i = 1,2,3)$, we define a stress tensor given by $\tau_{ij}(i,j = 1,2,3)$ that is a combination of the mechanical (viscous stress) and Maxwell (magnetostatic stress) tensors. The normal stress σ_n and shear stress τ_n on the plane with normal direction $\vec{n}$ are given as follows.

$$\sigma_n = \sum_{ij} \tau_{ij} n_i n_j \tag{5.2}$$

$$\sigma_n^2 + \tau_n^2 = \sum_{ijl} \tau_{ij} \tau_{il} n_{jl} \tag{5.3}$$

If the eigenvalues of τ_{ij} are $\sigma_1 \geq \sigma_2 \geq \sigma_3$, then equations (5.2) and (5.3) can be rewritten as

$$\sigma_n = \sigma_1 n_1^2 + \sigma_2 n_2^2 + \sigma_3 n_3^2 \tag{5.4}$$

$$\sigma_n^2 + \tau_n^2 = \sigma_1^2 n_1^2 + \sigma_2^2 n_2^2 + \sigma_3^2 n_3^2 \tag{5.5}$$

Graphically, points $(\sigma_2 + \sigma_3)/2$, $(\sigma_1 + \sigma_3)/2$, and $(\sigma_1 + \sigma_2)/2$ are drawn as the centers of circles with radii $(\sigma_2 - \sigma_3)/2$, $(\sigma_1 - \sigma_3)/2$, and $(\sigma_1 - \sigma_2)/2$, respectively. The area confined by the largest circle and the two inner circles defines all possible values of σ_n and τ_n (Vyalov, 1986).

In the case of squeeze strengthened MR fluids the yield stress before compression, τ_c is represented in Figure 5.5 by the distance ON. A line tangent to the largest circle and passing through N is drawn to locate the maximum allowed value of shear stress τ_n, represented by point M. The angle ϕ between line NM and the horizontal provides an relationship between the squeeze strengthening component of total yield stress τ_y^{SS} on the compressive stress σ_n as follows.

$$\tau_{SS} = \sigma_n \tan\phi \tag{5.6}$$

Therefore, an expression for the total yield stress, increased by squeeze-strengthening, can be written as shown below.

$$\tau_y = \tau_c + \tau_{SS} = \tau_c + \sigma_n \tan\phi \tag{5.7}$$

This is the Mohr-Coulomb formula, where $\tan\phi$ can be thought of as the 'internal friction' coefficient. Comparing this phenomenological model with the two-term empirical model in equation (5.1), it is clear that the $\tan\phi$ term serves the same role as the proportional constant $K_{(H)}$ in relating the applied compressive stress to the enhanced yield stress exhibited in squeeze-strengthened MR fluid tests (Tao, 2001).

A third model incorporating tribology theory is presented by Zhang et al. (2004). It accounts for the fact that particles in compression exhibit some deformation, increasing the interparticle contact area and the friction between particles linearly with the applied load. Defining a ratio C of the shear stresses transmitted by the interfacial film, τ_f, and particle, τ_0, provides the expression below relating the applied squeeze stress to the interparticle shear stress.

$$\tau_f = \frac{C}{[\alpha(1-C^2)]^{1/2}}\sigma \tag{5.8}$$

Here, α is the ratio of the squares of sliding stress, σ_s^2, and particle shear strength, τ_0^2. Again, this factor is similar to $\tan\phi$ in Tao (2001), but now accounts for the influence of the fluid film between particles. Additionally, an empirical contribution coefficient is required to match the model predictions with the experimental data. This empirical contribution coefficient is cast as a function of both applied magnetic field and squeeze stress intensity (Zhang et al., 2004).

The model developed in the present research combines the stress vector sum from the Mohr-Coulomb phenomenological model and the field- and squeeze stress-dependent contribution coefficient used in the tribological model. The compression-enhanced shear stress is written as the sum of the conventional yield stress and the squeeze-strengthened stress, each modified by a contribution coefficient, shown below.

$$\tau_y = K_1\tau_c + K_2\tau_{ss} \tag{5.9}$$

The vector sum of these forces taken over the entire Searle cell surface provides a model for the total stress within the MR fluid sample, which can be compared with experimental measurements.

$$F_{total}^2 = F_\tau^2 + F_\sigma^2 \tag{5.10}$$

Equations (5.9) and (5.10) are related by the fact that any stress is merely force per unit area. A schematic section of the eccentric Searle cell magnetorheometer is presented in Figure 5.6, along with the shear, compressive, and resultant total force vector components as described in the following derivations.

The squeeze strain, ε_s, is calculated as the ratio of eccentricity, ϵ, to gap height, h, shown in the equation below.

$$\varepsilon_s = \frac{\epsilon}{h} \tag{5.11}$$

Since the eccentric geometry of the custom Searle cell used in this experiment causes the gap size to change in a periodic fashion, we begin with defining gap height as a function of the angular position of the bob and strain, as shown in the following expression.

$$y = h(1 - \varepsilon_c \cos \boldsymbol{\theta}) \tag{5.12}$$

The force due to shearing on a differential element is derived as follows, substituting equation (2.5) for the shear rate.

$$dF_\tau = \tau_c \, dA = \eta\dot{\gamma} \, L_c(R + h)\boldsymbol{d\theta}$$

$$= \eta \frac{\boldsymbol{v}}{y} \, L_c(R + h)\boldsymbol{d\theta}$$

$$dF_\tau = \eta\boldsymbol{\omega} \frac{R}{h(1 + \varepsilon_s \cos \boldsymbol{\theta})} L_c(R + h)\boldsymbol{d\theta} \tag{5.13}$$

Here, the apparent viscosity is a function of shear rate and applied magnetic field, $\eta\left(\dot{\gamma}, \vec{H}\right)$. It's interesting to note that an eccentric bob produces larger torque due to pure shear stresses than a perfectly centered geometry, and larger eccentricities correspond to larger torques. This indicates that even without compression-assisted aggregation of MR chains, an eccentric geometry produces increased passive shear stresses (Meena and Kandaswamy, 1999; Escudier et al., 2002).

Similarly, the force due to compression from the changing gap size, or squeeze force, is

$$dF_\sigma = \sigma_S \cdot A = G\Delta y \, L_c(R + h)\boldsymbol{d\theta} = -G\left(y_i - y_f\right) L_c(R + h)\boldsymbol{d\theta}$$

$$= -G\left(h - h(1 - \varepsilon_s \cos \boldsymbol{\theta})\right) L_c(R + h)\boldsymbol{d\theta}$$

$$dF_\sigma = G(\varepsilon_s \cos \boldsymbol{\theta}) L_c(R + h)\boldsymbol{d\theta} \tag{5.14}$$

where the modulus is a function of the squeeze strain, $G(\epsilon)$, adapted from Mazlan et al. (2008). Equations (5.13) and (5.14) provide the fluid force transmitted to the cup as a function of rotation

angle, and can be integrated over the active area to generate estimates of the conventional and squeeze-strengthened yield stress components. In the previously developed models, the conventional yield stress term is left unmodified. However, the presence of eccentricity increases the conventional yield stress, so in the hybrid model the contribution coefficient K_0 is between 0 and 1; 0 indicating pure squeeze force, increasing up to 1 when the maximum eccentricity is reached. In the current experiment, real-time eccentricity measurement was not achievable, so the contribution coefficient K_0 is less than 1 when $\vec{H}_{crit} \leq 50[\frac{kA}{m}]$, and $K_0 = 1$ when $\vec{H}_{crit} > 50[\frac{kA}{m}]$.

Additionally, the present hybrid model, shown in the following expression, modifies the squeeze-strengthened component by a magnetic field-dependent quadratic term of contribution coefficients.

$$\tau_y = \tau_c \, K_0 + \tau_{ss} \, (K_1 H^2 + K_2 H) + K_3 \tag{5.15}$$

The first term in this qualitative expression, K_1, reflects the dependence of the interparticle magnetostatic force on the square of magnetization, and the second term K_2 shows that, like other models, the squeeze-strengthened stress component is linearly proportional to the magnitude of H. The third contribution coefficient, K_3, shifts the critical field strength, H_{crit}, and is consistent with previous research and present observations.

5.2.3. Squeeze-strengthening Searle cell magnetorheometer

A modified version of the custom Searle cell magnetorheometer from previous chapters was used in this study to provide reliable shear strain rate and shear stress measurements. As shown in Figure 5.7, the magnetorheometer consists of a steel flux path surrounding the electromagnetic coil, seated within a nonmagnetic cup. MR fluid samples are loaded into the central fluid chamber, and a modified steel bob is lowered into position and supported by a rotary ball bearing at the top and an additional sealed precision bearing at the bottom. The bob is modified with an 8 mm diameter

shaft extending from the base, which is inserted into the bottom bearing to provide a double cantilever support condition to the bob. Identical data acquisition and control systems are used in this setup, along with the cooling coil to provide temperature control and stabilization.

In the absence of an applied magnetic field, the rotating bob tends to be self-centering. However, when a large magnetic field is applied, the center position is an unstable equilibrium point, and so a slight deviation from the axis of the magnetic field results in the bob contacting the outer wall. The offset between the bob center and the MR cell center axes is referred to as eccentricity. Within the precision bearings themselves, there exists a small space between the balls and the race that contains them, otherwise known as radial slop. The amount of radial slop is inherent to the particular size and precision of the rotary bearing. To prevent contact due to this field-induced eccentricity, a sealed miniature precision bearing was used to affect a hard limit to the maximum eccentricity of the bob within the MR cell.

This modified Searle cell device uses eccentricity to provide shear and squeeze forces simultaneously to active MR fluid through this simple mechanism, taking advantage of small active gap sizes and high shear rate capability. By changing the aggregate microstructure in active MR fluids, their yield strength properties can be enhanced, and hybrid shear-squeeze mode MREAs for crashworthy systems can be made even smaller and more powerful than their pure shear mode counterparts.

5.2.4. Experiment

In the current study, a known eccentricity was introduced to the bob, which created a periodic change in MR gap as the bob rotates. The rotary bob is also pulled out of alignment with the cell rotational axis in strong magnetic fields, imparting a normal force on the active MR fluid. In the

narrowest nominal gap size used (25 particle diameters), this simultaneous normal force, bob eccentricity, and high shear rate provide the strain (normal and shear) required to reorient the particle chains into more robust BCT columns and high shearing rate, which increases the apparent yield stress of the MR fluid. Figure 5.8 demonstrates how the same bob eccentricity produces a larger compressive strain in a narrower gap.

Two different combinations of bob size and support conditions were used to evaluate the effect of squeeze-strengthening in MR fluid samples having different solids loading. The eccentricity is defined as the offset distance between the bob axis and the MR cell center axis. The nominal cell geometry and bob/bearing combinations are given in Table 5.1. This nominal geometry is altered when the magnetorheometer is operated, due to the offset servomotor and the applied magnetic field. This offset causes the bob to precess with a frequency equal to its rotation; if it were not for the supporting bearings, the bob may actually roll around the inside of the cup. Different support bearing arrangements with each bob size produce eccentricities ranging from 0.01 – 0.122 mm, which corresponded compressive strains ranging from 0.07 – 0.30. This periodic eccentricity is measured using a precision dial indicator mounted to the instrument base, as shown in Figure 5.11.

Table 5.1 – Squeeze strengthening Searle cell geometry for 1 mm and 0.25 mm gap configurations

Geometric Feature		**Value [m · 10^{-3}]**	
Bob radius, R		8.0	8.75
Gap height, h		1.0	0.25
Total gap length, L_c		12.0	
Bob/bearing combination		**Max Eccentricity, ϵ [m·10^{-6}]**	**Strain, ε_s**
A	8 mm bob, no bearings	122	0.12
B	8.75 mm bob, both bearings	76.2	0.30

From equation (5.11) the same eccentricity in a narrower gap will apply more squeeze strain to the MR chains. With the 8 mm bob, nominal shear rates over 2,500 s^{-1} are achieved. With no support bearings, this bob is free to deflect from the central axis up to 0.122 mm and produce a compressive strain on the active MR fluid within the gap of <0.15. Attaching the 8.75 mm bob and seating it in both top and bottom bearings maintains a field-independent eccentricity and strain of $\varepsilon_s < 0.30$ and nominal shear rates over 10,000 s^{-1}.

From equation (5.13), it can verified that increasing bob eccentricity corresponds to increasing torque due to shear forces, in support of the simulations presented by Escudier et al. (2002). Figure 5.9 shows the shear force applied on a differential element of the MR cell cup as a function of angular position for a perfectly centered bob, as well as the two eccentricity and gap size

combinations (A and B) used in the experiments. The total force due to this shear stress is calculated as the definite integral over one rotation period, $0 - 2\pi$, shown in the following expression.

$$F_\tau = \int_0^{2\pi} \tau_c dA = \eta \boldsymbol{\omega} \frac{R}{h} L_c (R + h) \int_0^{2\pi} \frac{1}{1 - \varepsilon_s \cos \boldsymbol{\theta}} d\boldsymbol{\theta} \quad \textbf{(5.16)}$$

Figure 5.10 shows the increase in the conventional shear stress as the eccentricity increases. The contribution coefficient, K_0, is determined from this increase to modify the conventional shear stress accordingly.

Based on the cell geometry, the rotation rate input, and torque output, knowledge of the nominal shear flow can be extracted according to Choi et al. (2005) and Hu and Wereley (2011) using equations (2.1) and (2.5):

$$\tau = \frac{M}{2\pi L_c (R + h)^2} \quad \textbf{(5.17)}$$

$$\dot{\gamma} = \frac{R}{h} \omega_i \quad \textbf{(5.18)}$$

Here M is the measured torque output, L_c is the active gap length, h is the nominal active gap height, and R is the bob radius. For the purposes of this investigation, the deviation from the nominal geometry is not accounted for here in order to characterize the "average" fluid response.

Comparing these dimensions and strain values to those reported by Mazlan et al. (2008), it is clear that for the 1 mm gap, single chains should be the dominant structure, while for the 0.25 mm gap, compression-assisted aggregation to BCT columns should occur. Though the strain is periodic (meaning for each compression there is an equal extension), there is no reported mechanism by

which extensional strain would change BCT columns into single chains, i.e. once aggregate columns are formed by compression, the columns persist until the field is removed.

5.3. Results

An example of one set of raw test data is shown in Figure 5.12. Current is applied to the coil before beginning the test, and an increasing angular velocity staircase profile is commanded to the servomotor. Data from the last 75% portion of each step is averaged to generate a sample flow curve consisting of quasi-steady measurements.

This flow curve is then passed to a least-squares curve fit routine which identifies each of the three Herschel-Bulkley parameters (Chaudhuri et al., 2006). In this study, the MR yield stress is of primary concern and will be the only parameter investigated, though (Becnel et al., 2012) presents more in-depth characterizations of the consistency and flow index parameters.

5.3.1. Single parameter empirical model

Figure 5.13 shows the resulting Herschel-Bulkley yield stress for MRF-132DG using setup A at three different temperatures and how it compares to published manufacturer's data for that fluid, reported for and operating temperature of 40 °C. This shows that the yield stress behaves as expected, even as the fluid is exposed to compressive strains up to 0.12. Recall from Figure 5.4 that this range of compressive strain is supported by the particle chains without causing aggregation into BCT columns, hence this can be considered the conventional yield stress behavior.

Comparing this to the fluid tested using setup B, a 0.25 mm gap with a squeeze strain $\varepsilon_s = 0.30$, it is clear that compression-strengthening of the particle structures has occurred. It can also be seen that above the previously reported field strength of 50 kA/m is when aggregation effects

become apparent. Figure 5.14 shows the total yield stress increases by over 50% near the saturation magnetization for the range of temperatures tested.

To investigate the contribution of squeeze strengthening to the overall yield stress, we employ equation (5.1) and find the difference between the measured yield stress in each setup and the conventional yield stress reported by the manufacturer. This result is shown for tests run at 51.7°C for purposes of comparison. A first order trend line is fit to the data points corresponding to applied fields above H_{crit} = 50 kA/m, and the results are shown in Figure 5.15.

For setup A, corresponding to compressive strain up to 0.12, the magnitude of the "additional" yield force – that is, beyond the yield force observed for pure shearing – is less than 10 kPa at the highest applied fields. In contrast, for setup B, corresponding to a compressive strain up to 0.30 and column aggregation, the compression strengthening effect increases the apparent yield stress by nearly 35 kPa, or 77% above the published yield stress.

To compare the effects of particle volume fraction on this aggregation effect, similar tests were performed on LORD MRF-140CG fluid using setup B, shown in Figure 5.16. While no reports on the compressive strain required to initiate particle chain aggregation for this 40 vol% MRF were available, it is shown that the squeeze strengthening can be achieved using a similar strain magnitude of 0.30 (Mazlan et al., 2008). Again, the squeeze strengthening effect becomes apparent above applied magnetic fields of 50 kA/m.

Figure 5.17 compares the absolute magnitude of the squeeze strengthened component of yield stress for MRF-132DG and MRF-140CG, and reveals the potential for employing the same method of squeezing stress application to different fluids.

An analysis similar to that performed by Tang et al. (2000) shows that, assuming a compressive strain of ε_s = 0.3 corresponds to a compression stress P_e = 40kPa from Mazlan et al. (2008), the slope of $K_{(H)}$ for MRF-132DG matches well with the reported values of ε_s = 0.221-0.267, shown in Table 5.2.

Table 5.2 – Squeeze-strengthening coefficients for 32 vol% and 40 vol% MR fluids

Fluid Sample, at P_e = 40 kPa	Slope of $K_{(H)}$
MRF-132DG	0.239
MRF-140CG	0.490

From this analysis, the squeeze strengthening effect is more pronounced at higher particle concentrations for the same applied field. A clearer comparison between the two fluids may be obtained by finding the increase in yield stress as a percent of the conventional shearing-only yield stress, shown in Figure 5.18. This presents a similar picture, showing that the squeeze strengthened yield stress as fraction of total yield stress is indeed higher for the higher particle concentration fluid, though the trend appears to have the same slope. This could be explained by realizing that because there are more particles per volume, the force required to yield and rearrange them would be proportionally larger at the same applied field strength.

5.3.2. Hybrid phenomenological model

Using the hybrid phenomenological model developed for an eccentric Searle cell geometry, presented previously as equation (4.1), the four contribution coefficients can be found using a least-squares curve fitting technique. Table 5.3 presents the empirical contribution coefficients used in this model.

The model fit for MRF-132DG is shown in Figure 5.19, along with the experimentally measured total yield stress and the conventional yield stress reported by LORD Corporation.

Table 5.3 - Contribution coefficients for the hybrid phenomenological model

Fluid Sample, at ε_s= 0.30	K_0	K_1 $[10^{-3}\frac{m^2}{A^2}]$	K_2 $[\frac{m}{A}]$	K_3 $[10^3]$
MRF-132DG	1	-1.3	0.75	-4.3
MRF-140CG	1	-5.5	1.7	-6.0

The yield stress below H_{crit} = 50 kA/m is purely due to the conventional mechanism and the eccentricity of the bob, as fields below this have been shown to be insufficient to support the reorganization of single chains into BCT columns. Figure 5.20 shows the conventional, measured, and modeled yield stresses for MRF-140. A similar regime border can be seen near the H_{crit} = 50 kA/m field strength. Clearly the increase in yield stress above H_{crit} appears to be quadratic with respect to the applied field, which can qualitatively be related to the source of this squeeze-strengthening phenomenon. The interparticle attractive force is proportional to H^2 according to the standard dipole approximation (Sherman and Wereley, 2013).

5.4. Conclusions

This research details a novel method of increasing the shear yield stress of magnetorheological (MR) fluids by combining shear and squeeze modes of operation to manipulate particle chain structures, to achieve so-called compression-assisted aggregation. The contribution of both active gap separation and particle concentration are experimentally measured using a custom-built Searle cell magnetorheometer, which is a model device emulating a rotary Magnetorheological Energy Absorber (MREA). Eccentricity was imparted to the rotating bob of the magnetorheometer to squeeze strengthen the active fluid and increase the available yield stress. This combined shear

and squeeze mode operation causes linked MR particles to transition from single chains into comparably stronger columns, thereby increasing the shear stress required to cause yielding.

By utilizing narrow active gaps, even a small amount of eccentricity provides the compressive strain required to reorient the particle chains into aggregated BCT columns. Squeeze strengthening of the MR fluid test samples was found to occur only for cases when the applied field exceeded 50 kA/m, which is in agreement with the results presented in Mazlan et al. (2008). The eccentricity was shown to be manageable and field-independent by using precision support bearings at both shaft ends of the rotating bob.

Particle volume concentration appears to influence the degree to which squeeze strengthening increases the total yield stress, with higher particle fractions corresponding to larger squeeze strengthened yield stress components. However, the trend of the field-dependent increase is roughly the same for both MRF-132DG and MRF-140CG, indicating that the mechanism by which squeeze strengthening occurs is the same in both fluids.

A four parameter hybrid phenomenological model relating the shear and squeeze forces generated by an eccentric Searle cell was developed. Taking the vector sum of these component forces, when integrated around the entire cell geometry, results in an estimate of the yield stress increase due to the aggregation of single particle chains into stronger BCT columns with robust ends.

The dial indicator used necessarily applied a slight lateral force due to the internal spring mechanism, designed to ensure contact with the bob's surface. In the future, an improved method of eccentricity measurement using a non-contact magnetostrictive sensor would provide a valuable improvement in the precision of the test conditions. Alternatively, non-circular bob geometries are

proposed that eliminate the requirement that the rotating element be eccentric, while still providing the normal and shear stresses simultaneously.

This study demonstrated that it is feasible, utilizing combined shear-squeeze mode operation to provide compression-enhanced shear yield stress, to either (1) design a rotary MREA of a given volume to achieve higher energy absorption density (energy absorbed normalize by device volume), or (2) reduce the volume of a given rotary MREA to achieve the same energy absorption density.

Currently, practical MREAs have found limited adoption in aerospace systems, since size and weight are primary concerns. Squeeze-strengthening in MR fluid devices offers a simple and promising solution to expand their design applications and improve adaptive energy absorption system performance.

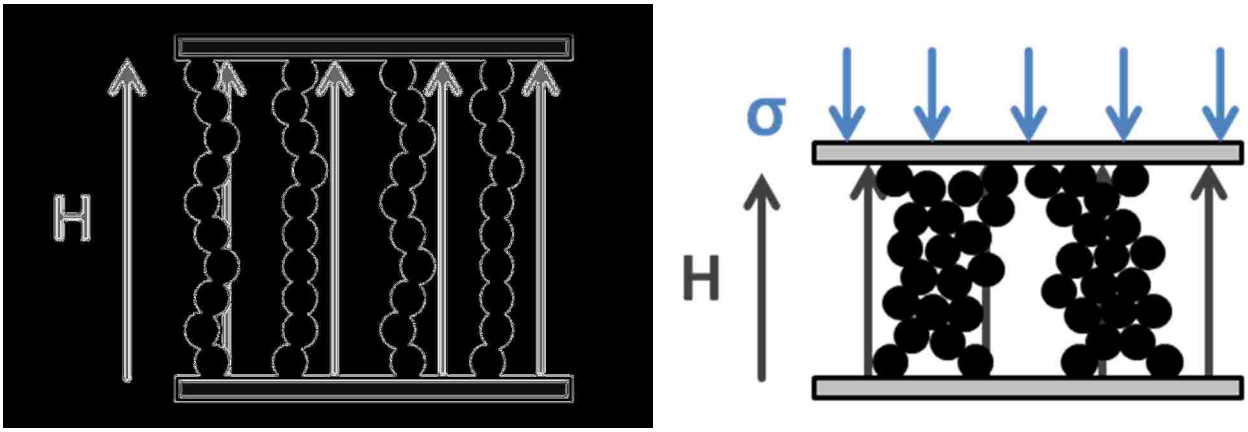

a) b)

Figure 5.1 – a) Single chains of active MR fluid and b) "squeeze-strengthened" MR fluid exhibiting BCT columns with robust ends

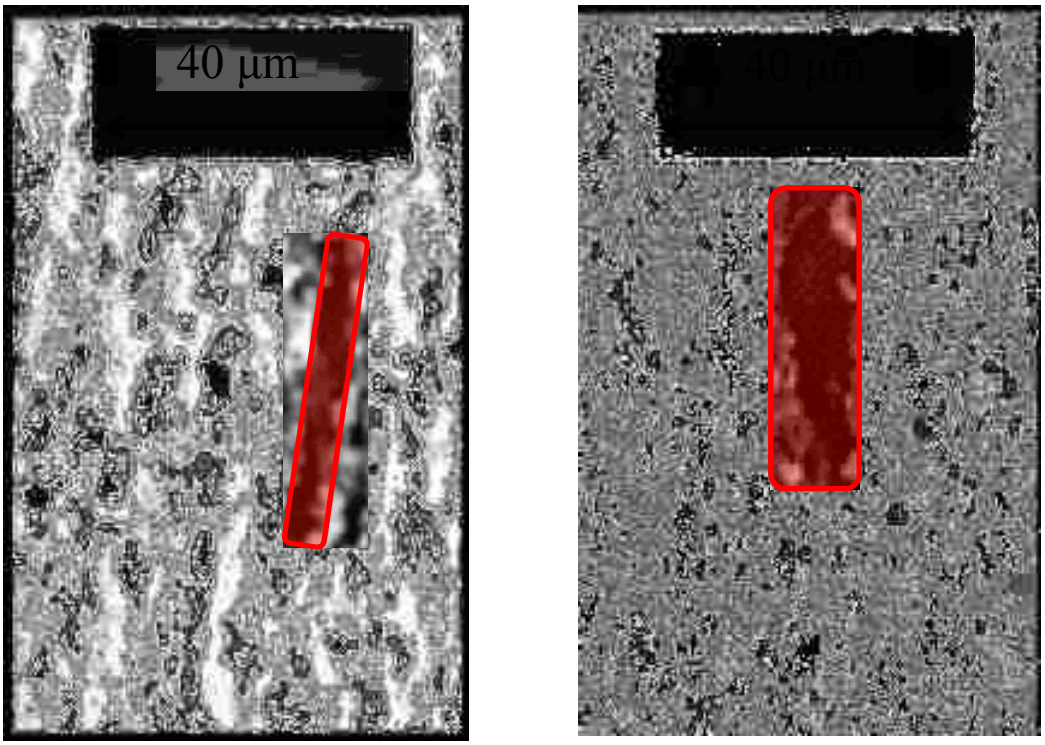

a) b)

Figure 5.2 - Micrograph of a) single chains in conventional MR fluid and b) BCT column structures in squeeze-strengthened MR fluid, adapted from (Tao, 2001).

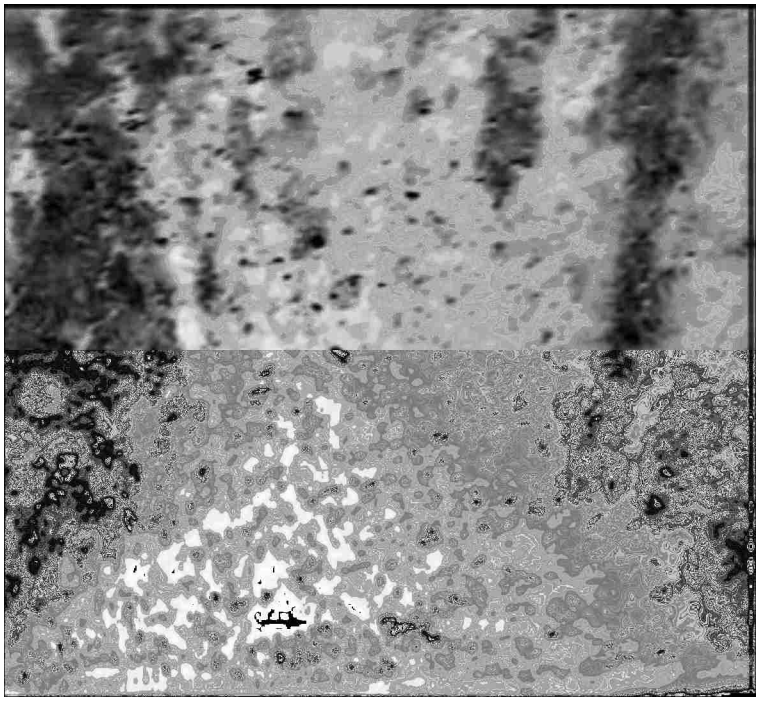

Figure 5.3 - Micrograph of robust column ends in squeeze-strengthened MR fluid, adapted from (Tao, 2001).

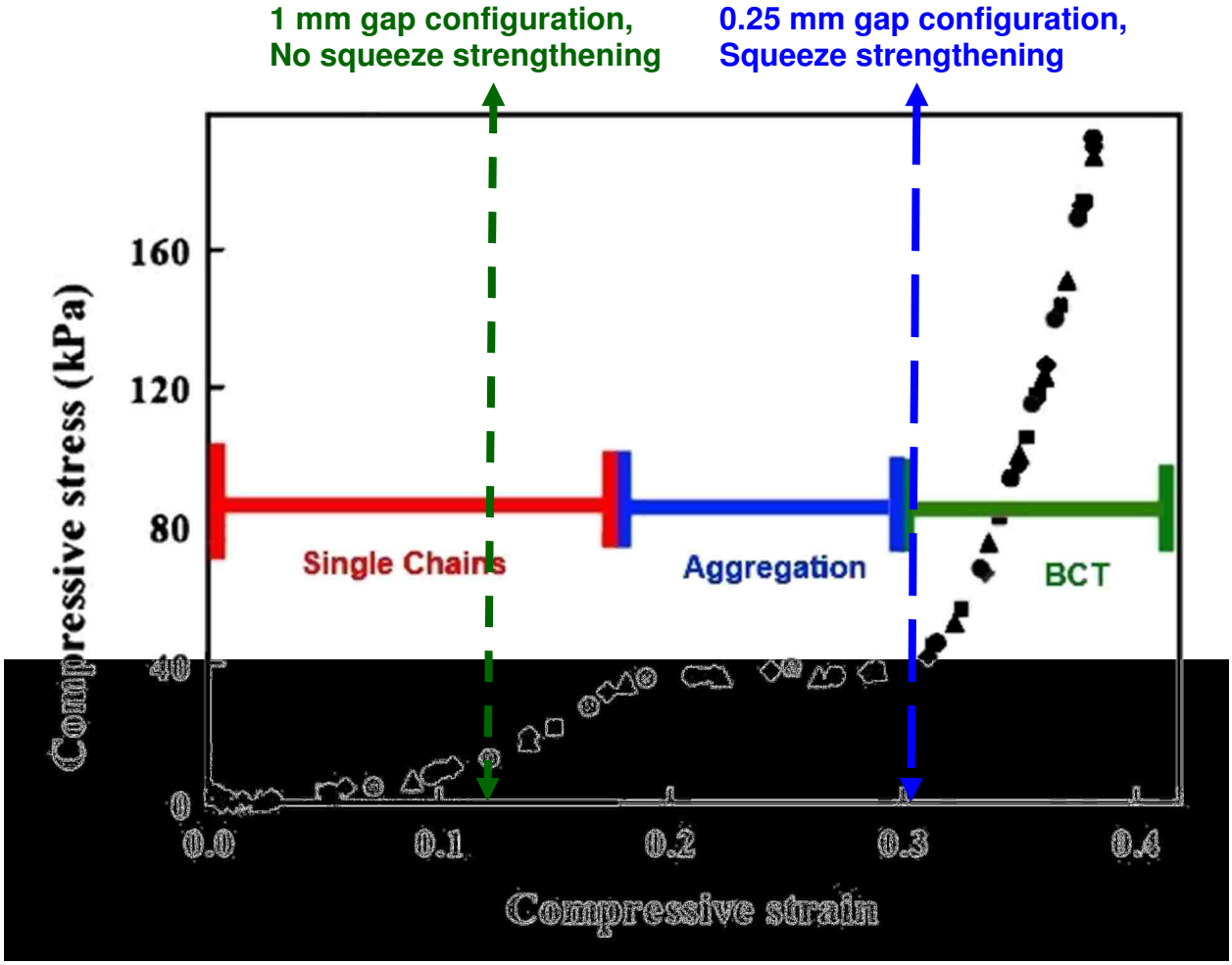

Figure 5.4 – Squeeze stress versus squeeze strain for LORD MRF-132DG, adapted from Mazlan et al. (2008).

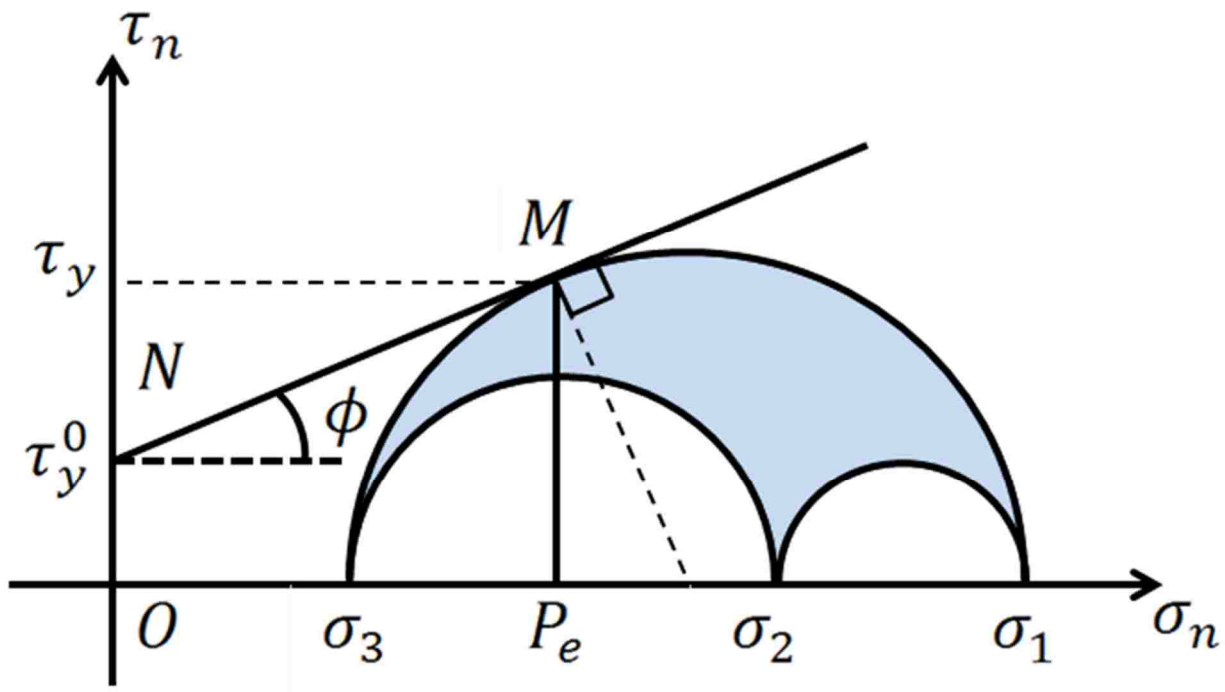

Figure 5.5 – Mohr's circle diagram to find the total yield stress in a squeeze strengthened MR fluid. Line ON represents the nominal yield stress, τ_y^0, and line NM is tangential to the largest circle such that $\tau_y^{SS} = \sigma_n \tan \phi$ and $\tau_y = \tau_y^0 + \tau_y^{SS}$.

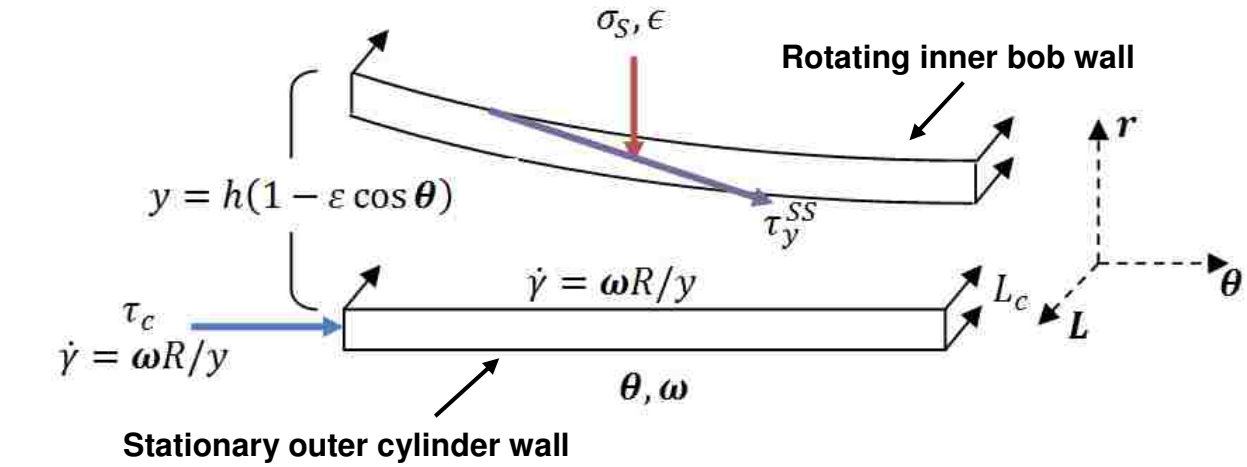

a)

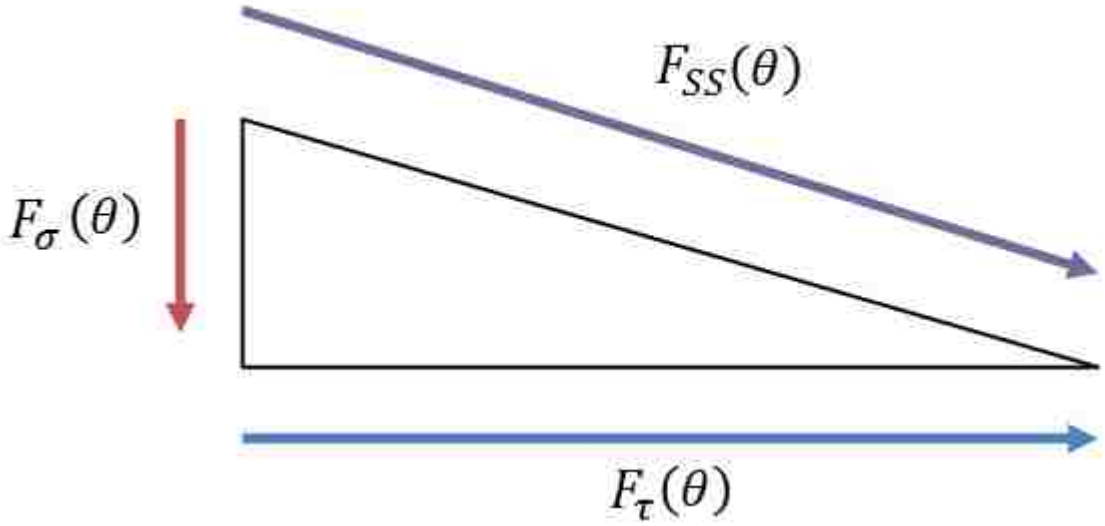

b)

Figure 5.6 - a) Differential force terms on a unit length eccentric Searle cell geometry, and b) vector sum of squeeze force and shear force components, squeeze-strengthened force.

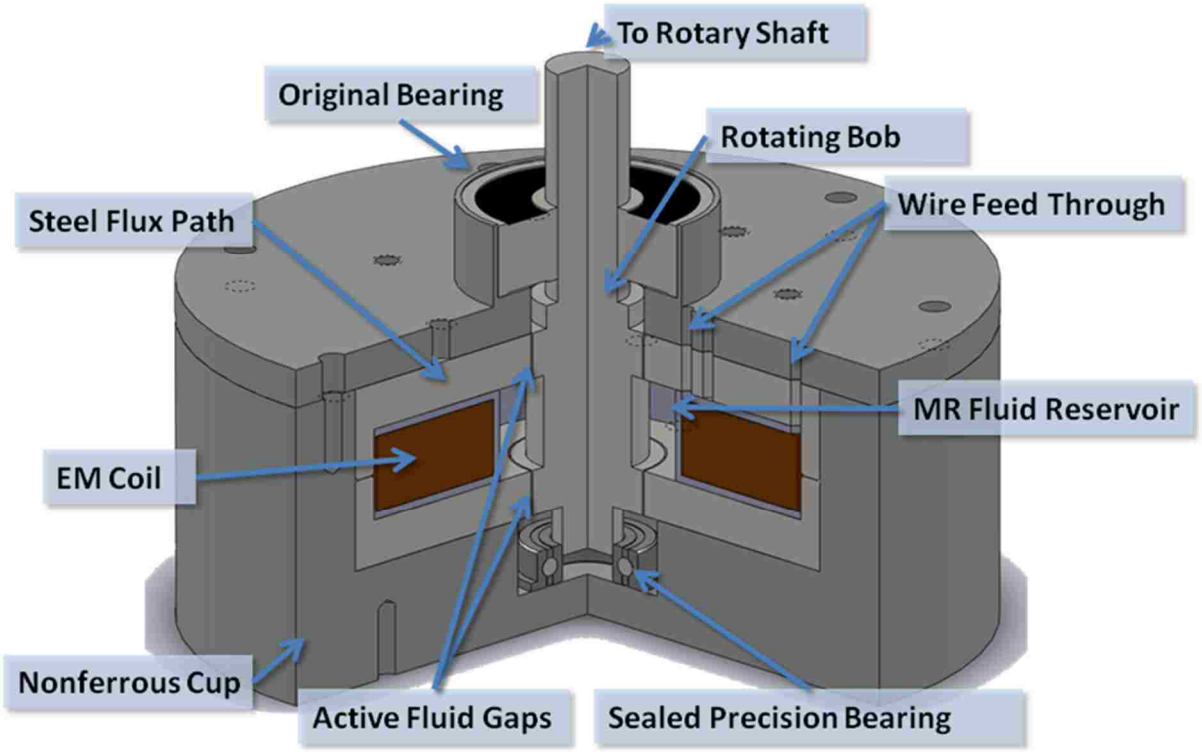

Figure 5.7 – Squeeze-strengthening Searle cell magnetorheometer. The precision bearings enforce a maximum limit to the bob eccentricity.

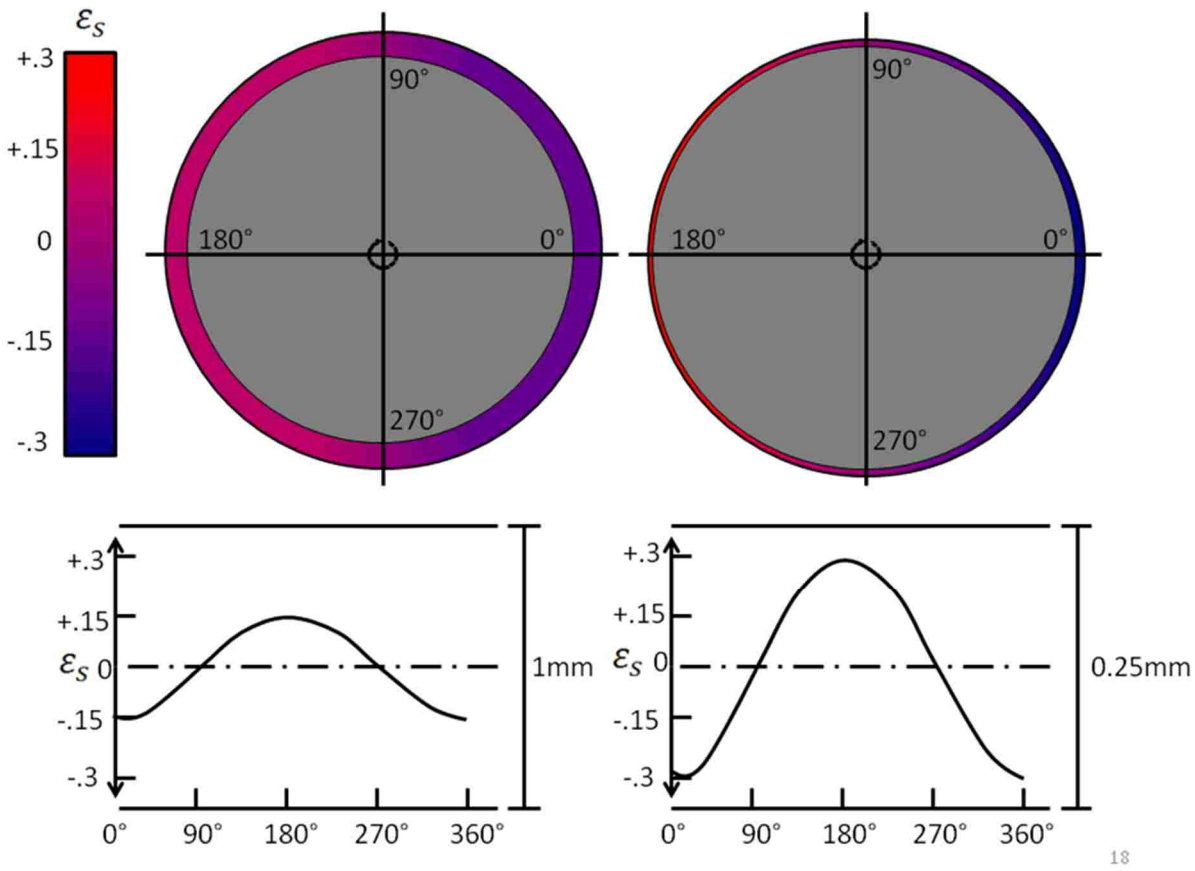

Figure 5.8 – Squeeze strain produced using the 1 mm and 0.25 mm gap configurations

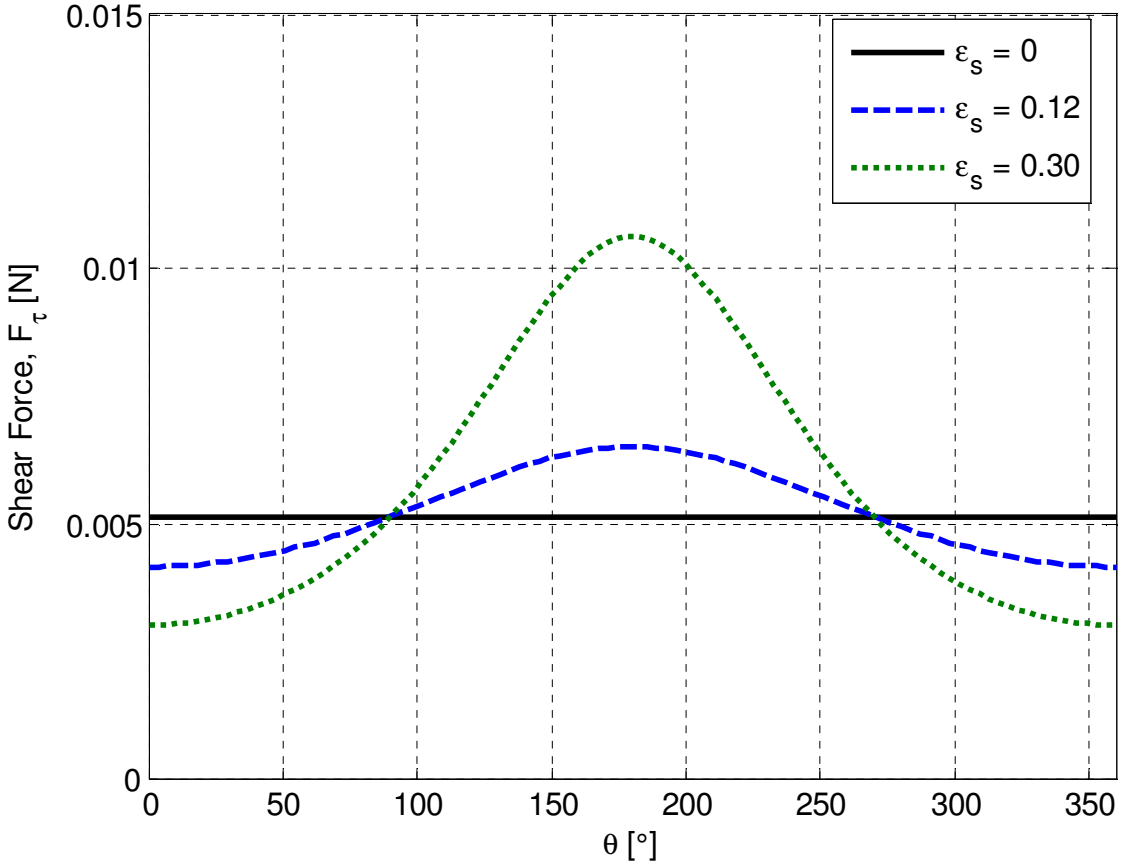

Figure 5.9 - Shear force component as a function of θ for three different squeeze strain values, representative of the experimental conditions used in this research

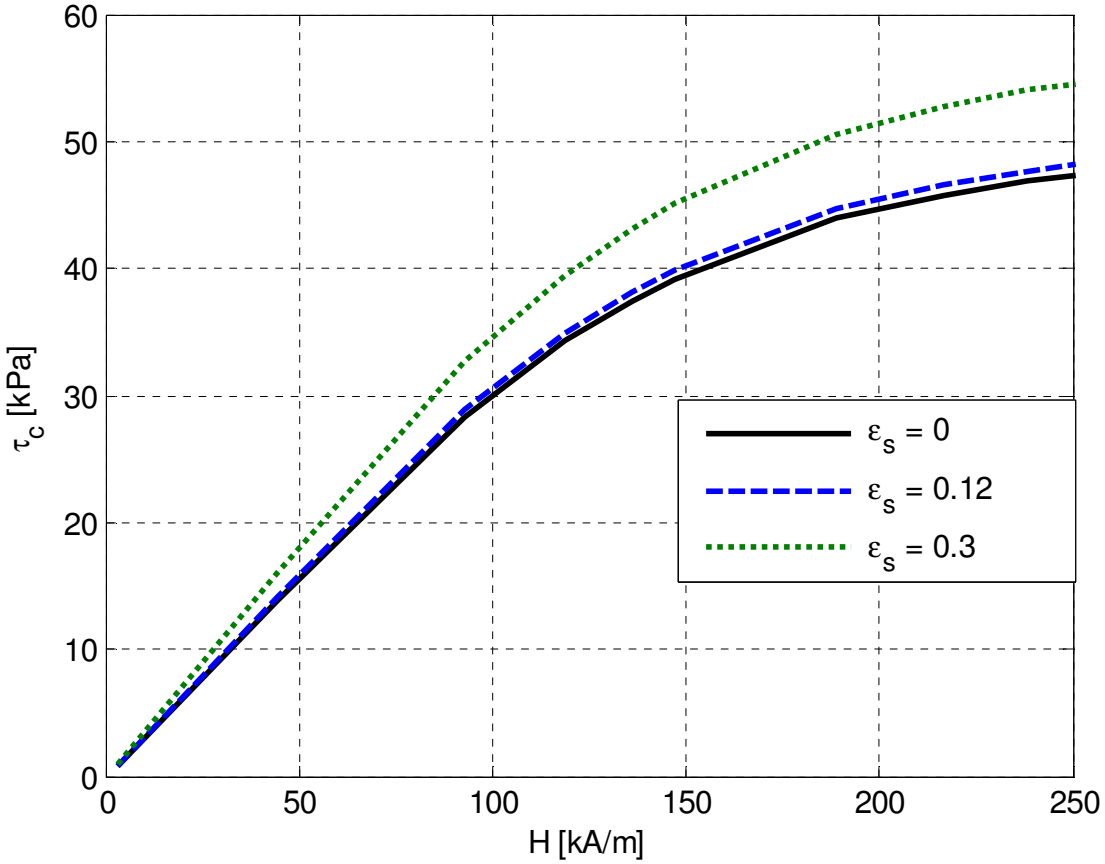

Figure 5.10 - Conventional shear stress versus magnetic field for three different squeeze strain values, representative of the experimental conditions used in this research

Figure 5.11 – Precision dial indicator used to measure the eccentricity of the rotating bob

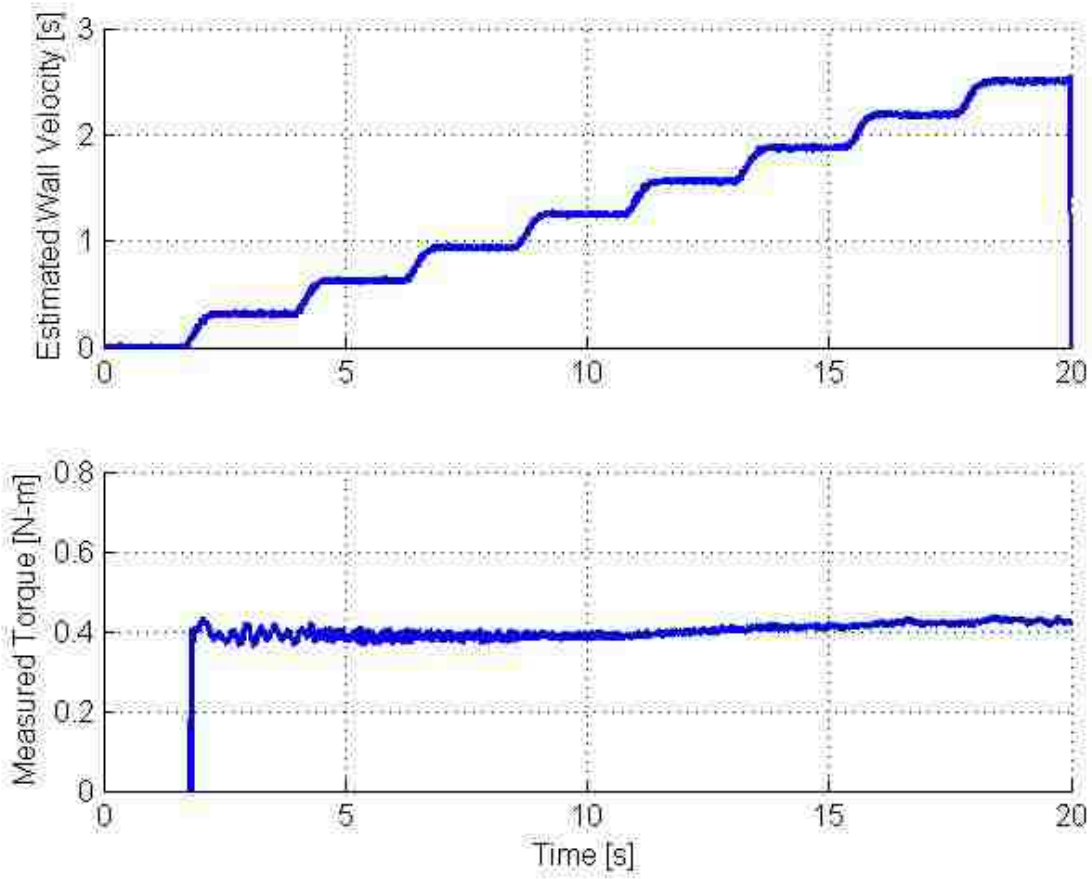

Figure 5.12 – Raw test data for squeeze strengthening tests contains input wall velocity and measured torque

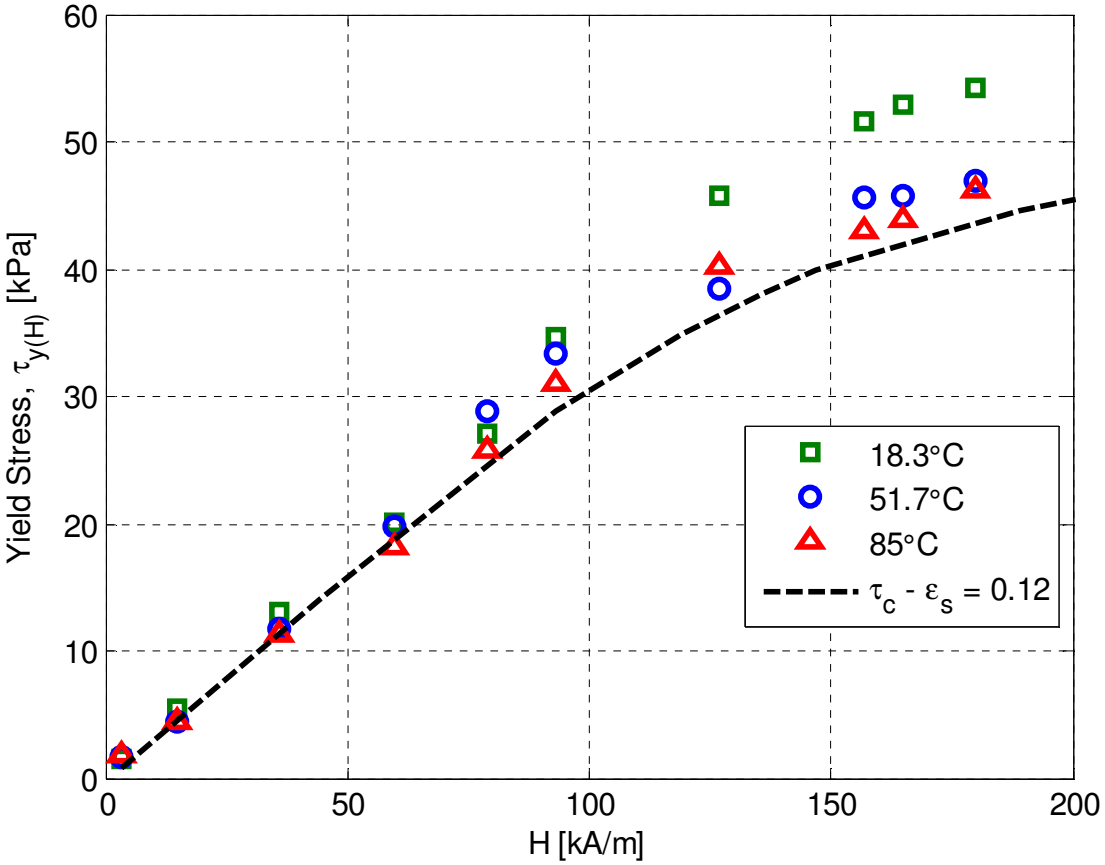

Figure 5.13 -Yield stress for MRF-132DG at three temperatures using setup A, a 1 mm gap height with no supporting bearings

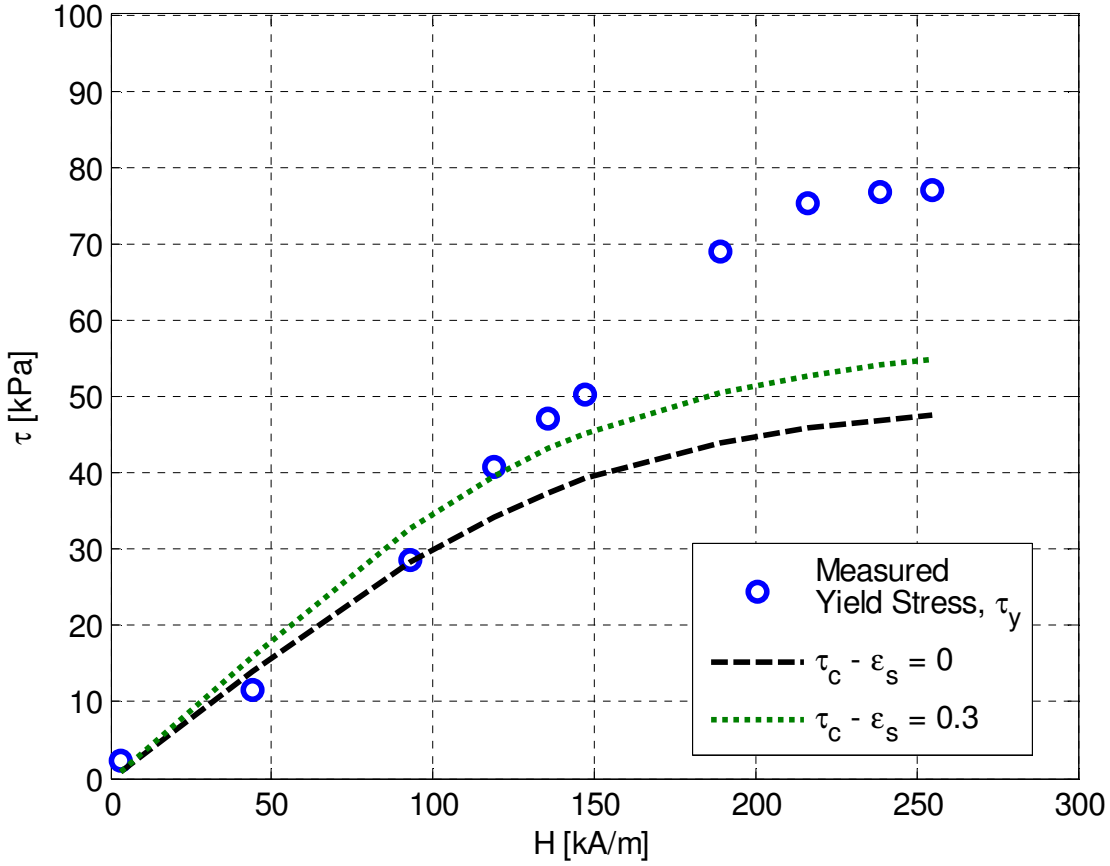

Figure 5.14 – Enhanced yield stress measurements for MRF-132DG at 51.7°C using setup B, a 0.25 mm nominal gap with top and bottom supporting bearings. Also shown is the conventional yield stress as reported by the fluid manufacturer, and for the eccentric.

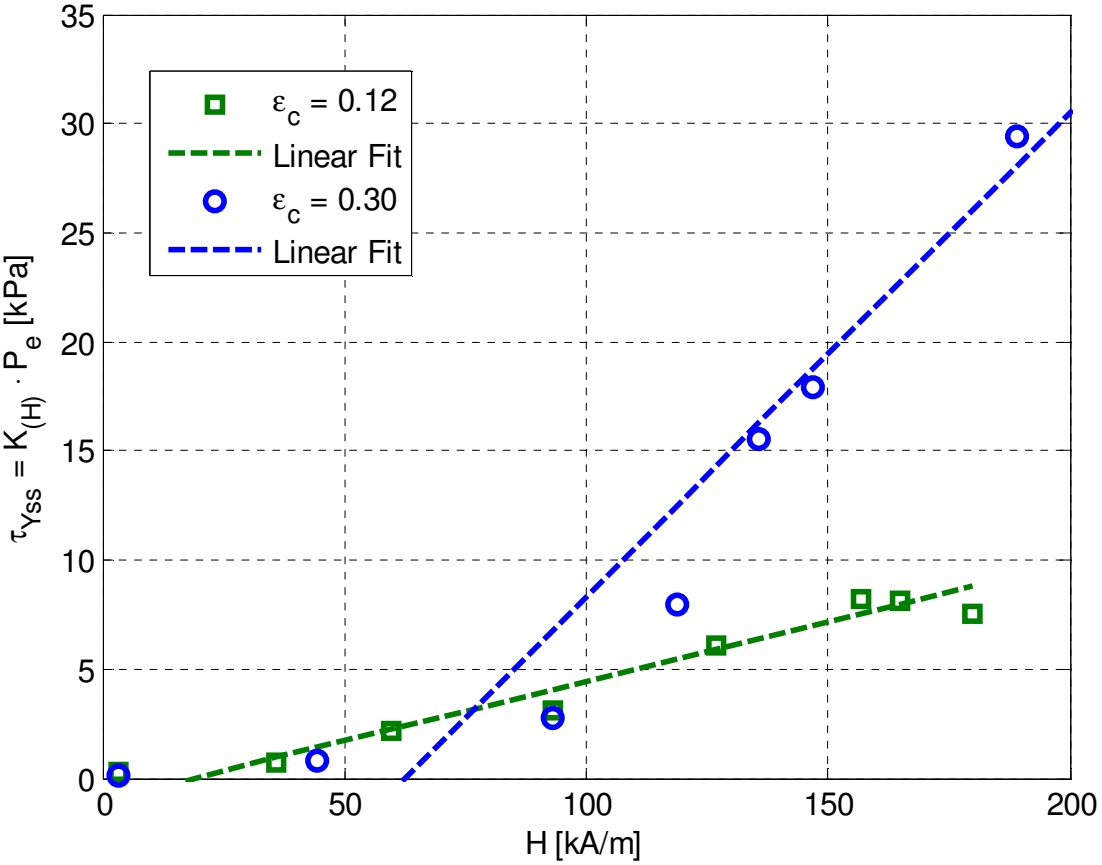

Figure 5.15 - Squeeze-strengthened yield stress component for single particle chains and BCT columns in MRF-132DG

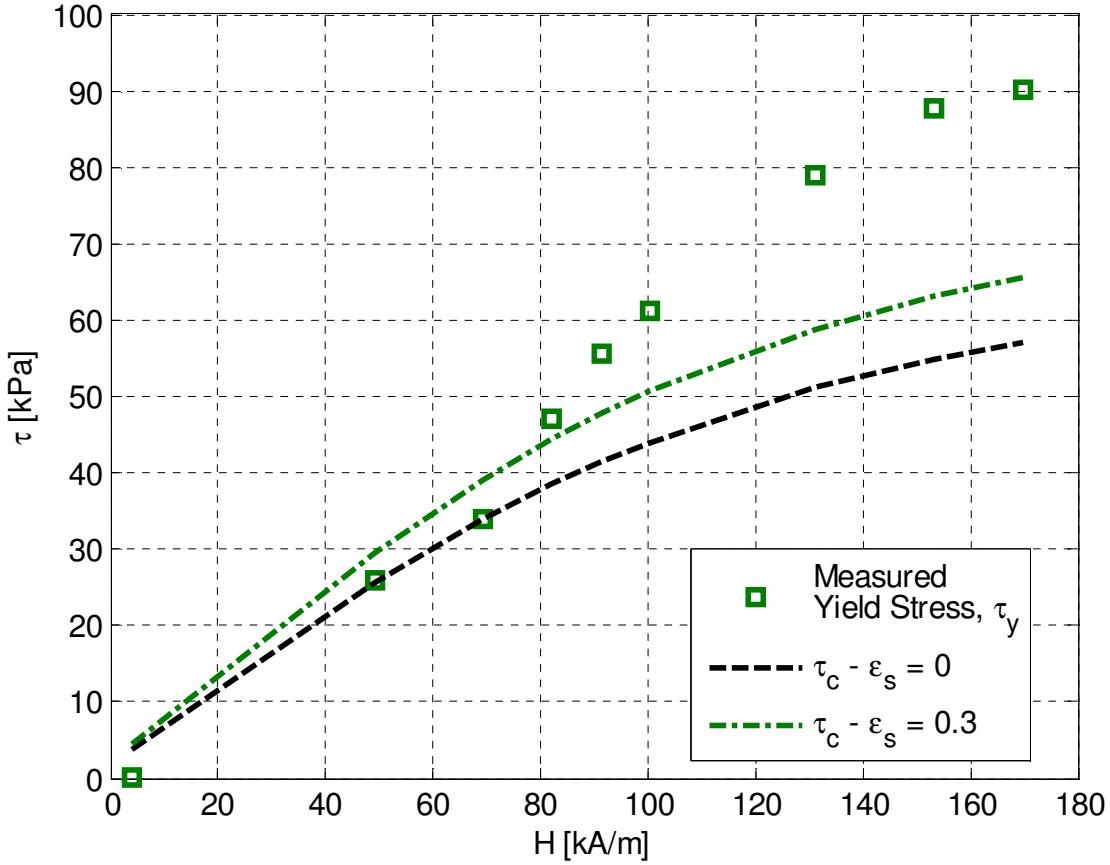

Figure 5.16 - Enhanced yield stress measurements for MRF-140DG at 51.7°C using setup B, a 0.25 mm nominal gap with top and bottom supporting bearings. Also shown is the conventional yield stress as reported by the fluid manufacturer, and for the eccentric case.

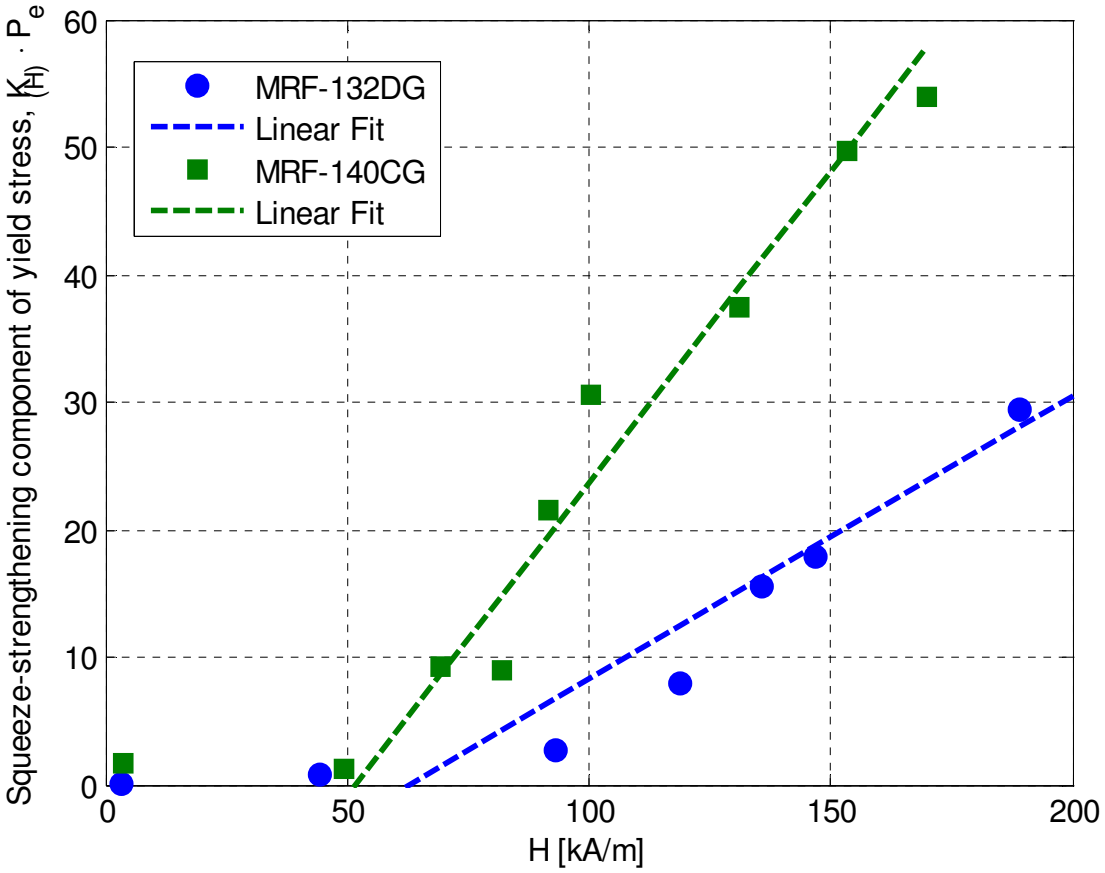

Figure 5.17 - Squeeze-strengthened yield stress component for BCT columns in MRF-132DG and MRF-140CG

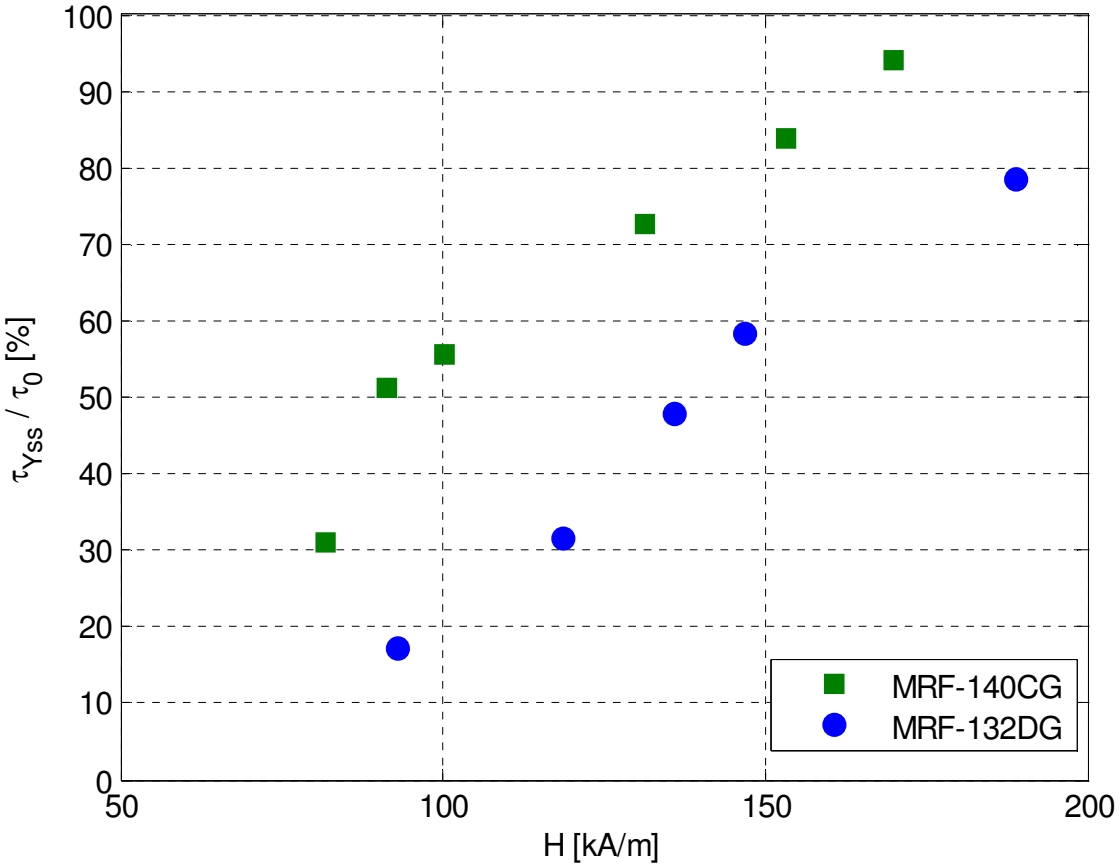

Figure 5.18 - Relative magnitude of squeeze strengthened yield stress component for 32 vol% and 40 vol% MR fluid

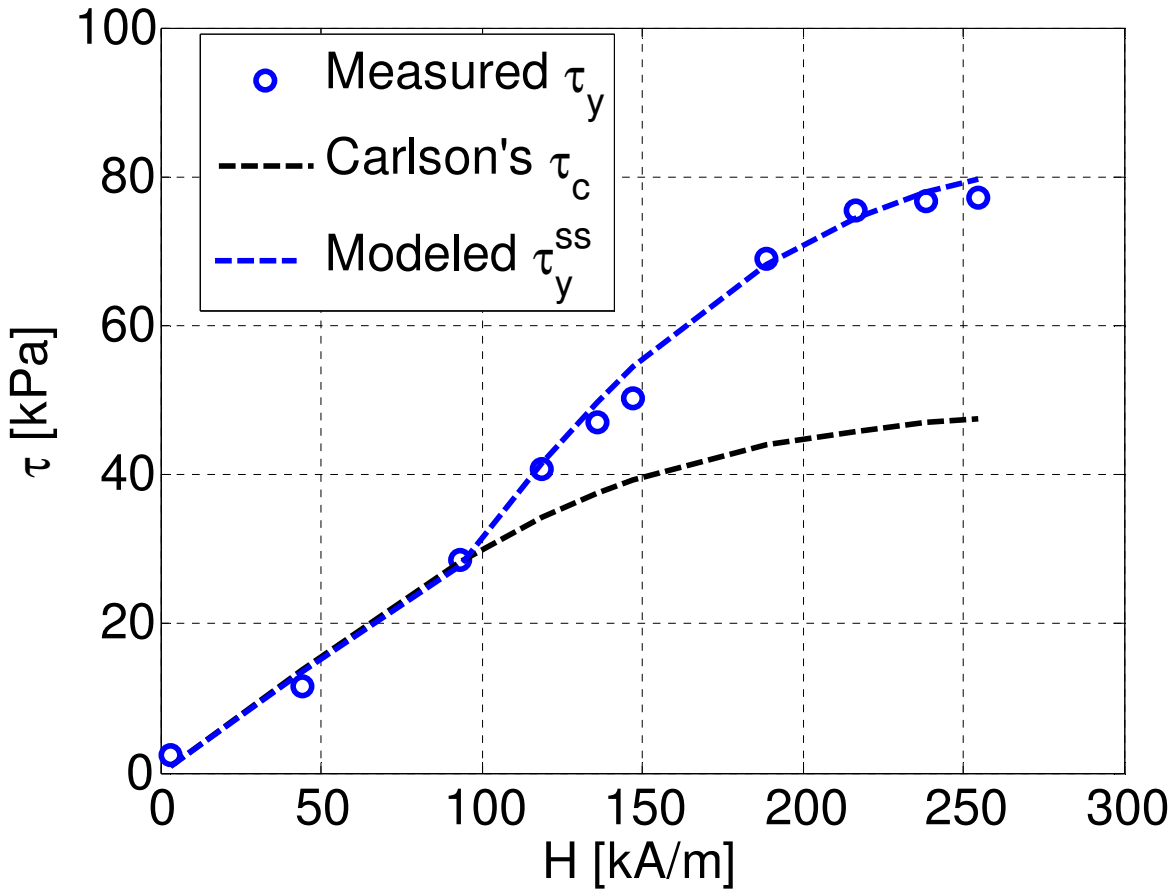

Figure 5.19 - Hybrid model results for squeeze strengthened yield stress in MRF-132DG

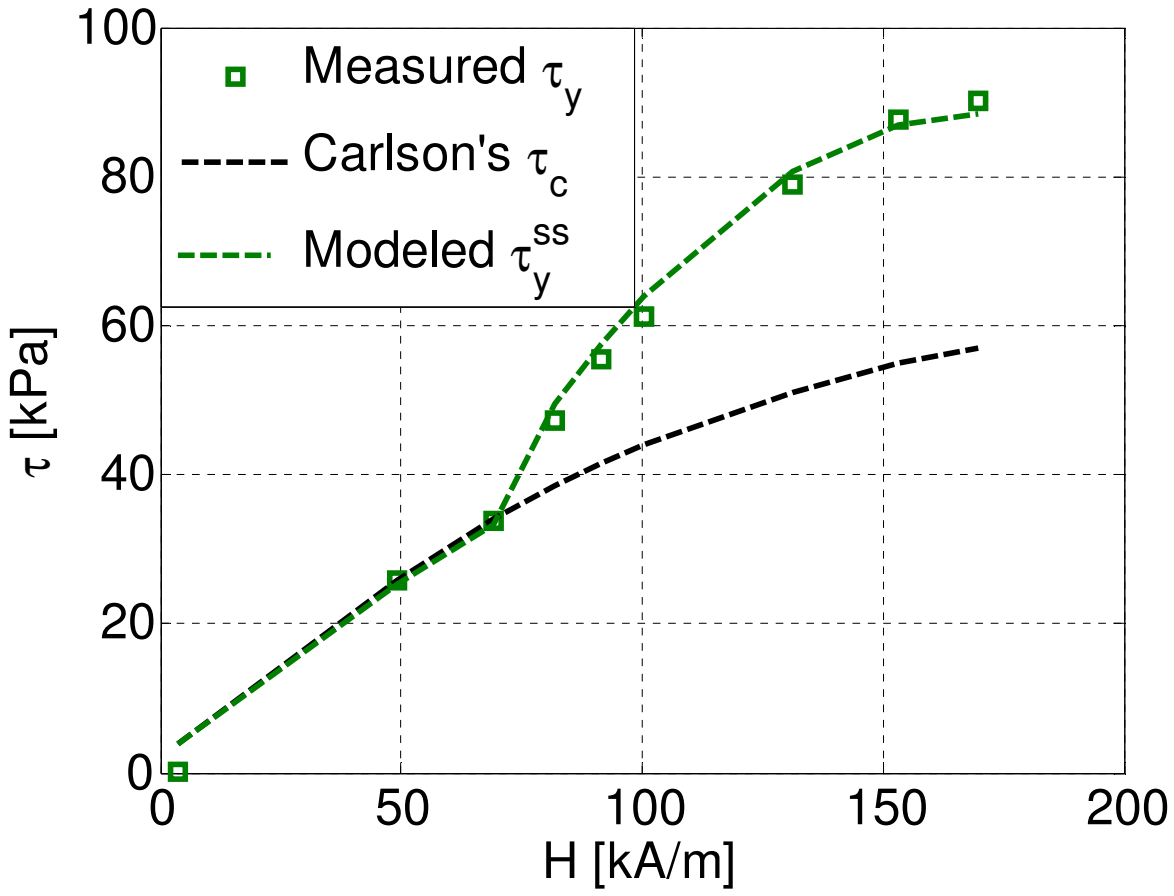

Figure 5.20 - Hybrid model results for squeeze strengthened yield stress in MRF-140CG

Chapter 6

6. CONCLUSIONS

Semi-active magnetorheological fluids are well-suited for use in adaptive shock absorbing devices such as crashworthy occupant protection systems. In addition to being inherently failsafe, the ability to adjust their load stroke profile to respond to changes in occupant mass and varying impact velocities makes magnetorheological energy absorbers a uniquely capable class of occupant protection technologies. To increase device controllability at high impact speeds (corresponding to high fluid shear rates), the established linear stroke geometry using flow mode operation was exchanged for a direct shear device in the form of a compact rotary vane damper. The research supporting this effort, presented in this dissertation, produced a number of original contributions and key conclusions relevant to the study of controllable fluid rheology and the application of MR fluids to compact energy absorbing devices, especially in volume- and weight-critical applications.

6.1. Summary of Research and *Original Contributions*

To realize this smaller, stronger MREA, a development program was undertaken beginning with a laboratory scale proof of concept and resulting in the final practical device. Along with an innovative application of nondimensional analysis to inform scaling between these two experiments and ultimately across a wide range of operating conditions, a novel squeeze-shear

mixed mode was investigated and demonstrates the potential for even smaller, stronger rotary MREAs.

6.1.1. Custom Searle cell magnetorheometer for high shear rate MR studies

A concentric cylinder, Searle cell magnetorheometer was used to verify that the MR effect persisted at shear rates up to 25,000 s^{-1}. Because rotation speed was limited, a key feature of this instrument was the use of sub-millimeter active gaps to achieve these high shear rates. Subsequent improvements to sample temperature control, magnetic field characterization, and instrument alignment allowed for the quantitative study of MR fluids under conditions similar to those expected during practical operation.

This instrument is the first concentric cylinder magnetorheometer capable of fluid characterization at such high shear rates, more than 10 times greater than existing commercial instruments.

Three commercially available MR fluids from LORD Corporation, ranging in volume fraction from 32 to 45%, were studied at shear rates corresponding to low speed impacts, up to 10,000 s^{-1}. As a result, a comprehensive set of high shear rate empirical data for these three widely used MR fluids was made available for application to future MREA designs.

6.1.2. Standard and nondimensional high shear rate characterization of MR fluids

To account for the shear thinning behavior of MR fluids, the nonlinear Herschel-Bulkley model was applied to produce experimental fits for the flow curve data, and these field-dependent parameters were reported. Notable trends with temperature, solids loading, and gap size/shear rate were discussed, and served as a basis for motivating the use of nondimensional analysis to reduce the number of interdependent variables. Having recorded MR fluid behavior across a range of

applied magnetic fields, shear rates, particle concentrations, and temperatures, it was desirable to distill this disparate information into a cohesive description for practical applications.

Using a method first developed for low shear rate, particle-level electrorheological fluid simulations, plotting the normalized apparent viscosity with a nondimensional Mason number produced a set of master curves which completely and succinctly describe the MR fluid characterization tests. Further, by incorporating the improved temperature control within the magnetorheometer and modeling temperature effects on the viscosity and magnetic permeability of the MR fluids, these individual temperature-dependent curves can be superimposed.

This represents the most expansive experimental validation that normalized apparent viscosity versus Mason number plots cause MR characterization data to collapse to a single master curve.

6.1.3. Scaling of MR devices through Mason number analysis

Based on the results of the smaller shear mode magnetorheometer, a practical rotary vane MREA was constructed for use in an SH-60 Seahawk crew seat system. Experiments to evaluate the performance of the MREA under shear rates corresponding to low-speed impacts were carried out on an industrial transmission testing rig, and a Bingham-plastic model fit verified that the MR effect remained consistent at shear rates up to 25,000 s^{-1}. It was noted that temperature increase, mainly due to resistive heating in the electromagnetic coil, did have a large effect on reducing the bulk fluid viscosity.

Encouraged by the successful application of nondimensional analysis to data sets collected from the Searle cell magnetorheometer, it was desirable to apply the same analysis to the full scale rotary vane MREA. Only by employing the novel temperature corrected Mason number was the

characteristic collapse of experimental measurements achieved, since the change in temperature during the tests with large applied currents was a contributing factor.

This analysis showed for the first time the nondimensional scaling method between test and full scale devices at different maximum shear rates and temperatures, and improves the ability of a narrow set of laboratory characterization data to be extrapolated to practical shear mode MREAs under a wide range of operating conditions.

6.1.4. Increase in yield stress through combined shear-squeeze mode operation

As a complimentary approach to developing smaller, stronger MREAs for shock absorption, the process known as compression-assisted aggregation or *squeeze-strengthening* was investigated using a modified Searle cell magnetorheometer. Additional bearing support was added to control the eccentricity of the bob, causing a precessing motion as it rotated. This precession lead to a periodic change in the active gap size, as measured by a precision dial indicator in contact with the rotating bob. By using different size bobs with different eccentricities, two values of normal strain – one which was predicted to induce squeeze-strengthening, and another which was not – were imparted to the active MR fluid while simultaneously shearing it. Measurements of the yield stress in two MR fluids indicated that the strength of the fluids was increased in the squeeze-strengthening case. A fluid with 32 vol% carbonyl iron showed a 78% increase in magnitude as compared to the conventional yield stress, while a 40 vol% fluid showed a 95% increase in yield stress. The linear trends of yield stress amplification in both fluids were similar in slope but different in magnitude, indicating that the mechanism of compression assisted aggregation was present in both and more pronounced at higher volume fractions.

The previously reported finding that squeeze strengthening would not occur at field strengths below ~50 kA/m was supported as well in this research. Using a previously developed empirical curve fit from one of the earliest published reports on squeeze strengthening for comparison, good agreement was found between fit parameters in each study. Furthermore, a 2nd order, field-dependent hybrid of phenomenological and tribological models was formulated to describe qualitatively the squeeze strengthening behavior of both MR fluids used in testing.

These results are the first recorded work using a rotating cylinder geometry to induce squeeze strengthening in MR fluids. Because this method of using mixed mode operation is amenable to rotary MREAs at high speeds, this research supports the application of squeeze strengthening in practical shock absorbing devices to increase their specific damping - energy absorbed per unit weight or per unit volume - performance.

6.2. Key Conclusions

Linear stroke magnetorheological energy absorbers (MREAs) have been applied successfully to adaptive occupant protections systems, but show performance reduction at high speeds, such as during a shock or crash event. Through this work, direct shear mode MREAs using rotary geometries have been shown to be a viable way to improve controllability during high speed operations. This improvement in controllability translates to smaller, lighter MREA solutions, expanding the design space of these semi-active systems to weight-critical applications like aircraft and spacecraft.

The design of any MREA, regardless of expected operating conditions, relied on characterized performance data for the MR fluid collected at low shear rates and narrow temperature ranges. Particularly when extrapolating to high ($< 10{,}000\ s^{-1}$) shear rates and extreme ends of the operating

temperature range, this data becomes much less predictive of actual device performance. This research shows that with a relatively narrow set of MR fluid force-velocity and viscosity-temperature data, appropriate nondimensionalized groups such as Mason number can provide more accurate estimates of device performance across a wide range of conditions. Critically, this has improved the applicability of precise measurements taken in the lab setting, showing how these can be scaled up and applied to practical design problems.

Additionally, the introduction of mixed mode squeeze-strengthening operation offers an alternative and complimentary method of improving specific device strength by increasing the yield stress of the working MR fluid. Previous investigations have relied on multi-step mode changes, i.e. compression followed by shear, and setups that achieve only small stroke lengths, These are, practically speaking, difficult to accomplish and ineffective for use outside of the laboratory. Rotary MREAs, however, have already shown their applicability, and this proof-of-concept work demonstrates the potential for improving the strength and effectiveness of these devices.

6.3. Future Work

This section suggests future areas of research that expand upon the topics covered in this dissertation. Lessons learned regarding the design of MR rheometry instruments, practical devices, and improved analysis strategies are presented with the aim of producing stronger and more compact MR fluid devices and developing a better understanding of MR fluid behavior under a wide array of operating conditions.

6.3.1. Improved Searle cell magnetorheometer

The narrow gap Searle cell magnetorheometer used in this study was heavily modified from its initial design to accomplish the high precision measurements presented in this research. Each modification added a layer of complexity to the operating procedure, so a magnetorheometer 2.0 that simplifies and combines a number of experimental steps is suggested. The stock servomotor should be replaced with an instrument-grade electric motor having a minimal amount of slop, to better control the alignment of the bob and MR cell along a common center. All components should be manufactured to a demanding precision, since any dimensions which differ from spec negatively impact the fidelity of simulation-experiment correlations. Surface finishes on steel parts which contact MR fluid samples must be characterized and maintained.

Temperature control should no longer be handled by an external cooling jacket, but instead by an integrated thermocouple, heatsink, and thermally conductive path that surrounds the electromagnetic coil to effectively divert the heat generated within the coil away from the MR fluid sample. This would drastically reduce the change in temperature within the test material to near zero, eliminating one of the confounding variables present in all rheometer experiments. A Peltier element as shown in Figure 6.1 (Steinbrecher, 2010) may perform well in this role and, with clever voltage control through LabVIEW, could be proportionally related to the applied magnetic coil current to exactly balance out any resistive heating.

Magnetic field intensity measurements should be performed continuously throughout an experiment using Hall sensors, and this can be accomplished using a modified bob having a smaller diameter at the top. With an upper gap near 1 mm, there is enough clearance to embed a compact Hall sensor or sensor suite directly in the field, and this data can be related to the field within the lower active gap. This gap may either be air filled or MR fluid filled, though an air-filled gap is

preferable for ease of use. Care must be taken to use a precisely known volume of MR fluid, since slight changes in the fluid level may affect the applied field intensity. Again, integration of these measurements into the existing *LabVIEW* instrument DAQ system interface is desirable.

Eccentricity measurements can be performed using a noncontact, magnetostrictive Galfenol sensor (Raghunath et al., 2013). This real time measurement will be invaluable, particularly in further squeeze strengthening research, since any field applied to an eccentric bob tends to pull it further out of center. The rates of rotation and bob precession may be measured using the same sensors and related to each other, which is currently impossible with the precision dial indicator. Additionally, the noncontact nature of these measurements should nullify any issues with bending moments being resolved through the torque measurement cell.

Hybrid magnetic circuits, which can be simple combinations of strong permanent magnets and EM coils or novel switchable electropermanent magnets, offer a way forward when power consumption should be minimized. For a well-designed magnetic circuit where the permanent field is exactly half of the available electromagnetic coil field, only half of the applied current would be needed (Bai and Wereley, 2014). Only cursory investigations were able to be performed in this research, but there appears to be much room for innovation in this area, particularly for rotary, shear mode applications. Switchable permanent magnetic circuits also may be investigated for zero-power, semi-active MR applications (Knaian, 2010).

6.3.2. Dynamic and near-zero shear rate studies

This dissertation focuses on the high shear rate operation of MREAs corresponding to large velocity crash and shock absorption events, but another major benefit of these devices is their application to low amplitude vibration attenuation. As such, studies of shear mode devices under

oscillatory action should be performed. These can either be accomplished using a rotational setup, such as the magnetorheometer or transmission testing rig, or by combining the device with a linear motion conversion system, such as a rack and pinion or worm gear arrangement.

Since oscillatory tests are necessarily low amplitude cases, the magnitude of the shear rates developed will be much lower than those presented in this dissertation. As such, a different MR fluid model should be employed to describe the behavior, one which more accurately reflects the near zero shear rate behavior of real fluids, i.e. one that is not piecewise linear and has no discontinuities. Additionally, hysteresis will most likely be present, and so some care should be taken to model this behavior as well. To this end, a 5 term Carreau-Yasuda model may be used to connect low shear rate oscillatory behavior with the shear thinning exhibited at high shear rates, and a hyperbolic tangent function can be used to describe the pre- and post-yield hysteresis behavior (Choi et al., 2005).

6.3.3. Squeeze strengthening in MR fluids

Perhaps the most exciting development to come from this research is the demonstration of squeeze strengthening in a shear mode device. This has direct applications to current MREAs, and points the way to dramatically improving the specific energy absorption capabilities of such MR fluid devices. While in this work an eccentric arrangement was used, i.e. circular cylinders with offset axes, there are a number of alternative shear mode geometries that could provide the same sort of active gap size change required to accomplish squeeze strengthening.

Theoretically, any non-circular cross section can cause the change in gap size required to squeeze the active MR and result in the compression assisted aggregation of chains into columns. Because of complexities which arise in the magnetic field due to these geometries, however, it's advisable

to use simple geometric permutations, such as ellipses or rounded Rouleaux polygons, shown in Figure 6.3. However, as more experience is gained with the magnetic circuit design and mixed shear-squeeze mode operation in general, more complex geometries may be investigated, such as the nested elliptical vane and the sawtooth patterned cylinder, shown in Figure 6.4. Additionally, a parallel plate modified to have a waveform profile such that an oscillating squeeze motion occurs as the plate rotates can also generate the combined shear-squeeze motion, and could be applicable to improved MR brakes and clutches, shown in Figure 6.5.

The effects of interparticle friction, particle plastic deformation, and the resulting changes in magnetization are all ripe areas for potential research into squeeze mode enhancements of MR fluid properties, and will likely lead to a new paradigm in mixed mode MREA design.

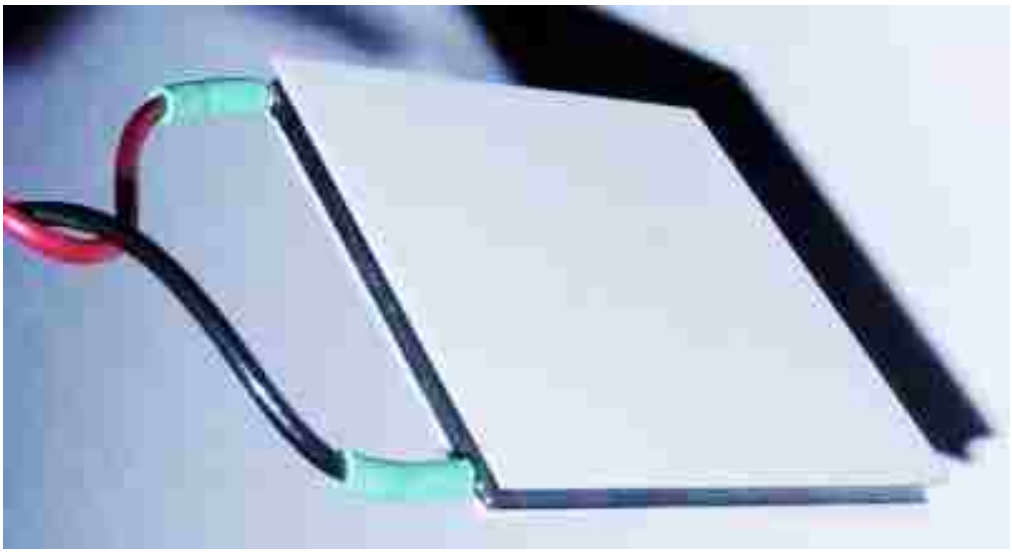

Figure 6.1 - Peltier thermoelectric element suited for MR cell temperature control [40 x 40 x 5 mm]. Adapted from www.heatsink-guide.com/peltier.htm

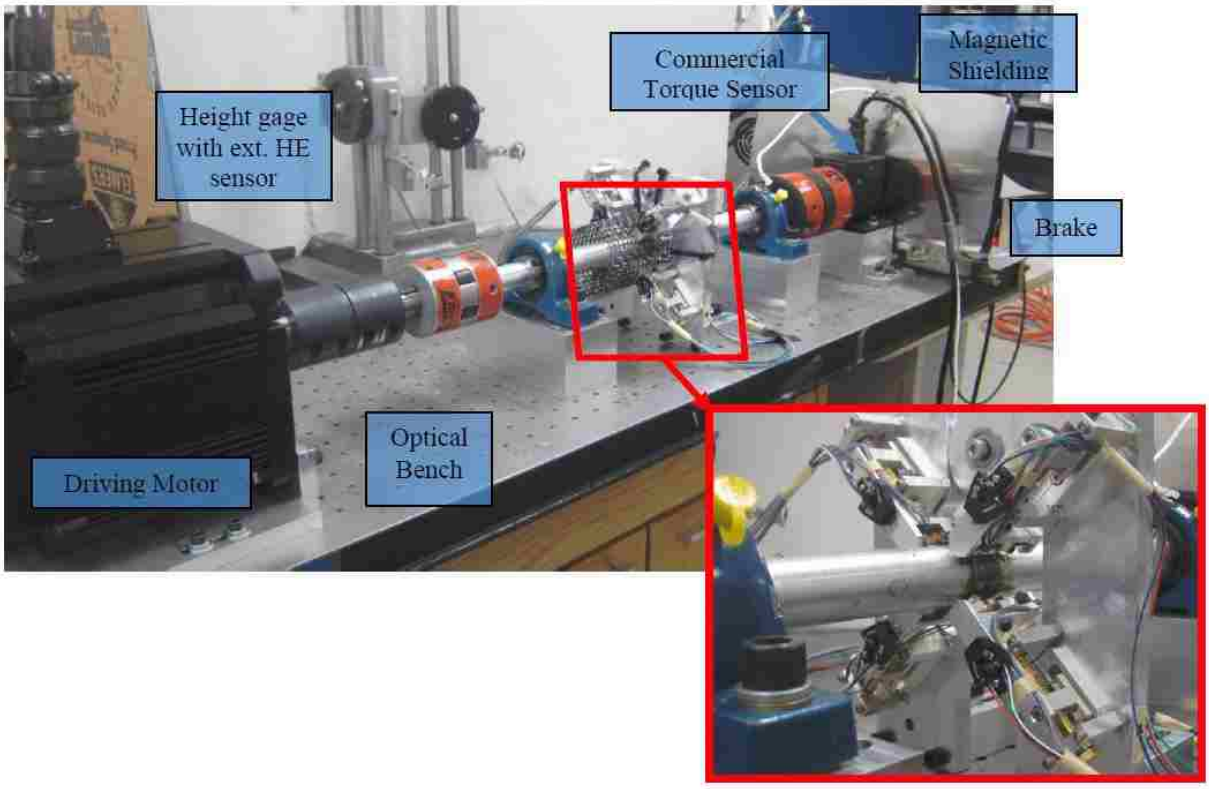

Figure 6.2 - Noncontact, magnetostrictive Galfenol sensor array used to measure torque, rotation speed and shaft eccentricity presented in (Raghunath et al., 2013)

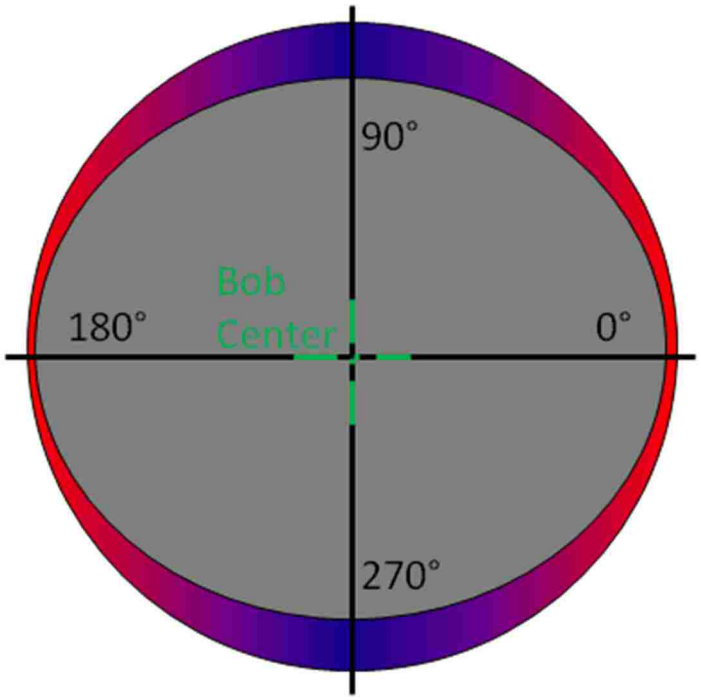

a)

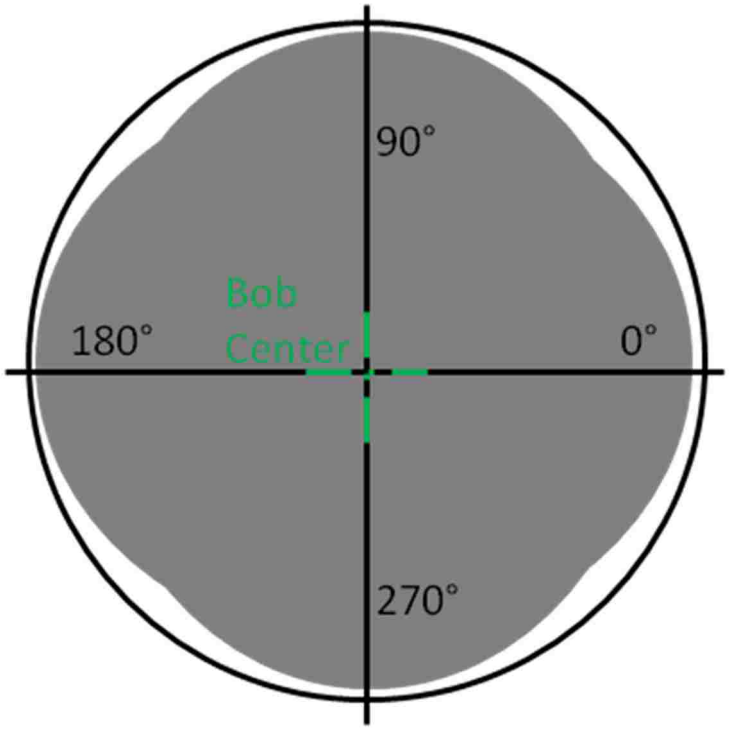

b)

Figure 6.3 – Simple noncircular cross sections used to generate squeeze strengthening in a rotating cylinder MREA. a) Elliptical bob and b) rounded Rouleux square bob

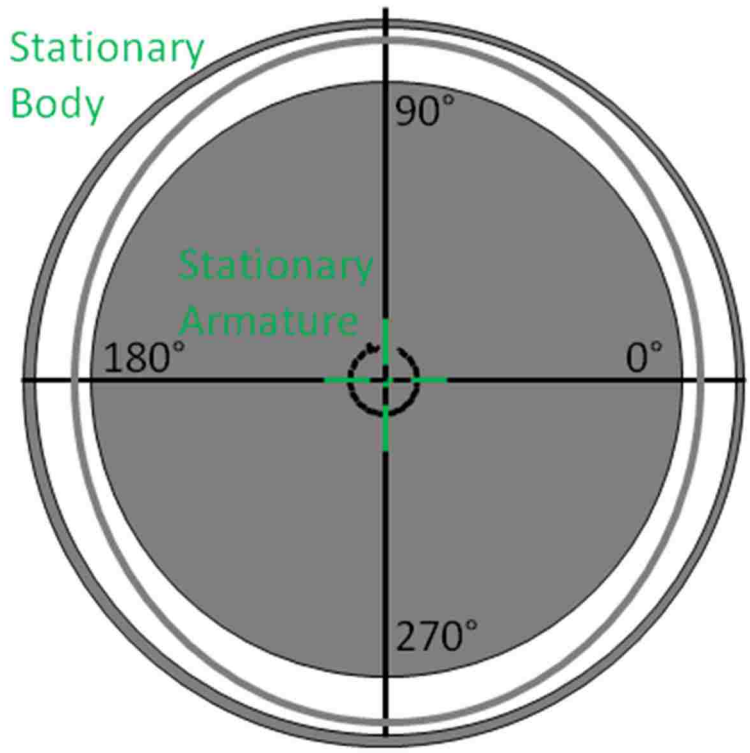

a)

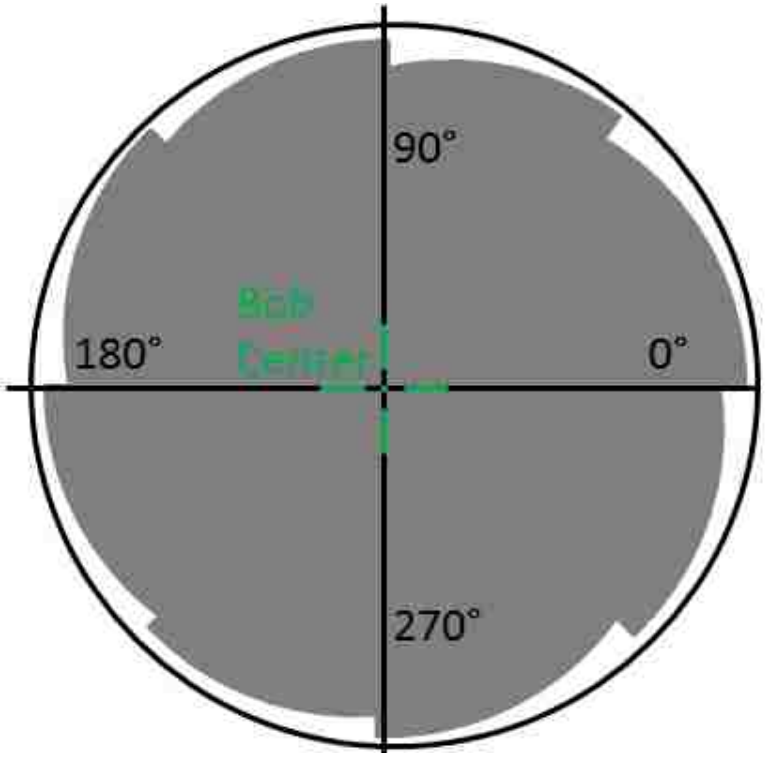

b)

Figure 6.4 - Complex cross sections used to generate squeeze strengthening in a rotating geometry MREA. a) Elliptical vane and b) sawtooth patterned bob

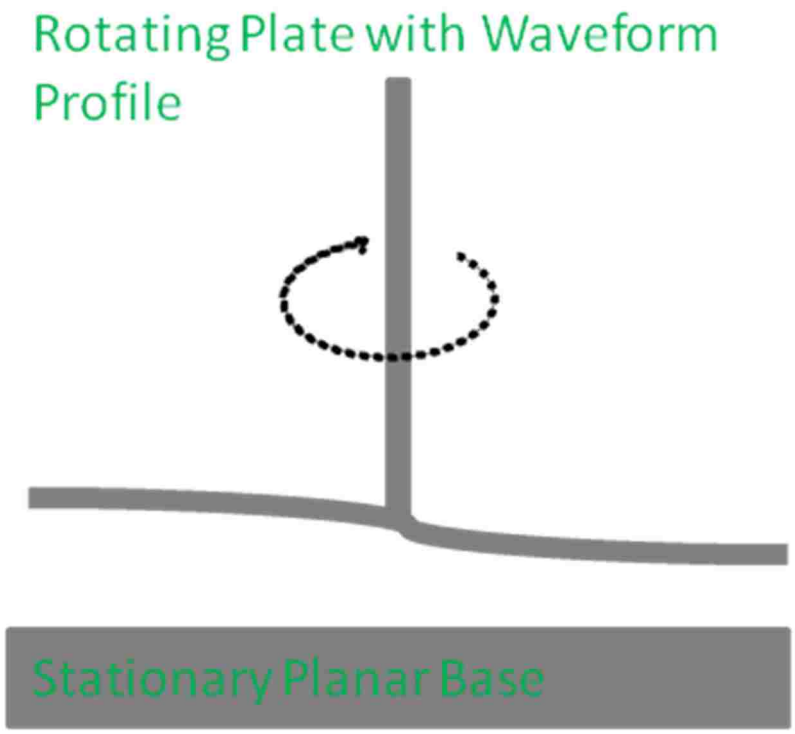

a)

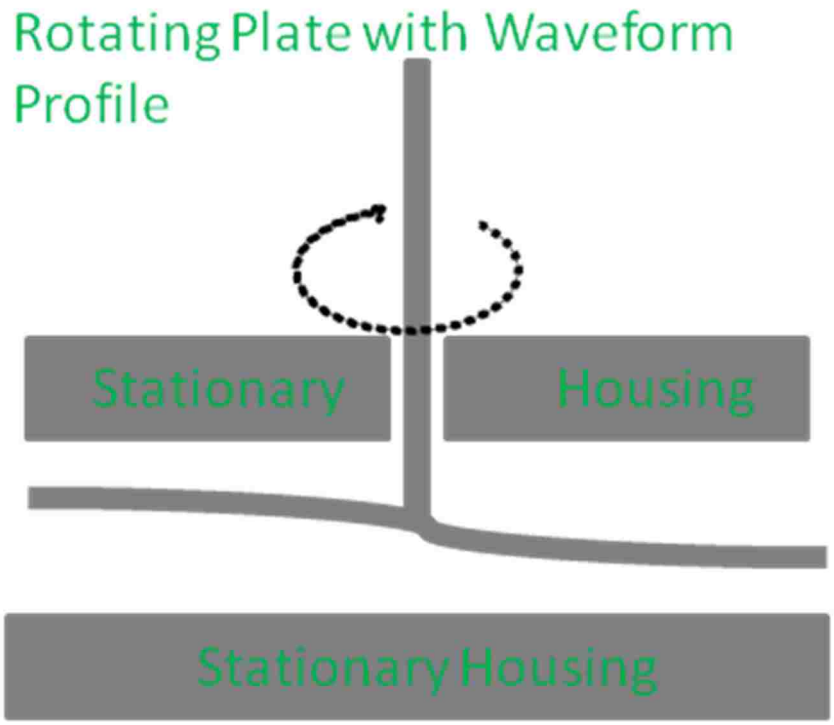

b)

Figure 6.5 – Parallel plate geometries with waveform profiles to generate mixed mode squeeze-shear operation as a) an experimental rheometer instrument and b) an enclosed MR brake or clutch.

Chapter 1 References

Batterbee, D.C., Sims, N.D., Stanway, R. and Rennison, M., 2007. Magnetorheological landing gear: 2. validation using experimental data. *Smart Materials and Structures*, 16(6), pp. 2441-52.

Becnel, A.C., Hu, W., Hiemenz, G.J. and Wereley, N.M., 2010. Design and testing of a magnetorheological damper to control both vibration and shock loads for a vehicle crew seat. In *Proceedings of SPIE 7643*. Long Beach, CA, 2010. SPIE.

Brigley, M., Choi, Y.T., Wereley, N.M. and Choi, S.B., 2007. Magnetorheological isolators using multiples fluid modes. *Journal of Intelligent Material Systems and Structures*, 18(12), pp. 1143-48.

Carlson, J.D., Catanzarite, D.M. and St. Clair, K.A., 1996. Commercial magneto-rheological fluid devices. *International Journal of Modern Physics B*, 10(23), pp. 2857-65.

Choi, Y.T., Cho, J.U., Choi, S.B. and Wereley, N.M., 2005. Constitutive models of electrorheological and magnetorheological fluids using viscometers. *Smart Materials and Structures*, 14, pp. 1025-36.

Choi, Y.T. and Wereley, N.M., 2004. Vibration control of a landing gear system featuring electrorheological/magnetorheological fluids. *AIAA Journal of Aircraft*, 40(3), pp. 432-39.

Choi, Y.T. and Wereley, N.M., 2005. Mitigation of biodynamic response ot vibratory and blast-induced shock loads using magnetorheological seat suspensions. *Proceedings of the Institution of Mechanical Engineers Part D: Journal of Automobile Engineering*, 219(6), pp. 741-53.

de Silva, C.W., 2005. *Vibration and Shock Handbook*. 1st ed. Boca Raton, FL: Taylor & Francis Group.

Dong-won, Y., Young-su, S., Hee-chang, P. and Sang-kyu, C., 2009. Design of a novel MR rotary brake. In *World Congress on Computer Science and Information Engineering*. Los Angeles, CA, 2009. IEEE.

Guo, H.T. and Liao, W.H., 2012. A novel multifunctional rotary actuator with magnetorheological fluid. *Smart Materials and Structures*, 21(6), p. 9.

Hiemenz, G.J., Choi, Y.T. and Wereley, N.M., 2007. Semi-active control of vertical stroking helicopter crew seat for enhanced crashworthiness. *Journal of Aircraft*, 44(3), pp. 1031-34.

Hiemenz, G.J., Hu, W. and Wereley, N.M., 2008. Semi-active magnetorheological helicopter crew seat suspension for vibration isolation. *Journal of Aircraft*, 45(3), pp. 945-53.

Hiemenz, G.J. and Wereley, N.M., 2013. *Rotary vane magnetorheological (MR) energy absorber*. Patent No. 8424656. US.

Hu, W. and Wereley, N.M., 2005. Magnetorheological fluid and elastomeric lag damper for helicopter stability augmentation. *International Journal of Modern Physics B*, 19(7-9), pp. 1471-77.

Hu, W. and Wereley, N.M., 2011. Behavior of MR fluids at high shear rate. *International Journal of Modern Physics B*, 25(7), pp. 979-85.

Jolly, M., Bender, J. and Carlson, J., 1999. Properties and applications of commercial magnetorheological fluids. *Journal of Intelligent Material Systems and Structures*, 10(1), pp. 5-13.

LORD Corporation, 2012. *MRF-132DG Magneto-Rheological Fluid*. [Online] Available at: http://www.lord.com/products-and-solutions/magneto-rheological-%28mr%29/product.xml/1645/2 [Accessed 2012].

LORD Corporation, 2012. *MRF-140CG Magneto-Rheological Fluid*. [Online] Available at: http://www.lord.com/products-and-solutions/magneto-rheological-%28mr%29/product.xml/1646 [Accessed 2012].

Mao, M., 2011. *Adaptive Magnetorheological Sliding Seat System for Ground Vehicles*. Ph.D. Thesis, Dept. of Aerospace Engineering, University of Maryland, College Park, MD.

Mao, M., Hu, W., Choi, Y.T. and Wereley, N.M., 2007. A magnetorheological damper with bifold valves for shock and vibration mitigation. *Journal of Intelligent Material Systems and Structures, 18(12)*, p. 1227.

Rabinow, J., 1948. The magnetic fluid clutch. *AIEE Transactions*, 67(2), pp. 1308-15.

Rabinow, 1951. *Magnetic fluid torque and force transmitting device*. US Patent No. 2575360. US.

Rana, R. and Soong, T.T., 1998. Parametric study and simplified design of tuned mass dampers. *Engineering Structures*, 20(3), pp. 193-204.

Singh, H.J., Choi, Y.T. and Wereley, N.M., 2009. Optimal control of vertically stroking crew seats employing magnetorheological energy absorbers. In *Proceedings of ASME 2009 Conference on Smart Materials, Adaptive Structures and Intelligent Systems*. Oxnard, CA, 2009. ASME.

Tang, X., Zhang, X., Tao, R. and Rong, Y., 2000. Structure-enhanced yield stress of magnetorheological fluids. *Journal of Applied Physics*, 87(5), pp. 2634-38.

Tao, R., 2001. Super-strong magnetorheological fluids. *Journal of Physics: Condensed Matter*, 13, pp. R979-99.

Wang, J., Meng, G., Feng, N. and Hahn, E.J., 2005. Dynamic performance and control of squeeze mode MR fluid damper-rotor system. *Smart Materials and Structures*, 14(4), p. 11.

Wereley, N.M., Cho, J.U., Choi, Y.T. and Choi, S.B., 2008. Magnetorheological dampers in shear mode. *Smart Materials and Structures*, 17(1), p. 11.

Wilson, N.L., 2012. *Semi-active Six Degree of Freedom Vibration Control*. Ph.D. Thesis, Dept. of Aerospace Engineering, University of Maryland, College Park, MD

Zhang, X.J. et al., 2011. Dynamic testing and modeling of an MR squeeze mount. *Journal of Intelligent Material Systems and Structures*, 22(15), pp. 1717-28.

Zhang, X.Z., Gong, X.L., Zhang, P.Q. and Wang, Q.M., 2004. Study on the mechanism of the squeeze-strengthen effect in magnetorheological fluids. *Journal of Applied Physics*, 96(4), pp. 2359-66.

Zhang, M.L. et al., 2009. Compression enhanced shear yield stress of electrorheological fluids. *Chinese Physics Letters*, 26(4), p. 4.

Chapter 2 References

ANSYS, Inc., 2009. *ANSYS Maxwell 2D Manual*. [Online] Available at: http://www.scribd.com/doc/100250275/Manual-Maxwell-2D [Accessed 26 Augustus 2013].

Atkinson, H.V., 2008. *Modelling of Semi-solid Processing*. Shaker.

Barber, E.M., Muenger, J.R. and Villforth, J..F.J., 1955. A high rate of shear rotational viscometer. *Analytical Chemistry*, 27(3), pp. 425-29.

Boese, H. and Ehrlich, J., 2010. Performance of magnetorheological fluids in a novel damper with excellent fail-safe behavior. *Journal of Intelligent Material Systems and Structures*, 21, pp. 1537-42.

Brooks, R.F., Dinsdale, A.T. and Quested, P.N., 2005. The measurement of viscosity of alloys - a review of methods, data and models. *Measurement Science and Technology*, 16(2), pp. 354-62.

Carlson, J.D., 2005. MR fluids and devices in the real world. *International Journal of Modern Physics B*, 19(7,8,9), pp. 1463-70.

Chaudhuri, A., Wereley, N.M., Radhakrishnan, R. and Choi, S.B., 2006. Rheological parameter estimation for a ferrous nanoparticle-based magnetorheological fluid using genetic algorithms. *J. Intel. Mat. Syst. Str.*, 17, p. 261.

Choi, Y.T., Cho, J.U., Choi, S.B. and Wereley, N.M., 2005. Constitutive models of electrorheological and magnetorheological fluids using viscometers. *Smart Materials and Structures*, 14, pp. 1025-36.

Choi, H.J. et al., 2005. Magnetorheology of synthesized core-shell structured nanoparticle. *IEEE Transactions on Magnetics*, 41(10), pp. 3448-50.

Colyer, A.A. and Clegg, D.W., eds., 1998. *Rheological Measurement*. 2nd ed. New York, US: Springer.

Estelle, P., Lanos, C. and Perrot, A., 2008. Processing the Couette viscometry data using a Bingham approximation in shear rate calculation. *Journal of Non-Newtonian Fluid Mechanics*, 154(1), pp. 31-38.

Ferguson, J. and Kemblowski, Z., 1991. *Applied Fluid Rheology*. 1991st ed. New York, NY: Springer.

Goncalves, F.D., Ahmadian, M. and Carlson, J.D., 2006. Investigating the magnetorheological effect at high flow velocities. *Smart Materials and Structures*, 15, pp. 75-85.

Hu, W., Becnel, A.C. and Wereley, N.M., 2012. Measurement of magnetorheological fluids properties at high shear rate with controlled temperature. In *ICAST2012: 23rd International Conference on Adaptive Structures and Technologies*. Nanjing, China, 2012.

Hu, W. and Wereley, N.M., 2011. Behavior of MR fluids at high shear rate. *International Journal of Modern Physics B*, 25(7), pp. 979-85.

Hu, W. et al., 2012. Lightweight magnetorheological energy attenuation system for rotorcraft seats. In *American Helicopter Society Forum 68*. Fort Worth, TX, 2012.

Hu, W. et al., 2012. Lightweight Magnetorheological Energy Attenuation System.

Janicke, J.M., 1997. *Magnetic Measurements Handbook*. 2nd ed. Butler, NJ: Magnetic Research Press.

Knezevic, D. and Savic, V., 2006. Mathematical modeling of changing of dynamic viscosity, as a function of temperature and pressure, of mineral oils for hydraulic systems. *Facta Universitatis : Mechanical Engineering*, 4(1), pp. 27-34.

Krieger, I.M. and Elrod, H., 1953. Direct determination of the flow curves of non-Newtonian fluid II: shear rate in the concentric cylinder viscometer. *Journal of Applied Physics*, 24(2), pp. 134-36.

Laun, H.M., Gabriel, C. and Kieburg, C., 2010. Twin gap magnetorheometer using ferromagnetic steel plates - performance and validation. *Journal of Rheology*, 54, pp. 327-54.

Laun, H.M., Kormann, C. and Willenbacher, M., 1996. Rheometry on magnetorheological (MR) fluids. I. Steady shear flow in stationary magnetic fields. *Rheologica Acta*, 35, pp. 417-32.

LORD Materials Division, 1999. *Engineering Note : Magnetic Circuit Design*. Cary, NC: LORD Corporation.

Macosko, C.W., 1994. *Rheology: Principles, Measurements, and Applications*. VCH.

Manrique, L.A. and Porter, R.S., 1975. An improved Couette high shear viscometer. *Rheologica Acta*, 14, pp. 926-30.

Merriam-Webster, 2013. *Rheology*. [Online] Available at: http://www.merriam-webster.com/dictionary/rheology [Accessed 19 August 2013].

Mooney, M., 1931. Explicit formulas for slip and fluidity. *Journal of Rheology*, 2(2), pp. 210-22.

Moore, F. and Davies, L.J., 1956. The consistency of ceramic slips. *Transactions of the British Ceramics Society*, 55, pp. 313-38.

Morrison, F.A., 2001. *Understanding Rheology*. 1st ed. New York, United States: Oxford University Press.

National Instruments, 2012. *LabVIEW Manual*. [Online] Austin, TX: National Instruments Available at: http://www.ni.com/pdf/manuals/320999e.pdf [Accessed 27 Augustus 2013].

Palma, G., Pezzin, G. and Busulini, L., 1967. Viscous heating in coaxial cylinder viscometers. *Rheologica Acta*, 6(3), pp. 259-64.

Pipe, C.J. and Majmudar, T.S..M.G.H., 2008. High shear rate viscometry. *Rheologica Acta*, 47(5-6), pp. 621–42.

QuickSilver Controls, Inc., 2011. [Online] Available at: www.qcontrol.com.

Reiner, M., 1964. The Deborah number. *Physics Today*, 17, p. 62.

Rhim, W., Ohsaka, K., Paradis, P. and Spjut, R.E., 1999. Noncontact technique for measuring surface tension and viscosity of molten materials using high temperature electrostatic levitation. *Review of Scientific Instruments*, 70(6), pp. 2796-801.

Ritwik, 2012. *Measuring the Viscous Flow Behaviour of Molten Metals Under Shear*. Uxbridge, UK: Brunel University.

Roach, S. and Henein, H., 2005. A new method to dynamically measure the surface tension, viscosity, and density of melts. *Mettalurgical and Materials Transactions B*, 36(5), pp. 667-76.

Sahin, H., Wang, X.J. and Gordaninejad, F., 2009. Temperature dependence of magneto-rheological materials. *Journal of Intelligent Material Systems and Sructures*, 20, pp. 2215-22.

van Os, N., van Helden, A. and van den Berg, W., 1982. A new concentric-cylinder high-shear rate viscometer for measuring the viscosity of engine lubricants. *SAE Technical Papers*.

Walker LDJ Scientific, 2013. [Online] Available at: http://www.laboratorio.elettrofisico.com/liquid-green/interna2.asp.

Wang, X. and Gordaninejad, F., 2006. Study of magnetorheological fluids at high shear rates. *Rheologica Acta*, 45(6), pp. 899-908.

Chapter 3 References

Allan, R.S. and Mason, S.G., 1962. Particle behaviour in shear and electric fields. I. Deformation and burst of fluid drops. *Proceedings of the Royal Society A*, 267(1328), pp. 45-61.

de Gans, B.J., Duin, N.J., van den Ende, D. and Mellema, J., 2000. The influence of particle size on the magnetorheological properties of an inverse ferrofluid. *Journal of Chemical Physics*, 113(5), p. 11.

Ginder, J.M. and Davis, L.C., 1994. Shear stresses in magnetorheological fluids: role of magnetic saturization. *Applied Physics Letters*, 65(26).

Hiemenz, G.J., Hu, W. and Wereley, N.M., 2008. Semi-active magnetorheological helicopter crew seat suspension for vibration isolation. *Journal of Aircraft*, 45(3), pp. 945-53.

Hiemenz, G.J., Hu, W. and Wereley, N.M., 2009. Adaptive magnetorheological seat suspension fo the expeditionary fighting vehicle. *Journal of Physics: Conference Series*, 149(1).

Hu, W., Becnel, A.C. and Wereley, N.M., 2012. Measurement of magnetorheological fluids properties at high shear rate with controlled temperature. In *ICAST2012: 23rd International Conference on Adaptive Structures and Technologies*. Nanjing, China, 2012.

Kavlicoglu, B., Gordaninejad, F. and Wang, X., 2011. A unified approach for flow analysis of magnetorheological fluids. *Journal of Applied Mechanics*, 78(4), p. 10.

Klingenberg, D.J., Ulicny, J.C. and Golden, M.A., 2007. Mason numbers for magnetorheology. *J. Rheol.*, 51(5), pp. 883-93.

Knezevic, D. and Savic, V., 2006. Mathematical modeling of changing of dynamic viscosity, as a function of temperature and pressure, of mineral oils for hydraulic systems. *Facta Universitatis : Mechanical Engineering*, 4(1), pp. 27-34.

LORD Corporation, 2012. *MRF-132DG Magneto-Rheological Fluid*. [Online] Available at: http://www.lord.com/products-and-solutions/magneto-rheological-%28mr%29/product.xml/1645/2 [Accessed 2012].

Mao, M., Hu, W., Choi, Y.T. and Wereley, N.M., 2007. A Magnetorheological Damper with Bifold Valves for Shock and Vibration Mitigation. *J. of Intel. Mater. Sys. Struct*, 18(12), p. 1227.

Marshall, L., Zukoski, C.F. and Goodwin, J.W., 1989. Effects of electric fields on the rheology of non-aqueous concentrated suspensions. *J. Chem. Soc., Faraday Trans.*, 1(85), pp. 2785-95.

MIL-STD-810F, 2003. *Military Specification 810F 3.7.4.2*. Military Specification. Department of Defense.

Sahin, H., Wang, X. and Gordaninejad, F., 2009. Temperature dependence of magneto-rheological materials. *Journal of Intelligent Material Systems and Structures*, 20(18), pp. 2215-22.

Sherman, S. and Wereley, N.M., 2014. [Online] *Journal of Applied Physics*.

Smit, J. and Wijn, H.P.J., 1959. *Ferrites*. 1st ed. Eindhoven, Holland: N.V. Philips' Research Laboratories.

Stachowiak, G.W. and Batchelor, A.W., 2005. *Engineering Tribology*. 3rd ed. Burlington, MA: Elsevier Inc.

Ulicny, J.C., Golden, M.A., Namuduri, C.S. and Klingenberg, D.J., 2005. Transient response of magnetorheological fluids: Shear flow between concentric cylinders. *Journal of Rheology*, 49(1), pp. 87-104.

Volkova, O., Bossis, G., Guyot, M.B.V. and Reks, A., 2000. Magnetorheology of magnetic holes compared to magnetic particles. *Journal of Rheology*, 44(1), p. 14.

Chapter 4 References

Becnel, A.C., Hu, W., Hiemenz, G.J. and Wereley, N.M., 2010. Design and testing of a magnetorheological damper to control both vibration and shock loads for a vehicle crew seat. In *Proceedings of SPIE 7643*. Long Beach, CA, 2010. SPIE.

Bongers, P.M.H.C.T.J. and Dijkstra, L., 1990. *Back pain and exposure to WBV in helicopter pilots, exposures for MH-60S pilots*. 33rd ed.

Choi, S.B., Choi, J.H., Nam, M.H. and Cheong, C.C.L.H.G., 1999. A semi-active suspension using ER fluids for a commercial vehicle seat. *Journal of Intelligent Material Systems and Structures*, 9(8), pp. 601-06.

Choi, S.B., Lee, H.K. and Change, E.G., 2001. Field test results of a semi-active ER suspension system associated with skyhook controller. *Mechatronics*, 11, pp. 345-53.

Choi, Y.T. and Wereley, N.M., 2005. Biodynamic response mitigation to shock loads using magnetorheological helicopter crew seat suspensions. *Journal of Aircraft*, 42(5), pp. 1288-95.

Desjardins, S.P., 2006. The evolution of energy absorption systems for crashworthy helicopter seats. *Journal of the American Helicopter Society*, 51(2), pp. 15-163.

Desjardins, S.P., Zimmerman, R.E..B.A.O. and Merritt, N.A., 1989. *Aircraft Crash Survival Design Guide vol. IV - Aircraft Seats, Restraints, Litters, and Cockpit/Cabin Delethalization*. USAAVSCOM Technical Report 89-D-22D. Aviation Applied Technology Directorate.

Harrer, K.L. et al., 2005. Whole body vibration exposure for MH-60S pilots. In *Proceedings of the 43rd Annual SAFE Association Symposium*. Salt Lake City, UT, 2005.

Hiemenz, G.J., 2007. Semi-active magnetorheological seat suspensions for enhanced crashworthiness and vibration isolation of rotorcraft seats. Ph.D. Dissertation. Dept. of Aerospace Engineering, University of Maryland, College Park, MD

Hiemenz, G.J., Choi, Y.T. and Wereley, N.M., 2007. Semi-active control of vertical stroking helicopter crew seat for enhanced crashworthiness. *Journal of Aircraft*, 44(3), pp. 1031-34.

Hiemenz, G.J. and Hu, W..W.N.M., Aug. 25-28, 2008. Adaptive magnetorheological seat suspension for the expeditionary fighting vehicle. In *11th Conference on Electrorheological Fluids and Magnetorheological Suspensions*., Aug. 25-28, 2008. Journal of Physics: Conference Series.

Hiemenz, G.J., Hu, W. and Wereley, N.M., 2008. Semi-active magnetorheological helicopter crew seat suspension for vibration isolation. *Journal of Aircraft*, 45(3), pp. 945-53.

Hiemenz, G.J. and Wereley, N.M., 2013. *Rotary vane magnetorheological (MR) energy absorber*. Patent No. 8424656. US.

Hu, W. et al., 2012. Lightweight magnetorheological energy attenuation system for rotorcraft seats. In *American Helicopter Society Forum 68*. Fort Worth, TX, 2012.

Hu, W. and Wereley, N.M., 2011. Behavior of MR fluids at high shear rate. *International Journal of Modern Physics B*, 25(7), pp. 979-85.

Karnopp, D., Crosby, M. and Harwood, R., 1974. Vibration control using semi-active force generators. *Journal of Engineering for Industry*, 96(2), pp. 619-26.

Klingenberg, D.J., Ulicny, J.C. and Golden, M.A., 2007. Mason numbers for magnetorheology. *Journal of Rheology*, 51(5), p. 883.

LORD Corporation, 2012. *MRF-140CG Magneto-Rheological Fluid*. [Online] Available at: http://www.lord.com/products-and-solutions/magneto-rheological-%28mr%29/product.xml/1646 [Accessed 2012].

Marshall, L., Zukoski, C.F. and Goodwin, J.W., 1989. Effects of electric fields on the rheology of non-aqueous concentrated suspensions. *Journal of the Chemical Society, Faraday Transactions 1: Physical Chemistry in Condensed Phases*, 85, pp. 2785-95.

McManus, S.J., St. Clair, K.A., Boileau, P.E. and Boutin, J., 2002. Evaluation of vibration and shock attenuation performance of a suspension seat with a semi-active magnetorheological fluid damper. *Journal of Sound and Vibration*, 253(1), pp. 313-27.

Morrison, F.A., 2001. *Understanding Rheology*. 1st ed. New York, United States: Oxford University Press.

Richards, M. and Podob, R., 1997. Development of an Advanced Energy Absorber. In *Proceedings of the 35th Annual SAFE Symposium*., 1997.

Shanahan, D.F., Mastroiane, G. and Reading, T.D., 1986. *Back discomfort in U.S. Army mility helicopter aircrew members*. AGARD-CP-378, Vol. 21. Neuilly-sur-Siene, France: AGARD.

Wereley, N.M. and Pang, L., 1998. Nondimensional analysis of semi-active electrorheological and magnetorheological dampers using approximate parallel plate models. *Smart Materials and Structures*, 7(5), pp. 732-43.

Wu, X. and Griffin, M.J., 1997. A semi-active control policy to reduce the occurrence of severity of end-stop impacts in a suspension seat with an electrorheological fluid damper. *Journal of Sound and Vibration*, 203(5), pp. 781-93.

Chapter 5 References

Allan, R.S. and Mason, S.G., 1962. Particle behaviour in shear and electric fields. I. Deformation and burst of fluid drops. *Proceedings of the Royal Society A*, 267(1328), pp. 45-61.

Ashour, O., Rogers, C.A. and Kordonsky, W., 1996. MR fluids: materials characterization, and devices. *Journal of Intelligent Material Systems and Structures*, 7, pp. 123-30.

Becnel, A.C., Hu, W. and Wereley, N.M., 2012. Measurement of magnetorheological fluid properties at shear rates of up to 25,000 1/s. *IEEE Transactions on Magnetics*, 48(11), pp. 3525-28.

Carlson, J.D., 2005. MR fluids and devices in the real world. *International Journal of Modern Physics B*, 19(7,8,9), pp. 1463-70.

Chaudhuri, A., Wereley, N.M., Radhakrishnan, R. and Choi, S.B., 2006. Rheological parameter estimation for a ferrous nanoparticle-based magnetorheological fluid using Genetic Algorithms. *J. Intel. Mat. Syst. Str.*, 17, p. 261.

Choi, Y.T., Cho, J.U., Choi, S.B. and Wereley, N.M., 2005. Constitutive models of electrorheological and magnetorheological fluids using viscometers. *Smart Materials and Structures*, 14, pp. 1025-36.

de Gans, B.J., Duin, N.J., van den Ende, D. and Mellema, J., 2000. The influence of particle size on the magnetorheological properties of an inverse ferrofluid. *Journal of Chemical Physics*, 113(5), p. 11.

Escudier, M.P., Oliveira, P.J. and Pinho, F.T., 2002. Fully developed laminar flow of purely viscous non-Newtonian liquids through annuli, including the effects of eccentricity and inner-cylinder rotation. *International Journal of Heat and Fluid Flow*, 23(1), pp. 52-73.

Ginder, J.M. and Davis, L.C., 1994. Shear stresses in magnetorheological fluids: role of magnetic saturization. *Applied Physics Letters*, 65(26).

Gulley, G.L. and Tao, R., 1993. Static shear stress of electrorheological fluids. *Physical Review E*, 48(4), pp. 2744-51.

Hiemenz, G.J., Hu, W. and Wereley, N.M., 2008. Semi-active magnetorheological helicopter crew seat suspension for vibration isolation. *Journal of Aircraft*, 45(3), pp. 945-53.

Hiemenz, G.J., Hu, W. and Wereley, N.M., 2009. Adaptive magnetorheological seat suspension fo the expeditionary fighting vehicle. *Journal of Physics: Conference Series*, 149(1).

Hu, W., Becnel, A.C. and Wereley, N.M., 2012. Measurement of magnetorheological fluids properties at high shear rate with controlled temperature. In *ICAST2012: 23rd International Conference on Adaptive Structures and Technologies*. Nanjing, China, 2012.

Hu, W. and Wereley, N.M., 2011. Behavior of MR fluids at high shear rate. *International Journal of Modern Physics B*, 25(7), pp. 979-85.

Kavlicoglu, B., Gordaninejad, F. and Wang, X., 2011. A unified approach for flow analysis of magnetorheological fluids. *Journal of Applied Mechanics*, 78(4), p. 10.

Klingenberg, D.J., Ulicny, J.C. and Golden, M.A., 2007. Mason numbers for magnetorheology. *J. Rheol.*, 51(5), pp. 883-93.

Knezevic, D. and Savic, V., 2006. Mathematical modeling of changing of dynamic viscosity, as a function of temperature and pressure, of mineral oils for hydraulic systems. *Facta Universitatis : Mechanical Engineering*, 4(1), pp. 27-34.

LORD Corporation, 2012. *MRF-132DG Magneto-Rheological Fluid*. [Online] Available at: http://www.lord.com/products-and-solutions/magneto-rheological-%28mr%29/product.xml/1645/2 [Accessed 2012].

Mao, M., Hu, W., Choi, Y.T. and Wereley, N.M., 2007. A Magnetorheological Damper with Bifold Valves for Shock and Vibration Mitigation. *J. of Intel. Mater. Sys. Struct*, 18(12), p. 1227.

Marshall, L., Zukoski, C.F. and Goodwin, J.W., 1989. Effects of electric fields on the rheology of non-aqueous concentrated suspensions. *J. Chem. Soc., Faraday Trans.*, 1(85), pp. 2785-95.

Martin, J.E., Odinek, J. and Halsey, T.C., 1992. Evolution of structure in a quiescent electrorheological fluid. *Physical Review Letters*, 69(10), pp. 1524-28.

Mazlan, S.A., Ekreem, N.B. and Olabi, A.G., 2008. An investigation of the behaviour of magnetorheological fluids in compression mode. *Journal of Materials Processing Technology*, 201, pp. 780-85.

Meena, S. and Kandaswamy, P., 1999. The hydromagnetic flow between eccentric cylinders with velocity slip at the cylinder walls. *Korean Journal of Computational and Applied Mathematics*, 6(2), pp. 385-400.

MIL-STD-810F, 2003. *Military Specification 810F 3.7.4.2*. Military Specification. Department of Defense.

Rabinow, J., 1948. The magnetic fluid clutch. *AIEE Transactions*, 67, pp. 1308-15.

Rabinow, 1951. *Magnetic fluid torque and force transmitting device*. US Patent No. 2575360. US.

Sahin, H., Wang, X. and Gordaninejad, F., 2009. Temperature dependence of magneto-rheological materials. *Journal of Intelligent Material Systems and Structures*, 20(18), pp. 2215-22.

See, H., Mackenzie, S. and Boon, T.C., 2006. Effect of compression on the response of a magneto-rheological suspension. *Korea-Australia Rheology Journal*, 18(3), pp. 121-26.

Sherman, S. and Wereley, N.M., 2014. *Journal of Applied Physics*.

Smit, J. and Wijn, H.P.J., 1959. *Ferrites*. 1st ed. Eindhoven, Holland: N.V. Philips' Research Laboratories.

Stachowiak, G.W. and Batchelor, A.W., 2005. *Engineering Tribology*. 3rd ed. Burlington, MA: Elsevier Inc.

Tang, X., Zhang, X., Tao, R. and Rong, Y., 2000. Structure-enhanced yield stress of magnetorheological fluids. *Journal of Applied Physics*, 87(5), pp. 2634-38.

Tao, R., 2001. Super-strong magnetorheological fluids. *Journal of Physics: Condensed Matter*, 13, pp. R979-99.

Tao, R., 2013. Microstructures and physics of super-strong magnetorheological fluids. In N.M. Wereley, ed. *Magnetorheology: Advances and Applications*. 1st ed. Cambridge, England: Royal Society of Chemistry. pp. 179-205.

Tao, R. and Jiang, Q., 1994. Simulation of structure formation in an electrorheological fluid. *Physical Review Letters*, 31(1), pp. 205-08.

Tao, R. and Sun, J.M., 1991. Three-dimensional structure of induced electrorheological solid. *Physical Review Letters*, 67, pp. 398-401.

Ulicny, J.C., Golden, M.A., Namuduri, C.S. and Klingenberg, D.J., 2005. Transient response of magnetorheological fluids: Shear flow between concentric cylinders. *Journal of Rheology*, 49(1), pp. 87-104.

Volkova, O., Bossis, G., Guyot, M.B.V. and Reks, A., 2000. Magnetorheology of magnetic holes compared to magnetic particles. *Journal of Rheology*, 44(1), p.14.

Vyalov, S.S., 1986. *Rheological Fundamentals of Soil Mechanics*. New York, NY: Elsevier.

Zhang, X.Z., Gong, X.L., Zhang, P.Q. and Wang, Q.M., 2004. Study on the mechanism of the squeeze-strengthen effect in magnetorheological fluids. *Journal of Applied Physics*, 96(4), pp. 2359-66.

Chapter 6 References

Bai, X. and Wereley, N.M., 2014. A fail-safe magnetorheological energy absorber for shock and vibration isolation. [Online] *Journal of Applied Physics*.

Choi, Y.T., Wereley, N.M. and Jeon, Y.S., 2005. Semi-active vibration isolation using magnetorheological isolators. *AIAA Journal of Aircraft*, 42(5), pp. 1244-51.

Knaian, A., 2010. *Electropermanent magnetic connectors and actuators: devices and their application in programmable matter*. Ph.D. Thesis, Dept. of Electrical Engineering and Computer Science, Massachussets Institute of Technology. Cambridge, MA

Raghunath, G., Flatau, A.B., Purekar, A. and Yoo, J.H., 2013. Non-contact torque measurement using magnetostrictive Galfenol. In *Proc. of the ASME 2013 Conference on Smart Materials, Adaptive Structures and Intelligent Systems*. Snowbird, UT, 2013. ASME.

Steinbrecher, T., 2010. *Heatsink Guide*. [Online] Available at: http://www.heatsink-guide.com/peltier.htm [Accessed 31 January 2014].